

Theoretical and Experimental Studies of Heterogeneous  
Chemical Processes leading to Stratospheric Ozone Depletion

by

Yves André Mantz

B.A. Chemistry  
Franklin & Marshall College, 1996

SUBMITTED TO THE DEPARTMENT OF CHEMISTRY IN PARTIAL  
FULFILLMENT OF THE REQUIREMENTS FOR THE DEGREE OF  
DOCTOR OF PHILOSOPHY IN CHEMISTRY  
AT THE  
MASSACHUSETTS INSTITUTE OF TECHNOLOGY  
FEBRUARY 2002

© 2002 Massachusetts Institute of Technology. All rights reserved.

Signature of Author: \_\_\_\_\_

Department of Chemistry  
December 17, 2001

Certified by: \_\_\_\_\_

Mario J. Molina  
Institute Professor  
Thesis Supervisor

Certified by: \_\_\_\_\_

Bernhardt L. Trout  
Doherty Assistant Professor of Chemical Engineering  
Thesis Supervisor

Accepted by: \_\_\_\_\_

Robert W. Field  
Chairman  
Departmental Committee on Graduate Students

This doctoral thesis was examined by a Thesis Committee of the Department of Chemistry whose members are:

Professor Jeffrey I. Steinfeld \_\_\_\_\_  
Chairman

Professor Mario J. Molina \_\_\_\_\_  
Thesis Supervisor

Professor Bernhardt L. Trout \_\_\_\_\_  
Thesis Supervisor

# Theoretical and Experimental Studies of Heterogeneous Chemical Processes leading to Stratospheric Ozone Depletion

by

Yves André Mantz

Submitted to the Department of Chemistry  
on December 17, 2001 in Partial Fulfillment of the  
Requirements for the Degree of Doctor of Philosophy in  
Chemistry

## ABSTRACT

The microscopic chemical mechanisms of heterogeneous reactions involving HCl on crystalline ice and nitric acid trihydrate (NAT) are of fundamental interest to physical chemists, because such reactions yield “active” chlorine compounds that are readily photolyzed to yield radicals responsible for the annual destruction of polar stratospheric ozone. Using molecular-orbital and density-functional-based computational methods that are extensively validated, partial dissociation of HCl is shown to be kinetically rapid and thermodynamically favorable on an extended ice *h* surface model with two dangling OH groups in close proximity to adsorbed HCl at a binding site on the surface. Additionally, surface disordering of this ice model is observed at polar stratospheric temperatures when HCl is adsorbed at this site. The partial dissociation of HCl on/atop ice will compete with other proposed mechanisms only if the local density of surface dangling OH groups is high. This alternative mechanism of chlorine activation is not important on NAT, based on the theoretical study of HCl interacting with various low index NAT faces. This is due to the fact that the NAT (001) face (which may be the most prevalent in the polar stratosphere) possesses a low surface density of dangling OH groups. In addition, other selected defect-free low-index NAT faces do not have their dangling OH groups situated favorably for effective partial solvation of HCl.

The efficiency of aluminum oxide particulate, which is emitted by solid rocket motors (SRMs), as a catalyst for “activating” chlorine involved in the less dramatic, but still consequential, depletion of ozone at mid-latitudes in the lower stratosphere is also of interest. The pseudo-first-order rate constants for the heterogeneous reaction of ClONO<sub>2</sub> + HCl on laboratory  $\alpha$ -alumina and actual SRM emissions are measured experimentally using a narrow-bore capillary tube interfaced to a chemical ionization mass spectrometer under reactant partial pressure and temperature conditions typically encountered in the mid-latitude lower stratosphere. Preliminary results indicate that the rate constants are the same. It is likely that the global atmospheric models that employ a reaction probability of 0.02 for ClONO<sub>2</sub> + HCl previously measured on laboratory  $\alpha$ -alumina do not need to be revised.

Thesis Supervisor: Mario J. Molina

Title: Institute Professor

Thesis Supervisor: Bernhardt L. Trout

Title: Doherty Assistant Professor of Chemical Engineering

## Table of Contents

Acknowledgments.....	7
Chapter 1: Introduction.....	8
1.1. Some properties of Earth’s atmosphere.....	8
1.2. Research motivation and organization of thesis.....	9
1.2.1. Molecular-level mechanism of polar ozone depletion.....	10
1.2.2. Chlorine activation by solid rocket motor emissions.....	14
1.3. Overview of quantum-chemical DFT approach.....	15
1.3.1. Wavefunction optimization.....	16
1.3.2. Geometry optimization.....	18
1.3.3. Classical Car-Parrinello molecular dynamics simulations.....	20
References for Chapter 1.....	20
List of Figures for Chapter 1.....	24
Figures for Chapter 1.....	25
Chapter 2: First-principles molecular-dynamics study of surface disordering of the (0001) face of hexagonal ice.....	28
Abstract.....	28
2.1. Introduction.....	28
2.2. Ice model.....	30
2.3. Methodology.....	32
2.4. Results and discussion.....	33
2.4.1. Translational disorder.....	33
2.4.2. Rotational disorder.....	35
2.4.3. Translational mobility.....	38
2.4.4. Hydrogen bonding analysis.....	38
2.4.5. Pair distribution functions.....	40
2.4.6. Heat capacity.....	42
2.4.7. Effect of fixing the bottommost bilayer.....	43
2.5. Summary of disorder analysis.....	44
2.6. Conclusions.....	46
2.7. Acknowledgements.....	46
2.8. Appendix.....	46
References for Chapter 2.....	49
List of Figures for Chapter 2.....	53
Figures for Chapter 2.....	55
Chapter 3: First-principles theoretical study of molecular HCl adsorption on a hexagonal ice (0001) surface.....	70
Abstract.....	70
3.1. Introduction.....	70
3.2. Ice surface models.....	73
3.3. Methodology.....	76
3.4. Optimized geometries and binding energies.....	78

3.4.1. HCl•H <sub>2</sub> O.....	78
3.4.2. Cluster model (4W1A).....	79
3.4.3. Infinite surface models.....	81
3.5. Further discussion of infinite-surface-model results.....	82
3.6. Atmospheric relevance and future work.....	85
3.7. Conclusions.....	85
3.8. Acknowledgements.....	86
References and notes for Chapter 3.....	87
Tables for Chapter 3.....	92
List of Figures for Chapter 3.....	96
Figures for Chapter 3.....	97
Chapter 4: The interaction of HCl with the (0001) face of hexagonal ice studied theoretically via Car-Parrinello molecular dynamics.....	100
Abstract.....	100
4.1. Introduction.....	100
4.2. Extended ice surface models and simulations.....	101
4.3. Results and discussion.....	102
4.3.1. Validation of computational approach: select optimizations....	102
4.3.2. Car-Parrinello molecular dynamics and energetics of HCl on hexagonal ice.....	102
4.3.3. Effect of HCl on the surface disordering of hexagonal ice.....	105
4.4. Atmospheric implications.....	106
4.5. Conclusions.....	106
4.6. Acknowledgements.....	107
References for Chapter 4.....	107
List of Figures for Chapter 4.....	109
Figures for Chapter 4.....	110
Chapter 5: A theoretical study of the interaction of HCl with crystalline NAT.....	115
Abstract.....	115
5.1. Introduction.....	116
5.2. Theoretical approaches.....	119
5.2.1. Brief description.....	119
5.2.2. Validation: Optimization of relevant “building blocks” and bulk NAT.....	120
5.3. Results and discussion.....	122
5.3.1. Optimization of low index NAT faces, and selection and analysis of the NAT (001) face.....	122
5.3.2. Geometry and energetics of molecular HCl adsorbed on NAT and coverage dependence.....	125
5.3.3. Car-Parrinello molecular dynamics of molecular HCl adsorbed on NAT.....	127
5.4. Atmospheric implications.....	129
5.5. Conclusions.....	130
5.6. Acknowledgments.....	131

References for Chapter 5.....	131
Tables for Chapter 5.....	134
List of Figures for Chapter 5.....	137
Figures for Chapter 5.....	139
Chapter 6: The reaction probability of ClONO <sub>2</sub> + HCl on SRM emissions.....	149
Abstract.....	149
6.1. Introduction.....	149
6.2. Experimental Setup.....	153
6.2.1. Miniaturized Flowtube CIMS.....	153
6.2.2. Sampling of Particulate SRM Emissions.....	155
6.2.3. Characterization of the Alumina Particles.....	155
6.2.4. Substrate Tube Preparation.....	155
6.3. Results and discussion.....	157
6.3.1. Spectroscopic Determination of Decay of ClONO <sub>2</sub> .....	157
6.3.2. Kinetics Measurements.....	158
6.4. Conclusions.....	161
6.5. Acknowledgements.....	162
6.6. Appendix.....	162
6.6.1. Synthesis of Chlorine Nitrate.....	162
6.6.2. Correction for Radial Diffusion.....	164
6.6.3. Correction for Internal Diffusion.....	166
6.6.4. Derived Expressions for the Reaction Probability.....	173
References for Chapter 6.....	176
Tables for Chapter 6.....	179
List of Figures for Chapter 6.....	182
Figures for Chapter 6.....	184
Chapter 7: Conclusions and future directions.....	192
References for Chapter 7.....	195
Curriculum Vitae.....	196

## Acknowledgments

I, along with Keith Broekhuizen, joined Mario Molina's research group in the fall of 1996, one year after he received the 1995 Nobel Prize in Chemistry along with Professors F. Sherwood Rowland and Paul J. Crutzen "for their work in atmospheric chemistry, particularly concerning the formation and decomposition of ozone." Five years later, I am absolutely convinced that I made the right decision. I thank Mario and his wife / closest collaborator Luisa for their guidance, insights, and encouragement during the past five years and for giving me the invaluable opportunity to work on both theoretical and experimental research projects.

Another individual at M.I.T. who deserves special recognition and thanks is Bernhardt Trout, who closely supervised my progress during the past three years while I was working with state-of-the-art theoretical methods. Bernhardt was an outstanding teacher who played an important role in my growth, development, and success as a research scientist. Most recently, he introduced me to Glenn Martyna, my current postdoctoral supervisor.

Because of the outstanding support structure of graduate students and postdoctoral associates that I was fortunate to be a part of during 1996 – 2001, my productivity and enjoyment of life as a graduate student were increased immeasurably. All of the graduate students and postdoctoral associates that I met during my tenure at M.I.T. were concerned, extremely helpful colleagues. In the Trout group, I would like to thank Claudiu Giurumescu, Cynthia Lo, and Jih-Wei Chu for working hard as our de facto system administrators and for teaching me about computers, Xi Lin, a fellow graduate student who offered insights into my research, Zhitao Cao for assistance using Gaussian, Ravi Radhakrishnan and Oleg Mazzyar, whose advice while I was making a postdoctoral decision was helpful, and Vivian McNeill, to whom I am passing the torch and who will begin by studying  $\text{ClONO}_2 + \text{HCl}$  on ice using CPMD. Others who deserve acknowledgement include Brian Anderson, Alexander Demurov, Philip Kwaako, Luke Shulenburg, and Brian Baynes.

Transitioning to the Molina group, I will begin by singling out Franz Geiger, who lent his considerable scientific expertise and experience to the theoretical chemistry research and trained me to write (scientific publications, research proposals, and even resumes!) more effectively. Markus Haider, who worked with me studying the reaction of  $\text{ClONO}_2 + \text{HCl}$  on SRM emissions, facilitated my learning, contributed many insights, and organized informal luncheons, ice skating excursions, trips to the M.I.T. Talbot House, etc., which I enjoyed. Renyi Zhang served as a mentor in the beginning, teaching me the basics of CIMS and advising me in various endeavors. Other members whom I would like to thank here include Leonard Newton, Francisco Tablas, Martin Hunter, Lukas Gutzwiller, Shan-Hu Lee, Christophe Guimbaud, Andrei Guschin, Allan Bertram, Manjula Canagaratna, Thomas Koop, Dara Salcedo, Jennifer Lipson, Geoff Smith, Keith Broekhuizen, and Bilal Zuberi.

Lastly and most importantly, I would like to thank with all my heart my parents, to whom this thesis is dedicated, as well as my grandparents, relatives, and friends for their advice, love, support, and encouragement (during my tenure as a graduate student).

## Chapter 1: Introduction

### 1.1. SOME PROPERTIES OF EARTH'S ATMOSPHERE

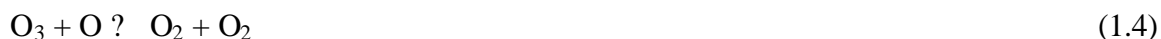
Earth's atmosphere comprises a tiny fraction of the mass and diameter of the planet. The total mass of the atmosphere,  $5.137 \times 10^{18}$  kg,<sup>1</sup> is only 0.000086 % of the Earth's mass.<sup>2</sup> Atmospheric pressure decreases exponentially with altitude (in regions of constant temperature),<sup>1</sup> so that the first 50 km of the atmosphere contains 99.9 % of the total atmosphere mass<sup>1</sup> but is only 0.78 % of the Earth's radius.<sup>2</sup>

The variation of the average temperature profile with altitude is the basis for dividing the atmosphere into layers.<sup>3</sup> The troposphere extends from ground level up to 10-15 km, depending on latitude (i.e., increasing as one approaches the equator), season, and meteorological conditions and is characterized by extensive vertical mixing due to decreasing temperature with altitude (and turbulence due to local topography). The chemistry is dominated by oxidation reactions of the trace radical OH. The stratosphere extends from the tropopause (at 10-15 km) up to 50 km, is characterized by slow vertical mixing due to the inverted or increasing temperature profile, and the chemistry is dominated by reactive processes leading to production and destruction of ozone. Higher layers include the mesosphere (from the stratopause up to 80-90 km), thermosphere (from ~100 km up to ~500 km), and exosphere (beyond ~500 km). The majority of air molecules are inert species, i.e., N<sub>2</sub> (78.1 %), O<sub>2</sub> (20.9 %), and noble gases.

The highest absolute and by far relative concentrations (or mole fractions / mixing ratios) of ozone are found in the lower stratosphere. "Good" stratospheric ozone attenuates the intensity of mutagenic UV-B sunlight (290-320 nm) that reaches the Earth's surface.<sup>4</sup> The deleterious effects of increased UV-B exposure include (1) increased incidence of cataract and skin cancer, (2) damage to plants and microbes and a shift in the balance of competition among higher plants, (3) decreased growth, photosynthesis, and reproduction of phytoplankton (thus affecting the food web), (4) an increase in "bad" tropospheric ozone in polluted areas (high NO<sub>x</sub>), and (5) degradation of the physical and mechanical properties of polymers.<sup>5</sup> Consequently, atmospheric chemistry that affects the abundance of stratosphere ozone is of paramount importance.



The steady-state production and destruction of stratospheric ozone is controlled by the gas-phase Chapman cycle involving an inert third body  $M = N_2$  or  $O_2$ , first proposed in 1930<sup>6</sup> and shown in Rxs. (1.1) – (1.4).



By themselves, Rxs (1.1) – (1.4) lead to an overestimation of ozone,<sup>3</sup> requiring the inclusion of gas-phase catalytic cycles involving as a first approximation  $NO_x$ ,<sup>7</sup>  $ClO_x$ ,<sup>8,9</sup> and  $HO_x$  species<sup>10</sup> that convert “odd oxygen” (O and  $O_3$ ) into  $O_2$ , as depicted in Rxs. (1.5) – (1.6), before the cycle is disrupted by a chain-terminating step. The predominant source of stratospheric  $NO_x$  is emissions from supersonic aircraft,<sup>11</sup> while  $ClO_x$  is generated from Cl radicals produced via photolysis of anthropogenic CFCs<sup>9</sup> and related manmade organic chlorine compounds ( $CCl_4$ ,  $CH_3CCl_3$ ) and predominantly natural  $CH_3Cl$ . Bromine compounds, e.g., halons, are also involved in gas-phase chemistry leading to stratospheric ozone destruction. Professors Crutzen, Rowland, and Molina, intimately involved in the elucidation of these cycles, were awarded the Nobel Prize in Chemistry in 1995. The investigation of heterogeneous atmospheric processes that affect the abundance of stratospheric ozone is the subject of this thesis.



## 1.2. RESEARCH MOTIVATION AND ORGANIZATION OF THESIS

From the formation of the Antarctic Ozone Hole to the chemistry of cloud droplets, stratospheric sulfate aerosols, and clear air aerosols (e.g., sea-salt particles), scientists now understand that the role played by heterogeneous chemistry in determining the chemical composition of Earth’s atmosphere is crucial. This fact is remarkable considering that prior to the publication of the discovery of the Antarctic Ozone Hole in 1985,<sup>12</sup> heterogeneous

atmospheric chemistry as a field of study was non-existent. However, a careful accounting and physiochemical understanding of heterogeneous processes is essential. Our objective is to advance the state of knowledge regarding heterogeneous atmospheric chemistry by focusing on processes that lead to the destruction of stratospheric ozone at the poles and mid-latitudes.

### 1.2.1 Molecular-level mechanism of polar ozone depletion

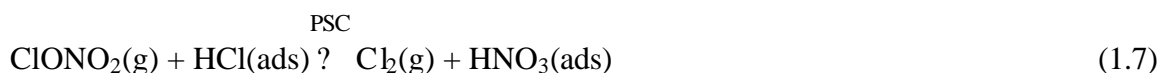
In 1985, Farman published the first evidence of anomalously large annual depletions in the total Antarctic ozone column density, i.e., the amount of O<sub>3</sub> in a column extending from ground to space, during early spring (the “Ozone Hole”).<sup>12</sup> Increasing in extent since 1985,<sup>13,14</sup> polar stratospheric ozone depletion may be leveling off: The 2001 Ozone Hole peaked at about 26 million km<sup>2</sup>, three times the size of the United States and about the same size as during the past three years, according to EPTOMS<sup>15</sup> and SBUV/2<sup>16</sup> satellite measurements (Figure 1.1).

<Figure 1.1 here>

Ozonesonde balloon soundings indicate ozone destruction occurs predominantly in the lower stratosphere, e.g., as the October 11, 2001 profile<sup>17</sup> of Antarctic ozone in Figure 1.2 shows. In 1997, the first observations of significant depletion of Arctic ozone were reported.<sup>18</sup>

<Figure 1.2 here>

In order to explain large depletions of polar ozone, heterogeneous chemistry<sup>19</sup> that refers to reactions or processes that occur in or on ambient condensed phases that are in contact with the gas phase is invoked.<sup>20,21</sup> Closed-shell molecular species exhibit, in the presence of specific catalytic solid or liquid particle surfaces, a high reactivity and efficient conversion into products. The “activation” of chlorine on the surfaces of polar stratospheric cloud (PSC) particles, e.g., Rx. (1.7), is critical to polar stratospheric ozone destruction (Figure 1.3).



During the polar winter, an atmospheric vortex (of wind circulation), particularly strong over Antarctica, is established. As the temperature of this isolated air mass falls, polar stratospheric clouds (PSCs) form. The PSC cloud particles, consisting either of water ice *Ice* below ~185 K, given typical ( $\sim 10^{-4}$  Torr) partial pressures of water vapor, or nitric acid trihydrate (NAT) below ~195 K, given typical partial pressures of  $\text{HNO}_3$  ( $\sim 10^{-8}$ - $10^{-7}$  Torr) and  $\text{H}_2\text{O}$ , catalytically “activate” reservoir forms of chlorine (and bromine). Additionally, in Rx. (1.7),  $\text{NO}_x$  is sequestered as  $\text{HNO}_3$ , preventing re-formation of  $\text{ClONO}_2$ , making Rx. (1.7) the most important chlorine activation reaction. When sunlight returns during early spring, the “active” chlorine (and bromine) compounds are photolyzed, releasing chlorine (and bromine) radicals that destroy ozone via gas-phase catalytic cycles, the most efficient of which<sup>22,23</sup> is shown in Figure 1.3. Recent model calculations suggest increased polar stratospheric ozone losses and delayed eventual recovery owing to increasing greenhouse-gas concentrations.<sup>24</sup>

<Figure 1.3 here>

While experimental measurements indicate that chlorine activation reactions involving HCl are able to proceed efficiently on solid PSC particles,<sup>25,26</sup> the fundamental microscopic chemical mechanisms of heterogeneous chlorine activation reactions involving HCl, such as Rx. (1.7), are still being actively debated. Langmuir isothermal co-adsorption<sup>27</sup> and subsequent reaction of co-adsorbates, e.g., HCl and  $\text{ClONO}_2$  in Rx. (1.7), might be the most likely possible mechanism, given the past successes of this model.<sup>27</sup> However, it is difficult to reconcile published measurements<sup>28-31</sup> of HCl surface coverage ( $\theta$ ) approaching one monolayer (ML) with calculations<sup>32,33</sup> of the physisorption energy of molecular HCl. Furthermore, previously published experimental studies<sup>25,26</sup> indicate that the efficiency of Rx. (1.7) is zeroth order with respect to the partial pressure of HCl above  $10^{-7}$  Torr, which however is greater than that typically encountered ( $10^{-8}$  –  $10^{-7}$  Torr) in the polar stratosphere.

An alternative mechanism proposed by Molina<sup>34</sup> is based on the fact that ice surfaces are significantly disordered at temperatures well below the bulk freezing point.<sup>35</sup> Molina hypothesizes that the PSC particle surface is significantly disordered at typical polar stratospheric temperatures (~190 K) in the presence of HCl, and partial solvation of HCl within

the disordered PSC particle surface occurs, leading to heterolytic dissociation of HCl and, in Rx. (1.7), facile attack by Cl<sup>-</sup> on the Cl<sup>+</sup> in ClONO<sub>2</sub>. This mechanism involves ionic Cl, explaining the rate enhancement of, e.g., Rx. (1.7) relative to the gas phase. However, there have been no experimental studies (e.g., ellipsometry) of the effect of HCl on the surface of either water ice or NAT, and only one recent classical-quantum theoretical study<sup>36</sup> indicating that the effect of HCl on ice surface disordering is negligible at low HCl coverage.

Based on the experimental observation<sup>37</sup> that the ice surface is very dynamic (exchanging more than 10 bilayers per second when in equilibrium with its vapor phase at 185 K), Bianco and Hynes suggest a third possible mechanism. Their mechanism involves dissociation ( $\Delta G = -28$  kJ/mol) of HCl incorporated within the dynamic ice lattice,<sup>38</sup> followed by S<sub>N</sub>2 attack by Cl<sup>-</sup> (at or near the surface), e.g., on the Cl<sup>+</sup> in ClONO<sub>2</sub> accompanied by a proton transfer to the ice lattice.<sup>39</sup> The formation of weakly held Cl<sub>2</sub> by this mechanism is consistent with the observed “prompt” appearance of Cl<sub>2</sub> over tens of milliseconds.<sup>40</sup> A final possible mechanism involving “attachment-detachment” by NO<sub>3</sub><sup>-</sup> ions is suggested by the work of Mebel and Morokuma.<sup>41</sup>

The uncertainty surrounding these proposed mechanisms, and the debate regarding the importance of each, is due to several factors including the following:

- (1) The state of HCl on PSC particles, i.e., molecularly or dissociatively adsorbed, is unclear experimentally. Both FTIR transmission spectroscopy<sup>42</sup> of thin (1 μm) crystalline ice films (T = 140 – 150 K, θ = 1 – 50 ML) and thermal desorption mass spectrometry<sup>43</sup> of crystalline films (T = 100 – 200 K, θ = 2250 ML) indicate that HCl is ionized at high surface coverages, where ionic hydrates of HCl are thermodynamically stable.<sup>34,44</sup> However, it is difficult to perform accurate measurements in the regions of relevance, and the state at stratospherically relevant coverage on ice is unclear: Static ion mass spectrometry<sup>45</sup> of crystalline films (T = 90 – 150 K, θ = 1 – 2 ML) indicates an ionic form, whereas FTIR spectroscopy<sup>46</sup> of D<sub>2</sub>O films (T = 125 – 145 K, θ = 0.3 ML) suggests a molecular form. Furthermore, there have been no experimental or theoretical studies that address this particular issue on NAT.
- (2) The presence of a disordered surface on PSC particles is only hypothesized and not yet verified experimentally. The only (theoretical) investigation<sup>36</sup> available does not address

the extent of ice surface disordering at near monolayer (stratospherically relevant) HCl coverage, and does not address the effect on NAT.

- (3) Other important variables, such as the role of surface dangling (non-hydrogen-bonding) OH groups, have not been adequately addressed. Experiments indicate that the surface density of dangling OH groups on amorphous ice is greater than on crystalline ice,<sup>47</sup> and that the density on liquid water exceeds 20 %, <sup>48</sup> but there are no quantitative measurements of dangling OH surface density on ice, no studies of dangling OH surface density on NAT, and no experimental studies of their role in promoting chlorine activation. Very recently, there have been limited theoretical studies<sup>49,50</sup> examining the interaction of HCl with surface dangling OH groups.

As a first step towards understanding better chlorine activation on PSC particles (and addressing the three points enumerated above), in this thesis we examine the interaction of HCl with ice and NAT using state-of-the-art theoretical methods. In Chapter 2, we develop an extended (periodic) model of an ice surface and characterize the surface by bilayer as a function of temperature from a surface disordering point of view by defining and analyzing various order parameters. In Chapter 3, we study the adsorption of molecular HCl on various extended model ice surfaces, paying particular attention to the effect of surface dangling OH groups. In Chapter 4, we perform dynamical simulations of HCl and conclude that adsorbed HCl is partially dissociated under certain conditions, depending on the number of surface dangling OH groups near the adsorption site. This implies that  $\text{Cl}^{\ominus}$  may attack  $\text{Cl}^{\oplus}$  of incident  $\text{ClONO}_2(\text{g})$  from atop the ice surface, a new alternative mechanism of chlorine activation. We also demonstrate that the surface of ice is disordered at stratospheric temperature for high HCl coverages under certain conditions. In Chapter 5, we develop and characterize a model of NAT and, paralleling the development in Chapters 2 – 4, characterize the adsorption of molecular HCl and the dynamical interaction on NAT, paying particular attention to the role of surface dangling OH groups. Each of these chapters is self-contained, with its own introduction and relevant background, results, discussion (including of atmospheric implications), and detailed conclusion; Chapters 2 – 4 each represent a recently published peer-reviewed scientific publication, and Chapter 5 was recently submitted for publication.

### 1.2.2 Chlorine activation by solid rocket motor emissions

With the realization that mid-latitude stratospheric ozone levels are falling by several percent/decade,<sup>13,14</sup> and that computer models excluding heterogeneous chemistry do not adequately predict the loss,<sup>3,51</sup> experimentalists are characterizing heterogeneous processes that may contribute to this loss. Substrates available for heterogeneous reaction at mid-latitudes include droplets of liquid H<sub>2</sub>SO<sub>4</sub>, soot, meteorite dust, and alumina (aluminum oxide, Al<sub>2</sub>O<sub>3</sub>).

The worldwide Junge layer of stratospheric sulfuric acid (SSA) droplets (~0.1 μm diameter, 60 – 80% wt H<sub>2</sub>SO<sub>4</sub>, 1 – 10/cm<sup>3</sup>, 1 μm<sup>2</sup>/cm<sup>3</sup>) is formed mainly by oxidation of OCS, although oxidation of SO<sub>2</sub> emissions from volcanic eruptions is also a significant source.<sup>3,19</sup> Despite its relative inefficiency in promoting chlorine activation (compared to PSCs),<sup>25,26</sup> it contributes significantly to stratospheric ozone destruction, in particular via hydrolysis of N<sub>2</sub>O<sub>5</sub>.<sup>3</sup>

Soot, or black carbon, is the carbonaceous fraction of ambient particulate matter consisting both of elemental carbon and a variety of organic compounds.<sup>3</sup> Unlike the micro- and macrostructure, the morphology of soot is highly variable. Aircraft soot is fractal, consisting of 20-nm branching chain aggregates with extremely high surface area, and an excellent candidate for heterogeneous reaction.<sup>52</sup> Several potentially important reactions on soot are being actively investigated,<sup>53-56</sup> and their effects on stratospheric ozone depletion are being ascertained.<sup>57</sup>

Meteorite debris is yet another substrate to consider. However, the fate of the debris is likely to become coated by H<sub>2</sub>SO<sub>4</sub> and serve as condensation nuclei for SSA.<sup>58</sup>

The adverse environmental impacts of the Space Shuttle are numerous,<sup>59</sup> including the effect of the chlorine emissions on stratospheric ozone.<sup>60</sup> Its solid-fuel rocket motors (SRM) also emit particulate alumina in copious<sup>59</sup> and (due to increased traffic) increasing amounts.<sup>61</sup> The ablation of spacecraft paint is another source of alumina.<sup>59</sup> Researchers have collected and characterized the emissions.<sup>62-66</sup> However, investigations of their chemical reactivity have relied on hexagonal-α alumina as a proxy for the actual emissions. Published studies employing α-alumina include adsorption and desorption of H<sub>2</sub>O,<sup>67-71</sup> HCl,<sup>72</sup> and alkane chains<sup>73</sup> and heterogeneous reaction of NO<sub>2</sub>.<sup>74</sup> The only study of chlorine activation is that of ClONO<sub>2</sub> + HCl on laboratory α-alumina by Molina and co-workers,<sup>75</sup> who measure a reaction probability of 2 %, or 0.02. This is a factor of 10 less than that on ice, consistent with a mechanism of

incomplete solvation of HCl in the several water layers adsorbed on alumina.<sup>75</sup> Employing this probability in their global atmosphere model, Jackman and co-workers report that the effect of ClONO<sub>2</sub> + HCl on  $\alpha$ -alumina results in an annually-averaged global total loss of 0.01 %, compared to 0.023 % from the emitted HCl participating in gas-phase chemistry.<sup>76</sup>

The study<sup>75</sup> by Molina and co-workers provides a useful measurement of a modeling parameter necessary to predict future levels of stratospheric ozone loss due to SRM emissions and the effect of different launch scenarios. However, the particulate emissions from SRMs are not identical to the clean, non-porous  $\alpha$ -alumina used as a proxy in the laboratory study. Real emissions are a mixture of hexagonal- $\alpha$  and cubic- $\gamma$  forms of alumina.<sup>77</sup> Additionally, the nature of the surfaces is known to be different, with the actual emissions contaminated by chlorides and oxychlorides.<sup>75</sup> Because the nature of the surface is crucial, measurement of the reaction probability of Rx. (7) on actual SRM emissions would serve as a useful validation.

Our most recent attempt to perform this measurement is described in Chapter 6. The particulate SRM emissions are obtained from Thiokol Inc., involving mg quantities, rather than from an actual launch site, where it would be possible to collect several grams. Use of a chemical ionization mass spectrometer interfaced to the traditional wide-bore flow tube is thus impractical for performing this measurement. A novel setup involving a narrow capillary tube is used instead, upon which limited substrate is much more easily and uniformly deposited.

### **1.3. Overview of quantum chemical DFT approach**

Towards better understanding polar stratospheric chlorine activation, we study as a first step the interaction of HCl with ice and NAT and its effect on the structure of the surface. State-of-the-art theoretical methods are used, which include plane-wave density-functional-based methods for optimizing the wave function and the geometry of systems and for performing classical MD simulations, as implemented in the code CPMD.<sup>78</sup> These methods are outlined below, specifying where appropriate the values of particular parameters/quantities that were actually used in the calculations described in Chapters (2) – (5) of this thesis; rigorous in-depth discussions of these different methods are provided elsewhere.<sup>79-82</sup> The justification for our choice of methods in this thesis is that the tradeoff between model size and accuracy of results is judiciously made.

### 1.3.1. Wavefunction optimization

The total energy  $E[\rho(\mathbf{r})]$  as a functional of the electronic density  $\rho(\mathbf{r}) = \sum_i^{\infty} n_i |\psi_i|^2$ , where  $0 = n_i = 1$  are occupation numbers and  $\{\psi_i(\mathbf{r})\} = \{\psi_i\}$  is the set of orbitals, of  $N_e$  interacting electrons at positions  $\mathbf{r}_i$  in an external potential  $v(\mathbf{r}; \mathbf{R})$  of  $N_n$  nuclei at positions  $\mathbf{R}_I$  is written as<sup>79</sup>

$$E[\rho(\mathbf{r})] = T[\rho(\mathbf{r})] + V_{ne}[\rho(\mathbf{r}); \mathbf{R}_I] + V_{ee}[\rho(\mathbf{r})] + V_{nn}(\mathbf{R}_I) \quad (1.8)$$

where  $T[\rho(\mathbf{r})]$  is the electronic kinetic energy,  $V_{ne}[\rho(\mathbf{r})]$  is the electron-nuclear attraction,  $V_{ee}[\rho(\mathbf{r})]$  is the electron-electron repulsion, and  $V_{nn}(\mathbf{R}_I)$  is the nuclear-nuclear repulsion. As written, Eq. (1.8) is impossible to solve. Fortunately, the total energy may also be expressed exactly as a unique functional of the density  $\rho(\mathbf{r}) = \sum_i^{N_e} |\psi_i|^2$  of a system of  $N_e$  *noninteracting* electrons in orthonormal orbitals  $\psi_i$  and  $N_n$  nuclei of charge  $Z_I e$  at positions  $\mathbf{R}_I$ .<sup>83,84</sup>

$$E[\rho(\mathbf{r}); \mathbf{R}_I] = T_s[\rho(\mathbf{r})] + V_{ne}[\rho(\mathbf{r})] + J[\rho(\mathbf{r})] + V_{xc}[\rho(\mathbf{r})] + V_{nn}(\mathbf{R}_I) \quad (1.9)$$

where (in atomic units)

$$T_s[\rho(\mathbf{r})] = \sum_{i=1}^{N_e} \langle \psi_i | -\frac{1}{2} \nabla^2 | \psi_i \rangle \quad (1.10)$$

$$V_{ne}[\rho(\mathbf{r})] = \int v(\mathbf{r}; \mathbf{R}_I) \rho(\mathbf{r}) \, d\mathbf{r} \quad (1.11)$$

$$J[\rho(\mathbf{r})] = \int \rho(\mathbf{r}) \rho(\mathbf{r}') / |\mathbf{r} - \mathbf{r}'| \, d\mathbf{r} \quad (1.12)$$



$$V_{nn}(\mathbf{R}_I) = \frac{1}{2} \sum_{I \neq J}^{N_n} Z_I Z_J / |\mathbf{R}_I - \mathbf{R}_J| \quad (1.13)$$

$$V_{xc}[\rho(\mathbf{r})] = T[\rho(\mathbf{r})] - T_s[\rho(\mathbf{r})] + V_{ee}[\rho(\mathbf{r})] - J[\rho(\mathbf{r})] \quad (1.14)$$

The exchange-correlation energy  $V_{xc}[\rho(\mathbf{r})]$  contains the difference between  $T[\rho(\mathbf{r})]$  and  $T_s[\rho(\mathbf{r})]$  and the nonclassical part of  $V_{ee}[\rho(\mathbf{r})]$ . It is approximated in actual calculations via a variety of schemes; in our calculations, the LDA<sup>85</sup> or BLYP<sup>86,87</sup> functionals are used.

Eq. (1.9) is solved variationally.<sup>88</sup> For periodic systems, the  $\psi_i$ 's satisfy the Bloch theorem and may be expanded in plane waves.

$$\psi_i^{\mathbf{k}} = e^{i\mathbf{k}\cdot\mathbf{r}} \sum_{\mathbf{g}} c_i^{\mathbf{k}}(\mathbf{g}) e^{i\mathbf{g}\cdot\mathbf{r}} \quad (1.15)$$

In Eq. (1.15),  $\mathbf{k}$  is a wave vector that lies within the Brillouin Zone of the reciprocal lattice of the simulation cell,  $\mathbf{g}$  is a reciprocal lattice vector of the simulation cell, and  $\frac{1}{2}(\mathbf{k} + \mathbf{g})^2 = E_{\text{cut}}$ , where  $E_{\text{cut}}$  is a selected cutoff energy. In our calculations, only  $\mathbf{k} = \mathbf{G} = (0 \ 0 \ 0)$  is used; consequently, the superscript  $\mathbf{k}$  in Eq. (1.15) is dropped, and  $E_{\text{cut}} = 70.0$  Rydbergs. The core electrons of atoms are, however, poorly described by plane waves; consequently, their collective behavior is described using smoothly varying atomic pseudopotentials, e.g., norm-conserving Troullier-Martins pseudopotentials.<sup>89</sup> This approximation is excellent because the behavior of chemical systems, e.g., bonding, is controlled by the valence electrons.

After making an initial guess in Eq. (1.15) for the Fourier components  $c_i(\mathbf{g})$ , Eqs. (1.16) – (1.18) are solved self-consistently. Eqs. (1.16) – (1.17) are the Kohn-Sham equations.

$$\left[-\frac{1}{2}\nabla^2 + v_{\text{eff}}\right]\psi_i = \epsilon_i\psi_i, \text{ where} \quad (1.16)$$

$$v_{\text{eff}} = v(\mathbf{r}; \mathbf{R}) + \int \rho(\mathbf{r}') / |\mathbf{r} - \mathbf{r}'| d\mathbf{r}' + \delta V_{xc}[\rho(\mathbf{r})] / \delta \rho(\mathbf{r}) \quad (1.17)$$

$$\rho(\mathbf{r}) = \sum_i^{N_e} |\psi_i|^2 \quad (1.18)$$

Once Eqs. (1.16) – (1.18) are solved self-consistently, the  $\rho(\mathbf{r})$  and  $\psi_i$  are used to compute  $E$  in Eq. (1.9). The nuclear positions are updated, and Eqs. (1.16) – (1.19) are re-solved, repeating the cycle until the criterion  $|\partial E / \partial c_i(\mathbf{g})|_{\max} = C$  is satisfied, where  $C = 10^{-6}$  a.u. in our calculations.

### 1.3.2. Geometry optimization

In order to optimize the geometry of our systems, two different methods are employed. The first method, GDIIIS,<sup>90,91</sup> is implemented by estimating (rather than solving analytically) the Hessian matrix elements  $\partial E / \partial \mathbf{R}_I \partial \mathbf{R}_J$ , and then, using these elements, each atom is moved accordingly. A subsequent wavefunction optimization is performed, the Hessian is recalculated, and these steps are repeated until the maximum force on any given atom  $|\partial E / \partial \mathbf{R}_I|_{\max} = F$ , where  $F$  is an arbitrary cutoff, typically  $10^{-4}$  a.u. in our calculations. However, it is difficult to converge to a (local) minimum of the potential energy surface using this method, and for large systems with shallow potential surfaces described in this thesis, this method is not very useful.

The second method of geometry optimization is based on “simulated annealing,”<sup>92</sup> except that the atomic velocities are (or system temperature is) initially zero rather than finite, and the velocity or temperature scaling factor is  $\sim 0.9$  instead of approaching one, e.g., 0.999. After optimizing the wavefunction, the forces acting on both nuclei and coefficients of the wavefunction are calculated *simultaneously*. This is accomplished from the Car-Parrinello Lagrangian

$$L = \frac{1}{2} \mu \sum_{\mathbb{I}}^{N_e} \int \dot{\psi}_i^* \dot{\psi}_i d\mathbf{r} + \frac{1}{2} \sum_{\mathbb{I}}^{N_I} \dot{\mathbf{R}}_I^2 - E([\psi_i], \mathbf{R}_I) + \sum_{\mathbb{I}}^{N_e} \sum_{\mathbb{J}}^{N_e} \Lambda_{i,j} (\int \psi_i^* \psi_j d\mathbf{r} - \delta_{i,j}) \quad (1.19)$$

of the system, a novel and clever expression that describes the quantum-mechanical component, i.e., the motion of the electrons, in the same manner as the classical component, i.e., the motion of the nuclei.<sup>93</sup> In Eq. (1.19),  $\mu$  is a parameter or “fictitious mass” (1100 a.u. in our calculations),

$\Lambda_{i,j}$  are a set of Lagrange multipliers used to enforce orthonormality, and  $E([\psi_i], \mathbf{R}_I)$  is the total energy functional of the system, analogous to Eq. (1.9). The equations of motion (1.20) – (1.21) follow from Eq. (1.19).

$$\mu \ddot{\Psi}_i = - \left[ -\frac{1}{2} \nabla^2 + v_{\text{eff}} \right] \Psi_i + \sum_{j \neq i}^N \Lambda_{i,j} \Psi_j \quad (1.20)$$

$$M_I \ddot{\mathbf{R}}_I = - \partial E([\psi_i], \mathbf{R}_I) / \partial \mathbf{R}_I \quad (1.21)$$

In order to perform a practical calculation of the nuclear forces  $\mathbf{F}_I$  from Eq. (1.21), the total ground-state eigenfunction  $\Psi_o$  is evaluated

$$\Psi_o = \frac{1}{\sqrt{N_e!}} \det[\psi_1 \psi_2 \psi_3 \dots \psi_{N_e}] \quad (1.22)$$

which allows use of the Hellman-Fenyman theorem, i.e., Eq. (1.23), where  $H([\psi_i], \mathbf{R}_I)$  is the many-body electronic Hamiltonian.

$$\mathbf{F}_I = - \partial E([\psi_i], \mathbf{R}_I) / \partial \mathbf{R}_I = \langle \Psi_i | - \partial H([\psi_i], \mathbf{R}_I) / \partial \mathbf{R}_I | \Psi_i \rangle \quad (1.23)$$

Once the forces on the nuclei are determined, the nuclei are propagated, e.g., via the velocity Verlet algorithm, i.e., Eq. (1.24).

$$\mathbf{R}_I(t + \Delta t) = -\mathbf{R}_I(t - \Delta t) + 2\mathbf{R}_I(t) + \frac{\Delta t^2}{M_I} \mathbf{F}_I \quad (1.24)$$

In our calculations, the chosen time step is typically  $\Delta t = 3.5$  a.u. = 0.085 fs. After updating both the positions of the nuclei and electrons simultaneously, the system is quenched according to the selected scaling factor, 0.9. The attractiveness of this method is that after performing an initial wavefunction optimization, the wavefunction does not need to be subsequently re-calculated; the

positions of the nuclei and electrons which follow nearly adiabatically are re-updated on the fly according to the scheme in Eqs. (1.20) – (1.24). Furthermore, convergence to a (local) minimum is more easily achieved for large systems with shallow potential wells.

### 1.3.3. Classical Car-Parrinello molecular dynamics simulations

The CPMD method is closely related to the second method of geometry optimization outlined above, except that (1) the temperature of the system is finite and controlled via typically one of two different computational schemes and (2) the system is not quenched, i.e., no scaling factor is used. The scheme employed to select and subsequently control the temperature of the system is chosen based on the type of simulation desired, either microcanonical (NVE) or canonical (NVT) in our calculations.

## REFERENCES FOR CHAPTER 1

- (1) Warneck, P. *Chemistry of the Natural Atmosphere*; Academic Press: San Diego, 1988; Vol. 41.
- (2) Gettys, W. E.; Keller, F. J.; Skove, M. J. *Physics: Classical and Modern*; McGraw-Hill: New York, 1989.
- (3) Seinfeld, J. H.; Pandis, S. N. *Atmospheric Chemistry and Physics: From Air Pollution to Climate Change*; Wiley: New York, 1998.
- (4) Wayne, R. P. *Chemistry of Atmospheres*, 2nd ed.; Clarendon Press: Oxford, 1991.
- (5) van der Leun, J. C.; Tang, X.; Tevini, M. "Environmental effects of ozone depletion: 1998 Assessment," United Nations Environment Programme (UNEP), 1998.
- (6) Chapman, S. *Mem. R. Meteorol. Soc.* **1930**, 3, 103.
- (7) Crutzen, P. J. *Q. J. R. Meteorol. Soc.* **1970**, 96, 320.
- (8) Stolarski, R. S.; Cicerone, R. J. *J. Can. Chem.* **1974**, 52, 1610.
- (9) Molina, M. J.; Rowland, F. S. *Nature* **1974**, 249, 810.
- (10) Bates, D. R.; Nicolet, M. *J. Geophys. Res.* **1950**, 55D, 301.
- (11) Johnston, H. S. *Science* **1971**, 173, 517.
- (12) Farman, J. C.; Gardiner, B. G.; Shanklin, J. D. *Nature* **1985**, 315, 207.
- (13) Staehelin, J.; Harris, N. R. P.; Appenzeller, C.; Eberhard, J. *Rev. Geophys.* **2001**, 39, 231.
- (14) Albritton, D. L.; Watson, R. T.; Aucamp, P. J.; Mégie, G. "WMO/UNEP Scientific Assessment of Ozone Depletion: 1998," World Meteorological Organization Global Ozone Research and Monitoring Project, 1998.
- (15) NOAA and NASA report, October 16, 2001 (date of web publication). <http://www.gsfc.nasa.gov/topstory/20011016ozonelayer.html>

- (16) NOAA SBUV/2 Satellite Program, 2001 Hemisphere Antarctic Ozone Hole Area. <http://www.ozonelayer.noaa.gov/data/antarctic.htm>
- (17) NOAA Climate Modeling and Diagnostics Lab, 2001 South Pole Ozone Profiles. <http://www.cmdl.noaa.gov/ozwv/ozsondes/spo/index.html>
- (18) Newman, P. A.; Gleason, J. F.; McPeters, R. D.; Stolarski, R. S. *Geophys. Res. Lett.* **1997**, *24*, 2689.
- (19) Kolb, C. E.; Worsnop, D. R.; Zahniser, M. S.; Davidovits, P.; Keyser, L. F.; Leu, M.-T.; Molina, M. J.; Hanson, D. R.; Ravishankara, A. R. Laboratory studies of atmospheric heterogeneous chemistry. In *Advances in Physical Chemistry Series (Progress and Problems in Atmospheric Chemistry)*; Barker, J. R., Ed.; World Scientific: London, 1995.
- (20) Solomon, S.; Garcia, R. R.; Rowland, F. S.; Wuebbles, D. J. *Nature* **1986**, *321*, 755.
- (21) Solomon, S. *Rev. Geophys.* **1999**, *37*, 275.
- (22) Molina, L. T.; Molina, M. J. *J. Phys. Chem.* **1987**, *91*, 433.
- (23) Kaledin, A. L.; Morokuma, K. *J. Chem. Phys.* **2000**, *113*, 5750.
- (24) Shindell, D. T.; Rind, D.; Lonergan, P. *Nature* **1998**, *392*, 589.
- (25) Sander, S. P.; Friedl, R. R.; DeMore, W. B.; Golden, D. M.; Kurylo, M. J.; Hampson, R. F.; Huie, R. E.; Moortgat, G. K.; Ravishankara, A. R.; Kolb, C. E.; Molina, M. J. *Chemical Kinetics and Photochemical Data for Use in Stratospheric Modeling, Supplement to Evaluation 12: Update of Key Reactions*; Jet Propulsion Laboratory: Pasadena, CA, 2000.
- (26) DeMore, W. B.; Sander, S. P.; Golden, D. M.; Hampson, R. F.; Kurylo, M. J.; Howard, C. J.; Ravishankara, A. R.; Kolb, C. E.; Molina, M. J. *Chemical Kinetics and Photochemical Data for Use in Stratospheric Modeling*; Jet Propulsion Laboratory: Pasadena, CA, 1997.
- (27) de Boer, J. H. *The dynamical character of adsorption*, 2nd ed.; Oxford University Press: New York, 1968.
- (28) Lee, S.-H.; Leard, D. C.; Zhang, R.; Molina, L. T.; Molina, M. J. *Chem. Phys. Lett.* **1999**, *315*, 7.
- (29) Abbatt, J. P. D.; Beyer, K. D.; Fucaloro, A. F.; McMahon, J. R.; Wooldridge, P. J.; Zhang, R.; Molina, M. J. *J. Geophys. Res.* **1992**, *97D*, 15819.
- (30) Leu, M.-T.; Keyser, L. F.; Timonen, R. S. *J. Phys. Chem. B* **1997**, *101*, 6259.
- (31) Foster, K. L.; Tolbert, M. A.; George, S. M. *J. Phys. Chem. A* **1997**, *101*, 4979.
- (32) Clary, D. C.; Wang, L. *J. Chem. Soc., Faraday Trans.* **1997**, *93*, 2763.
- (33) Kroes, G.-J.; Clary, D. C. *Geophys. Res. Lett.* **1992**, *19*, 1355.
- (34) Molina, M. J. The probable role of stratospheric 'ice' clouds: Heterogeneous chemistry of the 'ozone hole'. In *The Chemistry of the Atmosphere: Its Impact on Global Change*; Calvert, J. G., Ed.; Blackwell Scientific Publications: Oxford, 1994; p. 27.
- (35) Petrenko, V. F.; Whitworth, R. W. *Physics of Ice*; Oxford University Press: New York, 1999.
- (36) Gertner, B. J.; Hynes, J. T. *Faraday Discuss.* **1998**, *110*, 301.
- (37) George, S. M.; Livingston, F. E. *Surf. Rev. Lett.* **1997**, *4*, 771.
- (38) Gertner, B. J.; Hynes, J. T. *Science* **1996**, *271*, 1563.
- (39) Bianco, R.; Hynes, J. T. *J. Phys. Chem. A* **1999**, *103*, 3797.
- (40) Oppliger, R.; Allanic, A.; Rossi, M. J. *J. Phys. Chem. A* **1997**, *101*, 1903.
- (41) Mebel, A. M.; Morokuma, K. *J. Phys. Chem.* **1996**, *100*, 2985.

- (42) Pursell, C. J.; Zaidi, M.; Thompson, A.; Fraser-Gaston, C.; Vela, E. *J. Phys. Chem. A* **2000**, *104*, 552.
- (43) Banham, S. F.; Sodeau, J. R.; Horn, A. B.; McCoustra, M. R. S.; Chesters, M. A. *J. Vac. Sci. Technol. A* **1996**, *14*, 1620.
- (44) Hanson, D. R.; Mauersberger, K. *J. Phys. Chem.* **1990**, *94*, 4700.
- (45) Donsig, H. A.; Vickerman, J. C. *J. Chem. Soc., Faraday Trans.* **1997**, *93*, 2755.
- (46) Uras, N.; Rahman, M.; Devlin, J. P. *J. Phys. Chem. B* **1998**, *102*, 9375.
- (47) Schaff, J. E.; Roberts, J. T. *J. Phys. Chem.* **1994**, *98*, 6900.
- (48) Du, Q.; Superfine, R.; Freysz, E.; Shen, Y. R. *Phys. Rev. Lett.* **1993**, *70*, 2313.
- (49) Svanberg, M.; Pettersson, J. B. C.; Bolton, K. *J. Phys. Chem. A* **2000**, *104*, 5787.
- (50) Bolton, K.; Pettersson, J. B. C. *J. Am. Chem. Soc.* **2001**, *123*, 7360.
- (51) Lipson, J. B. Experimental Kinetics Studies of Gas Phase Halogen Reactions Involved in Stratospheric Ozone Depletion, Massachusetts Institute of Technology, 1999.
- (52) Blake, D. F.; Kato, K. *J. Geophys. Res.* **1995**, *100D*, 7195.
- (53) Rogaski, C. A.; Golden, D. M.; Williams, L. R. *Geophys. Res. Lett.* **1997**, *24*, 381.
- (54) Gerecke, A.; Thielmann, A.; Gutzwiller, L.; Rossi, M. J. *Geophys. Res. Lett.* **1998**, *25*, 2453.
- (55) Gao, R. S.; Kärcher, B.; Keim, E. R.; Fahey, D. W. *J. Geophys. Res.* **1998**, *25*, 3323.
- (56) Lary, D. J.; Lee, A. M.; Toumi, R.; Newchurch, M. J.; Pirre, M.; Renard, J. B. *J. Geophys. Res.* **1997**, *102D*, 3671.
- (57) Bekki, S. *J. Geophys. Res.* **1997**, *102D*, 10751.
- (58) Spencer, D. D. The Importance of Aluminum Oxide Aerosols to Stratospheric Ozone Depletion, Massachusetts Institute of Technology, 1996.
- (59) Potter, A. E. *J. Environ. Sci.* **1978**, *21*, 15.
- (60) Prather, M. J.; García, M. M.; Douglass, A. R.; Jackman, C. H.; Ko, M. K. W.; Sze, N. D. *J. Geophys. Res.* **1990**, *95D*, 18583.
- (61) Zolensky, M. E.; McKay, D. S.; Kaczor, L. A. *J. Geophys. Res.* **1989**, *94D*, 1047.
- (62) Brownlee, D. E.; Ferry, G. V.; Tomandl, D. *Science* **1976**, *191*, 1270.
- (63) Cofer, W. R., III; Lala, G. G.; Wightman, J. P. *Atmos. Environ.* **1987**, *21*, 1187.
- (64) Cofer, W. R., III; Purgold, G. C.; Winstead, E. L.; Edahl, R. A. *J. Geophys. Res.* **1991**, *96D*, 17371.
- (65) Dentamaro, A. V.; Dao, P. D.; Farley, R.; Ross, M. *Geophys. Res. Lett.* **1999**, *26*, 2395.
- (66) Ross, M. N.; Whitefield, P. D.; Hagen, D. E.; Hopkins, A. R. *Geophys. Res. Lett.* **1999**, *26*, 819.
- (67) Nelson, C. E.; Elam, J. W.; Cameron, M. A.; Tolbert, M. A.; George, S. M. *Surf. Sci.* **1998**, *416*, 341.
- (68) Elam, J. W.; Nelson, C. E.; Cameron, M. A.; Tolbert, M. A.; George, S. M. *J. Phys. Chem. B* **1998**, *102*, 7008.
- (69) Hass, K. C.; Schneider, W. F.; Curioni, A.; Andreoni, W. *J. Phys. Chem. B* **2000**, *104*, 5527.
- (70) Hass, K. C.; Schneider, W. F.; Curioni, A.; Andreoni, W. *Science* **1998**, *282*, 265.
- (71) Hass, K. C.; Schneider, W. F.; Curioni, A.; Andreoni, W. *Science* **1998**, *282*, 882.
- (72) Elam, J. W.; Nelson, C. E.; Tolbert, M. A.; George, S. M. *Surf. Sci.* **2000**, *450*, 64.

- (73) Bolton, K.; Bosio, S. B. M.; Hase, W. L.; Schneider, W. F.; Hass, K. C. *J. Phys. Chem. B* **1999**, *103*, 3885.
- (74) Goodman, A. L.; Miller, T. M.; Grassian, V. H. *J. Vac. Sci. Technol. A* **1998**, *16*, 2585.
- (75) Molina, M. J.; Molina, L. T.; Zhang, R. Y.; Meads, R. F.; Spencer, D. D. *Geophys. Res. Lett.* **1997**, *24*, 1619.
- (76) Jackman, C. H.; Considine, D. B.; Fleming, E. L. *Geophys. Res. Lett.* **1998**, *25*, 907.
- (77) Jackman, C. H.; Considine, D. B.; Fleming, E. L. *J. Geophys. Res.* **1996**, *101D*, 12523.
- (78) Hutter, J.; Alavi, A.; Deutsch, T.; Bernasconi, M.; Goedecker, St.; Marx, D.; Tuckerman, M.; Parrinello, M. *CPMD*; Max-Planck Institut für Festkörperforschung and IBM Zurich Research Laboratory, 1995-99.
- (79) Parr, R. G.; Yang, W. *Density-Functional Theory of Atoms and Molecules*; Oxford University Press: New York, 1989.
- (80) Galli, G.; Pasquarello, A. First principles molecular dynamics. In *Computer Simulations in Chemical Physics*; Allen, M. P., Tildesley, D. J., Eds.; Kluwer Academic Publishers: Dordrecht, 1993; Vol. 397; p. 261.
- (81) Parrinello, M. *Solid State Commun.* **1997**, *102*, 107.
- (82) Marx, D.; Hutter, J. Ab initio molecular dynamics: Theory and implementation. In *Modern Methods and Algorithms of Quantum Chemistry*; Grotendorst, J., Ed.; John von Neumann Institute for Computing: Jülich, 2000; Vol. NIC Series, Vol. 1; p. 301.
- (83) Kohn, W.; Sham, L. J. *Phys. Rev.* **1965**, *140*, A1133.
- (84) Kohn, W. *Rev. Mod. Phys.* **1999**, *71*, 1253.
- (85) Goedecker, S.; Teter, M. P.; Hutter, J. *Phys. Rev. B* **1996**, *54*, 1703.
- (86) Becke, A. D. *Phys. Rev. A* **1988**, *38*, 3098.
- (87) Lee, C.; Yang, W.; Parr, R. G. *Phys. Rev. B* **1988**, *37*, 785.
- (88) Hohenberg, P.; Kohn, W. *Phys. Rev.* **1964**, *136*, B864.
- (89) Troullier, N.; Martins, J. L. *Phys. Rev. B* **1991**, *43*, 1993.
- (90) Császár, P.; Pulay, P. *J. Mol. Struct.* **1984**, *114*, 31.
- (91) Fischer, T. H.; Almlöf, J. *J. Phys. Chem.* **1992**, *96*, 9768.
- (92) Kirkpatrick, S.; Gelatt, C. D., Jr.; Vecchi, M. P. *Science* **1983**, *220*, 671.
- (93) Car, R.; Parrinello, M. *Phys. Rev. Lett.* **1985**, *55*, 2471.

## **LIST OF FIGURES FOR CHAPTER 1**

Figure 1.1. The 2001 Antarctic Ozone Hole area reproduced from <http://www.ozonelayer.noaa.gov/data/antarctic.htm>. In the Figure, ozone levels are less than 220 D.U. (defined as the threshold level for a “Hole”).

Figure 1.2. Representative 2001 Antarctic Ozone Hole profile reproduced from <http://www.cmdl.noaa.gov/ozwv/ozsondes/spo/index.html>

Figure 1.3. Two-stage recipe for ozone depletion at the poles requiring establishment of a polar vortex and cold temperatures during the winter and springtime sunlight



Figure 1.1

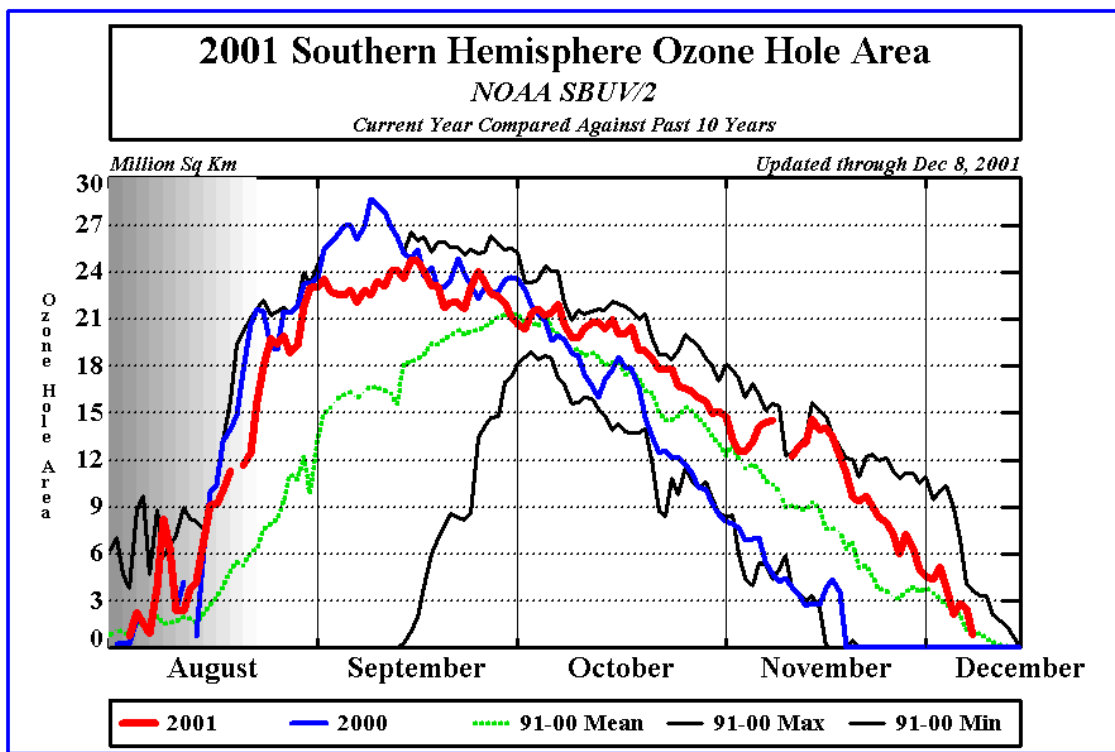


Figure 1.2

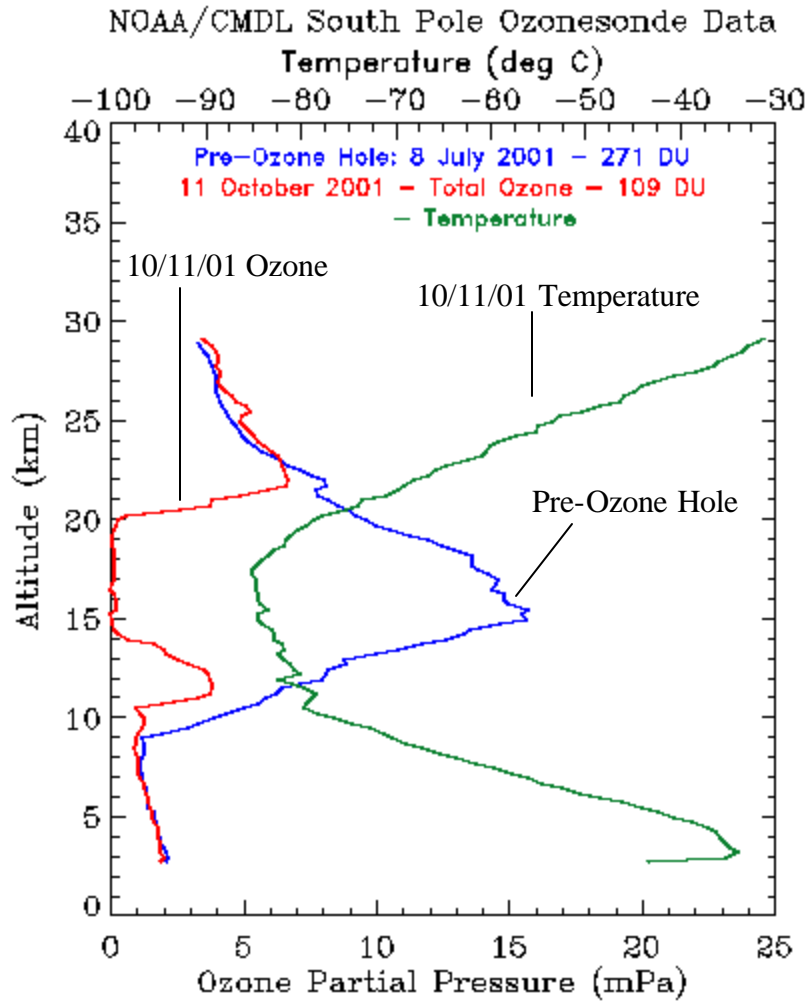
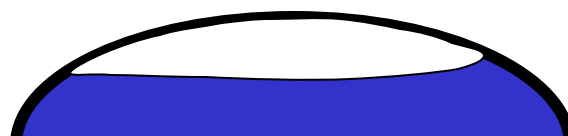
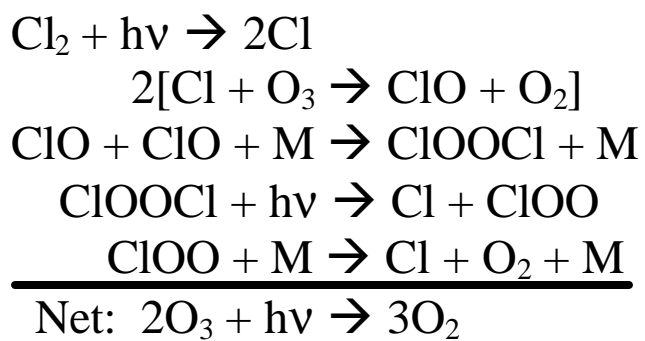
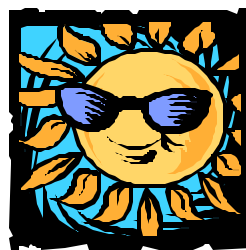
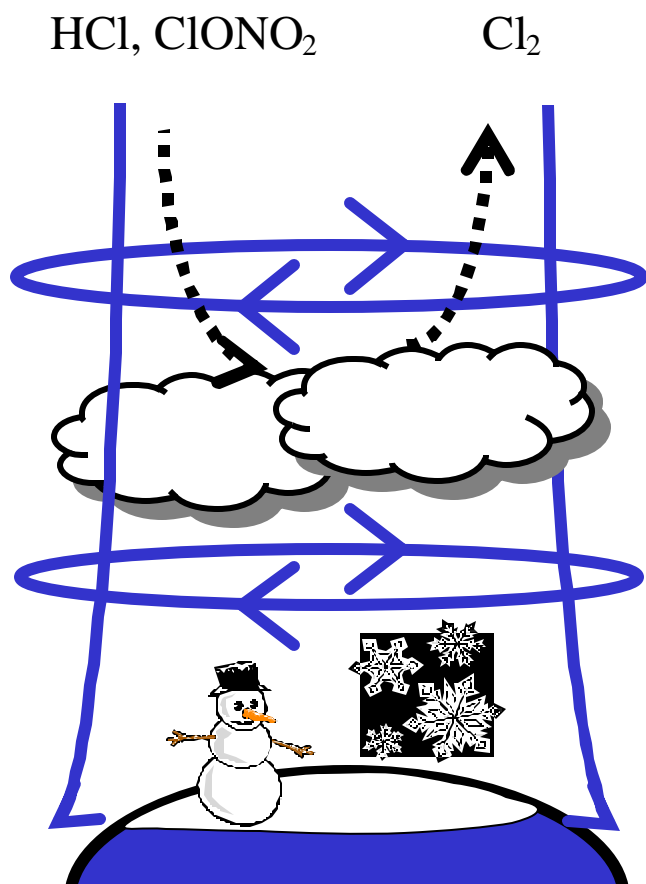


Figure 1.3



Winter

Spring

## Chapter 2: First-principles molecular-dynamics study of surface disordering of the (0001) face of hexagonal ice

Reproduced with permission from Mantz, Y. A.; Geiger, F. M.; Molina, L. T.; Molina, M. J.; Trout, B. L. *J. Chem. Phys.* 2000, *113*, 10733-10743. © 2000 American Institute of Physics.

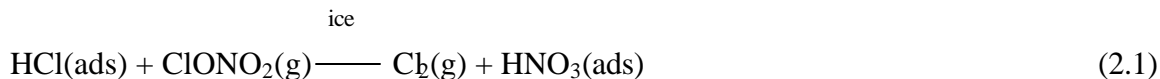
### ABSTRACT

In order to study surface disordering of ice at temperatures below the bulk melting point as a function of depth into the bulk, Car-Parrinello molecular dynamics simulations of a periodic model of the hexagonal ice (0001) surface were carried out. Partial disorder in the uppermost bilayer was observed at a simulation temperature of 190 K, which is ~30 K below the estimated bulk melting point, qualitatively validating earlier classical molecular dynamics studies of this phenomenon. Over 0.5 ps, the timescale of a simulation, there were three particularly useful (and complementary) measures of disorder: the pair distribution function  $g(r)$ , the distance of the oxygen atoms from the bottommost bilayer, and the distribution of angles  $\mathbf{f}$  and  $\mathbf{q}$  formed by the molecular dipole vector and the Cartesian axes. Our results set the stage for future studies addressing the effect of the disordered ice surface on heterogeneous atmospheric chemistry.

### 2.1. INTRODUCTION

The surfaces of many solids are disordered at temperatures below the bulk freezing point.<sup>1</sup> The partially disordered transition region on the surface of ice, often referred to as a quasi-liquid layer in the literature, is thought to be responsible for the sintering of ice and snow, glacial flow, frost heave, and the electrification of cold clouds and thunderstorms.<sup>2-4</sup> The existence of a quasi-liquid layer on ice is of particular interest from an atmospheric science point of view. Specifically, it is now known that the surface of ice plays a crucial role in the annual depletion of Antarctic and Arctic ozone.<sup>5-9</sup> In laboratory experiments under conditions similar to those in the lower polar stratosphere, ice is found to enhance greatly the rate of reaction between stable chlorine compounds that are non-reactive in the gas-phase, such as HCl and ClONO<sub>2</sub>.<sup>10</sup>

This leads to the formation of active products such as  $\text{Cl}_2$  that are implicated in the catalytic gas-phase destruction of ozone as well as the sequestration of  $\text{NO}_x$ .<sup>11,12</sup>



Our laboratory suggested that disordering caused by the breaking of the translational symmetry of the ice crystal at the surface would allow surface water molecules to solvate at least partially chlorine reservoirs like HCl.<sup>7</sup> This solvation is thought to play a key role in the catalytic activity of ice. In contrast to ice, other solids such as Teflon do not exhibit a catalytic effect, and the effect of aluminum oxide is at least one order of magnitude less.<sup>13</sup>

The existence of a disordered surface or quasi-liquid layer on ice was proposed as early as 1842 by Faraday; since then, many different experimental studies of the ice surface have been published.<sup>14,15</sup> In general, the experiments indicate that close to the freezing point the surface of ice exhibits properties different from those of the bulk. However, the temperature at which disorder on the surface is observed varies considerably due to (1) the conditions under which the experiment is performed, (2) the presence of surface impurities, and (3) the different nature and sensitivity of the techniques.<sup>14</sup> To illustrate this point, disordering of the hexagonal ice (0001) surface was first detected at  $-2$  °C using the optical technique of ellipsometry,<sup>16-18</sup> but at  $-13.5$  °C using glancing-angle x-ray scattering,<sup>19</sup> at  $-20$  °C and at  $-30$  °C using electrical conductivity and surface potential techniques, respectively,<sup>20,21</sup> at  $-35$  °C using wire regelation,<sup>22</sup> at  $-60$  °C using proton channeling,<sup>23</sup> at  $-100$  °C using nuclear magnetic resonance,<sup>24</sup> and at  $-160$  °C using photoemission.<sup>25</sup> In addition, the temperature dependence of disorder was found to be different from technique to technique. This wide range of experimental results provides a motivation for investigating the problem of surface melting theoretically.

Classical molecular dynamics simulations of the ice surface have been performed over tens of picoseconds for relatively large models consisting of hundreds of water molecules. In different studies by Kroes,<sup>26</sup> Karim and Haymet,<sup>27,28</sup> and Furukawa and Nada,<sup>17,18,29,30</sup> the TIP4P intermolecular water pair potential was used to study the disordering by layer of slab models of the hexagonal ice (0001) surface. In the study by Kroes,<sup>26</sup> proton-disordered TIP4P ice was used with a melting point of  $238 \pm 7$  K.<sup>31</sup> In the other studies,<sup>17,18,27-30</sup> proton-ordered TIP4P ice was

used with a melting point of  $214 \pm 6$  K.<sup>32</sup> Different order parameters were defined and calculated by layer based on the position or velocity of the molecules at each step. In these studies, as well as in a study by Karim *et al.* in which a simple point charge model for water was used,<sup>33</sup> the interfacial region was modeled as a discrete transition region. This is consistent with Knight's view that, according to Gibbs' phase rule, the surface of ice cannot be a distinct phase:<sup>34-36</sup> the so-called quasi-liquid layer should not be modeled as a homogeneous (water) layer of well-defined thickness except at the triple point. In these studies, a continuous disordering from the surface as temperature is raised was observed, in agreement with a recent prediction for a structure with slab geometry.<sup>37</sup>

One of the shortcomings of the classical studies mentioned above is that the form of the potentials of interaction is fixed. Furthermore, the TIP4P water pair potential is parameterized for the study of liquid water at standard temperature and pressure rather than for hexagonal ice.<sup>38</sup> In order to provide a test of the validity of the classical studies, we have chosen to study the hexagonal ice (0001) surface using Car-Parrinello molecular dynamics, a first-principles method. This method is very well suited for the study of extended systems such as the ice surface that can be modeled using periodic boundary conditions. No *ad hoc* potential is chosen or parameterized; instead, our potential is calculated at each step from first principles. By examining several order parameters and characterizing the ice surface over a wide temperature range in this study, we lay the groundwork for determining the effect of HCl on ice surface disordering, for investigating chemical reactions on the ice surface, and for addressing the role that the surface of ice plays in catalytic chlorine activation in future studies.

The organization of this paper is as follows. Our ice model is presented in Sec. 2.2, and our methodology including computational details is described in Sec. 2.3. The results are presented in Sec. 2.4, which includes the calculated geometry of bulk ice and then a detailed analysis of disorder by bilayer. A summary of our findings is given in Sec. 2.5. Concluding remarks are made in Sec. 2.6.

## 2.2. ICE MODEL

Shown in Figure 2.1 is our slab model of the hexagonal ice basal (0001) surface, which is perpendicular to the  $z$ -axis. The surface of our slab model was chosen based on the fact that the

(0001) surface is thought to be most prevalent under polar stratospheric conditions.<sup>6</sup> Our slab model satisfies the Bernal-Fowler ice rules,<sup>39</sup> where each oxygen atom is given two OH bonds and two hydrogen bonds in a tetrahedral arrangement. Like real ice, our model does not have an appreciable net dipole moment; at each step of the simulation, each bilayer nearly possesses an inversion center of symmetry. The slab model ends in a full-bilayer termination, where each surface water molecule forms three hydrogen bonds. A full-bilayer termination was found by Materer *et al.* to be much more stable than a half-bilayer termination, in which each surface water molecule forms only one hydrogen bond;<sup>40</sup> for two different periodic slab models, a stabilization of at least 58 kJ/mol per unit cell utilizing CRYSTAL at the Hartree-Fock level with a 6-31G\* basis set was found. (Their supercell is roughly two times smaller than our supercell).

<Figure 2.1 here>

The oxygen atoms were initially placed using crystallographic data for hexagonal ice at 273 K in order to form a hexagonal supercell with lattice constants  $2a = 9.046 \text{ \AA}$  and  $2c = 14.734 \text{ \AA}$ .<sup>41</sup> Periodic boundary conditions were used in all directions. A surface vacuum region of (at least)  $6 \text{ \AA}$  was added to our slab model in order to mimic an isolated slab, so that the  $2c$  lattice constant for the slab model supercell is (at least)  $20.734 \text{ \AA}$ . The variation in the total energy was less than 4 kJ/mol when the vacuum region was increased above  $6 \text{ \AA}$  and was determined to be due to small ( $\sim 0.1 \%$ ) fluctuations in the number of plane waves per unit volume upon changing the supercell size and not to the interaction between periodic images. Thus, we expect the order parameters will be unaffected by an increase in the size of the vacuum region above  $6 \text{ \AA}$ .

The hydrogen atoms were positioned such that the net dipole moment was minimized. This was done by writing a Fortran computer program to find allowed arrangements of the hydrogen atoms and calculate the components of the net dipole moment of the slab. The  $x$ -,  $y$ -, and  $z$ -components were calculated assuming that the dipole moment of each water molecule was  $3.09 \text{ D}$ ,<sup>42,43</sup> and that the dipole vector of each molecule went from the oxygen atom to the center-of-mass of the molecule. It is emphasized that bilayers 1 and 4 in our model have a different arrangement of hydrogen atoms and thus different hydrogen bonding, although they have the same total number of hydrogen bonds initially. In our model, layer 1 is identical to layer 5, layer 2 is identical to layer 6, layer 3 is identical to layer 7, and layer 4 is identical to layer 8, in terms

of hydrogen bonding, where “identical” really means “most closely resembles” during each step of the simulation.

### 2.3. METHODOLOGY

Five Car-Parrinello molecular dynamics simulations were performed over 1 ps using CPMD version 3.0f.<sup>44-50</sup> Pseudopotentials were used to describe the core and valence electrons of the hydrogen and oxygen atoms.<sup>51</sup> The pseudopotentials used for the hydrogen and oxygen atoms were of the Troullier-Martins type,<sup>52</sup> and they have been validated extensively elsewhere.<sup>53</sup> The BLYP functional was used to describe the exchange and correlation energy of the system,<sup>54,55</sup> and this functional was found in a previous study to be adequate for describing liquid water.<sup>53</sup> A fictitious electronic mass of 1100.0 a.u. was used, as was a basis set cutoff of 70.0 Rydbergs. A time step of 3.5 a.u. (0.085 fs) was used for the integration. Forces were computed using the Hellman-Feynman theorem, and the velocity verlet algorithm was used to integrate the ionic equations of motion and find new atomic positions.<sup>56</sup> We emphasize that the hydrogen atoms used in this study had a nuclear mass of 1.00 a.u. and were not deuterium atoms. In order to simulate within the canonical ensemble, a Nosé-Hoover chain thermostat was used with a chain length of four and a frequency of 3600  $\text{cm}^{-1}$ .<sup>57,58</sup> Although use of the Nosé-Hoover chain thermostat guarantees averaging of properties within the canonical ensemble at the specified temperature, we note that because of the necessary approximations used within density functional theory, we cannot calculate the exact electronic density distribution, and furthermore we have neglected quantum effects in the motion of the hydrogen nuclei; thus, the designated temperatures of our simulation are likely not equivalent to experimental temperatures. The best estimate of our slab melting point is  $\sim 220$  K, based on the fact that our choice of functional is known to underestimate hydrogen bond energies by 4 kJ (18%) for the  $\text{H}_2\text{O}$  dimer.<sup>53</sup> In addition, most of the results presented below indicate that the melting point of our model is between 190 and 230 K.

For four of five simulations, the bottom two layers (layers 7 and 8) of our model were fixed at their bulk optimized positions in order to mimic a semi-infinite system, and trajectories were run at 190, 230, 270, and 310 K, each for 1 ps. In order to test the effect of freeing the bottom two layers, a fifth 1-ps simulation was run at 230 K without fixing any atoms. In each



simulation, equilibration was achieved after 0.5 ps as tested by the slab energy, dipole moment of each layer, and atomic coordinates. Each of these properties was observed to change during the first 0.5 ps but to fluctuate around average values after that time. The order parameters that we define in Sec. 2.4 were averaged over the last 0.5 ps.

It was often desirable to compare our results to simulated liquid water over the same time scale of 0.5 ps. Accordingly, the trajectory for 32 deuterated water molecules in a periodic box with sides of 9.8652 Å at 300 K was obtained over 3.24 ps, and the final 0.5 ps were used. Due to the use of deuterium instead of hydrogen atoms, it was possible to use a larger time step of 7.0 a.u. (0.17 fs) for the integration to obtain the trajectory.

## 2.4. RESULTS AND DISCUSSION

In order to validate our methodology as well as obtain the initial geometry of a slab model which would be a good starting point for our studies, our first step was to perform a geometry optimization at 0 K of bulk ice (without a surface vacuum region of 6 Å).<sup>59</sup> Our optimized structure, with  $d_{\text{OO}} = 2.758\text{-}2.784$  Å,  $d_{\text{OH}} = 0.998\text{-}1.000$  Å,  $\langle \text{OOO} \rangle = 109.2\text{-}109.8^\circ$ ,  $\langle \text{HOH} \rangle = 106.1\text{-}106.7^\circ$ ,  $\langle \text{OHO} \rangle = 176.4\text{-}178.5^\circ$  and  $d_{\text{O-H}} = 1.759\text{-}1.785$  Å, is a reasonable approximation to the geometry of real ice, for which  $d_{\text{OO}} = 2.740\text{-}2.770$  Å,<sup>60,61</sup>  $d_{\text{OH}} = 0.96 \pm 0.03$  Å,<sup>62</sup>  $\langle \text{OOO} \rangle = 109.40\text{-}109.60^\circ$ ,<sup>61,63</sup>  $\langle \text{DOD} \rangle = 109.1\text{-}109.9^\circ$ ,<sup>61</sup> and (assuming  $\langle \text{OHO} \rangle = 180^\circ$ )  $d_{\text{O-H}} = 1.762\text{-}1.835$  Å.

### 2.4.1 Translational disorder

To measure the extent to which the oxygen atoms in a given layer remain in their ideal lattice positions in the slab model during the last 0.5 ps of a simulation, three (due to threefold symmetry) translational order parameters  $S_{Tm}$  where  $m = 1\text{-}3$  were defined that are identical to those defined by Kroes:<sup>26</sup>

$$S_{Tm} = \sum_{i=1}^4 \sum_{j=1}^4 \cos(\mathbf{k}_m \cdot \mathbf{r}_{ij}) / N_L^2, \quad (2.2)$$

where  $\mathbf{r}_{ij}$  is the vector from the oxygen atom of water molecule  $i$  to the oxygen atom of water molecule  $j$  in a given layer, for a total of 16 possible  $\mathbf{r}_{ij}$  by layer, four of which are the null vector,  $\mathbf{0}$ . The three  $\mathbf{k}_m$  are reciprocal lattice vectors in the two-dimensional reciprocal space of the  $N_L = 4$  oxygen atoms (and their periodic images). The  $\mathbf{k}_m$  are related by one or two subsequent rotations of  $120^\circ$ .

$$\mathbf{k}_1 = \frac{2\pi}{a} \left(1, -\frac{1}{\sqrt{3}}, 0\right), \quad (2.3)$$

where in Eq. (2.3)  $a = 4.523 \text{ \AA}$  for hexagonal ice at 273 K.<sup>41</sup> For a perfectly ordered layer,  $S_{Tm} = 1$  at each step, while for a completely disordered layer, after an initial decay the  $S_{Tm}$  will oscillate about a mean value,<sup>56</sup> in this case  $1/N_L = 1/4$ .

For each simulation, the three  $S_{Tm}$  were calculated at each step, averaged over 0.5 ps, and then the three  $S_{Tm}$  were averaged together to obtain an average  $S_T$  by layer. Layer results were averaged to obtain Figure 2.2, where average  $S_T$  is plotted at 190, 230, 270, and 310 K for bilayers 1, 2, and 3. For the fixed bilayer 4,  $S_T = 1$ . Also included is average  $S_T$  at 230 K for bilayers 1, 2, 3, and 4 when bilayer 4 was not fixed (*tf*). For reference, the average  $S_T$  for simulated deuterated water at 300 K ( $N_L = 32$ ) is  $S_T = 0.0137$  over the last 0.5 ps and  $S_T = 0.0128$  over the entire 3.24-ps trajectory, close to the theoretical mean value of  $1/N_L = 1/32 = 0.0313$ . The results reported by Kroes, obtained for a 40 ps trajectory of TIP4P water, are included in Figure 2.2; these results were obtained by averaging data in Tables 2a and 2b of his paper.<sup>26</sup>

<Figure 2.2 here>

Even over a short trajectory of 0.5 ps, the oxygen atoms in bilayer 1 at 190 K are significantly more ordered on average than at 230 K, in qualitative agreement with Kroes' results.<sup>26</sup> Above 230 K,  $S_T$  for bilayer 1 is essentially constant. Our bilayers 2 and 3 are only slightly disordered even at high temperature. Results obtained when bilayer 4 was not fixed are discussed in Sec. 2.4.7.

To quantify translational disorder in the  $z$ -direction, the distance of the oxygen atoms from the fixed bottom bilayer was calculated at each step, and the results were binned over 0.5 ps

in 0.1 Å increments to obtain a vertical density profile. For a perfectly ordered lattice, one distinct peak per layer is expected; the height of the peaks representing the fixed bilayer 4 is normalized to one. For a completely disordered region, a perfectly flat line is expected.

The results for bilayers 1, 2, 3, and 4 at 190, 230 and 270 K are shown in Figure 2.3. (The results for 310 K, not shown in Figure 2.3, are very similar to those at 270 K). Even at 190 K, we find that bilayer 1, and especially layer 1, is disordered to some extent, although two distinct peaks can still be resolved. These peaks correspond to planes of oxygen atoms in layers 1 and 2. Bilayers 2 and 3 are essentially ordered at 190 K. In fact, the full width at half height of 0.3 Å for the four peaks representing bilayers 2 and 3 at 190 K agree with experiment to within less than 0.1 Å: the root mean square amplitude of vibration of oxygen in ice at 263 K was measured to be 0.26 Å using x-ray diffraction,<sup>64</sup> while a value of 0.22 Å at 273 K was calculated from thermodynamic data.<sup>65</sup> The two main peaks of bilayer 1 are smeared out more at 230 K and are no longer distinct at 270 K. A smooth transition from order to disorder was also observed by Kroes,<sup>26</sup> who showed scrambling of molecules in bilayer 1 of his 12-layer TIP4P ice model at 190 K and complete merging of the two layers at 230 K. In qualitative agreement with our results, Nada and Furukawa observed a continuous transition from disorder to order over a temperature range of 170-220 K in 5-K increments.<sup>29</sup>

<Figure 2.3 here>

When bilayer 4 is not fixed, water molecules are free to migrate in the  $-z$ -direction, resulting in a greater relative displacement of bilayers 1, 2, and 3 from bilayer 4. When the results for bilayers 1 and 2 were shifted to overlap with those at 230 K when the bottom bilayer was fixed, a large degree of overlap was observed, validating the choice of our model. Other results obtained when bilayer 4 was not fixed are discussed in Sec. 2.4.7.

## 2.4.2. Rotational disorder

In order to measure the deviation of the orientation of the water molecular dipole vectors from their ideal lattice orientations, a rotational order parameter  $S_R$  was defined. For each simulation at each step,  $S_R$  was calculated using the following formula:

$$S_R = \sum_{i=1}^4 2.5(x_i^4 + y_i^4 + z_i^4 - 0.6)/N_L, \quad (2.4)$$

where the sum is over the  $N_L = 4$  molecules initially present in each layer. The coordinates  $x_i$ ,  $y_i$ , and  $z_i$  are not the same as those defined by Kroes, who also used Eq. (2.4).<sup>26</sup> Instead, the initial dipole vector of molecule  $i$  was normalized, then a rotation matrix for molecule  $i$  was obtained by transforming the normalized vector to (001). At each step, the dipole vector of molecule  $i$  was normalized and multiplied by the same rotation matrix to obtain  $x_i$ ,  $y_i$ , and  $z_i$ . For a perfectly ordered solid,  $S_R = 1$ , independent of time. For a liquid, they are predicted to decrease initially and oscillate about zero.<sup>56</sup>

The molecular  $S_R$  were plotted versus time and averaged to obtain  $S_R$  by layer and bilayer. Average  $S_R$  versus bilayer is shown in Figure 2.4 for each simulation. For reference, the average  $S_R$  computed for simulated deuterated water was 0.41 over the final 0.5 ps and 0.16 over 3.24 ps. Also included are results reported by Kroes over 40 ps that were obtained by averaging the data in Tables 3a and 3b of his paper.<sup>26</sup>

<Figure 2.4 here>

The trends are similar to those for translational order: bilayer 1 at 190 K is more ordered than at 230 K similar to Kroes' findings,<sup>26</sup> and bilayers 2 and 3 are more ordered than bilayer 1 at all temperatures. Results obtained when bilayer 4 was not fixed are discussed in Sec. 2.4.7.

Two more measures of rotational disorder were examined for each simulation: the molecular distribution of  $\mathbf{f}$ , which is the angle formed by the projection of the molecular dipole vector onto the (0001) surface and the  $+x$ -axis, and  $\mathbf{q}$ , the angle formed by the vector perpendicular to the surface and the molecular dipole vector. For hexagonal ice, six possible values of  $\mathbf{f}$  separated by  $60^\circ$  are observed, but only four per bilayer. For water with no fixed atoms and over a timescale that is relatively long compared to the period for a rotation at  $0^\circ\text{C}$  of  $\sim 10^{-11}$  s,<sup>66</sup> the distribution is expected to be flat.

The distribution of  $\mathbf{f}$  for bilayer 1 was binned in  $10^\circ$  increments and is shown in Figure 2.5 for three temperatures, 190, 230, and 270 K. (The distribution at 310 K is very similar to that

at 270 K). Bilayers 2 and 3 at all temperatures closely resemble bilayer 1 at 190 K, though the peaks are somewhat higher and sharper. At 190 K, four distinct peaks are present, but are smeared out to some extent at 230 K, and little further change is observed at 270 K, indicating bilayer 1 is disordered at 230 K with respect to this parameter. However, even over 0.5 ps, our results are in qualitative agreement with those of Kroes, who finds increased disorder in layers 1-4 as temperature increases.<sup>26</sup> Results when bilayer 4 was not fixed are discussed in Sec. 2.4.7.

<Figure 2.5 here>

Experimental corroboration of our results for the first bilayer in Figure 2.5 is possible using second harmonic generation, a surface-sensitive nonlinear optical technique.<sup>67-69</sup> At the unreconstructed  $3m$  symmetric basal (0001) ice surface, the intensity of the reflected signal polarized in the surface plane varies sinusoidally with  $f$  when the input light field is polarized parallel to the surface; control surfaces that are isotropic ( $8m$  symmetry), such as that of liquid water, do not show such signals.<sup>70</sup> While polarization studies as a function of rotational angle have not yet been obtained at the ice/water vapor interface, results for Si(100) and Si(111), two very-well characterized surfaces, have been obtained using second harmonic generation.<sup>71</sup>

The distribution of angles  $q$  for bilayer 1 at 190, 230, and 270 is shown in Figure 2.6. (The distribution at 310 K, which is not shown, is very similar to that at 270 K). Bilayers 2 and 3 at all temperatures closely resemble bilayer 1 at 190 K, though the peaks are higher and sharper. For hexagonal ice (and our fixed bilayer 4), two peaks symmetric about  $90^\circ$  are observed. For water, a flat distribution is expected over times long compared to the rotation period,  $\sim 10^{-11}$  s.<sup>66</sup>

<Figure 2.6 here>

In Figure 2.6, bilayer 1 is ordered at 190 K, but disordered at 230 K as shown by the flattening of the peak at  $60^\circ$  due to the greater rotation of the two water molecules in layer 1 with dangling OH groups and only three hydrogen bonds. The symmetrically-related water molecules in layer 2 with their OH group pointing in the  $-z$ -direction have four hydrogen bonds and are more restricted, hence the peak at  $120^\circ$  is observed even at 270 K and 310 K (not shown). The

trends observed by Kroes are qualitatively similar.<sup>26</sup> Results obtained when bilayer 4 was not fixed are discussed in Sec. 2.4.7.

### 2.4.3. Translational mobility

To quantify translational mobility, the center-of-mass, ensemble-averaged, mean-square displacement,  $\langle |\mathbf{r}_i(t) - \mathbf{r}_i(0)|^2 \rangle$ , was calculated. The mean square displacements for bilayers 1, 2 and 3 at 190 K and for bilayer 1 at 230 K over 0.25 ps were determined from the average of molecular results and are shown in Figure 2.7, along with results for simulated deuterated water at 300 K over 1.62 ps. Note that despite the short trajectories, we think our results may be qualitatively reliable because the trends presented below are physically reasonable.

<Figure 2.7 here>

In Figure 2.7, the mean square displacement for bilayer 1 at 190 K is greater than that for bilayer 2, which in turn is greater than that for bilayer 3. The fact that the mean square displacement for bilayer 1 at 190 K is intermediate between that for liquid water and that for bilayer 2 at 190 K is consistent with partial disorder in bilayer 1 at 190 K. The mean square displacement for bilayer 1 at 230 K, which is similar to the results for bilayer 1 at 270 and 310 K, is essentially identical to that for simulated deuterated water in Figure 2.7, which is consistent with complete disordering of bilayer 1 at 230 K. We emphasize that these comparisons are made in the inertial regime, which is  $\sim 0.4$  ps from our results for simulated deuterated water and from the results of other studies.<sup>27,53</sup> Our calculated<sup>56</sup> self-diffusion coefficient for simulated deuterated water,  $2.0 \times 10^{-5} \text{ cm}^2 \text{ s}^{-1}$ , is in excellent agreement with the experimental value for liquid water,  $1.97 \pm 0.02 \times 10^{-5} \text{ cm}^2 \text{ s}^{-1}$  at 287 K,<sup>18,72</sup> but this may be a coincidence. Results obtained when bilayer 4 was not fixed are discussed in Sec. 2.4.7.

### 2.4.4. Hydrogen bonding analysis

For each simulation, the hydrogen bonds between water molecules were analyzed at each step. Our definition of a hydrogen bond between surface water molecules is identical to that

used in a previous study:<sup>73</sup> a distance less than or equal to 2.40 Å between the hydrogen atom and the neighboring oxygen atom and an intermolecular <OHO angle greater than or equal to 120°. We found the OH length to be a poor criterion because it was essentially invariant even at 310 K.

For a given bilayer, a lengthening of the average hydrogen bond and the intermolecular distance between oxygen atoms was observed as well as a decrease in the intermolecular <OHO angle at higher temperature, while the standard deviation of these quantities was greater; all of these trends are reasonable. The actual changes were small on an absolute scale. The results obtained when bilayer 4 was not fixed are particularly significant and are discussed in Sec. 2.4.7.

In Figure 2.8, the fraction of intact hydrogen bonds (with a length less than 2.40 Å and an <OHO angle greater than or equal to 120°) relative to defect-free hexagonal ice over the final 0.5 ps is plotted as a function of bilayer. Note that a value of one was found for bilayer 4 for all five simulations. For comparison, the result for simulated deuterated water at 300 K is 0.31 over 0.5 ps, which lies within the range of experimental values at 300 K, 0.3-0.5, obtained by analysis of thermodynamic data,<sup>74</sup> molar volume data,<sup>75</sup> and the intensity of the  $n_T$  band in the Raman spectrum,<sup>76</sup> validating our definition of the hydrogen bond. It is worth mentioning, however, that the fraction of intact hydrogen bonds is very difficult to determine experimentally. At 273 K, for example, 18 estimates for liquid water ranging from 28.5 to 97.5 % have been reported.<sup>77</sup>

<Figure 2.8 here>

In Figure 2.8, essentially no hydrogen bonds are broken in bilayer 1 at 190 K, indicating that bilayer 1 is completely ordered with respect to this parameter. At 230 K and higher, over 8 % of the hydrogen bonds are broken on average at each step. The fraction broken in bilayer 1 at 270 K is larger than that at 310 K. The reason for this is not known; however, the average fraction broken throughout all moving bilayers 1, 2 and 3 is the same at 270 and 310 K, 5.0 %. At 230 K and higher, bilayer 1 is considerably more disordered than bilayers 2 or 3. The results obtained when bilayer 4 was not fixed are discussed in Sec. 2.4.7.

In qualitative agreement with our results, Kroes observes a decrease in the number of hydrogen bonds as temperature increases.<sup>26</sup> However, at 190, 210, and 230 K, Kroes observes excess surface hydrogen bonds, that is, more hydrogen bonds than an ideal unreconstructed

surface would have. In this study, we do not observe excess hydrogen bonds at any temperature. Our definitions of the hydrogen bond are, however, quite different; we use a geometric definition, while Kroes adopts an energetic definition.

#### 2.4.5. Pair distribution functions

In order to characterize the surface, pair distribution functions  $g_{HH}(r)$ ,  $g_{OH}(r)$ , and  $g_{OO}(r)$  were calculated for each bilayer. For a perfectly ordered hexagonal ice lattice, the pair distribution functions are a series of sharp peaks. The pair distribution functions for liquid water can be experimentally determined using neutron scattering.<sup>78</sup> Recently, the pair distribution functions for liquid water were calculated from a 10-ps trajectory for a periodic box model consisting of 64 deuterated water molecules at 318 K.<sup>79</sup> These 64-molecule results were in better agreement with the most recent neutron diffraction data at 298 K than the results of Sprik *et al.* from a 5-ps trajectory for 32 deuterated water molecules at 303 K.<sup>53</sup>

The pair distribution functions calculated from a 0.5-ps trajectory for simulated deuterated water at 300 K were compared to 32-molecule results of Sprik *et al.* over 5 ps in order to determine if a 0.5-ps trajectory was adequate. Our functions as well as those of Sprik *et al.* were obtained using a bin size of 0.07 Å and are compared in Figure 2.9.

<Figure 2.9 here>

The  $g_{HH}(r)$  and  $g_{OH}(r)$  curves in Figure 2.9 are nearly overlapping, while the results for  $g_{OO}(r)$  are satisfactory: the first peak at 2.8 Å for our  $g_{OO}(r)$  is coincident with that of Sprik *et al.*, while the peak at 4.5 Å is not smooth though possesses the same general shape. When  $g_{OO}(r)$  was calculated from the entire 3.24-ps trajectory rather than the last 0.5 ps, the ripples in this peak were greatly reduced. Our conclusion from Figure 2.9 is that a 0.5-ps timescale is sufficient to obtain reasonably accurate results for liquid water and thus by bilayer. The initial configuration of our simulated deuterated water was taken from a trajectory that was equilibrated stepwise for ~7 ps, starting with a configuration taken from an equilibrated classical molecular dynamics run.<sup>53,80</sup> It seems that once our deuterated water is equilibrated, we are able to calculate pair correlation functions from a 0.5-ps trajectory.



Using the procedure described by Allen and Tildesley and taking into account periodic boundary conditions,<sup>56</sup> pair distribution functions were calculated for each bilayer using a bin size of 0.07 Å. The total volume of a bilayer, a quantity that is impossible to define uniquely, was taken as one quarter of the volume of eight hexagonal ice unit cells.

Shown at the bottom of Figure 2.10 are  $g_{HH}(r)$  for bilayer 1 at 190 and 230 K and for bilayer 2 at 190 K. Results for bilayer 1 at 270 and 310 K are quantitatively very similar to those at 230 K, while bilayers 2 and 3 at higher temperature are similar to bilayer 2 at 190 K. Also included is  $g_{HH}(r)$  for 32 deuterated water molecules at 303 K from the study by Sprik *et al.*<sup>53</sup>

<Figure 2.10 here>

For bilayer 1, as temperature is raised from 190 to 230 K, the peak at 2.3-2.4 Å falls to approximately the height of that for liquid water, indicating a change from order to disorder. As indicated above, no further change in height is observed as temperature is raised further. In addition, the minimum at 3 Å rises as the temperature is raised, approaching that for liquid water. The height of the peak at 2.3-2.4 Å rises substantially upon going from bilayer 1 to bilayer 2 at 190 K. In addition, a local maximum of 0.5 at 2.9 Å is present in bilayer 2 at 190 K, which is characteristic of hexagonal ice.

In the middle of Figure 2.10,  $g_{OH}(r)$  is plotted for bilayer 1 at 190 and 230 K and for bilayer 2 at 190 K. Results for bilayer 1 at 270 and 310 K are quantitatively very similar to those at 230 K, while bilayers 2 and 3 at higher temperature are similar to bilayer 2 at 190 K. Also included is  $g_{OH}(r)$  for deuterated water at 303 K from the study by Sprik *et al.*<sup>53</sup> Similar trends as those for  $g_{HH}(r)$  are observed. First, the peak at 1.76 Å, the hydrogen bond distance in hexagonal ice, falls from 1.9 to 1.5 upon going from bilayer 1 at 190 K to 230 K. Further change upon raising the temperature was negligible, indicating that bilayer 1 is completely disordered at 230 K but only partially so at 190 K. Also, the local minimum at 2.5 Å rises from zero for bilayer 1 at 190 K to essentially the value for liquid water at 230 K. The peak at 3.3 Å falls upon going from bilayer 1 at 190 K to bilayer 1 at 230 K; the height of this peak at 190 K is only 0.1 greater than that for liquid water. The height of the peak at 1.8 Å (and at 3.3 Å) increases upon moving from bilayer 1 to bilayer 2 at 190 K, with a concomitant narrowing of the peak, indicating a

greater degree of order. Furthermore, a peak is present in bilayer 2 at 3.8 Å that is characteristic of hexagonal ice.

The last function,  $g_{OO}(r)$ , is plotted at the top of Figure 2.10 for bilayer 1 at 190 and 230 K and for bilayer 2 at 190 K. Results for bilayer 1 at 270 and 310 K are very similar to those at 230 K, while bilayers 2 and 3 at higher temperature are similar to bilayer 2 at 190 K. Also included is  $g_{OO}(r)$  for deuterated water at 303 K from the study by Sprik *et al.*<sup>53</sup> The same qualitative trends are evident as for  $g_{HH}(r)$  and  $g_{OH}(r)$ . The results obtained for  $g_{HH}(r)$ ,  $g_{OH}(r)$ , and  $g_{OO}(r)$  when bilayer 4 was not fixed are presented and discussed in Sec. 2.4.7.

#### 2.4.6. Heat capacity

The constant volume heat capacity  $C_v$  was determined for the entire slab as both an interval test of surface disorder and as another parameter to compare with experiment. At 298 K,  $C_v$  of water is  $75 \text{ J mol}^{-1} \text{ K}^{-1}$ ,<sup>81</sup> considerably different from that of ice at 230 K,  $29 \text{ J mol}^{-1} \text{ K}^{-1}$ .<sup>81</sup> Using Eq. (2.5),  $C_v$  for all 32 molecules, including fixed layers, was determined at each simulation temperature from the average of the fluctuations in the total (classical) energy of the system  $E_t$ , which consists of the electronic energy and the classical kinetic energy of the nuclei. We emphasize that  $C_v$  will be affected by the coupling of the slab to the Nosé thermostat, and this effect may be temperature-dependent. However, as described below, our results are in qualitative agreement with experiment, and thus we assume that this effect is not significant.

$$C_v = \frac{\langle (E_t - E_{avg})^2 \rangle_{NVT}}{kT^2}, \quad (2.5)$$

where  $E_t$  is the total energy at time  $t$ ,  $E_{avg}$  is the average  $E_t$ ,  $k$  is Boltzmann's constant, and  $T$  is absolute temperature.<sup>56</sup>

In Figure 2.11,  $C_v$  is plotted as a function of temperature, and experimental  $C_v$  for ice and liquid water are also shown. When the result of  $34 \text{ J mol}^{-1} \text{ K}^{-1}$  for the simulation at 230 K with bilayer 4 fixed is compared to the result of  $55 \text{ J mol}^{-1} \text{ K}^{-1}$  at 230 K with the bottom bilayer not fixed, our conclusion is that by fixing the bottom two layers the calculated  $C_v$  are skewed towards that of ice. Because the difference between 34 and  $55 \text{ J mol}^{-1} \text{ K}^{-1}$  is considerable,

calculated  $C_v$  were corrected by  $55 - 34 = 21 \text{ J mol}^{-1} \text{ K}^{-1}$ . Both calculated and corrected / adjusted  $C_v$  are shown in Figure 2.11.

<Figure 2.11 here>

Below 230 K and above 270 K,  $C_v$  is relatively constant, which is in agreement with experiment that indicates the temperature dependence is weak. Also, between 230 and 270 K, a large (but not necessarily abrupt) increase in  $C_v$  is observed, suggesting that the melting point of our slab lies between 230 and 270 K. This is lower than the actual melting point of ice but is higher than our earlier estimate of  $\sim 220 \text{ K}$ , which was made based on comparison of the calculated hydrogen bond strength of a water dimer to experiment. The corrected  $C_v$  for the slab at 190 and 230 K is intermediate between the experimental values for ice and liquid water, which is reasonable based on a picture of partial disorder below the melting point. At 270 and 310 K, the corrected  $C_v$  is essentially identical to that of water at 293 K, suggesting complete disorder.

#### 2.4.7. Effect of fixing the bottommost bilayer

Unlike our calculated heat capacity  $C_v$  for the entire slab, our results for bilayers 1, 2, and 3 at 230 K are not substantially affected when bilayer 4 is not fixed. Specifically, the average  $S_T$  for bilayer 1 rises from 0.59 to 0.76 in Figure 2.2 but still clearly indicates disorder. The distribution of oxygen atom distances from the bottommost bilayer is not affected once migration in the  $-z$ -direction is taken into account. In Figure 2.4, the average  $S_R$  for bilayer 1 is essentially unaffected by freeing bilayer 4, changing from 0.32 to 0.31, and it decreases by only 0.14 and 0.12 for bilayers 2 and 3. Although not shown in Figures 2.5 and 2.6, the distributions of  $\mathbf{f}$  and  $\mathbf{q}$  were not found to change appreciably. While the mean square displacement of bilayer 1 at 230 K shown in Figure 2.7 is greater when bilayer 4 is not fixed, 1.07 versus 0.73  $\text{\AA}^2$  after 0.25 ps, that for bilayers 2 and 3 changes by at most 0.01  $\text{\AA}^2$  (3 %). As shown in Figure 2.8, the fraction of hydrogen bonds broken in bilayers 1, 2, and 3 is basically unaffected. Lastly, when bilayer 4 is released, the height of the peaks representing bilayers 1 and 2 in Figure 2.10 changes by less than 10 %.

While the results for the upper bilayers 1, 2, and 3 are unaffected, the results at 230 K for bilayer 4, which is a surface when it is not fixed in our slab model, are substantially different from those of bilayer 1, the “other” surface. Specifically, bilayer 4 is substantially more ordered ( $S_T = 0.93$  and  $S_R = 0.65$ ) in Figures 2.2 and 2.4, respectively. In addition, although not shown in Figure 3, when bilayer 4 is not fixed, the oxygen atoms in bilayer 4 are less spread out. Although not shown in Figures 5 and 6, the distributions of  $\mathbf{f}$  and  $\mathbf{q}$  resemble bilayer 1 at 190 K rather than at 230 K. It is particularly surprising that for the  $\mathbf{q}$  distribution the peak at  $120^\circ$  in bilayer 4 is not flattened like the peak at  $60^\circ$  in bilayer 1 at 230 K. The mean square displacement is a factor of two smaller in bilayer 4 than in bilayer 1 at 230 K, 0.58 versus 1.07  $\text{\AA}^2$  after 0.25 ps (not shown in Figure 2.7). The fraction of the hydrogen bonds broken in bilayer 4 is 0 % (not shown in Figure 2.8), compared to more than 8 % in bilayer 1 at 230 K. Finally, the height of the  $g_{HH}(r)$  peak representing bilayer 4 is  $\sim 0.5$  greater than that for bilayer 1 at 230 K and in fact similar to bilayer 1 at 190 K (not shown in Figure 2.10); results for  $g_{OH}(r)$  and  $g_{OO}(r)$  are similar, indicating more order in bilayer 4 judging by the height of the peaks.

When bilayer 4 was not fixed at 230 K, the hydrogen bond, as defined in Sec. 2.4.4, was found to be stronger, or more like ice, on average in bilayer 4 than in bilayer 1. Specifically, the average hydrogen bond length in bilayer 4 was 1.850  $\text{\AA}$  versus 1.888  $\text{\AA}$  in bilayer 1, while the average  $\langle \text{OHO} \rangle$  angle was  $168.15^\circ$  in bilayer 4 versus  $164.65^\circ$  in bilayer 1. This stronger hydrogen bond in bilayer 4 may be a genuine electronic effect caused by subtle differences in the geometry of bilayer 4, or it may be a result of incomplete averaging due to the short simulation times. Running longer trajectories would allow one to distinguish between these two possibilities.

## 2.5. SUMMARY OF DISORDER ANALYSIS

Significant disordering of the uppermost bilayer was found at 190 K, which is 30 K below our estimated melting point of  $\sim 220$  K, with respect to four parameters: the vertical density profile, the rotational order parameter, the mean square displacement, and the constant volume heat capacity. At 230 K, disordering of the uppermost bilayer was indicated by the remaining parameters, including the translational order parameter, the distribution of angles  $\mathbf{f}$  and  $\mathbf{q}$ , the fraction of intact hydrogen bonds, and the pair distribution functions. Disordering of

bilayers 2 and 3 occurred to a much lesser extent over 0.5 ps at all temperatures. Our order parameters collectively suggest a partially disordered surface region at temperatures 30-40 K below the laboratory freezing point of hexagonal ice, 273 K. A continuous transition from disorder to order is suggested by our results, but more simulations would be needed to observe a continuous transition explicitly.

The approximations inherent in calculation of the pair distribution functions and the constant volume heat capacity, as well as our somewhat arbitrary form for the translational and rotational order parameters, make these parameters less desirable. Nonetheless, based on the interesting changes that we observed, the pair distribution function  $g(r)$  is recommended for characterizing disorder over a short timescale. We also recommend the vertical density profile for measuring translational disorder. The distribution of angles  $\mathbf{f}$  and  $\mathbf{q}$  is recommended for measuring rotational disorder. Because the fundamental vibrational modes for liquid water and ice are broad and not much different energetically ( $\sim 100\text{-}200\text{ cm}^{-1}$ ),<sup>82,83</sup> and because our spectral resolution was marginal ( $80\text{ cm}^{-1}$  for a 0.5-ps trajectory), the power spectrum,<sup>84,85</sup> uniquely available by bilayer from first-principles simulation, was found to be not particularly useful for characterizing disorder.

Some of the effects of a moving (non-fixed) bottommost bilayer on the bilayers above can be rationalized based on the fact that migration is allowed in the  $+z$ - and  $-z$ -directions, leading to a greater spacing between layers. The greater order of bilayer 4 when not fixed compared to bilayer 1 is attributed to stronger average hydrogen bonds that induce order over a 0.5-ps timescale. Thus, the arrangement of hydrogen atoms is very important for obtaining precise results over short timescales but not (as important) for detecting trends. This is in contrast to results from a 40-ps classical simulation of TIP4P ice, in which no dependency of disordering on proton arrangement was observed except near the melting point in layers 5 and 6 of a 12-layer hexagonal ice model.<sup>26</sup>

In terms of atmospheric implications, it is possible that stratospherically abundant HCl lowers the onset temperature for surface disordering significantly. One reason to expect this is that the freezing point of concentrated solutions of HCl is significantly depressed.<sup>7</sup> We are currently investigating the possibility of a mechanism of chlorine activation involving partial solvation of chlorine reservoir species with both theoretical and experimental techniques under temperature and partial pressure conditions typical of the polar stratosphere.

## 2.6. CONCLUSIONS

A multi-layer model of hexagonal ice was developed, and disordering of the basal (0001) surface was characterized by bilayer with respect to various order parameters using first-principles molecular dynamics. Evidence for surface disorder in bilayer 1 at least 30 K below the estimated melting point of our ice slab was found, as summarized in Sec. 2.5, validating in a qualitative way the classical studies of surface disordering. The results of this study will be used to undertake additional studies with HCl, a potentially reactive foreign molecule, interacting with ice. This will allow us to gain more insight into the likelihood of a quasi-liquid layer mechanism for chlorine activation and polar ozone depletion involving Rx. (2.1) as well as to study reactions on the surface.

## 2.7. ACKNOWLEDGEMENTS

We would like to thank Dr. Pier L. Silvestrelli for providing the pair distribution functions from Sprik *et al.* for deuterated liquid water at 303 K.<sup>53</sup> This work was partially supported by National Computational Science Alliance and utilized the NCSA SGI/CRAY Origin2000. Y.A.M. acknowledges partial support from the Center for Global Change Sciences at MIT. F.M.G. acknowledges support from the NOAA Postdoctoral Program in Climate and Global Change, administered by the University Corporation for Atmospheric Research. This work was supported by the NASA Upper Atmospheric Research Program.

## 2.8. APPENDIX

In this Appendix, which contains unpublished results, we evaluate the frequency of stretching of the OH bond by bilayer as an order parameter to study ice surface disordering. One of the advantages of our method is the ability to study bond stretching, without constraints such as a fixed OH distance. Over a 0.5-ps timescale, an ice or water molecule experiences many vibrations compared to other molecular motions: the vibrational period is  $\sim 10$  fs, which is much shorter than that for molecular rotation or translational displacement in ice,  $\sim 10^{-5}$  s, or liquid

water,  $\sim 10^{-11}$  s, and even that for libration, which is a molecular vibration about a lattice position,  $\sim 200$  fs.<sup>66</sup> Accordingly, the molecular lineshape  $I(\omega)$  can be obtained from the hydrogen-hydrogen velocity autocorrelation function,  $\langle \mathbf{v}_H(t) \cdot \mathbf{v}_H(0) \rangle$ .<sup>84</sup> The power spectrum  $P(\omega)$ , related to the vibrational spectrum, for each bilayer was obtained by averaging molecular  $I(\omega)$ , defined in Eq. (2.6), and using the relation  $P(\omega) \sim |I(\omega)|^2 + |I(-\omega)|^2$ .<sup>85</sup>

$$I(\omega) \sim \frac{1}{2\pi} \int_{-\infty}^{\infty} dt e^{-i\omega t} \langle \mathbf{v}_H(t) \cdot \mathbf{v}_H(0) \rangle \quad (2.6)$$

To assess the effects of the Nosé thermostat, vibrational spectra for a single isolated (gas-phase)  $\text{H}_2\text{O}$  molecule in a cubic supercell with sides of 7.5 Å at 230 K coupled and not coupled to a Nosé thermostat were calculated from a 4.74 ps trajectory with a resolution that was calculated to be 8  $\text{cm}^{-1}$ .<sup>85</sup> The results are shown in Figure 2.12. In the power spectrum for a water molecule coupled to a Nosé thermostat, strong peaks are located at 1615, 3220, and 3400  $\text{cm}^{-1}$ , the fundamental vibrational modes. Experimentally, for water vapor,  $\mathbf{n}_2 = 1595 \text{ cm}^{-1}$  (HOH bending mode),  $\mathbf{n}_1 = 3657 \text{ cm}^{-1}$  (OH symmetric stretch), and  $\mathbf{n}_3 = 3756 \text{ cm}^{-1}$  (OH antisymmetric stretch).<sup>86</sup> Also present but not shown in Figure 2.12 are peaks at 100  $\text{cm}^{-1}$ , more intense than the fundamentals by a factor of  $\sim 20$ , identified with the experimentally observed intense peak near 200  $\text{cm}^{-1}$  arising from molecular rotation at room temperature. The fundamental peaks in the power spectrum for a water molecule not coupled to a Nosé thermostat overlap almost perfectly, but additional spurious peaks are also observed, some of which are more intense than  $\mathbf{n}_2$ . These power spectra were only marginally improved by multiplying the velocity autocorrelation data by a Bartlett window function.<sup>85</sup> We conclude that reasonable agreement with experiment can be obtained with a Nosé thermostat.

<Figure 2.12 here>

As a test of our methodology, the power spectrum for simulated deuterated water at 300 K was also calculated with an 11  $\text{cm}^{-1}$  resolution from a 3.24 ps trajectory. This power spectrum is shown in Figure 2.13. Broad, intense peaks are observed at 1170 and 2360  $\text{cm}^{-1}$ , along with a peak at 400  $\text{cm}^{-1}$ . The former peaks were assigned to fundamental bands, observed

experimentally at energies  $n_2 = 1215$ ,  $n_1 = 2450$  and  $n_3 = 2540$   $\text{cm}^{-1}$ ,<sup>82</sup> while the latter band was matched to a broad libration at  $505$   $\text{cm}^{-1}$ .<sup>66</sup> The fundamental peaks are shifted relative to our single water molecule due to the isotope effect. Our peak positions are in excellent agreement with those from an earlier Car-Parrinello molecular dynamics study,<sup>87</sup> in which the deuterated water spectrum was computed from the ensemble average of the total dipole moment, where the electronic contribution was evaluated using the Berry phase formulation. In that work, four major features were found: a pronounced peak at  $165$   $\text{cm}^{-1}$ , a broad band centered around  $500$   $\text{cm}^{-1}$ , a narrow peak at  $1160$   $\text{cm}^{-1}$ , and a strong band centered around  $2300$   $\text{cm}^{-1}$ . In their study, the fundamentals were shifted as well to lower energies by  $50$ - $200$   $\text{cm}^{-1}$  compared to experiment.

<Figure 2.13 here>

With this test giving a satisfactory result, power spectra were calculated with an  $80$   $\text{cm}^{-1}$  resolution for each bilayer from the five  $0.5$ -ps trajectories. Typical results are shown in Figure 2.14, where the power spectra for bilayers 1, 2 and 3 are shown at  $230$  K.

<Figure 2.14 here>

The fundamental energies were estimated graphically to within  $\pm 5$   $\text{cm}^{-1}$  using bilayer spectra such as those in Figure 2.14. Due to the poor resolution, no effort was made to interpret peak width. Sometimes, a fundamental was very weak; in this case, assignment was facilitated by calculating a new power spectrum using  $\langle \mathbf{v}_{HO}(t) \cdot \mathbf{v}_{HO}(0) \rangle$ , where  $\mathbf{v}_{HO}(t) = \mathbf{v}_H(t) - \mathbf{v}_O(t)$ . Because they were similar, the fundamental energies for bilayers 1, 2, and 3 were averaged together for each of the five simulations, while those for bilayer 4 was taken from the simulation at  $230$  K without any fixed atoms, to obtain Figure 2.15.

<Figure 2.15 here>

In Figure 2.15, the fundamental  $n_2$  rises in energy by  $70$   $\text{cm}^{-1}$  moving into the bulk from bilayer 1 to 3, and it drops by roughly the same amount moving from bilayer 3 to (moving) bilayer 4, which is another surface. If this trend is real, it is not inconsistent with a



transformation from disorder to order based on the experimentally observed 5-cm<sup>-1</sup> “shift” of the fundamental  $\nu_2$  when comparing liquid water (1645 cm<sup>-1</sup>) to hexagonal ice (1650 cm<sup>-1</sup>).<sup>82,83</sup> A more compelling trend is a large decrease in the average energy of  $\nu_1$  and  $\nu_3$  moving from bilayer 1 to bilayer 2. The magnitude of this decrease, which is 134 cm<sup>-1</sup> for  $\nu_1$  and 188 cm<sup>-1</sup> for  $\nu_3$ , is greater than our calculated spectral resolution and furthermore is close to the observed difference between liquid water and ice: the broad OH stretch in ice is peaked at  $\nu_s = 3220$  cm<sup>-1</sup>, with strong shoulders at 3150 and 3380 cm<sup>-1</sup>,<sup>83</sup> whereas the liquid water OH symmetric and antisymmetric stretches are overlapping bands with maxima at  $\nu_1 = 3280$  cm<sup>-1</sup> and at  $\nu_3 = 3490$  cm<sup>-1</sup>.<sup>82</sup> Our energy decrease is suggestive of a change from disorder in bilayer 1 to order in bilayer 2 at all temperatures, which is qualitatively consistent with our earlier results, including the fact that above 230 K an appreciable fraction of the hydrogen bonds are broken in bilayer 1: more broken hydrogen bonds are expected to lead to stretching that is less hindered on average and consequently larger  $\nu_1$  and  $\nu_3$  compared to bilayer 2 and 3. Experimental corroboration of our results for the first bilayer is possible using sum frequency generation.

For any given bilayer, the expected increase of  $\nu_1$  and  $\nu_3$  as temperature is raised is not observed, but rather a seemingly random scattering. This is most likely a consequence of the short trajectory.

## REFERENCES FOR CHAPTER 2

- (1) van der Veen, J. F. *Surf. Sci.* **1999**, *435*, 1.
- (2) Wettlaufer, J. S.; Dash, J. G. *Sci. Am.* **2000**, *282*, 50.
- (3) Dash, J. G.; Fu, H. Y.; Wettlaufer, J. S. *Rep. Prog. Phys.* **1995**, *58*, 115.
- (4) Dash, J. G. *Contemp. Phys.* **1989**, *30*, 89.
- (5) Gertner, B. J.; Hynes, J. T. *Faraday Discuss.* **1998**, *110*, 301.
- (6) Gertner, B. J.; Hynes, J. T. *Science* **1996**, *271*, 1563.
- (7) Molina, M. J. The probable role of stratospheric 'ice' clouds: Heterogeneous chemistry of the 'ozone hole'. In *The Chemistry of the Atmosphere: Its Impact on Global Change*; Calvert, J. G., Ed.; Blackwell Scientific Publications: Oxford, 1994; p. 27.
- (8) Farman, J. C.; Gardiner, B. G.; Shanklin, J. D. *Nature* **1985**, *315*, 207.
- (9) Newman, P. A.; Gleason, J. F.; McPeters, R. D.; Stolarski, R. S. *Geophys. Res. Lett.* **1997**, *24*, 2689.
- (10) Lee, S.-H.; Leard, D. C.; Zhang, R.; Molina, L. T.; Molina, M. J. *Chem. Phys. Lett.* **1999**, *315*, 7.
- (11) Seinfeld, J. H.; Pandis, S. N. *Atmospheric Chemistry and Physics: From Air Pollution to Climate Change*; Wiley: New York, 1998.

- (12) Molina, M. J. *Angew. Chem. Int. Ed. Eng.* **1996**, *35*, 1778.
- (13) Molina, M. J.; Molina, L. T.; Zhang, R. Y.; Meads, R. F.; Spencer, D. D. *Geophys. Res. Lett.* **1997**, *24*, 1619.
- (14) Petrenko, V. F.; Whitworth, R. W. *Physics of Ice*; Oxford University Press: New York, 1999.
- (15) Jellinek, H. H. G. *J. Colloid Interface Sci.* **1967**, *25*, 192.
- (16) Furukawa, Y.; Yamamoto, M.; Kuroda, T. *J. Cryst. Growth* **1987**, *82*, 665.
- (17) Furukawa, Y.; Nada, H. *J. Phys. Chem. B* **1997**, *101*, 6167.
- (18) Furukawa, Y.; Nada, H. Anisotropy in Microscopic Structures of Ice-Water and Ice-Vapor Interfaces and its Relation to Growth Kinetics. In *Advances in the Understanding of Crystal Growth Mechanisms*; Nishinaga, T., Nishioka, K., Harada, J., Sasaki, A., Takei, H., Eds.; Elsevier Science Publishers: Amsterdam, 1997; p. 559.
- (19) Dosch, H.; Lied, A.; Bilgram, J. H. *Surf. Sci.* **1995**, *327*, 145.
- (20) Bullemer, B.; Riehl, N. *Solid State Commun.* **1966**, *4*, 447.
- (21) Mazzega, E.; del Pennino, U.; Loria, A.; Mantovani, S. *J. Chem. Phys.* **1976**, *64*, 1028.
- (22) Gilpin, R. R. *J. Colloid Interface Sci.* **1980**, *77*, 435.
- (23) Golecki, I.; Jaccard, C. *J. Phys. C. Solid State Phys.* **1978**, *11*, 4229.
- (24) Mizuno, Y.; Hanafusa, N. *J. Phys. C Suppl. 3* **1987**, *48*, C1.
- (25) Nason, D.; Fletcher, N. H. *J. Chem. Phys.* **1975**, *62*, 4444.
- (26) Kroes, G.-J. *Surf. Sci.* **1992**, *275*, 365.
- (27) Karim, O. A.; Haymet, A. D. J. *J. Chem. Phys.* **1988**, *89*, 6889.
- (28) Karim, O. A.; Haymet, A. D. J. *J. Chem. Phys. Lett.* **1987**, *138*, 531.
- (29) Nada, H.; Furukawa, Y. *Surf. Sci.* **2000**, *446*, 1.
- (30) Nada, H.; Furukawa, Y. *Appl. Surf. Sci.* **1997**, *121*, 445.
- (31) Gao, G. T.; Zeng, X. C.; Tanaka, H. *J. Chem. Phys.* **2000**, *112*, 8534.
- (32) Vlot, M. J.; Huinink, J.; van der Eerden, J. P. *J. Chem. Phys.* **1999**, *110*, 55.
- (33) Karim, O. A.; Kay, P. A.; Haymet, A. D. J. *J. Chem. Phys.* **1990**, *92*, 4634.
- (34) Knight, C. A. *J. Geophys. Res.* **1996**, *101D*, 12921.
- (35) Baker, M. B.; Dash, J. G. *J. Geophys. Res.* **1996**, *101D*, 12929.
- (36) Knight, C. A. *J. Geophys. Res.* **1996**, *101D*, 12933.
- (37) Sakai, H. *Surf. Sci.* **1996**, *348*, 387.
- (38) Jorgensen, W. L.; Chandrasekhar, J.; Madura, J. D.; Impey, R. W.; Klein, M. L. *J. Chem. Phys.* **1983**, *79*, 926.
- (39) Bernal, J. D.; Fowler, R. H. *J. Chem. Phys.* **1933**, *1*, 515.
- (40) Materer, N.; Starke, U.; Barbieri, A.; Van Hove, M. A.; Somorjai, G. A.; Kroes, G.-J.; Minot, C. *Surf. Sci.* **1997**, *381*, 190.
- (41) Megaw, H. D. *Crystal Structures*; TechBooks: Fairfax, VA, first published in 1973.
- (42) Batista, E. R.; Xantheas, S. S.; Jónsson, H. *J. Chem. Phys.* **1998**, *109*, 4546.
- (43) Batista, E. R.; Xantheas, S. S.; Jónsson, H. *J. Chem. Phys.* **1999**, *111*, 6011.
- (44) Bernholc, J. *Phys. Today* **1999** (Sept), *52*, 30.
- (45) Parr, R. G.; Yang, W. *Density-Functional Theory of Atoms and Molecules*; Oxford University Press: New York, 1989.

- (46) Galli, G.; Pasquarello, A. First principles molecular dynamics. In *Computer Simulations in Chemical Physics*; Allen, M. P., Tildesley, D. J., Eds.; Kluwer Academic Publishers: Dordrecht, 1993; Vol. 397; p. 261.
- (47) Parrinello, M. *Solid State Commun.* **1997**, *102*, 107.
- (48) Car, R.; Parrinello, M. *Phys. Rev. Lett.* **1985**, *55*, 2471.
- (49) Remler, D. K.; Madden, P. A. *Mol. Phys.* **1990**, *70*, 921.
- (50) Hutter, J.; Alavi, A.; Deutsch, T.; Bernasconi, M.; Goedecker, St.; Marx, D.; Tuckerman, M.; Parrinello, M. *CPMD*; Max-Planck Institut für Festkörperforschung and IBM Zurich Research Laboratory, 1995-99.
- (51) Cohen, M. L. *Phys. Today* **1979 (July)**, *32*, 40.
- (52) Troullier, N.; Martins, J. L. *Phys. Rev. B* **1991**, *43*, 1993.
- (53) Sprik, M.; Hutter, J.; Parrinello, M. *J. Chem. Phys.* **1996**, *105*, 1142.
- (54) Becke, A. D. *Phys. Rev. A* **1988**, *38*, 3098.
- (55) Lee, C.; Yang, W.; Parr, R. G. *Phys. Rev. B* **1988**, *37*, 785.
- (56) Allen, M., P.; Tildesley, D. J. *Computer Simulation of Liquids*; Clarendon Press: Oxford, 1987.
- (57) Nosé, S. *Mol. Phys.* **1984**, *52*, 255.
- (58) Martyna, G. J.; Klein, M. L.; Tuckerman, M. *J. Chem. Phys.* **1992**, *97*, 2635.
- (59) Kirkpatrick, S.; Gelatt, C. D., Jr.; Vecchi, M. P. *Science* **1983**, *220*, 671.
- (60) Lonsdale, K. *Proc. R. Soc. Lond., Ser. A* **1958**, *247*, 424.
- (61) Peterson, S. W.; Levy, H. A. *Acta. Crystallogr.* **1957**, *10*, 70.
- (62) Shimaoka, K. *J. Phys. Soc. Jpn.* **1960**, *15*, 106.
- (63) Brill, R. *Angew. Chem. Int. Ed. Eng.* **1962**, *1*, 563.
- (64) Owston, P. G. *Adv. Phys.* **1958**, *7*, 171.
- (65) Leadbetter, A. J. *Proc. R. Soc. London, Ser. A* **1965**, *287*, 403.
- (66) Eisenberg, D.; Kauzmann, W. *The Structure and Properties of Water*; Oxford University Press: New York, 1969.
- (67) Shen, Y. R. *The Principles of Nonlinear Optics*; Wiley: New York, 1984.
- (68) Eissenthal, K. B. *Chem. Rev.* **1996**, *96*, 1343.
- (69) Shen, Y. R. *Solid State Commun.* **1998**, *108*, 399.
- (70) Geiger, F. M.; Tridico, A. C.; Hicks, J. M. *J. Phys. Chem. B* **1999**, *103*, 8205.
- (71) Tom, H. W. K.; Heinz, T. F.; Shen, Y. R. *Phys. Rev. Lett.* **1983**, *51*, 1983.
- (72) Wang, J. H. *J. Phys. Chem.* **1965**, *69*, 4412.
- (73) Molteni, C.; Parrinello, M. *J. Am. Chem. Soc.* **1998**, *120*, 2168.
- (74) Némethy, G.; Scheraga, H. A. *J. Chem. Phys.* **1962**, *36*, 3382.
- (75) Grjotheim, K.; Krogh-Moe, J. *Acta. Chem. Scand.* **1954**, *8*, 1193.
- (76) Walrafen, G. E. *J. Chem. Phys.* **1966**, *44*, 1546.
- (77) Falk, M.; Ford, T. A. *Can. J. Chem.* **1966**, *44*, 1699.
- (78) Soper, A. K.; Bruni, F.; Ricci, M. A. *J. Chem. Phys.* **1997**, *106*, 247.
- (79) Silvestrelli, P. L.; Parrinello, M. *J. Chem. Phys.* **1999**, *111*, 3572.
- (80) Laasonen, K.; Sprik, M.; Parrinello, M.; Car, R. *J. Chem. Phys.* **1993**, *99*, 9080.
- (81) Lide, D. C. *CRC Handbook of Chemistry and Physics*, 72nd ed.; Chemical Rubber Publishing Co.: Boca Raton, 1991; Vol. 1.
- (82) Bayly, J. E.; Kartha, V. B.; Stevens, W. H. *Infrared Phys.* **1963**, *3*, 211.
- (83) Bertie, J. E.; Whalley, E. *J. Chem. Phys.* **1964**, *40*, 1637.
- (84) McQuarrie, D. A. *Statistical Mechanics*; HarperCollins: New York, 1976.

- (85) Press, W. H.; Teukolsky, S. A.; Vetterling, W. T.; Flannery, B. P. *Numerical Recipes in Fortran: The Art of Scientific Computing*, 2nd ed.; Cambridge University Press: Cambridge, 1994.
- (86) Benedict, W. S.; Gailer, N.; Plyler, E. K. *J. Chem. Phys.* **1956**, *24*, 1139.
- (87) Silvestrelli, P. L.; Bernasconi, M.; Parrinello, M. *Chem. Phys. Lett.* **1997**, *277*, 478.

## LIST OF FIGURES FOR CHAPTER 2

Figure 2.1. Our model of hexagonal ice. Large black circles represent oxygen atoms, small gray circles represent hydrogen atoms, and thin dashed lines represent hydrogen bonds. The supercell (without a surface vacuum region) is superimposed. Shown in (a) are molecules in the first bilayer of the surface of interest, the basal ( $0001$ ) face, and in (b) the ( $10\bar{1}0$ ) face, one of six prism faces perpendicular to ( $0001$ ). In (b), each bilayer is formed from a pair of layers, e.g., bilayer 1 consists of layers 1 and 2.

Figure 2.2. Average  $S_T$  by bilayer for five different simulations (black lines) compared to results from a classical study (gray lines). In this and subsequent legends,  $nf$  indicates that the atoms in bilayer 4 are not fixed.

Figure 2.3. Vertical density profile of the distance of oxygen atoms in layers 1-7 from the bottommost fixed layer 8 at simulation temperatures of 190, 230, and 270 K. The results were normalized such that unity height was assigned to the peaks at 0 and at  $0.90 \text{ \AA}$  representing fixed layers 8 and 7, respectively.

Figure 2.4. Average  $S_R$  by bilayer for five different simulations (black lines) compared to results from a classical study (gray lines).

Figure 2.5. The distribution of  $f$  for molecules in bilayer 1 calculated at three temperatures. The results were normalized such that a height of one was given to the four peaks (not shown) representing the fixed bilayer 4.

Figure 2.6. The distribution of  $q$  for molecules in bilayer 1 calculated at three temperatures. The results were normalized such that a height of one was given to the two peaks (not shown) representing the fixed bilayer 4.

Figure 2.7. Mean square displacement for simulated deuterated water at 300 K, and results for bilayers 1, 2, and 3 at 190 K and bilayer 1 at 230 K.

Figure 2.8. Fraction of hydrogen bonds that were not broken on average during each 0.5-ps simulation calculated for bilayers 1, 2, and 3. A hydrogen bond is defined in the text.

Figure 2.9. Pair distribution functions  $g_{HH}(r)$ ,  $g_{OH}(r)$ , and  $g_{OO}(r)$  for simulated deuterated water over 0.5 ps (thick lines) and over 5 ps (thin lines).

Figure 2.10. Pair distribution functions  $g_{HH}(r)$ ,  $g_{OH}(r)$ , and  $g_{OO}(r)$  as a function of bilayer and temperature compared to simulated deuterated water at 303 K (solid gray lines).

Figure 2.11. Constant volume heat capacity  $C_v$  plotted as a function of temperature for each of the five simulations. The adjusted  $C_v$  (small black circles), which can be compared to the experimental  $C_v$  for ice and liquid water (gray triangles), were obtained by adding  $21 \text{ J mol}^{-1} \text{ K}^{-1}$  to the calculated  $C_v$  with bilayer 4 fixed (large dark gray circles).

Figure 2.12. Vibrational spectrum for gas-phase water coupled and not coupled to a Nosé thermostat. The signal in the  $n_2$  region of each spectrum is enhanced by a factor of three.

Figure 2.13. Vibrational spectrum for simulated deuterated water coupled to a Nosé thermostat at 300 K.

Figure 2.14. Representative power spectra for bilayers 1, 2 and 3 coupled to a Nosé thermostat at 230 K with the bottom bilayer fixed.

Figure 2.15. Average fundamental energy calculated from five different simulations as a function of bilayers 1, 2 and 3. The fundamental energy for bilayer 4 is reported directly from the simulation without any fixed atoms at 230 K and is not an average.

Figure 2.1

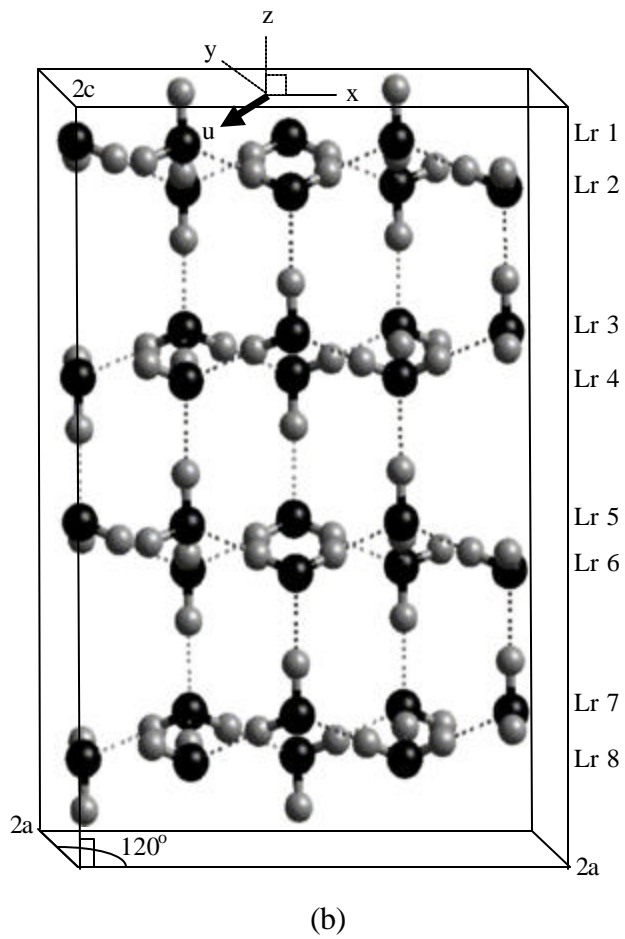
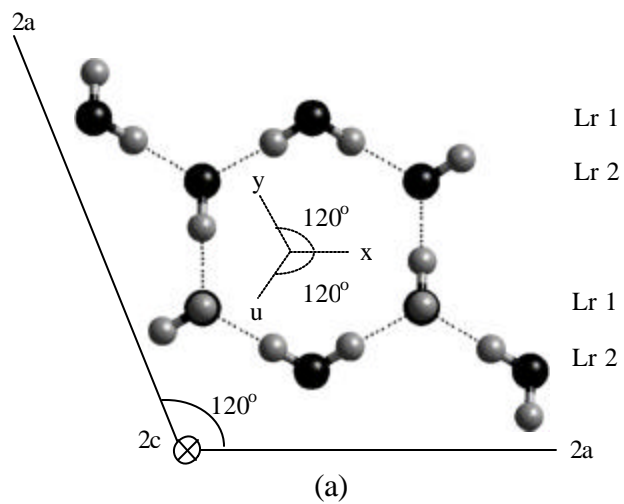


Figure 2.2

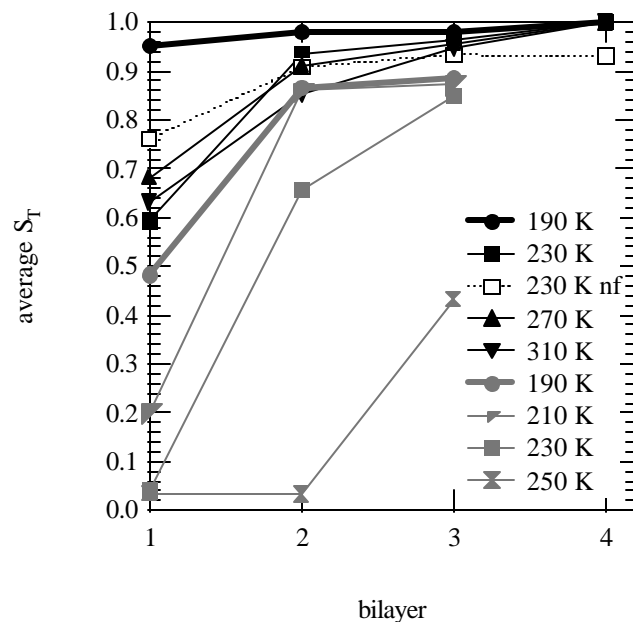




Figure 2.3

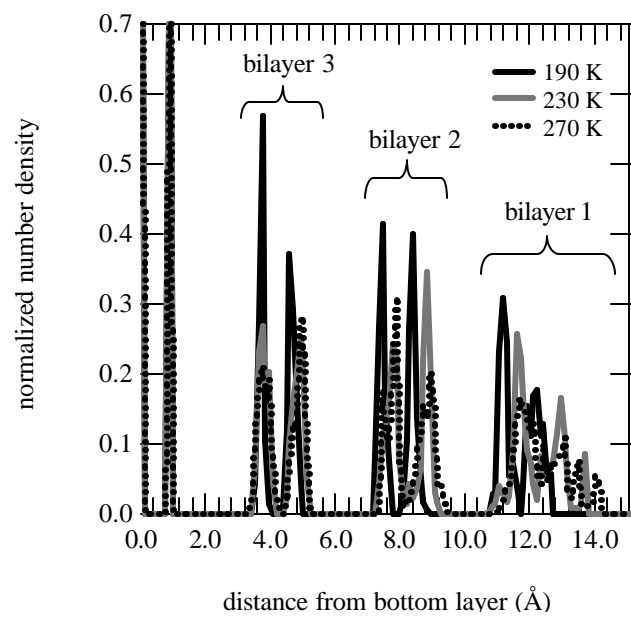


Figure 2.4

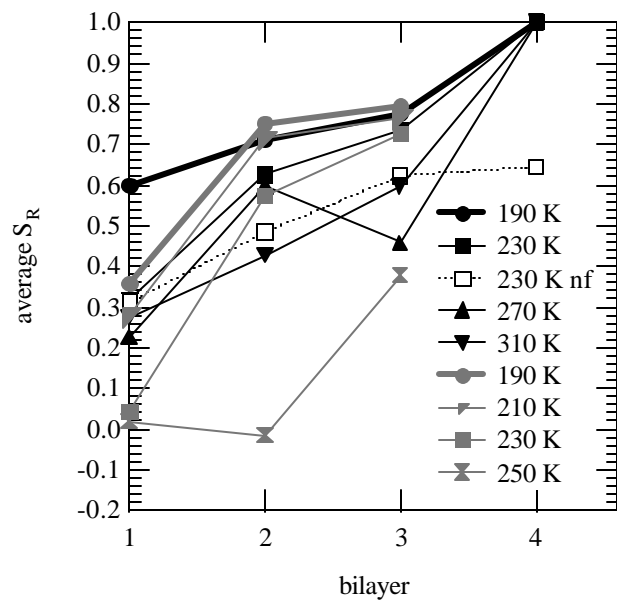


Figure 2.5

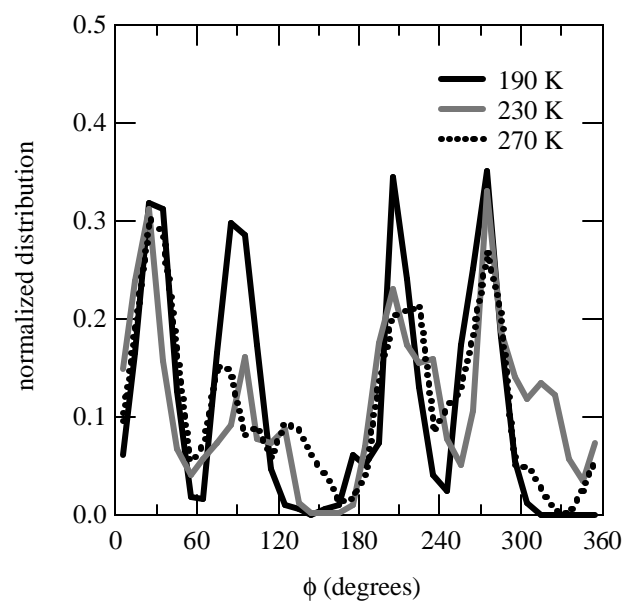


Figure 2.6

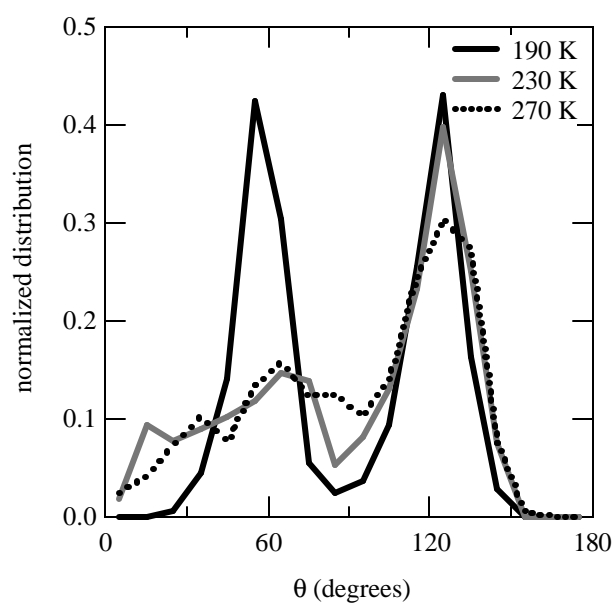


Figure 2.7

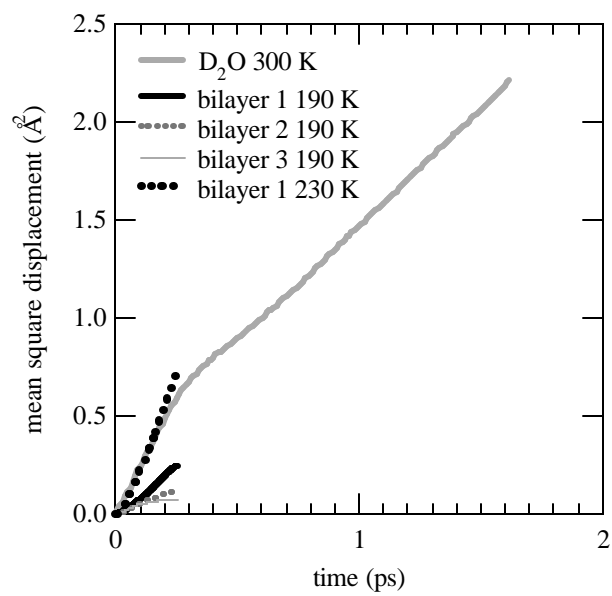


Figure 2.8

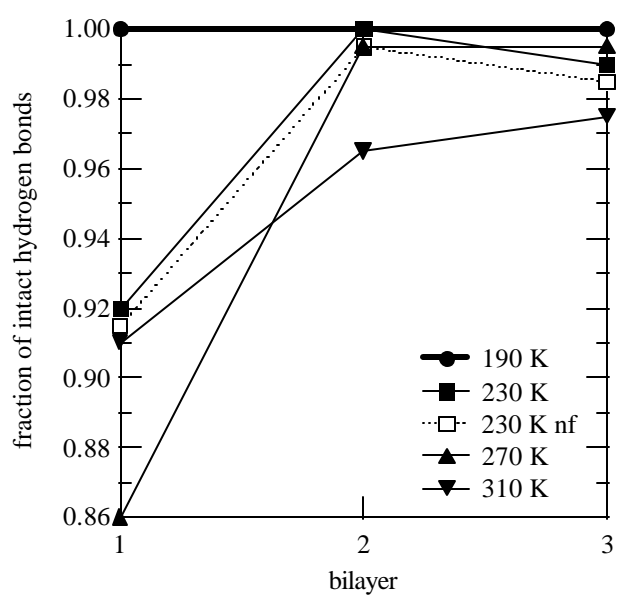


Figure 2.9

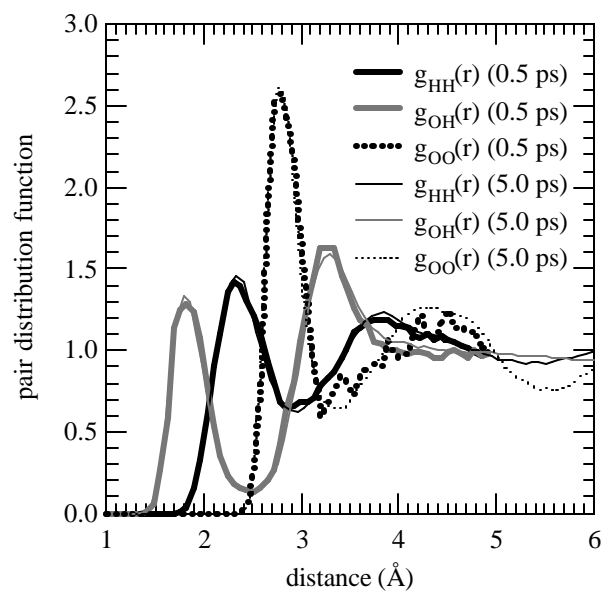


Figure 2.10

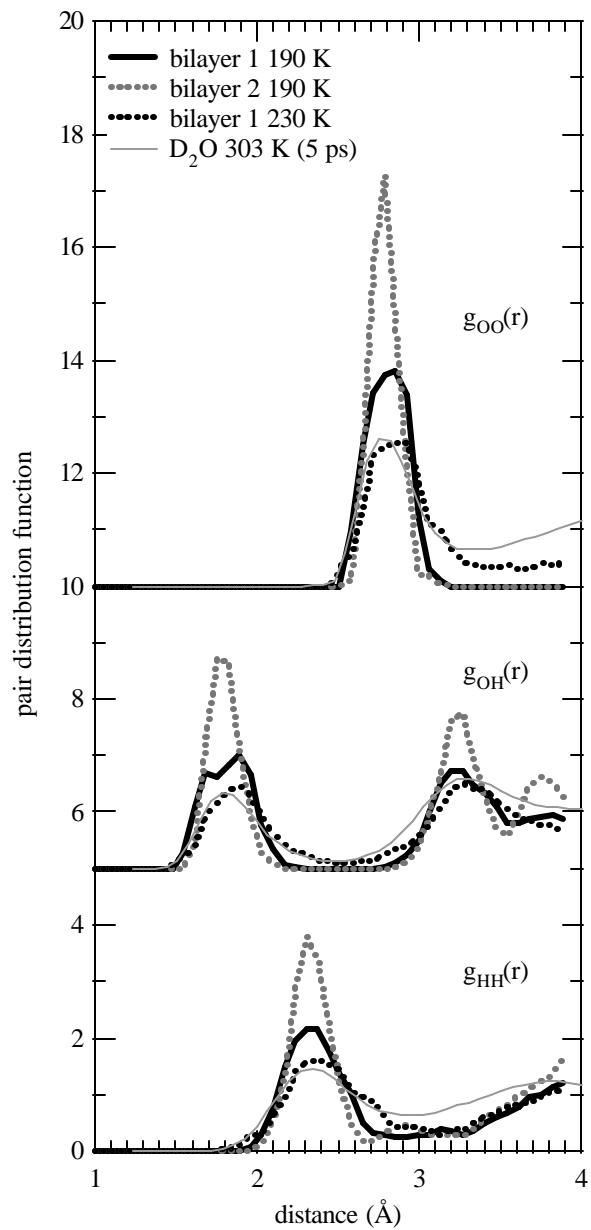




Figure 2.11

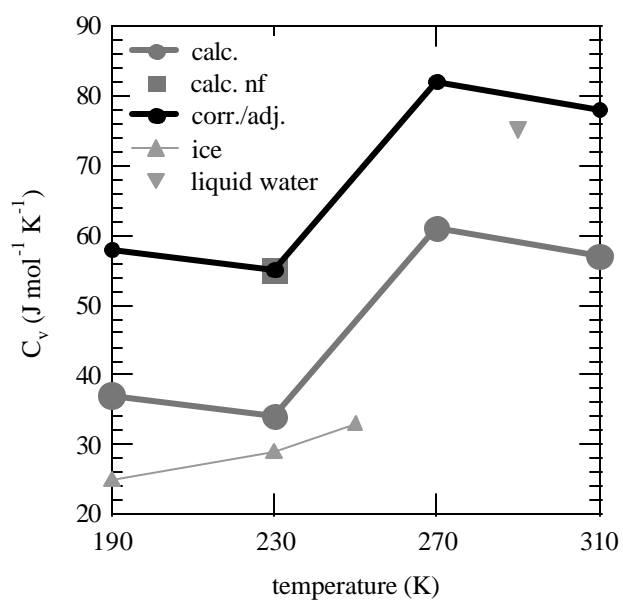


Figure 2.12

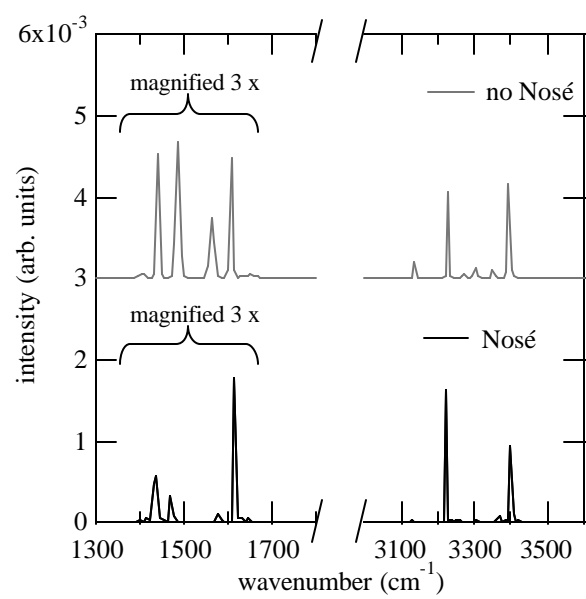


Figure 2.13

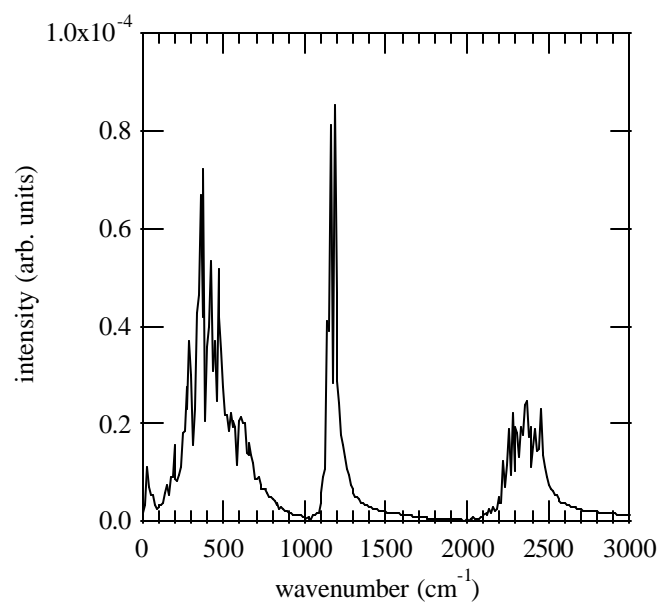


Figure 2.14

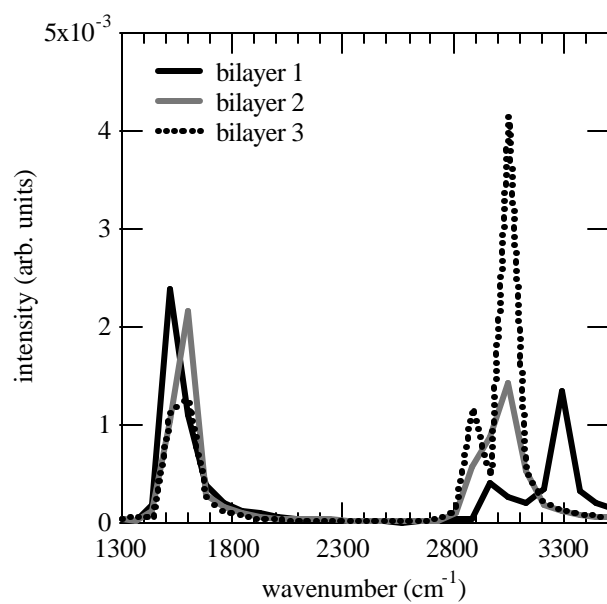
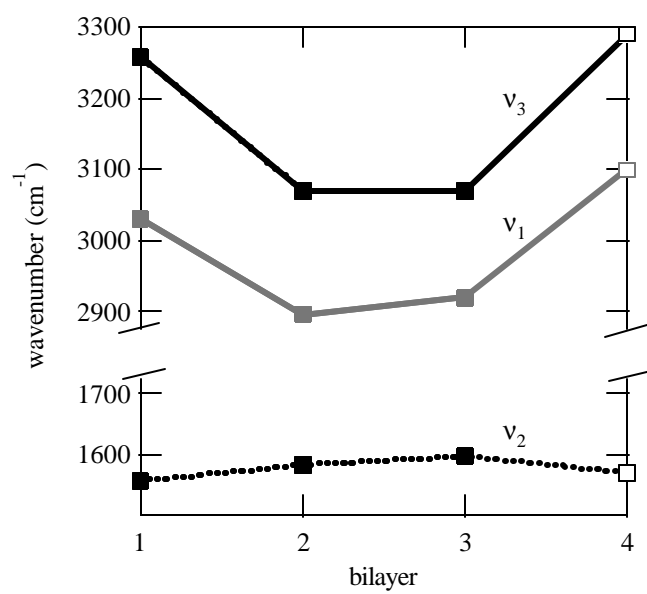


Figure 2.15



## Chapter 3: First-principles theoretical study of molecular HCl adsorption on a hexagonal ice (0001) surface

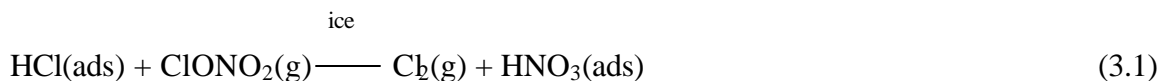
Reproduced with permission from Mantz, Y. A.; Geiger, F. M.; Molina, L. T.; Molina, M. J.; Trout, B. L. *J. Phys. Chem. A* 2001, *105*, 7037-7046. © 2001 American Chemical Society.

### ABSTRACT

A key step in the mechanism of polar ozone depletion involves the interaction of HCl with the particles that constitute polar stratospheric clouds. These particles exist as hexagonal ice *Ih* crystals below approximately 185 K. As a first step, we examine the binding of molecular HCl to a number of extended surface models of the basal (0001) face of hexagonal ice in addition to a cluster model representative of an unreconstructed adsorption site. Calculations are performed using gradient-corrected density-functional theory and high-order correlation methods. After correcting for zero-point energies, we estimate the molecular binding energy and enthalpy at 185 K to be 23 and 25 kJ/mol, respectively, for low (single-molecule) HCl coverage. These estimates decrease by a few kJ/mol at higher HCl coverage and are based partially on a low density of dangling surface OH groups. Our results set the stage for future studies addressing the possible ionization of molecularly adsorbed HCl using first-principles MD dynamics.

### 3.1. INTRODUCTION

It is now widely accepted that the annual formation of the Antarctic ozone hole during early polar spring is a direct result of the heterogeneous reaction of stable forms of chlorine on polar stratospheric clouds (PSCs) between 14-19 km altitude.<sup>1</sup> A very important example is Rx. (3.1) depicting production of active chlorine and sequestration of NO<sub>x</sub> on Type II PSCs (hexagonal ice *Ih* crystals), which form at a few degrees below the frost point of ice,<sup>2,3</sup> which is 188 K for a typical water vapor pressure of  $2.0 \times 10^{-4}$  Torr.<sup>4,5</sup> The photolysis of Cl<sub>2</sub>(g) ultimately leads to the gas-phase catalytic destruction of ozone, while sequestration of NO<sub>x</sub> prevents re-formation of relatively stable ClONO<sub>2</sub>(g).<sup>6</sup>



Although studied experimentally,<sup>7-9</sup> the mechanism of Rx. (3.1) (and other, related reactions) is still not known. The reaction of HCl with ClONO<sub>2</sub> on the surface of ice is known to proceed rapidly,<sup>10</sup> in contrast to the prohibitively slow gas-phase reaction;<sup>11</sup> this suggests an ionic-type mechanism may be operative in the presence of ice. As reviewed elsewhere,<sup>12,13</sup> a partially disordered transition region is present on the surface of ice at temperatures below the bulk freezing point. This “quasi-liquid layer,” as it is sometimes referred to in the literature, may facilitate ionic dissociation of HCl, a mechanism originally proposed by our laboratory.<sup>14</sup> Another possibility is that HCl is incorporated into the ice lattice at the surface,<sup>15,16</sup> which is known from experiments to be very dynamic: If the ice surface is in equilibrium with its vapor phase, ~10–100 bilayers per second are adsorbed and desorbed at 185 K.<sup>17</sup> Subsequent reaction of HCl with ClONO<sub>2</sub> involves proton transfer in the ice lattice accompanied by nucleophilic attack of Cl on the Cl<sup>δ+</sup> in ClONO<sub>2</sub>.<sup>18,19</sup> A third possibility involves several associative and dissociative steps catalyzed by NO<sub>3</sub><sup>-</sup>.<sup>20</sup>

A key first step involved in the mechanism of Rx. (3.1) is the uptake of HCl.<sup>21</sup> Using smooth and/or well-characterized ice films, experimentalists have shown the uptake of HCl is ~10<sup>13</sup>–10<sup>14</sup> molecule/cm<sup>2</sup> at stratospherically relevant temperatures and partial pressures.<sup>7,22,23</sup> Direct observation of HCl at ice surfaces remains difficult due to the technical challenges of performing experiments with molecular specificity under conditions typical of the polar stratosphere (~10<sup>-4</sup> Torr water vapor), where traditional surface-science techniques, which require ultra-high vacuum conditions, are often not feasible. Thus, it is not known whether HCl exists in an ionic or molecular form at (or near) the ice surface. Spectroscopic,<sup>24-26</sup> and other,<sup>27</sup> evidence indicates an ionic form of HCl at low temperatures (less than 180 K) and partial pressures where ionic hydrates of HCl are known to be thermodynamically stable. However, on the basis of the HCl-ice phase diagram,<sup>28,29</sup> bulk hydrates of HCl are not thought to exist in the polar stratosphere. In addition, other experimentalists infer a molecularly adsorbed form.<sup>30-35</sup>

Several of the experimental studies that suggest a molecular form give an estimate of the energy of interaction, but many assumptions are necessary in order to obtain values.

Furthermore, these experiments are not generally performed under both temperature and equilibrium conditions with respect to water vapor applicable to the polar stratosphere. In a recent molecular beam study,<sup>31</sup> a lower limit of 31-38 kJ/mol to the binding energy at 165 K of HCl on slowly condensing ice with less than  $5 \times 10^{12}$  molecule HCl/cm<sup>2</sup> adsorbed was found. An upper limit of 25 kJ/mol for HCl interacting with slowly evaporating HCl-covered ice was also determined assuming a frequency factor of  $10^{13} \text{ s}^{-1}$ , suggesting a coverage dependence of 10 kJ/mol. In two other experimental studies, the activation energy for desorption was estimated. In the first study,<sup>32</sup> molecular beams of HCl were reflected from amorphous and crystalline ice surfaces held at 100-126 K, were detected using mass spectroscopy, and a model was developed to obtain activation energies for HCl desorption of  $28 \pm 2$  and 26 kJ/mol, respectively. In the second study,<sup>33</sup> adopting a value of  $10^{13} \text{ s}^{-1}$  for the frequency factor, a value of  $33 \pm 5$  kJ/mol assumed to be independent of the total surface coverage of HCl was estimated at 140 K from temperature-programmed desorption. Lastly, an HCl binding enthalpy of 46 kJ/mol at 200 K was estimated by Elliott *et al.*,<sup>34</sup> who analyzed an experimental isotherm reported by Hanson and Mauersberger<sup>29</sup> and then assumed that the change in entropy was the same as that for liquefaction of pure HCl(g). For reference, note the limiting enthalpy of solution of HCl, which describes  $\text{HCl(g)} \rightarrow \text{H}^+(\text{aq}) + \text{Cl}^-(\text{aq})$  at 298 K and includes ionization of HCl and hydration of infinitely separated product ions, is 75 kJ/mol.<sup>36,37</sup> This summary indicates that there is currently uncertainty in the measured value of the energy of adsorption, providing another motivation to study the interaction of HCl with ice theoretically.

As a first step, theorists have studied the interaction of molecular HCl with model ice surfaces. Small cluster models have been (by necessity) used in high-level *ab initio* studies.<sup>38-42</sup> Other studies with periodic surfaces, which are a more realistic model of an unreconstructed hexagonal ice surface, have either been performed with a limited basis set at the Hartree-Fock level of theory, requiring an indirect estimate of correlation effects,<sup>43</sup> or have relied on an adjustable potential parameterized for the study of liquid water at STP rather than hexagonal ice.<sup>44-47</sup> In recent years, using cluster<sup>38,48,49</sup> as well as extended surface models,<sup>15,16,50,51</sup> several theoretical studies have focused on the role that water molecules play in the ionization of HCl, but these studies also suffer from one (or more) of the above limitations.

In this article, we lay the groundwork for investigating, using first-principles molecular dynamics, the atmospheric fate and the possible ionization of HCl on ice. We perform geometry



optimizations of molecular HCl on cluster and well as extended ice surface models, thereby allowing comparison of different models in a careful, consistent manner. Binding energies incorporating zero-point energies are also calculated. Our method treats exchange and correlation effects explicitly and employs large basis sets, thereby providing a test of the validity of, and serving as an important complement to, previous theoretical approaches. In this study, both the surface coverage of HCl and the number of dangling (non-hydrogen-bonding) OH groups are varied. To our knowledge, there are no previous theoretical studies of varying HCl surface coverage, and there is only one recent quantum-classical study investigating the role of varying number of OH groups on the ionization of HCl.<sup>52</sup>

The organization of this paper is as follows. Our models and our system of nomenclature are described in Sec. 3.2. Our approach is described in Sec. 3.3. The main results are presented in Sec. 3.4. A correction estimate for our use of the BLYP functional and pseudopotentials/plane waves is developed in Sec. 3.4.1, while correction estimates to the binding energy and enthalpy incorporating zero-point energies and thermal effects are made in Sec. 3.4.2. Results for molecular HCl adsorption on extended ice surface models incorporating these corrections are then given in Sec. 3.4.3. The results on extended surfaces are discussed further, and a best estimate of the binding energy and enthalpy at finite temperatures is developed, in Sec. 3.5. Atmospheric implications are briefly discussed in Sec. 3.6. Concluding remarks are made in Sec. 3.7.

## 3.2. ICE SURFACE MODELS

As a first attempt to model adsorption of molecular HCl on a hexagonal ice basal (0001) face,<sup>53</sup> which may be the most prevalent under polar stratospheric conditions,<sup>16</sup> the interaction of molecular HCl with a single water molecule as well as with a small cluster model representative of an adsorption site was studied. These models are depicted in Figure 3.1. Each model was placed in a large cubic simulation cell with  $a = 10 \text{ \AA}$  to prevent interaction with periodic images.<sup>54</sup> The cluster model is named 4W1A in order to distinguish it from the cyclic structure  $\text{HCl}\cdot(\text{H}_2\text{O})_4$ ,<sup>40</sup> which corresponds to the global minimum for HCl interacting with four water molecules.

< Figure 3.1 here >

Infinite surface or slab models were developed for comparison to simple cluster models. This development follows our earlier study of an ice slab.<sup>13</sup> Because the density of dangling OH groups on ice is not known experimentally, models with different numbers of dangling OH groups were developed. Other considerations included having each model satisfy the Bernal-Fowler ice rules,<sup>55</sup> where each oxygen atom is given two OH bonds and two hydrogen bonds arranged tetrahedrally; having a full-bilayer termination, where each surface water molecule forms three hydrogen bonds, which is more stable by 58 kJ/mol (per simulation cell) at the Hartree-Fock level than a half-bilayer termination, where each surface water molecule forms only one hydrogen bond;<sup>56</sup> and, lastly, having a net dipole moment as small as possible, because real ice is known to possess a zero net dipole moment due to proton disorder.<sup>57</sup>

Our extended surface models with the maximum possible number of HCl adsorbates are shown in Figure 3.2. To differentiate the models on the basis of the total number  $x$  of water molecules, the number  $y$  and position  $p$  of HCl adsorbates, the number  $z$  of dangling OH groups, and whether or not the bottom bilayer is fixed  $f$  to its optimized bulk position, a straightforward nomenclature  $xWyA^p zH(f)$  is adopted. To illustrate, 16W1A2Hf specifies a model with **16 Water molecules**, **1 HCl Adsorbate** bonded to oxygen atom O1, **2 dangling OH groups**, and a fixed bottom bilayer. If the site O2 (or O3) is occupied instead of O1, this is explicitly indicated, *e.g.*, 16W1A<sup>O2</sup>2Hf. If no HCl molecules are adsorbed to the slab,  $yA$  is omitted, *e.g.*, 16W2Hf. As the final example, the name of a model with **32 Water molecules**, **2 HCl Adsorbates** bonded to oxygen atoms O1 and O2, **2 dangling OH groups**, and no fixed bottom bilayer is 32W2A2H.

< Figure 3.2 here >

For our slab models, the oxygen atoms were placed such that a hexagonal ice super cell with full-bilayer termination was formed with dimensions  $2a = 9.046 \text{ \AA}$  and  $c = 7.367 \text{ \AA}$ , where the lattice constants  $a = 4.523 \text{ \AA}$  and  $c = 7.367 \text{ \AA}$  are, from experiment, those of hexagonal ice at 273 K.<sup>58</sup> For models with eight layers and 32 water molecules, the dimensions are  $2a = 9.046 \text{ \AA}$  and  $2c = 14.734 \text{ \AA}$ . A total number of (bare oxygen) adsorption sites of three, two, or one are available for models with one, two, or three dangling OH groups, respectively, giving a

maximum possible surface coverage of  $4.2 \times 10^{14}$  molecule/cm<sup>2</sup> equal to three divided by the rhombus area.

To create a slab model with a specified number of dangling OH groups, all possible arrangements of the hydrogen atoms that satisfied the Bernal-Fowler ice rules were generated systematically with a computer program written in our laboratory (see Supporting Information), and from all of these allowed models, the model with the smallest net dipole moment was selected. Other methods<sup>59,60</sup> have been developed to create models of bulk ice with a zero net dipole moment; our method, however, is readily applied to slab models because it takes into account a (surface) termination of the hydrogen-bond network. The net dipole moment of each slab model was calculated using two methods. First, we assumed that each water molecule had a dipole moment of 3.09 D,<sup>61,62</sup> and that the dipole vector went from the oxygen atom through the molecule's center-of-mass, which gave the same results as the center-of-charge assuming  $+d$  on each hydrogen atom and  $-2d$  on each oxygen atom. In addition, each HCl molecule was given a dipole moment of 1.11 D.<sup>39</sup> For the second method, Berry-phase calculations were performed,<sup>63</sup> with corrections according to King-Smith and Vanderbilt.<sup>64</sup> These first-principles calculations were performed with a plane-wave basis set and periodic boundary conditions applied as described in Sec. 3.3.

The net dipole moment for the optimized ice slabs 16W2Hf and 32W2H, each with two dangling OH groups, is between 0.01-0.1 D assuming fixed dipole values and is only slightly larger, 0.2 and 1.6 D, respectively, when calculated from first principles. The net dipole moment for the optimized ice slab 16W1Hf is 13.1 D assuming fixed values and 8.1 D from first principles, while that for 16W3Hf is 12.2 D and 7.2 D assuming fixed values and from first principles, respectively. The projection of the net dipole moment in the  $x,y$ -plane is less than 1 D for these models. The net dipole moments for slab models with HCl adsorbed are given in Sec. 3.4.3. The large net dipole moments of 16W1Hf and 16W3Hf are a consequence of the top (surface) bilayer and (because of the ice rules) each underlying bilayer having an unequal number of dangling OH groups pointing “up” versus “down” into the bulk. In Sec. 3.5, we discuss the consequences of the large net dipole moments and show that they do not lead to a large variation in the binding energy of HCl.

A three-dimensional perspective of one slab model interacting with two HCl molecules is shown in Figure 3.3. The  $c$ -dimension of the simulation cell is  $8 \text{ \AA} + c = 15.367 \text{ \AA}$  (or  $8 \text{ \AA} + 2c$

= 22.734 Å for slabs with 32 water molecules), where a consistent-sized surface vacuum region of 8 Å was added in order to mimic an isolated slab. To select an appropriate-sized vacuum region, the vacuum region of the model with the largest dipole moment (16W2A1Hf) was systematically increased and the model re-optimized until the change in atomic positions was negligible, of the order of a few thousandths of one angstrom (for atoms involved in binding, and less for other atoms), as was the change in binding energy of molecular HCl, less than 1 kJ/mol.

<Figure 3.3 here>

In Sec. 3.4.3 we present results that show that four layers, with the bottom two fixed, are adequate for modeling adsorption. For a model with four layers, the lateral cell dimensions are as large as computationally practical.

### 3.3. METHODOLOGY

Density-functional theory<sup>65,66</sup> using a plane-wave basis set<sup>67-69</sup> was used to describe the electronic state of our system. The BLYP functional<sup>70,71</sup> was used for the exchange and correlation energies of the system, and Troullier-Martins pseudopotentials<sup>72,73</sup> were used to describe the core and valence atomic regions. This functional and pseudopotentials were found previously to describe both liquid water<sup>54</sup> and hexagonal ice<sup>13</sup> accurately. CPMD version 3.0f was used for all geometry optimizations except for those with constrained dihedral angles, for which CPMD version 3.3f was used.<sup>74</sup> Periodic boundary conditions were used in all directions. In order to facilitate convergence, initial geometries similar to previously published structures were used for HCl·H<sub>2</sub>O, 4W, and 4W1A.<sup>39,41</sup> Optimized bulk ice<sup>13</sup> was the starting point for the slabs. Other studies<sup>44,52</sup> have shown that HCl binds preferentially with its hydrogen to a surface water oxygen atom. The geometry reported for 4W1A at the MP2 level of theory with a 6-311++G(d,p) basis set was used for initial placement of the HCl adsorbate(s).<sup>39</sup> The bottom bilayer of our slab models was held fixed in order to mimic an infinite bulk, and in Sec. 3.4.3, it is shown that the interaction of HCl is not affected.

Two different methods were used to optimize the geometry. The first method, DIIS with three vectors combined with a quasi-Newton method (using BFGS) for optimization of the ionic

positions,<sup>75,76</sup> was used to optimize HCl, H<sub>2</sub>O, HCl·H<sub>2</sub>O, and the test molecules Cl<sub>2</sub>, ClO, HOCl, and ClONO<sub>2</sub>. The second method, based on simulated annealing,<sup>77</sup> was used to optimize 4W and 4W1A with constrained dihedral angles, as well as the slab models. For both methods, a basis-set cutoff of 70.0 Rydbergs was used; for the second method, a scaling factor of 0.9 for the velocities was used in addition to a fictitious mass of 1100.0 a.u. for the electrons and a time step of 7.0 a.u. (0.17 fs) for the integrator. For the slab models, convergence was slow due to a shallow potential surface and a large number of hydrogen-bonding interactions. Optimizations performed with either method are labeled “BLYP/plane waves” in subsequent tables.

Before performing any geometry optimizations with HCl, an important first step was the development of a pseudopotential for chlorine. In order to test our method with different chlorine pseudopotentials, geometries for HCl and other small, stratospherically relevant molecules containing chlorine atoms were optimized, including Cl<sub>2</sub>, ClO, HOCl, and ClONO<sub>2</sub>. Our choice of pseudopotential and functional overestimates slightly most bond lengths, and Cl-O and Cl-Cl bonds by less than 0.1 Å. In Table 3.1, results for HCl are summarized, along with previously published theoretical results<sup>40,41</sup> and the experimental bond length.<sup>78</sup> The density-functional methods seem to overestimate the HCl bond length by a few hundredths of one Ångstrom. Our equilibrium dissociation energy  $D_e$  of 421 kJ/mol for HCl underestimates the experimental value of 445.5 kJ/mol calculated from the spectroscopic dissociation energy  $D_o$  and anharmonicity constants  $w_e$  and  $w_e c_e$  using  $D_e \sim D_o + \frac{1}{2} w_e - \frac{1}{4} w_e c_e$ .<sup>78</sup> In this study, because elongation of HCl is not substantial and dissociation does not occur, it is reasonable to assume that our systematic underestimation of the HCl bond energy of 25 kJ/mol will not significantly affect binding energy calculations. Our results and those of Packer and Clary for H<sub>2</sub>O are also given in Table 3.1. Our results using plane waves are identical to those previously obtained.<sup>54</sup> The results for H<sub>2</sub>O are accurate to within 0.01-0.02 Å and 1-2°.<sup>79</sup>

Use of the BLYP functional and pseudopotentials in a plane-wave calculation is known to underestimate the hydrogen-bond energy for the water dimer by 4 kJ/mol (18 %), the smallest error of the variety of functionals used.<sup>54</sup> In order to estimate the error for the various hydrogen bonds in our study, HCl·H<sub>2</sub>O and its constituent molecules were optimized using Gaussian 94,<sup>80</sup> fixing symmetries and the hydrogen-bond angle to  $\angle\text{HOCl} = 180^\circ$  for HCl·H<sub>2</sub>O. Optimizations were performed at the MP2 level of theory<sup>81,82</sup> with the 6-311++G(d,p) basis set,<sup>83-88</sup> at the MP2 and BLYP levels of theory with larger basis sets, cc-pVTZ and cc-pVQZ,<sup>89-91</sup> and at a higher

level of theory, QCISD(T),<sup>92</sup> with the 6-311++G(d,p) basis set; these method/basis-set combinations are labeled in Table 3.1 as MP2/6-311++G(d,p), BLYP/cc-pVTZ, and so on.

For comparison to results obtained experimentally on bulk ice, optimizations of HCl, 4W, and 4W1A were performed in Gaussian 94 using density-functional theory with a BLYP functional and a 6-311++G(d,p) basis set. Zero-point energies were calculated as well as thermal corrections from harmonic frequencies generated using a frequency scaling factor<sup>93,94</sup> of 0.9940 in order to obtain energies and enthalpies at 165, 185, and 200 K, where 165 and 200 K were chosen to compare with experiment.

### 3.4. OPTIMIZED GEOMETRIES AND BINDING ENERGIES

#### 3.4.1. HCl·H<sub>2</sub>O

The calculated geometry and binding energy of HCl·H<sub>2</sub>O is given in Table 3.1 using different methods and basis sets, and these results are compared with previously published theoretical<sup>40,41</sup> and experimental<sup>95</sup> data. The different theoretical approaches are in reasonable agreement: Upon forming the complex, HCl elongates slightly, while the geometry of H<sub>2</sub>O in the complex is not significantly different from that of the isolated molecule. Ideally, we would like to be able to compare the binding energies in Table 3.1 to an experimental value. An alternative is comparison with a high-level theoretical result, which is estimated below and presented in Table 3.1 as “basis set, correlation corrected.”

< Table 3.1 here >

We first make an estimate of the binding energy in the infinite basis set limit at the MP2 level of theory. From Table 3.1, the uncorrected binding energies at the MP2 level of theory with a cc-pVTZ and a cc-pVQZ basis set are 29 and 26 kJ/mol, respectively, while the binding energies corrected for basis set superposition error using the function counterpoise method<sup>41,96,97</sup> are 22 and 23 kJ/mol, respectively. The function counterpoise method only provides an upper limit to the true basis set superposition error. Accordingly, binding energies corrected for the *actual* basis set superposition error lie between 22-29 kJ/mol and 23-26 kJ/mol at the MP2 level

of theory with cc-pVTZ and cc-pVQZ basis sets, respectively. (The range 23-26 kJ/mol is smaller because of the greater number of atomic basis functions in the cc-pVQZ basis set to describe the valence electrons participating in binding). We make the assumption that the midpoint of each range gives the best estimate of the binding energy. Therefore, 25.5 and 24.5 kJ/mol are our best estimates corrected for the *actual* basis set superposition error at the MP2 level of theory with a cc-pVTZ and a cc-pVQZ basis set, respectively. Extrapolating these results, a reasonable estimate of the MP2 binding energy in the infinite basis set limit is 24 kJ/mol.

Next, we provide an estimate of correlation effects not included in the MP2 method. Referring to Table 3.1, we estimate binding energies corrected for the *actual* basis set superposition error at the MP2 and QCISD(T) levels of theory with a 6-311++G(d,p) basis set to be 23.5 and 22 kJ/mol, respectively. This suggests a correction to the MP2 method for higher-order correlation effects of  $22 - 23.5 = -1.5$  kJ/mol.

Adding our correction for higher-order correlation effects to our estimate of the MP2 binding energy in the infinite basis set limit, we obtain  $24 - 1.5 = 22.5 = 23$  kJ/mol. This “basis set, correlation-corrected” binding energy is identical to the binding energy obtained for HCl·H<sub>2</sub>O in the plane-wave calculation. We conclude that for the plane-wave method, the error resulting from the approximate form of the BLYP functional, the use of pseudopotentials, and a finite basis set all cancel each other. We can estimate the magnitude of the canceling errors: The binding energy corrected for the *actual* basis set superposition error using the BLYP functional with a (relatively large) cc-pVQZ basis set (and no pseudopotentials) is 23 kJ/mol, identical to the “basis set, correlation-corrected” result. We conclude that both the error associated with the use of the BLYP functional and with pseudopotentials/plane waves is zero for HCl·H<sub>2</sub>O.

### 3.4.2. Cluster model (4W1A)

The geometry of HCl interacting with a water cluster representative of an adsorption site on the (0001) ice surface was determined and is reported in Table 3.2 and compared to results from Geiger *et al.*<sup>39</sup> and to other studies that used different cluster models.<sup>41-43</sup> Comparing our geometry for 4W1A to that for HCl·H<sub>2</sub>O (Table 3.1), the HCl bond is slightly longer, while the

hydrogen bond is 0.081 Å shorter and  $\langle\text{OHCl}\rangle$  is 15.4° smaller, consistent with results by Packer and Clary.<sup>41</sup> Distortion of both HCl and the water cluster in the complex is relatively minor, in agreement with Geiger *et al.*<sup>39</sup>

<Table 3.2 here>

Examining the binding energies in Table 3.2,<sup>98</sup> our binding energy of 27 kJ/mol using plane waves and not corrected for zero-point energies is larger than that for HCl·H<sub>2</sub>O, 23 kJ/mol (Table 3.1), which is consistent with the findings of Packer and Clary.<sup>41</sup> Their results of 32 and 30 kJ/mol for HCl·(H<sub>2</sub>O)<sub>2</sub> and HCl·(H<sub>2</sub>O)<sub>3</sub>, respectively, are larger than their result for HCl·H<sub>2</sub>O, 22 kJ/mol. Our binding energy of 27 kJ/mol is in excellent agreement with Geiger *et al.*, 26 kJ/mol.<sup>39</sup> The values reported by Allouche *et al.*<sup>42</sup> and Bussolin *et al.*<sup>43</sup> for HCl adsorbed on a (H<sub>2</sub>O)<sub>6</sub> cluster with a frozen, chair-shaped geometry are 11-13 kJ/mol larger, likely due to the formation of two weak hydrogen bonds between nearby dangling OH groups and chlorine in their model. The lengths of these hydrogen bonds are indicated in Table 3.2.

Making an argument similar to that in Sec. 3.4.1 and referring to results in Table 3.2 obtained by Geiger *et al.*,<sup>39</sup> we estimate that the HCl binding energy for 4W1A corrected for the *actual* basis set superposition error at the MP2 level of theory with a 6-311++G(d,p) basis set is 30 kJ/mol. Interestingly, if we apply our correction for higher-order correlation effects obtained for HCl·H<sub>2</sub>O of -1.5 kJ/mol, a binding energy only 1.5 kJ/mol larger than the plane-wave result is obtained.

According to our results in Table 3.2 using the BLYP functional with a 6-311++G(d,p) basis set, the zero-point correction is -9 kJ/mol. Our correction is close to -8 kJ/mol that was determined by Bussolin *et al.*<sup>43</sup> and to -11 and -12 kJ/mol that were determined by Packer and Clary<sup>41</sup> for HCl·(H<sub>2</sub>O)<sub>2</sub> and HCl·(H<sub>2</sub>O)<sub>3</sub>, respectively. Although not shown in Table 3.2, binding energies  $-\Delta U_T^B$  and enthalpies  $-\Delta H_T^B$  at various temperatures  $T$  were also calculated. This was done using a thermal correction to the energy,  $-\Delta U_{trans}(T) - \Delta U_{rot}(T) - \Delta U_{vib}(T)$ , and an additional  $RT$  to obtain the enthalpy.<sup>99,100</sup> Results for 4W1A using the BLYP functional with a 6-311++G(d,p) basis set, which to within 1 kJ/mol are temperature independent from 165-200 K, are  $-\Delta U_{200}^B = 24$  kJ/mol, and  $-\Delta H_{200}^B = 26$  kJ/mol.



### 3.4.3. Infinite surface models

Following optimization of the ice slab models without HCl adsorbates, the geometry of the surface bilayer was found to be similar to that of optimized bulk ice *Ih* described in an earlier paper.<sup>13</sup> This indicates that, at least at 0 K, surface reconstruction is minor. The change in distance between neighboring oxygen atoms was typically at most several hundredths of one Ångstrom. In all cases, the symmetric, hexagonal arrangement of molecules was preserved in the first (surface) bilayer.

Following optimization with HCl adsorbates using plane waves, a change of the Mulliken population<sup>82,101-103</sup> from  $-0.50$  to  $-0.43$  on the binding oxygen atom was typically observed, as was a change from  $0.23$  to  $0.18$  on the hydrogen atom and  $-0.08$  to  $-0.19$  on the chlorine atom of HCl. In terms of a Lewis-base argument, the oxygen atom of water partially donates a lone pair of electrons to HCl to form a hydrogen bond, and chlorine subsequently withdraws electrons from hydrogen. The changes for our slab models were similar to those for 4W1A,  $-0.50$  to  $-0.45$ ,  $0.23$  to  $0.18$ , and  $-0.08$  to  $-0.17$ , respectively. The charges on other atoms were essentially unchanged, consistent with a study of aqueous HCl dissociation to form a contact ion pair, the respective changes in that study being  $-0.975$  to  $-0.593$ ,  $0.298$  to  $0.327$ , and  $-0.417$  to  $-0.846$ .<sup>104</sup>

Calculated geometries for HCl interacting with five different slab models are shown in Table 3.3.<sup>105</sup> In our slab models, a single HCl molecule is almost always held more tightly than in 4W1A: The HCl bond is longer, the hydrogen bond lengths are typically shorter, and the  $\langle\text{OHCl}\rangle$  angles are greater. This trend is also observed in the study of Bussolin *et al.*<sup>43</sup> Also, the first bilayer of the slab is distorted upon adsorption; a change of  $\pm 0.1$  Å between the adsorption site and adjacent oxygen atoms was typical.

<Table 3.3 here>

Results for the binding energy of HCl are also given in Table 3.3.<sup>106</sup> Our  $-\Delta E_e^B$  result for 16W1A2Hf agrees to within 3 kJ/mol with that of Bussolin *et al.* using a nearly identical slab model but a different method,<sup>43</sup> despite the fact their hydrogen bond is substantially longer by 0.30 Å and that the distance between chlorine and the dangling OH groups is greater in their model, 3.63 and 4.05 Å versus 2.967 and 3.358 Å calculated here. However, HCl is less

perturbed in their study, with only a 0.01 Å difference between the HCl bond length in the slab and the cluster versus 0.036 Å in this study. We also compare our  $-\Delta U_T^B$  result of 30 kJ/mol for 16W1A2Hf with those obtained by Clary and Wang.<sup>46</sup> In their quantum-classical molecular dynamics study at 190 K of HCl interacting with a slab model consisting of 12 layers and 30 molecules per layer, the HCl bond length and distance of the center-of-mass from the surface were treated quantum mechanically but all other degrees of freedom were treated classically. Their  $-\Delta U_T^B$  result for HCl interacting with a defect-free (0001) surface is 25 kJ/mol, larger than their purely classical result<sup>45</sup> of 19 kJ/mol and smaller than our  $-\Delta U_T^B$  result of 30 kJ/mol. Their results for two slabs with defects are 32 and 33 kJ/mol, respectively.

An important conclusion from Table 3.3 is that our results for a slab with 32 water molecules are essentially identical to those for the slab with 16 water molecules with two dangling OH groups. This demonstrates that underlying layers do not affect surface adsorption for either one-molecule coverage, which is consistent with the results of others,<sup>43</sup> or for two-molecule coverage. This also demonstrates that the binding of HCl is unaffected by fixing the second bilayer. We believe these conclusions apply to slab models with one and three dangling OH groups as well, because the geometry changes for *all* models take place almost entirely at the adsorption site.

Our results in Table 3.3 also show that the average binding energy per site decreases by 5 kJ/mol, given a constant number of dangling OH groups, as coverage increases from one to two HCl molecules. This is likely due to the greater distortion of the first bilayer as well as the weak (few kJ/mol) dipolar repulsion between HCl adsorbates separated by 4-5 Å.

### 3.5. FURTHER DISCUSSION OF INFINITE-SURFACE-MODEL RESULTS

To address the potential problem of overbinding of HCl, a dipolar molecule, on slab models with a large net dipole moment, and furthermore to understand better the mechanism of binding, the dipole-dipole interaction energy of HCl interacting with each water molecule in the slab was calculated directly.<sup>107</sup> As in Sec. 3.2, a dipole moment of 3.09 D for each water molecule and 1.11 D for HCl was assumed. The interaction of HCl with the periodic images of the water molecules was included. Our results are shown in Table 3.4. We conclude that despite the varying net dipole moments in the individual slabs, the HCl binding energy varies by only 5

kJ/mol and independently of net dipole moment. The lack of dependence is due to the inverse cubic dependence of interaction energy with increasing separation of the center-of-charges.<sup>107</sup> The water molecule interacting directly with HCl contributes by far the most to binding (60-90 %). The dipolar interaction of HCl with the entire slab is always given to within 15 % (and usually to within a few percent) by the interaction of HCl with the water molecule directly involved in binding and the three neighboring water molecules in the second layer to which that water molecule is hydrogen bonded.

<Table 3.4 here>

A  $l^3$  dependence of binding energy on hydrogen bond length  $l$  for three molecules with gas-phase dipole moments of 1.3 D (HOCl), 1.08 D (HCl), and 0 D ( $\text{Cl}_2$ ) adsorbed on 4W was recently reported, and it was concluded dipolar coupling was largely responsible for binding.<sup>39</sup> For our slab models, comparing the binding energies in Tables 3.3 and 3.4 indicates that dipolar coupling is largely, though not entirely, responsible for binding. This conclusion is supported by plotting binding energy per site versus  $l$  using the plane-wave results from Tables 3.1 – 3.3, and noting that the best fit of the form  $cl^d$ , where  $c$  and  $d$  are variables, is proportional to  $l^{3.11 \pm 0.91}$  ( $R^2 = 0.49$ ). It is worth mentioning that hydrogen bonding (of hydrogen in HCl to oxygen in the water molecule) also contributes significantly to the binding energy. The contribution from layers three and four in Table 3.4 implies the contribution from hypothetical layers five and six would be small, further evidence that four layers are sufficient for modeling the interaction.

The effect of varying OH groups on binding is also significant. The binding energy of HCl at O1 versus O2 in our model with two dangling OH groups (16W1A2Hf versus 16W1A<sup>O2</sup>2Hf) is larger by 7 kJ/mol. This difference is due to the fact that HCl at O1 is in close proximity to two dangling OH groups (Figure 3.2), which interact favorably with chlorine. As indicated in Table 3.3, the nearest OH groups are 3.522 and 4.403 Å from chlorine versus 2.967 and 3.358 Å when HCl is adsorbed at O1. Not surprisingly, because of these interactions, HCl is stretched to a greater extent, and the surface is more distorted as neighboring water molecules rearrange to bind with the chlorine atom.

Although HCl binding at sites in close proximity to dangling OH groups is energetically more favorable, binding at sites where there are few or no OH groups to interact appreciably

with HCl is quite possibly *more* representative of adsorption on Type II PSC particles. Crystalline ice is conjectured not to have a high surface density of dangling OH groups based on a comparison of the vibrational spectrum and surface properties of crystalline and amorphous ice.<sup>108</sup> The actual surface density of dangling OH groups on crystalline ice is, however, not known definitively. On liquid water, it is estimated using infrared-visible sum-frequency generation to be more than 20 %.<sup>109</sup>

Assuming a molecular HCl surface coverage corresponding to one molecule per simulation cell ( $1.4 \times 10^{14}$  molecule/cm<sup>2</sup>), from Table 3.3 we estimate a range of binding energies of 23-30 kJ/mol and binding enthalpies of 25-32 kJ/mol at 185 K. However, the lower end of the range may be more likely and adsorption may best be modeled on 16W1Hf or at O2 in 16W2Hf due to the conjectured low surface density of dangling OH groups on crystalline ice. For a surface coverage corresponding to  $2.8 \times 10^{14}$  molecule/cm<sup>2</sup>, the binding energy and enthalpy per site are 14-30 and 16-32 kJ/mol, respectively. The average binding energy and enthalpy per site are 20-22 and 22-24 kJ/mol, respectively, where again the lower end of the range may be more likely.

For a low (sub-monolayer) coverage corresponding to one molecule per simulation cell ( $1.4 \times 10^{14}$  molecule/cm<sup>2</sup>), from the preceding discussion we conclude reasonable, accurate values for the binding energy and enthalpy of HCl on Type II PSCs are 23 and 25 kJ/mol, respectively. For a higher (monolayer) coverage corresponding to two molecules per simulation cell ( $2.8 \times 10^{14}$  molecule/cm<sup>2</sup>), reasonable values for the average binding energy and enthalpy are 20 and 22 kJ/mol, respectively. These estimates, independent of temperature between 165-200 K (and only slightly less at lower temperatures), agree with some of the experimental data, which exhibits a wide range, given in Table 3.3. Andersson *et al.* also report a decrease, albeit larger, of binding energy with increasing HCl coverage in their molecular beam study.<sup>31</sup> Their absolute binding energies may be larger than ours due to the high temperature of the measurements, which may mean processes more complicated than simple adsorption are occurring at the ice surface. Agreeing well with our estimated binding energy of 23 kJ/mol, Isakson and Sitz estimate the activation energy of desorption to be 26 kJ/mol for low HCl coverage.<sup>32</sup> Their result was obtained on crystalline ice (at least) several thousand Ångstroms thick. Our slab models, with the bottom bilayer fixed, may *more* accurately depict this type of surface rather than the ultrathin (5-20 monolayers thick) ice films studied by Graham and

Roberts.<sup>33</sup> According to these authors, their films are likely rich in defects, and thus may have a higher density of dangling OH groups, which would explain why their activation energy of desorption of 33 kJ/mol is larger. Preliminary experimental results from our group indicate a binding enthalpy of 25-30 kJ/mol for low HCl coverage, 16-21 kJ/mol smaller than Elliott *et al.*<sup>34</sup> but which agrees well with our estimate given above of 25 kJ/mol.

Besides the fact the surface density of dangling OH groups and the surface coverage of HCl on Type II PSCs are unknown, there may be other sources of error. Although our binding energy for HCl·H<sub>2</sub>O agrees to within 1 kJ/mol with a high-level theoretical estimate, implying cancellation of errors associated with use of the BLYP functional and pseudopotentials/plane waves, there is no guarantee the same is true for our slab models. Also, our zero-point and thermal corrections are harmonic approximations.

### 3.6. ATMOSPHERIC RELEVANCE AND FUTURE WORK

Correlated with adsorption, a slight elongation of HCl (by up to 0.086 Å, 7 %) occurs at all sites, but dissociation is not observed, even though our homolytic dissociation energy for HCl is underestimated by 25 kJ/mol (6 %). This indicates that there is a barrier to dissociation of HCl of unknown magnitude but does not indicate whether molecular or ionized HCl is more stable at 185 K. This barrier may be as large as 33.9 – 6.3 = 28 kJ/mol based on a rough estimate for HCl atop an ice surface (versus 0.4 kJ/mol for HCl incorporated into the first bilayer of the ice lattice).<sup>110</sup> Preliminary theoretical results from our group indicate that under certain circumstances it may be significantly less. With a better understanding of the processes that HCl undergoes initially during adsorption, we are interested in elucidating the subsequent fate of HCl at the ice surface to understand better chlorine activation, *i.e.*, Rx. (3.1). We are investigating the possibility of ionization of HCl following adsorption using *ab initio* molecular dynamics<sup>13</sup> in conjunction with experiments under typical polar stratospheric conditions.

### 3.7. CONCLUSIONS

In this work, both cluster and extended surface models of the hexagonal ice basal (0001) face for modeling the interaction of HCl on Type II PSC particles were described, and results for

the molecular adsorption of HCl on each were compared in Sec. 3.4. Our molecular HCl binding energy at 0 K corrected for zero-point error is 27 kJ/mol for HCl adsorbed in close proximity to two dangling OH groups on a periodic slab model. This value is very similar to 25 kJ/mol from Bussolin *et al.* using a different method.<sup>43</sup>

As discussed in Sec. 3.5, our best estimate of the binding energy and enthalpy of molecular HCl on hexagonal ice *Ih* crystals at 165-200 K (assuming molecular HCl does in fact exist) are 23 and 25 kJ/mol, respectively, for low (single-molecule) HCl coverage, decreasing to 20 and 22 kJ/mol, respectively, as the coverage of HCl increases. Our estimates would be a few kJ/mol smaller at lower temperatures, decreasing to 20 kJ/mol (low coverage) and 17 kJ/mol (high coverage) at 0 K. These estimates are based on a low surface density of dangling (non-hydrogen-bonding) OH groups.

Our results also indicate that there is a barrier of unknown magnitude to the ionization of HCl upon adsorption. We are investigating the possible ionization of HCl following adsorption, a question of great atmospheric importance, at stratospherically relevant temperatures using the results of this work.

*Supporting Information Available:* Our optimized structures in Tables 3.1, 3.2, and 3.3; a computer program to find ice slab models with a net dipole moment as small as possible; and a program to calculate the net dipole moment with and without HCl adsorbates. This information is available free of charge via the Internet at <http://pubs.acs.org>.

### 3.8. ACKNOWLEDGEMENTS

This work was partially supported by the NASA Upper Atmospheric Research Program under Grant No. NAG5-8887. Y.A.M. acknowledges partial support from the MIT Center for Global Change Sciences. F.M.G. acknowledges support from the NOAA Postdoctoral Program in Climate and Global Change, administered by the University Corporation for Atmospheric Research. This work was also partially supported by the National Computational Science Alliance under a Boston University MARINER/Alliance startup allocation (Project No. 60390) and under Proposal No. CTS990016N and utilized the Boston University SGI/CRAY Origin2000 and the NCSA SGI/CRAY Origin2000, respectively.

### REFERENCES AND NOTES FOR CHAPTER 3

- (1) Molina, M. J. *Angew. Chem. Int. Edit. Engl.* 1996, 35, 1778.
- (2) Chang, H.-Y. A.; Koop, T.; Molina, L. T.; Molina, M. J. *J. Phys. Chem. A* 1999, 103, 2673.
- (3) Tabazadeh, A.; Toon, O. B.; Jensen, E. J. *Geophys. Res. Lett.* 1997, 24, 2007.
- (4) Turco, R. P.; Toon, O. B.; Hamill, P. J. *Geophys. Res.* 1989, 94D, 16493.
- (5) List, R. J. *Smithsonian Meteorological Tables*, 6th revised ed.; Smithsonian Institution: Washington, D.C., 1951.
- (6) Seinfeld, J. H.; Pandis, S. N. *Atmospheric Chemistry and Physics: From Air Pollution to Climate Change*; Wiley: New York, 1998.
- (7) Lee, S.-H.; Leard, D. C.; Zhang, R.; Molina, L. T.; Molina, M. J. *Chem. Phys. Lett.* 1999, 315, 7.
- (8) Horn, A. B.; Sodeau, J. R.; Roddis, T. B.; Williams, N. A. *J. Phys. Chem. A* 1998, 102, 6107.
- (9) Oppliger, R.; Allanic, A.; Rossi, M. J. *J. Phys. Chem. A* 1997, 101, 1903.
- (10) Sander, S. P.; Friedl, R. R.; DeMore, W. B.; Golden, D. M.; Kurylo, M. J.; Hampson, R. F.; Huie, R. E.; Moortgat, G. K.; Ravishankara, A. R.; Kolb, C. E.; Molina, M. J. *Chemical Kinetics and Photochemical Data for Use in Stratospheric Modeling, Supplement to Evaluation 12: Update of Key Reactions*; Jet Propulsion Laboratory: Pasadena, CA, 2000.
- (11) Molina, L. T.; Molina, M. J.; Stachnik, R. A.; Tom, R. D. *J. Phys. Chem.* 1985, 89, 3779.
- (12) Petrenko, V. F.; Whitworth, R. W. *Physics of Ice*; Oxford University Press: New York, 1999.
- (13) Mantz, Y. A.; Geiger, F. M.; Molina, L. T.; Molina, M. J.; Trout, B. L. *J. Chem. Phys.* 2000, 113, 10733.
- (14) Molina, M. J. The probable role of stratospheric 'ice' clouds: Heterogeneous chemistry of the 'ozone hole'. In *The Chemistry of the Atmosphere: Its Impact on Global Change*; Calvert, J. G., Ed.; Blackwell Scientific Publications: Oxford, 1994; p. 27.
- (15) Gertner, B. J.; Hynes, J. T. *Science* 1996, 271, 1563.
- (16) Gertner, B. J.; Hynes, J. T. *Faraday Discuss.* 1998, 110, 301.
- (17) George, S. M.; Livingston, F. E. *Surf. Rev. Lett.* 1997, 4, 771.
- (18) Bianco, R.; Hynes, J. T. *J. Phys. Chem. A* 1999, 103, 3797.
- (19) McNamara, J. P.; Tresadern, G.; Hillier, I. H. *J. Phys. Chem. A* 2000, 104, 4030.
- (20) Mebel, A. M.; Morokuma, K. *J. Phys. Chem.* 1996, 100, 2985.
- (21) Kroes, G.-J. *Comments At. Mol. Phys.* 1999, 34, 259.
- (22) Leu, M.-T.; Keyser, L. F.; Timonen, R. S. *J. Phys. Chem. B* 1997, 101, 6259.
- (23) Foster, K. L.; Tolbert, M. A.; George, S. M. *J. Phys. Chem. A* 1997, 101, 4979.
- (24) Pursell, C. J.; Zaidi, M.; Thompson, A.; Fraser-Gaston, C.; Vela, E. *J. Phys. Chem. A* 2000, 104, 552.
- (25) Delzeit, L.; Powell, K.; Uras, N.; Devlin, J. P. *J. Phys. Chem. B* 1997, 101, 2327.
- (26) Banham, S. F.; Sodeau, J. R.; Horn, A. B.; McCoustra, M. R. S.; Chesters, M. A. *J. Vac. Sci. Technol. A* 1996, 14, 1620.
- (27) Donsig, H. A.; Vickerman, J. C. *J. Chem. Soc., Faraday Trans.* 1997, 93, 2755.

- (28) Abbatt, J. P. D.; Beyer, K. D.; Fucaloro, A. F.; McMahon, J. R.; Wooldridge, P. J.; Zhang, R.; Molina, M. J. *J. Geophys. Res.* 1992, *97D*, 15819.
- (29) Hanson, D. R.; Mauersberger, K. *J. Phys. Chem.* 1990, *94*, 4700.
- (30) Sadtchenko, V.; Giese, C. F.; Gentry, W. R. *J. Phys. Chem. B* 2000, *104*, 9421.
- (31) Andersson, P. U.; Någård, M. B.; Pettersson, J. B. C. *J. Phys. Chem. B* 2000, *104*, 1596.
- (32) Isakson, M. J.; Sitz, G. O. *J. Phys. Chem. A* 1999, *103*, 2044.
- (33) Graham, J. D.; Roberts, J. T. *J. Phys. Chem.* 1994, *98*, 5974.
- (34) Elliott, S.; Turco, R. P.; Toon, O. B.; Hamill, P. *J. Atmos. Chem.* 1991, *13*, 211.
- (35) Uras, N.; Rahman, M.; Devlin, J. P. *J. Phys. Chem. B* 1998, *102*, 9375.
- (36) Atkins, P. W. *Physical Chemistry*, 5th ed.; W. H. Freeman & Co.: New York, 1994.
- (37) Rossini, F. D. *J. Res. N.B.S.* 1932, *9*, 679.
- (38) Bacelo, D. E.; Binning, R. C., Jr.; Ishikawa, Y. *J. Phys. Chem. A* 1999, *103*, 4631.
- (39) Geiger, F. M.; Hicks, J. M.; de Dios, A. C. *J. Phys. Chem. A* 1998, *102*, 1514.
- (40) Re, S.; Osamura, Y.; Suzuki, Y.; Schaefer, H. F., III. *J. Chem. Phys.* 1998, *109*, 973.
- (41) Packer, M. J.; Clary, D. C. *J. Phys. Chem.* 1995, *99*, 14323.
- (42) Allouche, A.; Couturier-Tamburelli, I.; Chiavassa, T. *J. Phys. Chem. B* 2000, *104*, 1497.
- (43) Bussolin, G.; Casassa, S.; Pisani, C.; Ugliengo, P. *J. Chem. Phys.* 1998, *108*, 9516.
- (44) Kroes, G.-J.; Clary, D. C. *J. Phys. Chem.* 1992, *96*, 7079.
- (45) Kroes, G.-J.; Clary, D. C. *Geophys. Res. Lett.* 1992, *19*, 1355.
- (46) Clary, D. C.; Wang, L. *J. Chem. Soc., Faraday Trans.* 1997, *93*, 2763.
- (47) Jorgensen, W. L.; Chandrasekhar, J.; Madura, J. D.; Impey, R. W.; Klein, M. L. *J. Chem. Phys.* 1983, *79*, 926.
- (48) Estrin, D. A.; Kohanoff, J.; Laria, D. H.; Weht, R. O. *Chem. Phys. Lett.* 1997, *280*, 280.
- (49) Planas, M.; Lee, C.; Novoa, J. J. *J. Phys. Chem.* 1996, *100*, 16495.
- (50) Casassa, S. *Chem. Phys. Lett.* 2000, *321*, 1.
- (51) Robertson, S. H.; Clary, D. C. *Faraday Discuss.* 1995, *100*, 309.
- (52) Svanberg, M.; Pettersson, J. B. C.; Bolton, K. *J. Phys. Chem. A* 2000, *104*, 5787.
- (53) For ice  $I_h$ , there are six symmetry-related planes parallel to the hexagonal axis  $c$  (or  $z$ ) passing through origin  $o$ . These so-called prism faces (and, for consistency, the orthogonal basal faces) are named using Miller-Bravais indices in order not to obscure the symmetry relations: The plane  $(hkil)$  makes axial intercepts in the ratio  $a/h : a/k : a/i : c/l$ , where indices  $h$ ,  $k$ ,  $i$ , and  $l$  refer, respectively, to redundant axes  $ox$ ,  $oy$ , and  $ou$  separated by  $120^\circ$  and  $oz$ . From Megaw (Ref. 58).
- (54) Sprik, M.; Hutter, J.; Parrinello, M. *J. Chem. Phys.* 1996, *105*, 1142.
- (55) Bernal, J. D.; Fowler, R. H. *J. Chem. Phys.* 1933, *1*, 515.
- (56) Materer, N.; Starke, U.; Barbieri, A.; Van Hove, M. A.; Somorjai, G. A.; Kroes, G.-J.; Minot, C. *Surf. Sci.* 1997, *381*, 190.
- (57) Fletcher, N. H. *The Chemical Physics of Ice*; Cambridge University Press: New York, 1970.



- (58) Megaw, H. D. *Crystal Structures*; TechBooks: Fairfax, VA, first published in 1973.
- (59) Hayward, J. A.; Reimers, J. R. *J. Chem. Phys.* 1997, *106*, 1518.
- (60) Rahman, A.; Stillinger, F. H. *J. Chem. Phys.* 1972, *57*, 4009.
- (61) Batista, E. R.; Xantheas, S. S.; Jónsson, H. *J. Chem. Phys.* 1998, *109*, 4546.
- (62) Batista, E. R.; Xantheas, S. S.; Jónsson, H. *J. Chem. Phys.* 1999, *111*, 6011.
- (63) Vanderbilt, D.; King-Smith, R. D. *Phys. Rev. B* 1993, *48*, 4442.
- (64) King-Smith, R. D.; Vanderbilt, D. *Phys. Rev. B* 1993, *47*, 1651.
- (65) Kohn, W. *Rev. Mod. Phys.* 1999, *71*, 1253.
- (66) Parr, R. G.; Yang, W. *Density-Functional Theory of Atoms and Molecules*; Oxford University Press: New York, 1989.
- (67) Parrinello, M. *Solid State Commun.* 1997, *102*, 107.
- (68) Galli, G.; Pasquarello, A. First principles molecular dynamics. In *Computer Simulations in Chemical Physics*; Allen, M. P., Tildesley, D. J., Eds.; Kluwer Academic Publishers: Dordrecht, 1993; Vol. 397; p. 261.
- (69) Payne, M. C.; Teter, M. P.; Allan, D. C.; Arias, T. A.; Joannopoulos, J. D. *Rev. Mod. Phys.* 1992, *64*, 1045.
- (70) Becke, A. D. *Phys. Rev. A* 1988, *38*, 3098.
- (71) Lee, C.; Yang, W.; Parr, R. G. *Phys. Rev. B* 1988, *37*, 785.
- (72) Troullier, N.; Martins, J. L. *Phys. Rev. B* 1991, *43*, 1993.
- (73) Cohen, M. L. *Phys. Today* 1979 (July), *32*, 40.
- (74) Hutter, J.; Alavi, A.; Deutsch, T.; Bernasconi, M.; Goedecker, St.; Marx, D.; Tuckerman, M.; Parrinello, M. *CPMD*; Max-Planck Institut für Festkörperforschung and IBM Zurich Research Laboratory, 1995-99.
- (75) Fischer, T. H.; Almlöf, J. *J. Phys. Chem.* 1992, *96*, 9768.
- (76) Császár, P.; Pulay, P. *J. Mol. Struct.* 1984, *114*, 31.
- (77) Kirkpatrick, S.; Gelatt, C. D., Jr.; Vecchi, M. P. *Science* 1983, *220*, 671.
- (78) Huber, K. P.; Herzberg, G. *Molecular Spectra and Molecular Structure IV. Constants of Diatomic Molecules*; Van Nostrand: New York, 1979.
- (79) Benedict, W. S.; Gailer, N.; Plyler, E. K. *J. Chem. Phys.* 1956, *24*, 1139.
- (80) Frisch, M. J.; Trucks, G. W.; Schlegel, H. B.; Gill, P. M. W.; Johnson, B. G.; Robb, M. A.; Cheeseman, J. R.; Keith, T. A.; Petersson, G. A.; Montgomery, J. A.; Raghavachari, K.; Al-Laham, M. A.; Zakrzewski, V. G.; Ortiz, J. V.; Foresman, J. B.; Cioslowski, J.; Stefanov, B. B.; Nanayakkara, A.; Challacombe, M.; Peng, C. Y.; Ayala, P. Y.; Chen, W.; Wong, M. W.; Andres, J. L.; Replogle, E. S.; Gomperts, R.; Martin, R. L.; Fox, D. J.; Binkley, J. S.; Defrees, D. J.; Baker, J.; Stewart, J. P.; Head-Gordon, M.; Gonzalez, C.; Pople, J. A. *Gaussian 94 (Revision E.3)*; Gaussian, Inc.: Pittsburgh, PA, 1995.
- (81) Møller, C.; Plesset, M. S. *Phys. Rev.* 1934, *46*, 618.
- (82) Szabo, A.; Ostlund, N. S. *Modern Quantum Chemistry: Introduction to Advanced Electronic Structure Theory*, 2nd revised ed.; Dover: New York, 1989.
- (83) For H and O, the 6-311G basis and polarization functions of Krishnan *et al.* (Ref. 84). For Cl, a (12s9p)/[631111,52111] "negative-ion/Cl" basis (Ref. 85) and polarization functions of Francl *et al.* (Ref. 86). Diffuse functions from Frisch *et al.* (Ref. 87), who cites Clark *et al.* (Ref. 88).
- (84) Krishnan, R.; Binkley, J. S.; Seeger, R.; Pople, J. A. *J. Chem. Phys.* 1980, *72*, 650.

- (85) McLean, A. D.; Chandler, G. S. *J. Chem. Phys.* 1980, 72, 5639.  
 (86) Francl, M. M.; Pietro, W. J.; Hehre, W. J.; Binkley, J. S.; Gordon, M. S.; DeFrees, D. J.; Pople, J. A. *J. Chem. Phys.* 1982, 77, 3654.  
 (87) Frisch, M. J.; Pople, J. A.; Binkley, J. S. *J. Chem. Phys.* 1984, 80, 3265.  
 (88) Clark, T.; Chandrasekhar, J.; Spitznagel, G. W.; Schleyer, P. v. R. *J. Comput. Chem.* 1983, 4, 294.

(89) Obtained by Gaussian, Inc. from the Extensible Computational Chemistry Environment Basis Set Database, as developed and distributed by the Molecular Science Computing Facility, Environmental and Molecular Sciences Laboratory which is part of the Pacific Northwest Laboratory, P.O. Box 999, Richland, Washington 99352, USA, and funded by the U.S. Department of Energy. The Pacific Northwest Laboratory is a multi-program laboratory operated by Battelle Memorial Institute for the U.S. Department of Energy under contract DE-AC06-76RLO 1830. For primitive exponents (1<sup>st</sup> column) and coefficients (2<sup>nd</sup>-*n*<sup>th</sup> columns), select CODE: SUPERMOLECULE or Dalton at <http://www.emsl.pnl.gov:2080/forms/basisform.html>. Also see Dunning (Ref. 90) and Woon and Dunning (Ref. 91). Contact David Feller or Karen Schuchardt for further information.

- (90) Dunning, T. H., Jr. *J. Chem. Phys.* 1989, 90, 1007.  
 (91) Woon, D. E.; Dunning, T. H., Jr. *J. Chem. Phys.* 1993, 98, 1358.  
 (92) Pople, J. A.; Head-Gordon, M.; Raghavachari, K. *J. Chem. Phys.* 1987, 87, 5968.  
 (93) Wong, M. W. *Chem. Phys. Lett.* 1996, 256, 391.  
 (94) Scott, A. P.; Radom, L. *J. Phys. Chem.* 1996, 100, 16502.  
 (95) Legon, A. C.; Willoughby, L. C. *Chem. Phys. Lett.* 1983, 95, 449.  
 (96) Uncorrected binding energies  $-\Delta E_e^N$  were calculated, as well as  $-\Delta E_e^B$  corrected for basis set superposition error *BSSE* (as indicated by a superscript *B*) but not for zero-point energies (as indicated by a subscript *e*) using  $-\Delta E_e^B = -\Delta E_e^N + BSSE = D_e^{HCl \cdot H_2O} - D_e^{HCl} - D_e^{H_2O} + BSSE$ , where  $D_e = -E_e > 0$ , and  $BSSE = D_e^{HCl--(?_{HCl})} - D_e^{HCl--(?_{HCl} ?_{H_2O})} + D_e^{--H_2O} (?_{H_2O}) - D_e^{--H_2O} (?_{HCl} ?_{H_2O})$ . Here,  $D_e^{HCl--(?_{HCl} ?_{H_2O})}$  is the absolute energy of HCl in the full dimer basis  $?_{HCl} ?_{H_2O}$  and in the cluster geometry,  $D_e^{HCl--(?_{HCl})}$  is the absolute energy of HCl with only its own basis set  $?_{HCl}$  but again at the geometry it has within the cluster, and so on (Ref. 41, 97). For methods using localized basis sets,  $BSSE < 0$ , but  $BSSE = 0$  using a plane-wave (non-localized) basis set, in principle for any value of the basis-set cutoff.

(97) Boys, S. F.; Bernardi, F. *Mol. Phys.* 1970, 19, 553.

(98) In order to calculate  $-\Delta E_e^N$  and  $-\Delta E_e^B$ , the equations given in Ref. 96 were used after replacing H<sub>2</sub>O with the cluster model. In addition,  $-\Delta E_o^B$  corrected for both *BSSE* and for zero-point energies (as indicated by a subscript *o*) were calculated using  $-\Delta E_o^B = -\Delta E_o^N + BSSE = D_o^{4W1A} - D_o^{HCl} - D_o^{4W} + BSSE$ , where  $D_o \sim D_e - \frac{1}{2} w_e$ , and *BSSE* is defined as in Ref. 96.

(99) Binding energy  $-\Delta U_T^B$  at temperature *T* was calculated using  $-\Delta U_T^B = -\Delta E_o^B - DU_{trans}(T) - DU_{rot}(T) - DU_{vib}(T) = -\Delta E_o^B + 5/2 RT - DU_{vib}(T)$ , where in this equation  $-DU_{trans}(T) = U_{trans}^{HCl}(T) + U_{trans}^{4W}(T) - U_{trans}^{4W1A}(T) = 3/2 RT$ ,  $-DU_{rot}(T) = U_{rot}^{HCl}(T) + U_{rot}^{4W}(T) - U_{rot}^{4W1A}(T) = RT$ , and  $-DU_{vib}(T) = U_{vib}^{HCl}(T) + U_{vib}^{4W}(T) - U_{vib}^{4W1A}(T) < 0$ . The binding enthalpy  $-\Delta H_T^B = -\Delta U_T^B + RT$ .

- (100) McQuarrie, D. A. *Statistical Mechanics*; HarperCollins: New York, 1976.
- (101) In order to calculate Mulliken populations (Ref. 102), the wavefunctions calculated using plane waves are first projected onto atomic pseudo-wavefunctions. These are described by a minimal basis of Slater orbitals for the valence electrons, with exponents taken from the Clementi-Raimondi table (Ref. 103).
- (102) Mulliken, R. S. *J. Chem. Phys.* 1955, 23, 1833.
- (103) Clementi, E.; Raimondi, D. L. *J. Chem. Phys.* 1963, 38, 2686.
- (104) Ando, K.; Hynes, J. T. *J. Phys. Chem. B* 1997, 101, 10464.
- (105) Results for a slab with no dangling OH groups (16WyA0Hf, where  $y = 1-4$ ), as well as for a slab with one dangling OH group (16W3A1Hf) that satisfied the ice rules were obtained. However, convergence was very slow, and sometimes HCl was dissociated in the "optimized" geometry. We believe HCl dissociation was a consequence of long-range dipole-dipole coupling between periodic images.
- (106) For our plane-wave results,  $BSSE = 0$ , hence  $-\Delta E_e^B = -\Delta E_e^N$ . Our zero-point correction (-9 kJ/mol) and thermal contributions to the energy (3 kJ/mol) and enthalpy (5 kJ/mol) for 4W1A were used to estimate  $-\Delta E_o^B = -\Delta E_e^B - 9$  kJ/mol,  $-\Delta U_{165}^B = -\Delta E_o^B + 3$  kJ/mol, and  $-\Delta H_{200}^B = -\Delta E_o^B + 5$  kJ/mol for the slab models.
- (107) Maitland, G. C.; Rigby, M.; Smith, E. B.; Wakeham, W. A. *Intermolecular Forces: Their Origin and Determination*; Oxford University Press: New York, 1981.
- (108) Schaff, J. E.; Roberts, J. T. *J. Phys. Chem.* 1994, 98, 6900.
- (109) Du, Q.; Superfine, R.; Freysz, E.; Shen, Y. R. *Phys. Rev. Lett.* 1993, 70, 2313.
- (110) Bianco, R.; Gertner, B. J.; Hynes, J. T. *Ber. Bunsenges. Phys. Chem.* 1998, 102, 518.

**TABLE 3.1. Optimized geometry of H<sub>2</sub>O, HCl, and HCl·H<sub>2</sub>O and binding energy of HCl·H<sub>2</sub>O uncorrected (- ? E<sub>e</sub><sup>N</sup>) and corrected (- ? E<sub>e</sub><sup>B</sup>) for basis set superposition error using the function counterpoise method**

Method/basis set	Isolated molecules			Isolated HCl·H <sub>2</sub> O							
	HCl	H <sub>2</sub> O		HCl	O---H	<OHCl	OCl	OH	<HOH	- ? E <sub>e</sub> <sup>N</sup>	- ? E <sub>e</sub> <sup>B</sup>
	(Å)	OH (Å)	<HOH (degrees)	(Å)	(Å)	(degrees)	(Å)	(Å)	(degrees)	(kJ/mol)	(kJ/mol)
BLYP/plane waves <sup>a</sup>	1.304	0.973	104.4	1.332	1.842	179.5	3.174	0.973	105.2	...	23
B3LYP/D95++(p,d) <sup>b</sup>	1.289	...	...	1.313	1.820	177.6	...	0.968	...	28	19
MP2/6-31G(2dp) <sup>c</sup>	1.271	0.961	104.8	1.287	1.910	...	3.196	0.962	105.2	...	22
MP2/6-311++G(d,p)	1.273	0.960	103.4	1.287	1.902	180	3.189	0.961	104.3	27	20
MP2/cc-pVTZ	1.273	0.959	103.5	1.293	1.849	180	3.141	0.961	104.4	29	22
MP2/cc-pVQZ	1.273	0.958	104.0	1.292	1.852	180	3.145	0.959	104.8	26	23
QCISD(T)/6-311++G(d,p)	1.278	0.960	103.4	1.288	1.935	180	3.223	0.961	104.2	26	18
BLYP/cc-pVTZ	1.293	0.972	103.8	1.322	1.831	180	3.152	0.973	104.7	29	22
BLYP/cc-pVQZ	1.292	0.970	104.2	1.319	1.849	180	3.168	0.972	104.9	25	21
basis set, correlation corrected	...	...	...	...	...	...	...	...	...	...	23
experiment	1.27455 <sup>d</sup>	0.9572 <sup>e</sup>	104.52 <sup>e</sup>	...	...	180.0 <sup>f</sup>	3.2151 <sup>f</sup>	...	...	...	...

<sup>a</sup> For methods using (non-local) plane waves, basis set superposition error is zero. <sup>b</sup> ref. 40 <sup>c</sup> ref. 41 <sup>d</sup> ref. 78 <sup>e</sup> ref. 79 <sup>f</sup> ref. 95. Structure of <sup>35</sup>ClH--OH<sub>2</sub> was obtained from analysis of microwave data.

**TABLE 3.2. Interaction of HCl with isolated cluster model 4W<sup>a</sup>**

Method/basis set	HCl (Å)	O---H (Å)	<OHCl (degrees)	Cl---H' (Å)	- ? E <sub>e</sub> <sup>N</sup> (kJ/mol)	- ? E <sub>e</sub> <sup>B</sup> (kJ/mol)	- ? E <sub>o</sub> <sup>B</sup> (kJ/mol)
BLYP/plane waves <sup>b</sup>	1.354	1.761	164.1	...	...	27	...
BLYP/6-311++G(d,p)	1.339	1.768	169.5	...	33	30	21
MP2/6-311++G(d,p) <sup>c</sup>	1.296	1.894	155.9	...	34	26	...
MP2/6-31G(2dp) <sup>d</sup>	1.303, 1.323	1.787, 1.657	.....	.....	.....	32, 30	21, 18
MP2/6-31G(d,p) <sup>e,f</sup>	1.294	1.835	...	2.974, ~3	...	38	...
corr. HF/6-31G(d) <sup>e,g</sup>	1.28	1.95	...	3.15, 3.85	46	40	32

<sup>a</sup> Unless otherwise noted. Column headings are as follows: Optimized geometry, nearest dangling OH group(s) (Cl---H'), and binding energies uncorrected (- ? E<sub>e</sub><sup>N</sup>), corrected for basis set superposition error using the function counterpoise method but not for zero-point energies (- ? E<sub>e</sub><sup>B</sup>), and corrected for both basis set superposition error and for zero-point energies (- ? E<sub>o</sub><sup>B</sup>). <sup>b</sup> For methods using (non-local) plane waves, basis set superposition error is zero. <sup>c</sup> ref. 39 <sup>d</sup> ref. 41. Results are for globally minimized cyclic complexes HCl·(H<sub>2</sub>O)<sub>n</sub> in which n = 2 and 3, respectively. <sup>e</sup> Results are for HCl on an isolated (H<sub>2</sub>O)<sub>6</sub> cluster with a frozen, chair-shaped geometry. <sup>f</sup> ref. 42 <sup>g</sup> ref. 43. Their HF result is corrected for electron correlation by adding 9 kJ/mol determined using MP2.

**TABLE 3.3. Interaction of HCl with slab models<sup>a</sup>**

Slab model (method/basis set)	HCl (Å)	O---H (Å)	<OHCl (degrees)	Cl---H <sup>†</sup> (Å)	$\mu_c$ (D)	$\mu_{fp}$ (D)	$-\Delta E_e^B$ (kJ/mol)	$-\Delta E_o^B$ (kJ/mol)	$-? U_T^B$ (kJ/mol)	$-\Delta H_{200}^B$ (kJ/mol)
16W1A1Hf <sup>b</sup>	1.371	1.647	171.8	3.530	13.9	11.3	31	22	25	27
16W1A <sup>O2</sup> 1Hf <sup>b</sup>	1.357	1.742	171.0	3.692	14.0	11.0	30	21	24	26
16W1A <sup>O3</sup> 1Hf <sup>b</sup>	1.358	1.713	179.3	4.822	14.0	11.5	33	24	27	29
16W1A2Hf <sup>b</sup>	1.390	1.597	171.4	2.967, 3.358	1.9	4.8	36	27	30	32
32W1A2Hf <sup>b</sup>	1.389	1.595	171.6	2.957, 3.351	2.2	6.5	36	27	30	32
16W1A <sup>O2</sup> 2Hf <sup>b</sup>	1.369	1.654	171.5	3.522, 4.403	1.7	4.0	29	20	23	25
16W1A3Hf <sup>b</sup>	1.384	1.600	172.6	3.601, 3.732, 4.998	11.0	4.9	33	24	27	29
16W2A1Hf <sup>b,c</sup>	1.356	1.688	169.7	3.513	15.1	13.8	31	22	25	27
	1.337	1.856	173.2	4.892	...	...	21	12	15	17
16W2A2Hf <sup>b,c</sup>	1.368	1.678	169.6	2.911, 3.246	2.6	6.1	36	27	30	32
	1.353	1.717	171.8	3.820, 4.505	...	...	20	11	14	16
32W2A2Hf <sup>b,c</sup>	1.362	1.706	169.1	2.961, 3.301	3.2	8.6	36	27	30	32
	1.351	1.735	170.5	3.586, 4.471	...	...	20	11	14	16
other models <sup>d</sup>										
corr. HF/6-31G(d) <sup>e</sup>	1.29	1.90	...	3.63, 4.05	...	...	33	25	...	...
classical <sup>f</sup>	...	...	...	...	...	...	...	...	19	...
q.-classical <sup>g</sup>	...	...	...	...	...	...	...	...	25, 32, 33	...
experiment <sup>h</sup>	...	...	...	...	...	...	...	...	$> 35 \frac{+3}{-4}, < 25$	...
experiment <sup>i</sup>	...	...	...	...	...	...	...	...	$E_a^d = 26$	...
experiment <sup>j</sup>	...	...	...	...	...	...	...	...	$E_a^d = 33(5)$	...
experiment <sup>k</sup>	...	...	...	...	...	...	...	...	...	46

<sup>a</sup> Column headings are as follows: Optimized geometry, nearest dangling OH group(s) (Cl---H<sup>†</sup>), the total net dipole moment calculated assuming a constant dipole moment for each H<sub>2</sub>O and HCl ( $\mu_c$ ) and also from first principles ( $\mu_{fp}$ ), binding energies corrected for basis set superposition error using the function counterpoise method but not for zero-point energies ( $-\Delta E_e^B$ ) and for zero-point energies ( $-\Delta E_o^B$ ) (emphasizing that no correction for basis set superposition error was done for the plane-wave calculations), binding energies at T = 165 K (unless noted otherwise) ( $-? U_T^B$ ), activation energies for desorption ( $E_a^d$ ), and binding enthalpies at 200 K ( $-\Delta H_{200}^B$ ). <sup>b</sup> For these models, density-functional theory with plane waves was used, and basis set superposition error is zero. <sup>c</sup> For these models, results for HCl adsorbed at O1 are given in the first row, while results for HCl adsorbed at O2 are given in the second row. <sup>d</sup> A model most similar to 16W1A2Hf was studied. <sup>e</sup> ref. 43. Their HF result is corrected for electron correlation by adding 9 kJ/mol determined using MP2, and the repulsion between HCl and its periodic image is subtracted out. <sup>f</sup> ref. 45, T = 190 K. <sup>g</sup> ref. 46. The three results are for HCl interacting with a defect-free (0001) face and faces with three and six water molecules removed, respectively, at 190 K. <sup>h</sup> ref. 31. Limits are for HCl on ice with low surface coverage and ice with high surface coverage of HCl, respectively. The uncertainty is indicated. <sup>i</sup> ref. 32.  $E_a^d$  was measured at 100-126 K. <sup>j</sup> ref. 33.  $E_a^d$  was measured at 140 K; the uncertainty is given in units of the last digit. <sup>k</sup> ref. 34

**TABLE 3.4. Calculated dipole-dipole interaction energy, in kJ/mol, of HCl with the entire slab, with only the water molecule directly involved in binding, with the binding H<sub>2</sub>O and its nearest neighbors, and with each layer**

Model	$\mu_c$ (D)	Entire slab (kJ/mol)	Binding H <sub>2</sub> O (kJ/mol)	Binding and neighboring H <sub>2</sub> O (kJ/mol)	Layer 1 (kJ/mol)	Layer 2 (kJ/mol)	Layer 3 (kJ/mol)	Layer 4 (kJ/mol)
16W1A1Hf	13.9	18.9	12.8	18.5	12.6	4.5	1.2	0.6
16W1A <sup>O2</sup> 1Hf	14.0	14.6	10.1	14.4	10.2	3.0	0.8	0.6
16W1A <sup>O3</sup> 1Hf	14.0	17.3	14.9	18.3	13.1	1.5	1.2	1.5
16W1A2Hf	1.9	20.1	11.7	17.1	12.3	6.7	0.5	0.6
16W1A <sup>O2</sup> 2Hf	1.7	18.9	13.0	19.0	13.6	5.1	0.0	0.2
16W1A3Hf	11.0	18.5	12.2	18.4	14.6	6.5	-2.1	-0.5

### LIST OF FIGURES FOR CHAPTER 3

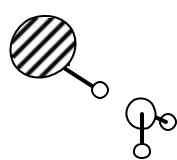
Figure 3.1. Depiction of  $\text{HCl}\cdot\text{H}_2\text{O}$  and the cluster 4W1A.

Figure 3.2. The (100) face depicted for 16W3A1Hf, 16W2A2Hf, 32W2A2H, and 16W1A3Hf. The simulation cell is outlined in thick black. White atoms are in the top (first) layer, while black atoms are in the underlying (second) layer; for clarity, only atoms in the top (first) bilayer are shown. As a reminder that periodic boundary conditions were used in all directions, a  $3 \times 3$  periodic representation of 16W2A2Hf (or 32W2A2H) is shown. The naming of these models is explained in the text. Models with either 16 or 32 water molecules have either four or eight layers, respectively, of four water molecules each. The adsorption sites O1, O2, and O3 are labeled if there is more than one possible adsorption site.

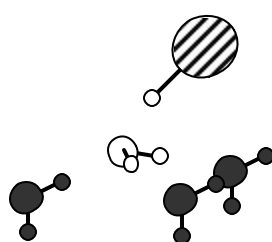
Figure 3.3. The (110) face, one of six prism faces perpendicular to (100), of the optimized slab model 16W2A2Hf. The simulation cell, with the surface vacuum region of 8 Å, is superimposed.



Figure 3.1



**HCl·H<sub>2</sub>O**



**4W1A**

Figure 3.2

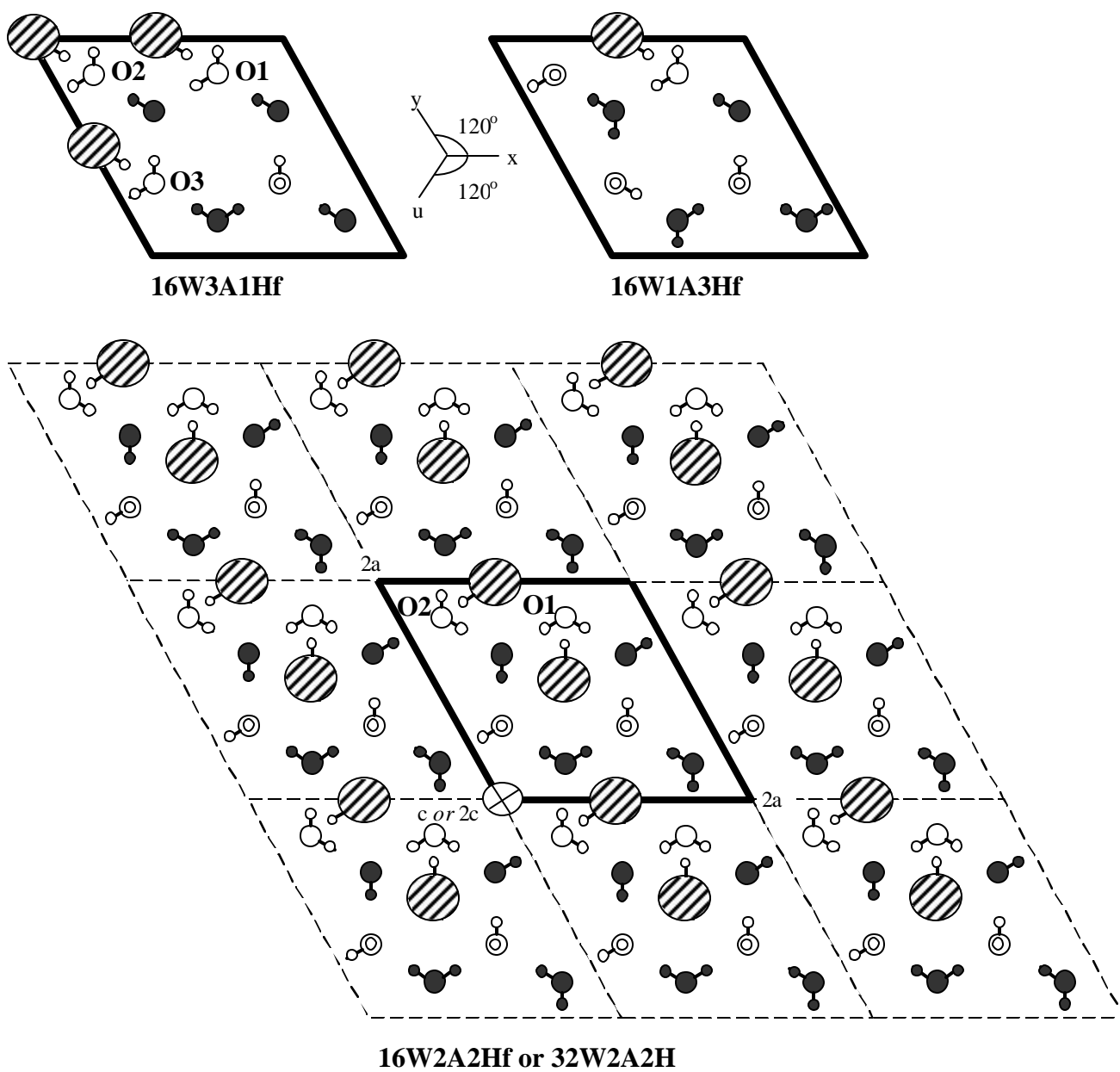
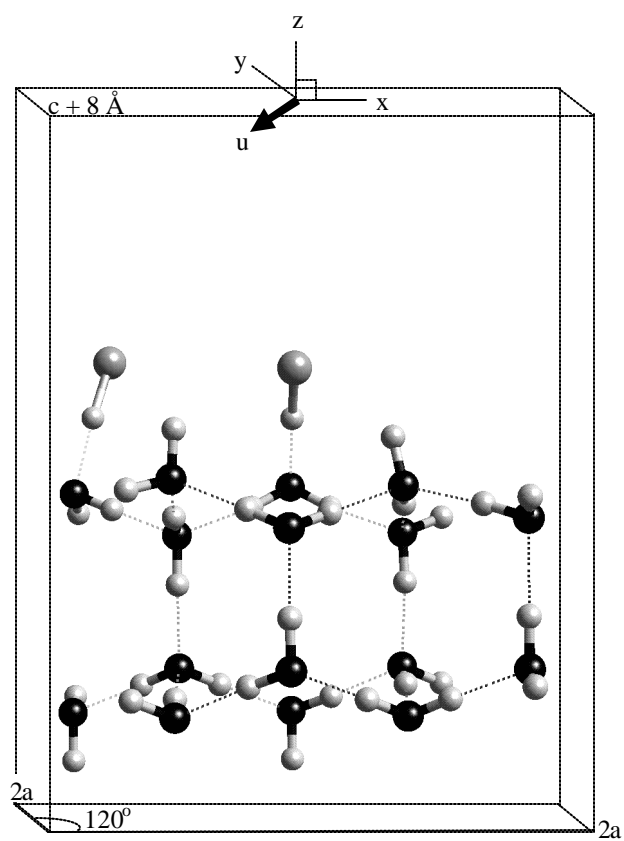


Figure 3.3



## Chapter 4: The interaction of HCl with the (0001) face of hexagonal ice studied theoretically via Car-Parrinello molecular dynamics

Reproduced with permission from Mantz, Y. A.; Geiger, F. M.; Molina, L. T.; Molina, M. J.; Trout, B. L. *Chem. Phys. Lett.* **2001**, 348, 285-292. © 2001 Elsevier Science

### ABSTRACT

The depletion of stratospheric ozone at high latitudes is caused by gas-phase catalytic cycles involving active chlorine compounds produced through heterogeneous chemical reactions involving HCl. In this Letter, results aimed at understanding the activation of chlorine on ice cloud particle surfaces are presented. We focus specifically on HCl interacting with the ice surface prior to reaction. We conclude that, in regions with a low surface density of dangling OH groups, HCl may be either ionically or molecularly adsorbed, but in regions with a high surface density of dangling OH groups, HCl is ionically adsorbed.

### 4.1. INTRODUCTION

Heterogeneous chemical reactions are now recognized to lead ultimately to the depletion of polar stratospheric ozone (as described, e.g, in the review by Solomon<sup>1</sup>). An important example is Rx. (4.1), which occurs rapidly<sup>2</sup> and possibly in a single elementary step<sup>3,4</sup> on the surfaces of ice cloud particles. The interaction of HCl with the ice surface is a key step preceding reaction and thus is of particular interest from a mechanistic point of view.<sup>5</sup>



Measurements<sup>2,6</sup> indicate that the uptake of HCl on smooth, well-characterized ice films ranges from  $2 \times 10^{13}$  to  $4 \times 10^{14}$  molecule/cm<sup>2</sup> under conditions approaching those resulting in the formation of ice clouds in the polar stratosphere (185 K,  $\sim 10^{-4}$  torr H<sub>2</sub>O,  $10^{-8}$ - $10^{-7}$  torr HCl). Both IR spectroscopy<sup>7,8</sup> and TPD measurements<sup>8</sup> between 60-150 K and 100-200 K, respectively, indicate that ionic hydrates of HCl are formed for HCl exposures estimated to yield

at least one monolayer ( $\sim 10^{15}$  molecule/cm<sup>2</sup>) coverage. At submonolayer levels, however, there is spectroscopic evidence for molecular HCl at 125-145 K,<sup>9</sup> although secondary ion mass spectrometry provides conflicting evidence for ionization at 90-150 K.<sup>10</sup> These techniques both require ultra-high vacuum conditions, making their application under polar stratospheric conditions, where the water vapor pressure above ice is  $\sim 10^{-4}$  torr and where bulk hydrates of HCl do not form,<sup>11</sup> difficult and motivating a theoretical approach.

To model the interaction of HCl with ice, many theoretical approaches have been used,<sup>12-19</sup> but there is a trade-off between the sophistication of the theoretical method and the appropriateness of the model. In this Letter, which is a follow-up to our earlier related publications,<sup>20,21</sup> the Car-Parrinello technique<sup>22-24</sup> is used to investigate the interaction of HCl with extended surface models of ice, with special attention given to the role that dangling (non-hydrogen-bonding) OH groups play.

## 4.2. EXTENDED ICE SURFACE MODELS AND SIMULATIONS

The ice *Ih* basal (0001) face, highly relevant (Sec. 4.4), is modeled using defect-free periodic surfaces or slabs consisting of 24 or 32 water molecules with eight H<sub>2</sub>O molecules per bilayer in a hexagonal simulation cell with dimensions (based on results in Sec. 4.3.1) of 9.046 Å × 19.051 Å or 9.046 Å × 22.734 Å, respectively. A sufficiently large<sup>20</sup>  $\sim 8$  Å vacuum region is included, periodic boundary conditions are applied, and the bottom bilayer is held fixed to its bulk optimized position in order to create an infinite surface. Adsorbed HCl is 7.834 Å from its nearest periodic image and thus essentially isolated. Each model satisfies the ice rules,<sup>25</sup> ends in a full-bilayer termination,<sup>25</sup> and possesses the smallest possible net dipole moment.<sup>20,21</sup>

As described in detail elsewhere,<sup>20,21</sup> all geometry optimizations and Car-Parrinello molecular dynamics simulations<sup>22-24</sup> are performed using the BLYP functional<sup>26,27</sup> with a plane-wave cutoff of 70.0 Ry and Troullier-Martins pseudopotentials<sup>28</sup> and using only the  $\Gamma$  point for Brillouin-zone sampling. Geometry optimizations in Sec. 4.3.1 are converged using fractional cutoffs (ranging from 70.000 to 70.300 Ry) to fix the basis set “size,” i.e., the number of plane waves per unit volume. Simulations in Sec. 4.3.2 are reasonably stable, as judged by the small drift ( $< 10^{-5}$  a.u.) in the Hamiltonian of the entire system, including the thermostat.

### 4.3. RESULTS AND DISCUSSION

#### 4.3.1. Validation of Computational Approach: Select optimizations

Our approach is appropriate for describing  $\text{H}_2\text{O}$ ,  $(\text{H}_2\text{O})_2$ , liquid water,<sup>29</sup> and  $\text{HCl}^{\text{p0}}$  and yields 421 kJ/mol for  $\text{HCl}(\text{g}) \rightarrow \text{H}(\text{g}) + \text{Cl}(\text{g})$  and 1389 kJ/mol for  $\text{HCl}(\text{g}) \rightarrow \text{H}^+(\text{g}) + \text{Cl}(\text{g})$  compared to literature values<sup>30,31</sup> of  $D_o = 428$  kJ/mol and  $428 + 1313 - 349 = 1392$  kJ/mol, respectively. Our slight underestimation of the HCl bond strength is compensated to some degree by the likely underestimation of the strength of the Cl—H hydrogen bonds formed during dissociation (Sec. 4.3.2).

The geometry of a bulk ice *Ih* simulation cell ( $2a \times c$ ) was optimized to a fully converged minimum for different values of the lattice constants (Fig. 4.1). The most stable structure is associated with  $a = 4.523 \pm 0.05$  Å and  $c = 7.514 \pm 0.08$  Å, compared to experimental results at 10 K of  $a = 4.49693 \pm 0.00022$  Å and  $c = 7.32109 \pm 0.00074$  Å.<sup>25</sup> Because of our slightly larger ratio of  $c/a$ , we observe a difference between the  $d_{\text{OO}}$ 's along the  $c$  vector versus those perpendicular to it. Consequently, our most stable structure yields a larger range of values for  $d_{\text{OO}} = 2.763\text{-}2.826$  Å,  $d_{\text{O-H}} = 1.772\text{-}1.831$  Å,  $\angle\text{OOO} = 108.6\text{-}110.2^\circ$ , and  $\angle\text{OHO} = 176.7\text{-}178.6^\circ$  compared to measurements at 15 K of  $d_{\text{OO}} = 2.750\text{-}2.751$  Å and  $\angle\text{OOO} = 109.33\text{-}109.61^\circ$ .<sup>25</sup> However, our  $d_{\text{OH}} = 0.995\text{-}1.000$  Å and  $\angle\text{HOH} = 106.0\text{-}106.7^\circ$  compare better to measured  $d_{\text{OH}} \sim 0.985 \pm 0.005$  Å and  $\angle\text{HOH} \sim 106.6 \pm 1.5^\circ$ .<sup>25</sup> Our energy calculated to convert the non-vibrating crystal at 0 K to non-vibrating molecules at 0 K is 0.251 eV/bond, which underestimates the experimental result, 0.306 eV/bond,<sup>25</sup> by an amount comparable to that for  $(\text{H}_2\text{O})_2$ , 0.041 eV/bond.<sup>29</sup> We conclude that the Car-Parrinello technique reasonably describes both the bulk and the surface<sup>21</sup> and may be confidently used to study surface processes.

<Figure 4.1 here>

#### 4.3.2. Car-Parrinello molecular dynamics and energetics of HCl on hexagonal ice

In this section, the dynamics and energetics of HCl at three different binding sites distinguished by the local density of dangling OH groups is reported. In all cases, a geometry

optimization was performed before commencing a dynamical simulation. Initial configurations at 0 ps therefore correspond to local minima on the potential energy surface. Based on a rough estimate of 220 K for the melting point of our slab models,<sup>21</sup> simulation temperatures of 150, 190, and 230 K correspond to atmospheric temperatures of  $150 \times 273/220 = 190$ , 240, and 290 K, respectively. Note that these estimates were not made rigorously and are not considered precise. Lastly, potential energies of interaction are reported with respect to the isolated molecule and surface, i.e.,  $\text{HCl} + \text{slab} \rightarrow \text{HCl-slab}$ , and are calculated at a given simulation time by optimizing the atomic positions, removing HCl, and optimizing the distorted slab. Zero-point energies are not taken into account, because we are interested in the differences between molecular and dissociated HCl, and the correction for zero-point energies (about  $-10$  kJ/mol to the binding energy of molecular HCl)<sup>20</sup> will be identical to within a few kJ/mol.

The dynamics of HCl on model surface one,<sup>21</sup> having *two* dangling OH groups, is shown in Fig. 4.2a. Dissociation of HCl and a concomitant decrease in the distance of both dangling OH groups from the chlorine atom occurs at 0.2 ps at 150 K (Figs 4.2a and 4.2b), 0.6 ps at 190 K, and 0.65 ps at 230 K. Because dissociation is stochastic, our results do not imply temperature dependence. The product  $\text{H}^{\delta+}-\text{Cl}^{\delta-}$  retains a partial ionic character: From the simulation at 150 K, we calculate (as described previously)<sup>20</sup> Mulliken populations of 0.18 (H) and -0.19 (Cl) at 0 ps, 0.20 (H) and -0.30 (Cl) at 0.17 ps, and 0.26 (H) and -0.43 (Cl) at 0.43 ps (with all other atoms essentially unchanged). In contrast, when HCl is adsorbed at a different water molecule on model surface one, so that the chlorine atom is further from the dangling OH groups (Fig. 4.3a), or when HCl is adsorbed on model surface two as closely as possible to the single dangling OH group (Fig. 4.4a), dissociation of HCl is not observed. (In Fig. 4.3a, HCl does trace out a counterclockwise circle while interacting noticeably with both dangling OH groups). In Figs. 4.3b and 4.4b, the HCl vibrational frequencies are, from the Fourier transform of the hydrogen-chlorine velocity autocorrelation function, centered at 2150 and 2190  $\text{cm}^{-1}$ , with calculated spectral resolutions of 18.7 and 33.3  $\text{cm}^{-1}$ , respectively. Given the bandwidth, the vibrational frequency is, in both cases,  $\sim 2200$   $\text{cm}^{-1}$ , which is compared to that calculated (with a 4.6  $\text{cm}^{-1}$  resolution) for an isolated gas-phase HCl molecule at 190 K,  $2600$   $\text{cm}^{-1}$ , red-shifted relative to experiment, 2885  $\text{cm}^{-1}$ .<sup>30</sup>

<Figures 4.2, 4.3, and 4.4 here>

We conclude that dissociation is kinetically rapid, and essentially barrier-less, with HCl interacting strongly with at least two dangling OH groups (Fig. 4.2a). Other studies finding molecular HCl atop an ice surface constrained to its ideal structure do not take into account the role of dangling OH groups.<sup>32</sup> In contrast, when HCl is interacting weakly with both dangling OH groups (Fig. 4.3a) or with only one dangling OH group (Fig. 4.4a), dissociation is not barrier-less. Based on the small sample of trajectories obtained on model surfaces one and two, there may be additional dissociation paths that are significant at  $\geq 1$  ps time scales for the models depicted in Figs. 4.3a and 4.4a. Our findings are consistent with semiempirical QM/MM classical MD simulations<sup>17</sup> performed over 100 ps, in which molecular HCl adsorbed on a periodic surface ultimately “flips” (within 30 ps) from a central surface hexagon with one dangling OH group to a neighboring hexagon with two dangling OH groups and then rapidly dissociates.

The average interaction energy of  $\text{H}^{\delta+}-\text{Cl}^{\delta-}$  in Fig. 4.2a, based on optimizations of the atomic positions at 0.43 and 0.96 ps, is 57 kJ/mol, greater than that of molecularly adsorbed HCl, 36 kJ/mol.<sup>20</sup> To determine the interaction energy of  $\text{H}^{\delta+}-\text{Cl}^{\delta-}$  with the ice slabs depicted in Figs. 4.3a and 4.4a, separated  $\text{H}_3\text{O}^+$  and  $\text{Cl}^-$  ions were placed on the previously optimized slabs, and optimizations were performed. Formation of a contact ion pair (Fig. 4.3c) and molecular HCl (Fig. 4.4c) is ultimately observed. The net binding energy of the contact ion pair is 35 kJ/mol, slightly greater than molecular binding energies of 29, 29, 31, 26, and 29 kJ/mol obtained for the HCl-ice system in Fig. 4.3a at 0.00, 0.34, 0.92, 1.49, and 1.79 ps, respectively. The (molecular) binding energy obtained for the final structure in Fig. 4.4c is 30 kJ/mol, compared to 37 kJ/mol obtained for the HCl-ice system in Fig. 4.4a at 0.00 ps. The smaller binding energy of Fig. 4.4c is attributed to greater distortion of the ice surface resulting from a stronger Cl—H hydrogen bond (2.47 Å versus 4.89 Å). Interestingly, because of minimal surface distortion and a short (1.643 Å) H—O hydrogen bond, 37 kJ/mol is larger than values of 29-31 kJ/mol calculated<sup>20</sup> for HCl molecularly adsorbed on another ice slab also with one dangling OH group but a completely different arrangement of the hydrogen atoms.

We conclude that dissociation is thermodynamically favorable under the conditions depicted in Fig. 4.2a, based on the difference in the interaction energies of dissociated and molecular HCl, 57 and 36 kJ/mol, respectively, consistent with 64 and 41 kJ/mol, respectively,



determined in the semiempirical QM/MM study.<sup>17</sup> Our results agree with the finding that clusters with at least four water molecules<sup>12-14</sup> and periodic models<sup>16,18,19</sup> with dissociated HCl are more stable than those with molecular HCl. In contrast, we conclude that dissociation is either weakly favored or not favored thermodynamically under the conditions depicted in Figs. 4.3a and 4.4a, respectively.

### 4.3.3. Effect of HCl on the surface disordering of hexagonal ice

The surface of ice is known to possess a partially disordered transition region at temperatures below the bulk freezing point.<sup>21,25</sup> In the presence of HCl, this “quasi-liquid layer” may facilitate HCl dissociation.<sup>11</sup> In Fig. 45, the average oxygen-oxygen pair distribution functions  $g_{oo}(r)$  by bilayer are compared for ice slabs without HCl at simulation temperatures of 190 and 230 K,<sup>21</sup> as well as for model surfaces one and two interacting with HCl as shown in Figs. 4.2a, 4.3a, and 4.4a at a simulation temperature of 150 K. For the case where HCl partially dissociates (Fig. 4.2a), the  $g_{oo}(r)$  calculated from atomic trajectories for the top bilayer and the one below obtained during 0.5-1.0 ps and 0.5-1.65 ps at 150 K are similar, supporting the conclusions from an earlier study<sup>21</sup> that our system is in equilibrium and that 0.5 ps is sufficient time to obtain accurate results. The  $g_{oo}(r)$  for bilayers one and two are comparable to those calculated for plain ice (without HCl) at a simulation temperature where disordering indicative of melting is observed, 230 K.<sup>21</sup> For the two cases where HCl dissociation is not observed (Figs. 4.3a and 4.4a), the  $g_{oo}(r)$  are narrower and sharper than those calculated for plain ice at 190 K. The same trends are observed when, e.g., rotational disorder is evaluated by calculating molecular distributions of the azimuthal and polar angles in each bilayer.<sup>21</sup>

<Figure 4.5 here>

We conclude that for a high surface coverage of HCl in close proximity to two dangling OH groups, the temperature at which disordering is first observed is depressed to polar stratospheric temperatures of about 190 K, and that disordering extends to the second bilayer. Disordering is not observed with molecularly adsorbed HCl. For the hypothetical case of HCl near dangling OH groups on a model with more water molecules per bilayer, disordering may

well be confined to a localized region, i.e., the two water molecules with dangling OH groups and their nearest neighbors, which would be consistent with the findings of Gertner and Hynes. In their theoretical study of HCl interacting with a hexagonal ice model 15.50 Å across and 18.27 Å thick, a “quasi-liquid layer” was neither induced by HCl incorporated into the ice lattice nor was required for HCl ionization.<sup>18</sup>

#### 4.4. ATMOSPHERIC IMPLICATIONS

Ice cloud particles, which grow under near equilibrium conditions with respect to water vapor, are thought to be most likely single crystals, with low index faces exposed.<sup>33</sup> An experimental study of the crystalline ice *1h* surface indicates that the density of dangling OH groups is low,<sup>34</sup> with measurements indicating ~10 “bulk” OH stretches in the first bilayer for each dangling OH bond stretch.<sup>35</sup> Model surfaces one (Figs. 4.2 and 4.3) and two (Fig. 4.4) have a dangling OH group for every 7 and 15 “bulk” OH’s in the first bilayer, respectively. Our results suggest that regions with a high density of dangling OH groups (e.g., step edges<sup>33</sup> and grain boundaries) will promote the dissociation of HCl. The ice lattice may also play a role, however, in promoting an ionic reaction between HCl and ClONO<sub>2</sub>.<sup>3,4</sup>

#### 4.5. CONCLUSIONS

In this Letter, we address the state of HCl on ice, the role of dangling OH groups, and the existence of, and effect of HCl on, the disordering of the surface of ice. Car-Parrinello molecular dynamics simulations indicate that HCl ionizes with essentially no barrier at stratospherically relevant temperatures in surface regions with a high density of dangling OH groups. The ionized form is 21 kJ/mol more stable than molecularly adsorbed HCl. Conversely, there is a barrier to dissociation of unknown magnitude in regions with a low OH density, and (at most) only a weak thermodynamic preference for dissociated HCl. A disordered ice surface exists below ionized, but not molecular, HCl.

## 4.6. ACKNOWLEDGMENTS

This work was partially supported by the NASA Upper Atmospheric Research Program (Grant No. NAG5-8887). Y.A.M. acknowledges partial support from the MIT Center for Global Change Sciences. F.M.G. acknowledges support from the NOAA Postdoctoral Program in Climate and Global Change, administered by the University Corporation for Atmospheric Research. This work was also partially supported by the National Computational Science Alliance (Proposal No. CTS990016Nr00 and CHE010020N) and utilized the NCSA SGI/CRAY Origin2000.

## REFERENCES FOR CHAPTER 4

- (1) Solomon, S. *Rev. Geophys.* **1999**, *37*, 275.
  - (2) Lee, S.-H.; Leard, D. C.; Zhang, R.; Molina, L. T.; Molina, M. J. *Chem. Phys. Lett.* **1999**, *315*, 7.
  - (3) Bianco, R.; Hynes, J. T. *J. Phys. Chem. A* **1999**, *103*, 3797.
  - (4) McNamara, J. P.; Tresadern, G.; Hillier, I. H. *J. Phys. Chem. A* **2000**, *104*, 4030.
  - (5) Kroes, G.-J. *Comments At. Mol. Phys.* **1999**, *34*, 259.
  - (6) Leu, M.-T.; Keyser, L. F.; Timonen, R. S. *J. Phys. Chem. B* **1997**, *101*, 6259.
  - (7) Pursell, C. J.; Zaidi, M.; Thompson, A.; Fraser-Gaston, C.; Vela, E. *J. Phys. Chem. A* **2000**, *104*, 552.
  - (8) Banham, S. F.; Sodeau, J. R.; Horn, A. B.; McCoustra, M. R. S.; Chesters, M. A. *J. Vac. Sci. Technol. A* **1996**, *14*, 1620.
  - (9) Uras, N.; Rahman, M.; Devlin, J. P. *J. Phys. Chem. B* **1998**, *102*, 9375.
  - (10) Donsig, H. A.; Vickerman, J. C. *J. Chem. Soc., Faraday Trans.* **1997**, *93*, 2755.
  - (11) Molina, M. J. The probable role of stratospheric 'ice' clouds: Heterogeneous chemistry of the 'ozone hole'. In *The Chemistry of the Atmosphere: Its Impact on Global Change*; Calvert, J. G., Ed.; Blackwell Scientific Publications: Oxford, 1994; p. 27.
  - (12) Bacelo, D. E.; Binning, R. C., Jr.; Ishikawa, Y. *J. Phys. Chem. A* **1999**, *103*, 4631.
  - (13) Re, S.; Osamura, Y.; Suzuki, Y.; Schaefer, H. F., III. *J. Chem. Phys.* **1998**, *109*, 973.
  - (14) Ando, K.; Hynes, J. T. *J. Phys. Chem. B* **1997**, *101*, 10464.
  - (15) Toubin, C.; Hoang, P. N. M.; Picaud, S.; Girardet, C. *Chem. Phys. Lett.* **2000**, *329*, 331.
  - (16) Casassa, S. *Chem. Phys. Lett.* **2000**, *321*, 1.
  - (17) Svanberg, M.; Pettersson, J. B. C.; Bolton, K. *J. Phys. Chem. A* **2000**, *104*, 5787.
- Also see Bolton, K.; Pettersson, J. B. C. *J. Am. Chem. Soc.* **2001**, *123*, 7360.
- (18) Gertner, B. J.; Hynes, J. T. *Faraday Discuss.* **1998**, *110*, 301.
  - (19) Robertson, S. H.; Clary, D. C. *Faraday Discuss.* **1995**, *100*, 309.

- (20) Mantz, Y. A.; Geiger, F. M.; Molina, L. T.; Molina, M. J.; Trout, B. L. *J. Phys. Chem. A* **2001**, *105*, 7037.
- (21) Mantz, Y. A.; Geiger, F. M.; Molina, L. T.; Molina, M. J.; Trout, B. L. *J. Chem. Phys.* **2000**, *113*, 10733.
- (22) Car, R.; Parrinello, M. *Phys. Rev. Lett.* **1985**, *55*, 2471.
- (23) Marx, D.; Hutter, J. Ab initio molecular dynamics: Theory and implementation. In *Modern Methods and Algorithms of Quantum Chemistry*; Grotendorst, J., Ed.; John von Neumann Institute for Computing: Jülich, 2000; Vol. NIC Series, Vol. 1; p. 301.
- (24) J. Hutter, A. Alavi, T. Deutsch, M. Bernasconi, St. Goedecker, D. Marx, M. Tuckerman, and M. Parrinello, CPMD version 3.0, Max-Planck Institut für Festkörperforschung and IBM Zurich Research Laboratory, 1995-99.
- (25) Petrenko, V. F.; Whitworth, R. W. *Physics of Ice*; Oxford University Press: New York, 1999.
- (26) Becke, A. D. *Phys. Rev. A* **1988**, *38*, 3098.
- (27) Lee, C.; Yang, W.; Parr, R. G. *Phys. Rev. B* **1988**, *37*, 785.
- (28) Troullier, N.; Martins, J. L. *Phys. Rev. B* **1991**, *43*, 1993.
- (29) Sprik, M.; Hutter, J.; Parrinello, M. *J. Chem. Phys.* **1996**, *105*, 1142.
- (30) Huber, K. P.; Herzberg, G. *Molecular Spectra and Molecular Structure IV. Constants of Diatomic Molecules*; Van Nostrand: New York, 1979.
- (31) Hotop, H.; Lineberger, W. C. *J. Phys. Chem. Ref. Data* **1985**, *14*, 731.
- (32) Bianco, R.; Gertner, B. J.; Hynes, J. T. *Ber. Bunsenges. Phys. Chem.* **1998**, *102*, 518.
- (33) Hobbs, P. V. *Ice Physics*; Clarendon Press: Oxford, 1974.
- (34) Schaff, J. E.; Roberts, J. T. *J. Phys. Chem.* **1994**, *98*, 6900.
- (35) Wei, X.; Miranda, P. B.; Shen, Y. R. *Phys. Rev. Lett.* **2001**, *86*, 1554.

## LIST OF FIGURES FOR CHAPTER 4

Figure 4.1. Energies in kJ/mol relative to the most stable bulk ice *Ih* simulation cell plotted as a function of relative lattice constants.

Figure 4.2. (a) Snapshots of HCl on a periodic ice *Ih* model with two dangling OH' groups and (b) the evolution of atomic distances during a 1.65 ps simulation at 150 K. In (a), only the top bilayer of the ice model is shown in each frame.

Figure 4.3. (a) Snapshots and (b) the evolution of atomic distances depicted from a 1.79 ps simulation at 150 K. (c) Snapshots from a geometry optimization with  $\text{H}_3\text{O}^+$  and Cl ions initially separated. In (a) and (c), an ice model identical to that in Figure 4.2 is used, and only the top bilayer is shown in each frame.

Figure 4.4. (a) Snapshots and (b) evolution of atomic distances depicted from a 1.0 ps simulation at 150 K. (c) Snapshots from a geometry optimization with  $\text{H}_3\text{O}^+$  and Cl ions initially separated. In (a) and (c), the same periodic ice *Ih* model with one dangling OH' group is used, and only the top bilayer is shown in each frame.

Figure 4.5. The average pair distribution function  $g_{\text{OO}}(r)$  calculated for bilayer 1 over 0.5 and 1.2 ps for the simulation depicted in Figure 4.2, over 0.5 ps for that depicted in Figures 4.3 and 4.4, and over 0.5 ps for ice at 190 and 230 K. This function is also shown for bilayer 2 over 0.5 and 1.2 ps for the simulation depicted in Figure 4.2 and over 0.5 ps for plain ice at 190 and 230 K but not for the simulations depicted in Figures 4.3 and 4.4 because in those simulations a model with three bilayers was used, placing bilayer 2 next to fixed atoms.

Figure 4.1

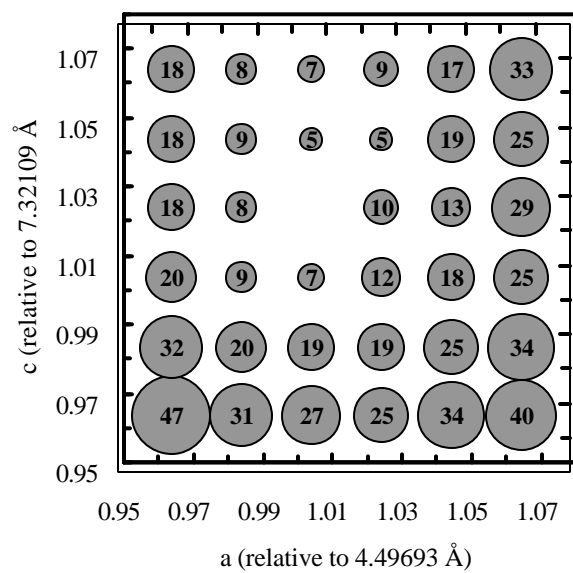
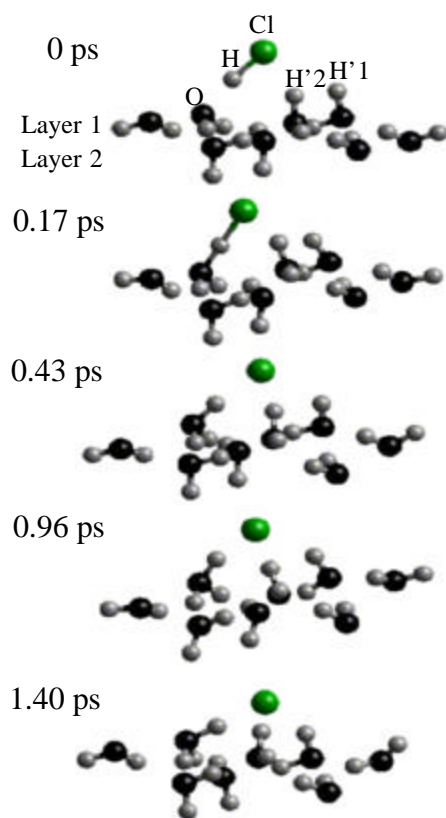
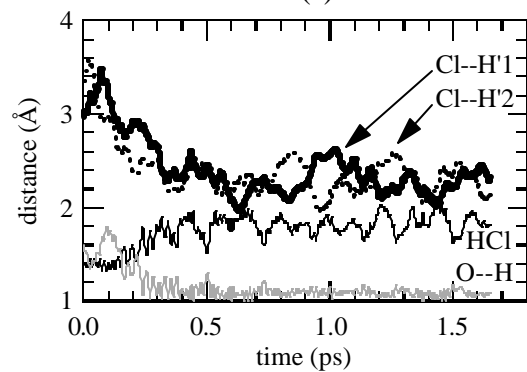


Figure 4.2



(a)



(b)

Figure 4.3

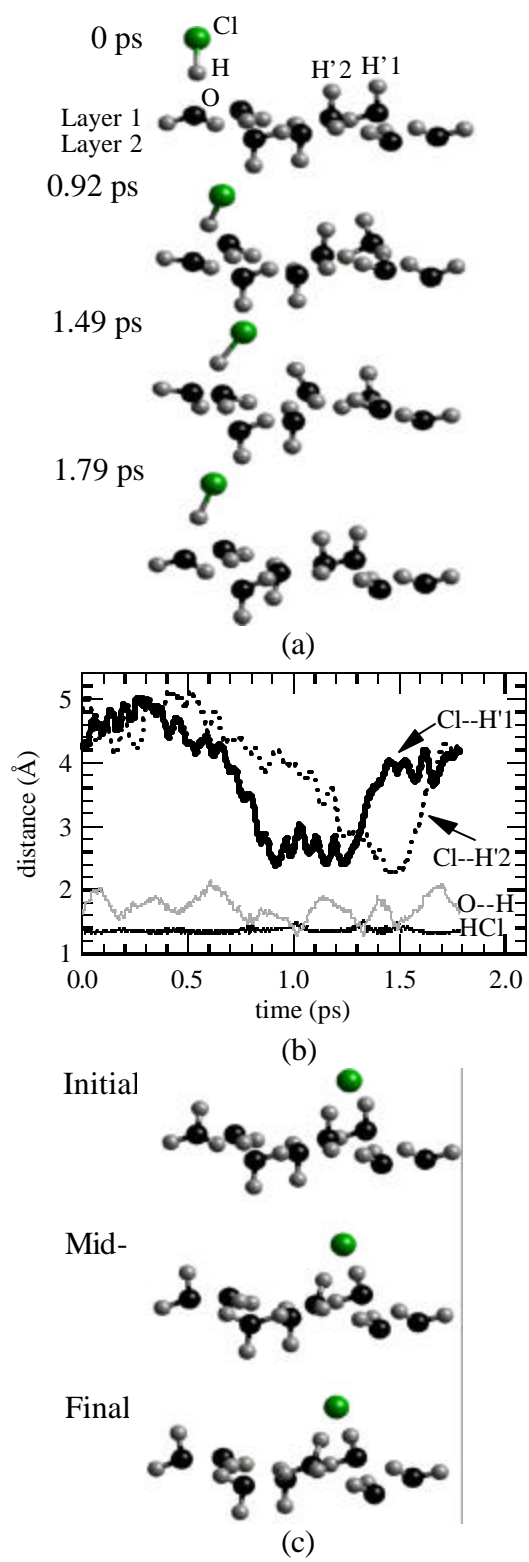




Figure 4.4

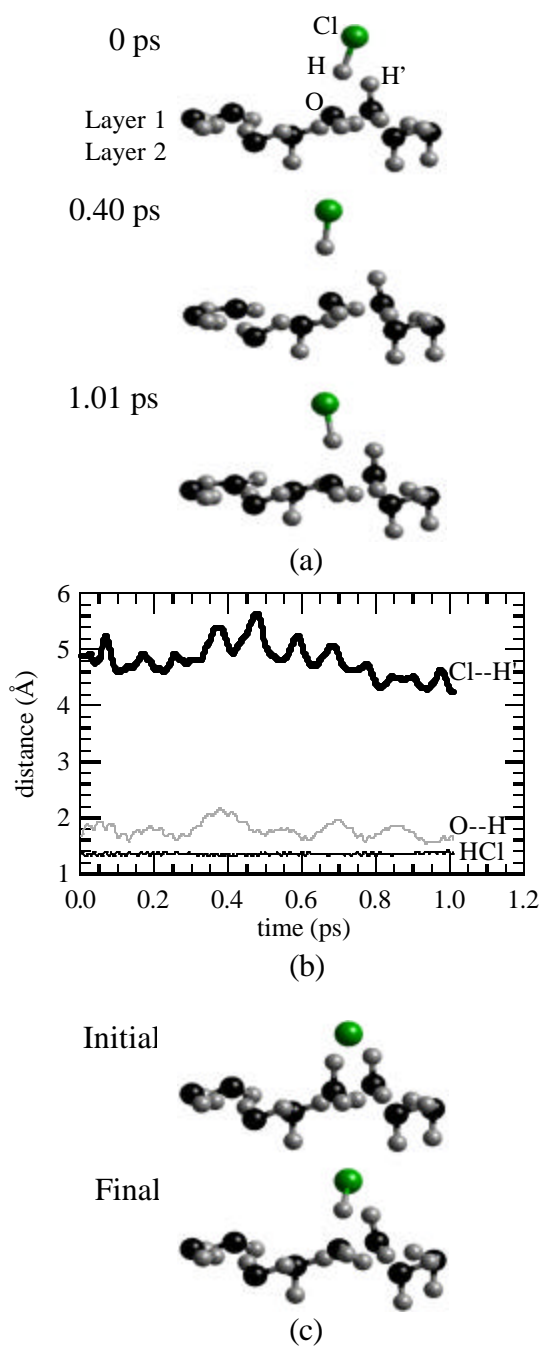
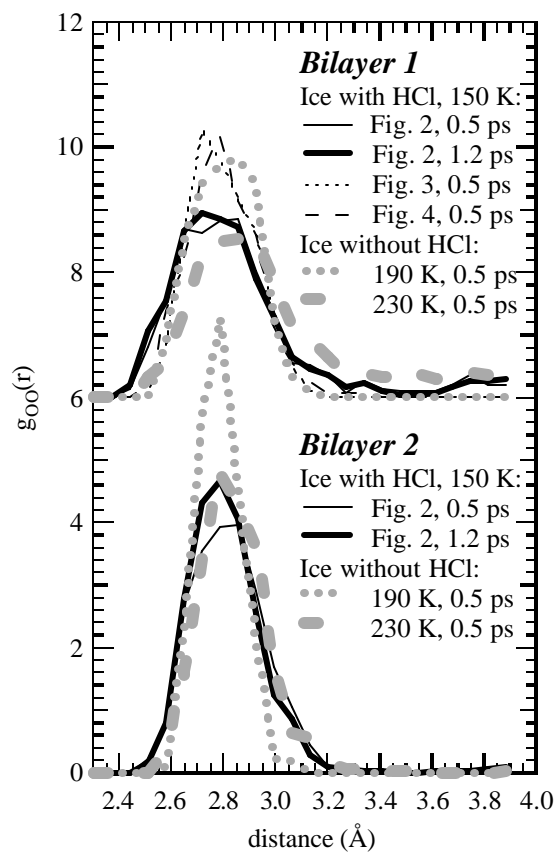


Figure 4.5



## Chapter 5: A Theoretical Study of the Interaction of HCl with Crystalline NAT

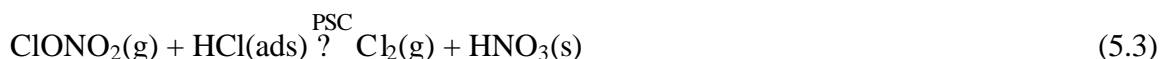
Reproduced with permission from Journal of Physical Chemistry A, submitted for publication.  
Unpublished work © 2001 American Chemical Society.

### ABSTRACT

Using density-functional-plane-wave-based and localized-orbital computational methods, we systematically examine the binding of molecular HCl at a variety of surface sites on crystalline nitric acid trihydrate (NAT), a step preceding the chlorine activation reactions that contribute to the depletion of stratospheric ozone at high latitudes. We pay particular attention to the role played by surface dangling (non-hydrogen-bonding) OH groups. After optimizing six low index faces, we find that NAT (001) and (00 $\bar{1}$ ) faces are thermodynamically the most stable. Only one surface site on the (001) face, with one nearby dangling OH group, exhibits a high affinity for HCl. At this binding site, adsorbed HCl forms a strong H••O hydrogen bond with an NO<sub>3</sub><sup>-</sup> ion and a weaker Cl••H hydrogen bond with a nearby H<sub>2</sub>O molecule. The interaction energy and enthalpy at 190 K corrected for zero-point energies are 23 and 25 kJ/mol, respectively. The presence of one strong binding site per simulation cell, versus at least three previously reported on the (0001) face of ice *Ih* [Mantz, Y. A.; Geiger, F. M.; Molina, L. T.; Molina, M. J.; Trout, B. L. *J. Phys. Chem. A* **2000**, *105*, 7037], leads to a prediction of a lower HCl surface coverage on NAT than on ice, qualitatively consistent with experiments conducted on these surfaces. Additionally, we present kinetic and thermodynamic evidence that molecular HCl, adsorbed near one or two dangling OH groups, does not dissociate on NAT. By contrast, molecularly adsorbed HCl likely dissociates when interacting strongly with two dangling OH group on the ice *Ih* (0001) face as reported in previously published theoretical studies [Svanberg, M.; Pettersson, J. B. C.; Bolton, K. *J. Phys. Chem. A* **2000**, *104*, 5787; Mantz, Y. A.; Geiger, F. M.; Molina, L. T.; Molina, M. J.; Trout, B. L. *Chem. Phys. Lett.* **2001**, *348*, 285].

## 5.1. INTRODUCTION

The surfaces of polar stratospheric cloud (PSC) particles, formed during the cold polar winter, are now widely recognized to catalyze halogen activation reactions, e.g., Rxs. (5.1) – (5.3), which result in the production of “active” halogen compounds, e.g.,  $\text{Cl}_2$  and  $\text{HOCl}$ .<sup>1-4</sup> These “active” compounds are photolyzed by sunlight during early spring to yield radicals that efficiently destroy polar stratospheric ozone via gas-phase catalytic cycles.<sup>1-4</sup> Two general types of solid PSC particles are thought to exist composed primarily of nitric acid trihydrate (NAT) crystals (Type Ia PSCs) and of ice *Ih* crystals (Type II PSCs).<sup>1,2</sup> Another significant form of PSC is composed of droplets of supercooled  $\text{HNO}_3/\text{H}_2\text{SO}_4/\text{H}_2\text{O}$  ternary solutions (Type Ib PSCs).<sup>1,2</sup> One area of research interest in the atmospheric sciences is the molecular-level elucidation of chlorine-activation mechanisms, i.e., Rxs. (5.1) – (5.3), on solid PSC particle surfaces.



Chlorine activation on water-ice surfaces is currently being investigated most actively, due to the comparatively simple chemical composition of Type II PSC particles, which consist mainly of only one chemical species,  $\text{H}_2\text{O}$ . However, the detailed surface structure of water-ice crystals under stratospheric conditions, including, e.g., the degree and extent of reconstruction and surface disordering,<sup>5</sup> the surface density of dangling (non-hydrogen-bonding) OH groups,<sup>6</sup> and the occurrence frequency of defects,<sup>5</sup> is not well established. Consequently, the relative importance of the several proposed mechanisms for Rxs. (5.1)<sup>7-9</sup> and (5.3)<sup>10-23</sup> on Type II PSCs is still being debated. For Rx. (5.1), experimental findings on ice surfaces include cleavage of the Cl-ONO<sub>2</sub> bond,<sup>24</sup> the controversial “presence” of an  $\text{H}_2\text{OCl}^+$  intermediate,<sup>13,25,26</sup> and slow (~minutes) autocatalytic production of  $\text{HOCl}$  dependent on  $\text{ClONO}_2$  exposure;<sup>7</sup> and for Rx.

(5.3), experiments show the absence of surface HOCl<sup>7</sup> and prompt (~tens of milliseconds) appearance of Cl<sub>2</sub>.<sup>27</sup> For Rx. (5.3), surface dangling OH groups likely play a role in the formation of an H<sup>δ+</sup>••Cl<sup>δ-</sup> contact ion pair at sites on the ice surface which are reactive towards Cl<sup>δ+</sup>NO<sub>3</sub><sup>δ-</sup> (g), based on theoretical findings from our group and others.<sup>16,17,19,20</sup>

Progress towards understanding chlorine activation on Type Ia PSC particle surfaces, thought to be composed primarily of thermodynamically stable NAT crystals,<sup>28-30</sup> is not as advanced as that on Type II PSC particles, and the mechanism of Rx. (5.1) on NAT is presently unclear. Experimentally, the efficiency of Rx. (5.1) on NAT at a given temperature depends strongly on the relative humidity.<sup>3,4</sup> If the partial pressure of water vapor is adjusted to approach that of ice, the measured efficiency of Rx. (5.1) on NAT approaches ~1 % of that measured on ice, but as the relative humidity is decreased, the efficiency of Rx. (5.1) on NAT decreases by two orders of magnitude.<sup>31</sup> For a given partial pressure of water vapor, the temperature dependence of Rx. (5.1) on NAT may also be weakly negative.<sup>32</sup> Both dependences might be explained by the presence of H<sub>2</sub>O molecules adsorbed at the “neat” NAT surface.<sup>32,33</sup> Alternatively, the explanation may lie in a partially disordered “quasi-liquid” layer formed by incorporated H<sub>2</sub>O molecules, which may depend at a given temperature on the ambient H<sub>2</sub>O and HNO<sub>3</sub> partial pressures.<sup>15</sup> For a specified set of conditions, either “H<sub>2</sub>O-rich” or “HNO<sub>3</sub>-rich” NAT in equilibrium with ice *Ih* or nitric acid monohydrate (NAM), respectively, or an intermediate form may be present.<sup>15</sup> The *bulk* chemical composition of these different forms differs by arbitrarily small amounts from the stoichiometric 3:1 ratio, but the *surface* chemical compositions may be very different, a hypothesis that is compatible with the Gibbs phase rule.

Experiments indicate that the efficiency of Rx. (5.3) on NAT also exhibits a strong dependence on the relative humidity/H<sub>2</sub>O partial pressure, independent of the partial pressure of HCl: The dependences observed in flow-tube experiments by Abbatt and Molina<sup>31</sup> (202 K, 1 – 9 × 10<sup>-6</sup> Torr ClONO<sub>2</sub>, 4 – 10 × 10<sup>-6</sup> Torr HCl) and Hanson and Ravishankara<sup>34</sup> (191 K, ~2.5 – 5 × 10<sup>-8</sup> Torr ClONO<sub>2</sub>, 5 – 10 × 10<sup>-8</sup> Torr HCl) are quantitatively very similar despite the factor of 100 difference in partial pressures of HCl used. The (essentially identical) dependence on relative humidity observed in both experiments may be due to the varying affinity of HCl for the NAT surface depending on the availability of co-adsorbed H<sub>2</sub>O molecules. However, attempts to model this dependence using, e.g., a simple co-adsorption approach,<sup>35</sup> have not been successful.<sup>36</sup> Similar to the H<sub>2</sub>O partial pressure dependence of Rx. (5.3) on NAT, Rx. (5.3) on

NAT also depends on the HCl partial pressure at a given relative humidity: Abbatt and Molina<sup>31</sup> observe an enhancement by a factor of four of the efficiency of Rx. (5.3) on “HNO<sub>3</sub>-rich” NAT (H<sub>2</sub>O partial pressure of  $2.5 \times 10^{-4}$  Torr) when the partial pressure of HCl is increased from  $1.5$  to  $8 \times 10^{-5}$  Torr. The preceding summary of chlorine activation on NAT suggests the need for additional careful experimental studies of Rx. (5.1) – (5.3) on NAT over a range of stratospherically relevant conditions of temperature and HCl and H<sub>2</sub>O partial pressures.

A key step preceding Rx. (5.3) on NAT is the interaction of HCl with the NAT surface. An HCl surface coverage of  $8 \times 10^{13}$  to  $5 \times 10^{14}$  molecule/cm<sup>2</sup> was measured by Chu et al.<sup>37</sup> using an HCl partial pressure of  $4.5 \times 10^{-7}$  Torr and NAT substrates maintained at 188 K with surface compositions intermediate between “H<sub>2</sub>O-rich” and “HNO<sub>3</sub>-rich” forms. This range of surface coverage is comparable to that measured on water-ice surfaces, from  $2 \times 10^{13}$  to  $4 \times 10^{14}$  molecule/cm<sup>2</sup> (180 to ~220 K,  $10^{-9}$  –  $2 \times 10^{-5}$  Torr HCl).<sup>38-40</sup> On “HNO<sub>3</sub>-rich” NAT, the uptake of HCl is a linear function of the HCl partial pressure, ranging from  $8 \times 10^{12}$  to  $2 \times 10^{14}$  molecule/cm<sup>2</sup> ( $4 \times 10^{-6}$  –  $10^{-4}$  Torr HCl and  $5 \times 10^{-4}$  Torr H<sub>2</sub>O at 202 K).<sup>31</sup> At stratospherically relevant HCl partial pressures ( $10^{-8}$  –  $10^{-7}$  Torr HCl), a surface coverage of  $10^{10}$  –  $10^{11}$  molecule/cm<sup>2</sup> is estimated by linear extrapolation for this surface.

The state of HCl on NAT, i.e., molecularly or dissociatively adsorbed, is not known, because neither experimental nor theoretical studies have been performed to address this issue. Heterogeneous chlorine activation reactions involving HCl on water-ice surfaces are very rapid in comparison to the prohibitively slow gas-phase rates,<sup>4</sup> leading in the past to the suggestion that a mechanism with a low activation energy involving at least some degree of HCl dissociation is operative on ice surfaces. By contrast, the efficiency of Rx. (5.3) on “HNO<sub>3</sub>-rich” NAT is enhanced relative to the gas phase but is orders of magnitude smaller than on “H<sub>2</sub>O-rich” NAT or water ice, resulting perhaps from a less efficient mechanism with a higher activation energy that does not necessarily require the same degree of HCl dissociation as on ice surfaces, and/or from a lower reactant surface coverage.<sup>3,4</sup>

Theoretical studies utilizing periodic models of both the bulk and clean surface of NAM<sup>41,42</sup> as well as of bulk NAT<sup>43</sup> have provided a basis for understanding the interaction of HCl with the NAT surface and ultimately for detailed mechanistic studies of chlorine activation. While NAM is less atmospherically relevant, more extensive theoretical studies have been performed on this solid due to its smaller (and less anisotropic) unit cell and consequently greater

tractability. Poshusta et al.<sup>41</sup> obtained the first detailed theoretical description of bulk NAM using CRYSTAL92. Based on their finding that bulk NAM is composed of weakly bound puckered layers, a surface that exposes such a puckered layer was reasoned to have the minimum surface energy and hence be most prevalent. This surface (consisting of the [001] family of planes in the nonstandard  $P2_1cn$  space group) was characterized in order to predict favorable sites for physisorption and potentially important sites for surface catalysis. It was later suggested by Tóth<sup>42</sup> that this surface of NAM does not act catalytically, based on two sets of results using CPMD. First, from a few select geometry optimizations of HCl, ClONO<sub>2</sub>, and H<sub>2</sub>O placed initially at random positions on the (001) surface, small 0 K physisorption energies not corrected for zero-point energies were calculated (e.g., 15 kJ/mol for HCl). Second, no reasonable change in the adsorbate geometries was observed during a 0.5 ps CPMD simulation at 195 K.

It is unclear whether the findings of Tóth<sup>42</sup> apply as well to the crystalline NAT surface. Due to its larger unit cell size, there are very few (if any) published theoretical studies of the NAT surface or of chlorine activation on NAT surfaces; only recently have the structural, spectroscopic, and dynamic properties of bulk NAT been characterized theoretically.<sup>43</sup> These investigations would be relevant given the relative abundance (particularly in the Arctic) of Type Ia PSCs, which are observed at several degrees above the ice frost point. An additional caveat in performing theoretical studies on NAT is that the variety of possible adsorption sites is large (as discussed in section 5.3.1). High-level *ab initio* approaches using cluster models representative of the variety of adsorption sites would be impractical. Furthermore, no potentials are available that are parameterized for the study of crystalline NAT under any conditions, precluding classical simulation approaches. This article represents a needed initial effort towards elucidating theoretically the mechanism(s) of chlorine activation and parallels that of our recent studies of HCl interacting with ice *Ih*.<sup>16,17</sup>

## 5.2. THEORETICAL APPROACHES

### 5.2.1. Brief Description

For both geometry optimizations and simulations performed using the CPMD code,<sup>44</sup> the electronic state is described using density-functional theory with either the BLYP<sup>45,46</sup> or (when specified) the LDA<sup>47</sup> functional, atomic norm-conserving pseudopotentials,<sup>48</sup> and using only the

$\Gamma$  point for Brillouin-zone sampling. A plane-wave basis set with a 70 Ry cutoff (unless otherwise noted) is used.

The approaches implemented in CPMD for the geometry optimization of relevant test molecules, including  $\text{H}_2\text{O}$ ,  $(\text{H}_2\text{O})_2$ , HCl, and  $\text{HNO}_3$  (section 5.2.2), and for larger systems, including  $\text{HNO}_3\cdot\text{H}_2\text{O}$  (section 5.2.2), bulk NAT (section 5.2.2), the “neat” NAT surface (section 5.3.1), and HCl adsorbed on the “neat” NAT surface (section 5.3.2) are described in detail elsewhere.<sup>17</sup> For optimizing the geometry of HCl adsorbed on the “neat” NAT surface (section 5.3.2), we do not sample the  $3N-6$ -dimensional potential surface as thoroughly as either “simulated annealing”<sup>49</sup> (with a non-zero initial temperature and a scaling factor larger than 0.9 used here) or a highly methodical sampling (with respect to  $r$ ,  $\mathbf{q}$ , and  $\mathbf{f}$  of all possible configurations of adsorbed HCl interacting with each surface site) would. Our optimizations, however, are fully converged (to local minima) within a reasonable amount of computational time. We note that  $\text{HNO}_3\cdot\text{HCl}$  isomers (section 5.3.2) were optimized using Gaussian 94,<sup>50</sup> and a vibrational mode analysis was performed using a frequency scaling factor of 1.0119<sup>51</sup> which we verified yields reasonable vibrational spectra for  $\text{HCl}$ <sup>52</sup> and  $\text{HNO}_3$ .<sup>53</sup>

Three dynamical simulations using the Car-Parrinello technique<sup>54,55</sup> of HCl interacting with NAT (section 5.3.3) were performed at a simulation temperature of 155 K, as described in our study of surface disordering of an extended surface model of ice  $\bar{h}$  as a function of temperature.<sup>18</sup> The choice of 155 K, 40 K below the typical formation temperature (195 K) of Type Ia PSCs, was made based on an estimate<sup>18</sup> of 220 K for the melting point of an ice  $\bar{h}$  slab model which was not made rigorously<sup>56</sup> and is not considered precise.

### 5.2.2. Validation: Optimization of Relevant “Building Blocks” and Bulk NAT

As described elsewhere, the bond lengths and bond angles of  $\text{H}_2\text{O}$ ,<sup>57</sup>  $(\text{H}_2\text{O})_2$ ,<sup>57</sup> and  $\text{HCl}$ <sup>6</sup> are predicted to within a few hundredths of an Ångström and one degree of experimental values using CPMD with the BLYP functional. In addition, results for  $\text{H}_2\text{O}$ ,  $\text{HNO}_3$  and  $\text{HNO}_3\cdot\text{H}_2\text{O}$  (Figure 5.1), important “building blocks” in this study, are reported in Table 5.1. For  $\text{HNO}_3\cdot\text{H}_2\text{O}$ , geometry optimizations were performed both with the planarity of the ring constrained (by fixing the  $z$ -coordinates of all atoms except the free hydrogen of  $\text{H}_2\text{O}$  to zero) and with the ring free to relax (i.e., no constraints). These results are reported under the column



headings “fixed planar” and “fully relaxed,” respectively. Our computed geometries for H<sub>2</sub>O, HNO<sub>3</sub> and HNO<sub>3</sub>·H<sub>2</sub>O compare well to other theoretical predictions.<sup>42,58-60</sup> Our computed geometries also compare well to the experimental data for HNO<sub>3</sub>·H<sub>2</sub>O<sup>61</sup> (consistent with a structure that forms a planar, six-membered ring), HNO<sub>3</sub>,<sup>62</sup> and H<sub>2</sub>O.<sup>63</sup> For HNO<sub>3</sub>·H<sub>2</sub>O in particular, the six-membered ring formed by our optimized structure obtained without constraints is nearly planar (with absolute deviations of *z*-coordinates from zero of less than 0.06 Å), while the geometry is very similar and the binding energy of 35 kJ/mol is identical to that of the constrained structure. Our predicted binding energy for HNO<sub>3</sub>·H<sub>2</sub>O is similar to that reported by Tóth,<sup>42</sup> who also uses CPMD but with a smaller cutoff of 40.0 Ry and Vanderbilt ultrasoft pseudopotentials, and is slightly less than the value reported by Tao et al.<sup>58</sup> at the MP2 level of theory with a localized 6-311++G(2d,p) basis set and corrected for both zero-point energies and basis set superposition error. No experimental binding energy for HNO<sub>3</sub>·H<sub>2</sub>O is available.

<Table 5.1 and Figure 5.1 here>

The geometry of bulk crystalline NAT, modeled using a 128-atom, 1 × 1 × 2 arrangement of orthorhombic unit cells<sup>64</sup> periodically repeated *ad infinitum* (Figure 5.2), was optimized for a few selected values of the lattice constants. As for bulk ice *Ih*,<sup>16</sup> fractional cutoffs ranging from 70.000 – 70.070 Ry (BLYP) and 70.000 – 70.052 (LDA) were used in order to fix the basis set density, i.e., the number of plane waves per unit volume. For each optimization, each lattice constant was varied by the same percentage relative to the accepted experimental value at 85 K,<sup>64</sup> in increments of 2.5 %. We point out that the initial atomic coordinates were not simply “scaled,” but changed so as to preserve the space group P2<sub>1</sub>2<sub>1</sub>2<sub>1</sub> symmetry. A more thorough testing (i.e., varying *a*, *b*, and *c* independently in smaller increments) was not performed, because of computational cost. The most stable simulation cell obtained with the BLYP functional from a thermodynamic point of view is associated with lattice constants only 3.4 % greater than experiment,<sup>64</sup> at the minimum of the best-fit (*R*<sup>2</sup> = 0.999) quadratic curve in Figure 5.2. This result is reasonable given that BLYP, as a general rule, slightly overestimates lattice constants. In particular, it overestimates by slightly less than 3 % the *c* lattice constant of bulk ice *Ih*.<sup>16</sup> By contrast, the LDA functional generally

underestimates lattice constants, as our prediction in Figure 5.2 of lattice constants only 97.5 % of the experimental results at 85 K suggests.

<Figure 5.2 here>

The geometry of the BLYP-optimized simulation cell whose lattice constants are 2.5 % greater than experiment<sup>64</sup> compares satisfactorily with x-ray diffraction data<sup>64</sup> (Table 5.2 and Figure 5.3). The agreement is best for intramolecular distances and angles, i.e.,  $d_{\text{NO}}$  and  $\angle\text{ONO}$ , due to the fact that our lattice constants are larger than experiment, an overestimation that affects intermolecular distances and angles. Not shown in Table 5.2 is the fact that our calculated OH bond lengths, which correspond to predicted most probable internuclear distances, are 0.11 – 0.19 Å greater than the OH bond lengths determined by x-ray diffraction, which measures electron density distributions.<sup>65</sup> According to our calculations, the electron density forms a tear-shaped lobe with the base centered on the oxygen atom, which is the reason for the shorter experimentally determined OH bonds. We conclude that CPMD, which was also used successfully to describe both NAM<sup>42</sup> as well as NAT<sup>43</sup> by others and to study the interaction of HCl with ice *Ih* by our laboratory,<sup>16,17</sup> may be confidently used to study the interaction of HCl with NAT. The lowest energy simulation cells obtained with the BLYP and LDA functionals (with dimensions 9.722 Å × 15.051 Å × 7.043 Å and 9.247 Å × 14.317 Å × 6.699 Å, respectively) are our starting points for optimizing the surface.

<Table 5.2 and Figure 5.3 here>

### 5.3. RESULTS AND DISCUSSION

#### 5.3.1. Optimization of Low Index NAT Faces, and Selection and Analysis of the (001) Face

Different families of low index faces of NAT exhibit significantly different structure and polarity characteristics, e.g., the relatively smooth (010) face consists of a top layer of  $\text{H}_3\text{O}^+$  ions, while the jagged (100) face and the similarly rough (001) face consist of alternating  $\text{H}_3\text{O}^+$  ions,  $\text{NO}_3^-$  ions, and  $\text{H}_2\text{O}$  molecules at the surface. A detailed study of HCl adsorption on each low

index face of NAT would be extremely time consuming, given the large variety of possible adsorption sites, and would not be necessary if it were known which faces were most prevalent. At the melting point of  $-18.5\text{ }^{\circ}\text{C}$ , the growth of NAT crystals from solution occurs preferentially along the  $c$ -axis suggesting that [100] and [010] families of faces might be more relevant than the [001] family for crystals grown directly from the vapor phase under polar stratospheric conditions.<sup>64</sup> There may, however, be a growth-rate switchover at lower temperatures, similar to that observed in ice *Ih*: For ice *Ih* crystals grown directly from the vapor phase, the basal (0001) face is most relevant at temperatures below about  $-11\text{ }^{\circ}\text{C}$ , while the prism family of faces including [1000], [0100], and [0010] are more relevant at temperatures above  $-11\text{ }^{\circ}\text{C}$ .<sup>66,67</sup> One reason to believe a switchover may not occur in NAT is that ice *Ih* is structurally and chemically quite different. Experimental growth data as obtained for ice *Ih* are needed for confirmation.

In bulk NAT, longer (and therefore weaker) hydrogen bonds typically run along the crystal  $c$ -axis.<sup>64</sup> We predict, therefore, that the smallest amount of energy will be required to expand the space between two layers along the  $c$ -axis, or to cleave along this direction. Consequently, the [001] family of faces, from a thermodynamic point of view, is likely prevalent. This prediction was tested by optimizing the (100), ( $\bar{1}00$ ), (010), ( $0\bar{1}0$ ), (001) and ( $00\bar{1}$ ) faces of NAT (Figures 5.4 and 5.5).

<Table 5.3 and Figure 5.4 here>

Each face was modeled by adding a sufficiently large<sup>17</sup> surface vacuum region of  $8\text{ \AA}$  in the appropriate direction to the optimized bulk NAT simulation cell (section 5.2.2), applying periodic boundary conditions, and fixing underlying atoms to their bulk optimized positions in order to mimic the effects of an infinite bulk. Importantly, the same number of each chemical group (i.e.,  $\text{NO}_3^-$ ,  $\text{H}_3\text{O}^+$ , and  $\text{H}_2\text{O}$ ) was fixed making comparison between different faces possible. Fractional cutoffs of 70.010 – 70.060 Ry (BLYP) and 70.004 – 70.050 (LDA) were used in order to fix the basis set density, i.e., the number of plane waves per unit volume.<sup>16</sup> Interestingly, during optimizations with either functional, proton transfer at the (100), ( $\bar{1}00$ ), (010), and ( $0\bar{1}0$ ) faces is observed (Figure 5.4). This occurs in order to bring closer together oppositely charged  $\text{NO}_3^-$  and  $\text{H}_3\text{O}^+$  chemical groups. As expected, there is an energetic penalty

associated with the formation of each face examined (Table 5.3); furthermore, for a given face, the penalty obtained with the LDA functional is greater than that obtained with BLYP, due to the fact that LDA typically overestimates bond strengths, whereas BLYP typically (slightly) underestimates bond energies. The surface energy of either (001) or (00 $\bar{1}$ ) faces is smallest, as shown in Table 5.3, independent of functional. Consequently, out of the faces examined, we predict from a thermodynamic point of view that (001) or (00 $\bar{1}$ ) faces are favored (a conclusion further supported by results in Section 5.3.3). This prediction does not necessarily mean that (001) or (00 $\bar{1}$ ) faces of Type Ia PSC particles will be most prevalent in the polar stratosphere, because of the limited subset of faces examined, the role of surface defects in minimizing surface energy, and the fact that kinetic (rather than thermodynamic) barriers to growth determine relative face abundance. Furthermore, we select for detailed study HCl interacting with the (001) as opposed to the (00 $\bar{1}$ ) face, which does not have a surface dangling OH group. Subsequently, based on these results, we predict which sites on the (100), ( $\bar{1}00$ ), (010), and (0 $\bar{1}0$ ) faces are likely to exhibit a significant interaction with HCl and examine these sites.

<Figure 5.5 here>

The optimized geometry of the (001) face of NAT obtained with the BLYP functional is reported in Table 5.2. Surface reconstruction upon optimization is minor, as indicated by comparison of distances and angles to the bulk optimized structure. In order to predict favorable binding sites for HCl on the (001) face, and compare electronic properties of the surface and bulk, electron localization function<sup>68</sup> (*ELF*) isosurfaces were computed. The *ELF*, defined elsewhere,<sup>68</sup> is a measure of electron localization and does *not* depend on performing a unitary transformation to generate localized orbitals; such transformations of the (generally delocalized) canonical orbitals (of Hartree-Fock theory) are done in order to give a more intuitive feel for bonding but are non-unique and may result in qualitatively different views of certain bonding situations (i.e., the dichotomy between “ $\sigma$ - $\pi$ ” and “bent” multiple bonds).<sup>68</sup> The *ELF* ranges between 0 – 1, where a value of one indicates that the electron is most localized. Selected isosurfaces (*ELF* = 0.8 and 0.9) for the (001) face and bulk are shown in Figure 5.5. The *ELF* = 0.8 isosurfaces are halo-shaped and symmetrically centered about the oxygen atoms within the

crystal bulk (as observed in liquid water),<sup>69</sup> but not near the surface where they protrude into the vacuum in order to minimize electrostatic repulsions. The  $ELF = 0.9$  isosurfaces reveal the presence of two lobes on the oxygen atoms each corresponding to an electron lone pair. Extending our analysis of electronic properties, we note that the total electronic density of states for the (001) face and bulk are similar (Figure 5.6). The separation (of 9 eV) between groups of bands is characteristic of an insulating ionic solid; further insight may be gained by comparing Figure 5.6 to the qualitatively similar density of states obtained for NAM by Poshusta et al.<sup>41</sup>

<Figure 5.6 here>

### 5.3.2. Geometry and Energetics of Molecular HCl Adsorbed on NAT and Coverage Dependence

Optimized geometries and binding energies for HCl in 54 different initial configurations on the NAT (001) face (as modeled in section 5.3.1) were calculated. A systematic procedure for selecting initial configurations was adopted. First, complexes with HCl oriented approximately perpendicular to each chemical group (such as  $\text{NO}_3^-$  or  $\text{H}_2\text{O}$ ) that comprise the (001) surface were examined. Configurations with the  $\text{Cl}^\delta-$  of HCl interacting (as opposed to the  $\text{H}^\delta+$  of HCl interacting) with the surface were concluded to be at best only weakly binding, based on a few trial optimizations and results for HCl interacting with ice Ih,<sup>20,70</sup> and were thus ruled out. Also ruled out were configurations resulting in overcrowding or juxtaposition of like (atomic) charges. The HCl molecule was oriented always with the (slightly) positive end towards the surface, and positioned based on the charge of the interacting chemical group; for neutral  $\text{H}_2\text{O}$ , typical results<sup>17</sup> for the  $\text{HCl}\cdot\text{H}_2\text{O}$  complex were used ( $d_{\text{H}\cdots\text{O}} \sim 1.9 \text{ \AA}$  and  $\langle\text{ClHO} \sim 180^\circ$ ), while a somewhat longer or shorter hydrogen bond was chosen when the interacting chemical group was  $\text{H}_3\text{O}^+$  or  $\text{NO}_3^-$ , respectively. After all of the plausible so-called “90° orientations” were optimized, complexes with HCl oriented *roughly* 45° to each chemical group were sampled (i.e., with the  $\text{Cl}^\delta-$  of HCl able to form a hydrogen bond with the same or a different chemical group), following the same criteria. Chemical groups buried within the slab were ignored.

The 18 different configurations (out of 54 tested) resulting in a binding energy of at least 4 kJ/mol are shown in Figure 5.7. Examining the results, we note that there is only one configuration with a binding energy of 27 kJ/mol, approaching that of about 30 kJ/mol typically calculated<sup>17</sup> for HCl on ice *1h*; the next largest binding energy on a different NO<sub>3</sub><sup>-</sup> group is only 14 kJ/mol, while H<sub>2</sub>O and H<sub>3</sub>O<sup>+</sup> chemical groups form only weak ~10 kJ/mol hydrogen bonds with HCl. The variation in binding energy for a given chemical group (and between different chemical groups) is rationalized based on the different lengths of the H••O hydrogen bonds (which affects the strength of either the dipole-dipole or ion-dipole interactions), the different extents of surface distortion (relative to the isolated slab) that disrupt the surface bonding network, and (if applicable) the stabilizing influence of the Cl••H hydrogen bond. To gain further insight and examine the effect of increasing surface coverage, four additional two-adsorbate systems were generated (Figure 5.7), in each case by adding an HCl molecule to the HCl•NAT system with the largest binding energy, 27 kJ/mol. In two cases, the additional HCl molecule was placed on the same NO<sub>3</sub><sup>-</sup> ion, in one case on a nearby NO<sub>3</sub><sup>-</sup> ion, and in the final case on a nearby H<sub>2</sub>O molecule. In all four cases, the average binding energy of the optimized two-adsorbate systems (9, 14, 12, and 15 kJ/mol) is less than the sum-average of the binding energies of the individual HCl•NAT systems, i.e.,  $(27 + 11)/2 = 19$ ,  $(27 + 18)/2 = 23$ ,  $(27 + 12)/2 = 20$ , and  $(27 + 6)/2 = 17$  kJ/mol. Equivalently, for each two-adsorbate configuration, the binding energy calculated for HCl at the second (additional) site is either only slightly positive (either 0 or 2 kJ/mol) or actually negative (either -8 or -5 kJ/mol). The difference between the average HCl binding energy and the sum-average of the individual HCl binding energies is smallest when the two HCl molecules are adsorbed on different chemical groups, as one would expect. We conclude that intramolecular sites near the 27-kJ/mol binding site compete very unfavorably for HCl, and that only one site on the (001) surface exhibits a high affinity for HCl.

<Figure 5.7 here>

The site that exhibits the greatest affinity for HCl on the (001) face involves the interaction of molecular HCl with a NO<sub>3</sub><sup>-</sup> ion as well as with the dangling OH group of a nearby H<sub>2</sub>O molecule. On the (100) face, there are two NO<sub>3</sub><sup>-</sup> ions (per simulation cell) that would allow HCl to interact simultaneously with *two* dangling OH groups, forming a NO<sub>3</sub><sup>-</sup>••HCl••2H<sub>2</sub>O

complex that would be less bent (and consequently more stable) than analogous complexes formed on other faces, i.e., (010). As observed on ice *Ih*,<sup>16,17</sup> increasing the number of surface dangling OH groups may lead to a greater binding energy and ultimately partial dissociation of HCl. Two trial configurations of HCl at a binding site on the (100) face were optimized (Figure 5.8). The results in Figure 5.8 indicate that there are potential surface sites involving two dangling OH groups that show a high affinity for HCl. However, our 23-kJ/mol configuration involving two interacting dangling OH groups (Figure 5.8) is lower in energy than the 27-kJ/mol configuration depicted in Figure 5.7, despite the additional Cl...H hydrogen bond.

<Figure 5.8 here>

Before concluding this section, we note that in order to obtain binding energies or enthalpies at 190 K, a total correction (including zero-point energies) to the values in Figures 5.7 and 5.8 of either  $-5$  to  $-4$  kJ/mol or  $-3$  to  $-2$  kJ/mol, respectively, as the strength of the Cl...H hydrogen bond increases is estimated. These correction estimates are based on the actual corrections calculated for two gas-phase  $\text{HNO}_3 \cdot \text{HCl}$  complexes with the optimized structures at the BLYP level of theory with a 6-311++G(d,p) basis set shown in Figure 5.9. We note that our calculated corrections (and binding energies) for the  $\text{HNO}_3 \cdot \text{HCl}$  complexes are of the same order of magnitude as those obtained in a recent theoretical study of the stability of hydrogen-bonded complexes of  $\text{HNO}_3$  with various bases.<sup>71</sup>

<Figure 5.9 here>

### 5.3.3. Car-Parrinello Molecular Dynamics of Molecular HCl Adsorbed on NAT

In order to investigate the atmospheric fate of HCl, three CPMD simulations were performed (Figure 5.10). The first simulation was performed with HCl initially adsorbed at the 27-kJ/mol binding site with one dangling OH group on the (001) face. During this simulation, the HCl bond length does not change by more than several hundredths of an Ångstrom from its equilibrium value of  $1.38 \text{ \AA}$ , and the HCl molecule remains hydrogen-bonded to the  $\text{NO}_3^-$  ion; however, the HCl molecule frequently breaks and re-forms its single Cl...H hydrogen bond with

H<sub>2</sub>O (Figure 5.10a). We emphasize that HCl forms at most a single Cl...H hydrogen bond at any time during the simulation, and always with the same H<sub>2</sub>O molecule. Our results suggest that dissociation of adsorbed HCl on the (001) face is not kinetically rapid, although we note that only one trajectory was obtained, and it is possible (although not expected) that there are additional paths that are significant at  $\geq 1$  ps time scales.

<Figure 5.10 here>

As the intermolecular atomic distances in Figure 5.10a imply, the (001) surface of NAT is quite dynamic and expands by 3 – 4 Å in the *c*-direction at 155 K. The expansion observed during the simulation likely arises from the comparatively weaker hydrogen binding along the *c*-axis and the fact that the BLYP functional underestimates hydrogen bond strengths, e.g., that of (H<sub>2</sub>O)<sub>2</sub>.<sup>57</sup> In order to test this hypothesis, a second (otherwise identical) simulation was performed using the LDA functional. The intermolecular atomic distances are more “well behaved” (Figure 5.10b) and expansion is not observed, verifying our hypothesis. Sharing of the H<sup>δ+</sup> of HCl between C<sup>δ-</sup> and NO<sub>3</sub><sup>-</sup> is observed during this simulation, although the HCl bond length (1.5 Å) is still considerably shorter than that obtained<sup>16</sup> with BLYP when HCl partially dissociates on ice *Ih* when interacting with two dangling OH groups (1.8 Å). This sharing occurs because the H••O and Cl...H hydrogen bond strengths are likely overestimated, compensating for the fact that LDA yields  $D_e = 483$  kJ/mol for HCl(g) → H(g) + Cl(g) compared to the BLYP value<sup>16</sup> of  $D_e = 421$  kJ/mol and the experimental value<sup>52,72</sup> of  $D_o = 428$  kJ/mol (an estimate of the experimental dissociation energy of adsorbed HCl on ice, which includes zero-point energies). Lastly, a third simulation was performed with HCl initially adsorbed at the 23-kJ/mol binding site with two dangling OH groups on the (100) face (Figure 5.8) using the BLYP functional. During the simulation, appreciable expansion of NAT along the *a*-axis is not observed. Interestingly, HCl does not interact with either dangling OH group (Figure 5.10c), preferring instead a perpendicular surface orientation, suggesting that dissociation of HCl on the (100) face is not kinetically rapid.

In order to test whether or not dissociation of adsorbed HCl on NAT is thermodynamically favorable, the 27-kJ/mol binding site depicted in Figure 5.7 was modified by cleaving the HCl bond and forming an O<sub>3</sub>NH...Cl...H<sub>2</sub>O complex as part of the NAT (001)



surface (with  $d_{\text{O}_3\text{N}\cdots\text{H}} = 1.00 \text{ \AA}$ ,  $d_{\text{H}\cdots\text{Cl}} = 1.96 \text{ \AA}$ ,  $d_{\text{Cl}\cdots\text{H}} = 2.10 \text{ \AA}$ , and  $\angle\text{OHCl} = 174.8^\circ$ ). The  $\text{HNO}_3$  comprising the  $\text{O}_3\text{NH}\cdots\text{Cl}\cdots\text{H}_2\text{O}$  complex was nearly planar, with a geometry that was similar to gas-phase  $\text{HNO}_3$ , and was not significantly strained. A geometry optimization was subsequently performed. During the optimization, a single proton transfer was observed, reforming the 27-kJ/mol binding site with slightly different geometric parameters (i.e.,  $d_{\text{O}_3\text{N}\cdots\text{H}} = 1.56 \text{ \AA}$ ,  $d_{\text{HCl}} = 1.38 \text{ \AA}$ ,  $d_{\text{Cl}\cdots\text{H}} = 2.10 \text{ \AA}$ , and  $\angle\text{OHCl} = 172.9^\circ$ ) but the same binding energy, thereby demonstrating that (partially) dissociated HCl readily reforms molecular HCl at this binding site.

#### 5.4. ATMOSPHERIC IMPLICATIONS

As pointed out in the Introduction, experimental studies indicate that the surface coverage of HCl on “ $\text{HNO}_3$ -rich” NAT is likely at least one order of magnitude less than that measured on either forms of NAT intermediate between “ $\text{HNO}_3$ -rich” and “ $\text{H}_2\text{O}$ -rich” or on ice *Ih*. This is consistent with our theoretical finding that only one adsorption site on the (likely prevalent) NAT (001) face results in appreciable binding, implying a lower surface coverage of HCl on “ $\text{HNO}_3$ -rich” NAT. Only one site on the NAT (001) face forms a hydrogen bond of appreciable energy (27 kJ/mol) with HCl, whereas on ice *Ih* it was shown<sup>17</sup> that three sites on the ice *Ih* (0001) face interact as strongly with HCl. Based on the dimensions of our PSC particle simulation cells, we estimate a saturated surface coverage of  $s_0 = 1/(9.722 \text{ \AA} \times 15.051 \text{ \AA}) = 6.8 \times 10^{13}$  molecule/cm<sup>2</sup> on the NAT (001) face, but a larger value of  $s_0 = 3/(9.046 \text{ \AA} \times 9.046 \text{ \AA} \times \sin 60^\circ) = 4.2 \times 10^{14}$  molecule/cm<sup>2</sup> on the ice *Ih* (0001) face. Note that we assume  $\Delta H_{ads} \sim 25$  kJ/mol for each surface in contrast to an early estimate of  $\sim 74$  kJ/mol on ice *Ih* and “ $\text{H}_2\text{O}$ -rich” NAT and  $\sim 54$  kJ/mol on “ $\text{HNO}_3$ -rich” NAT.<sup>73</sup> We also are able to explain why the surface coverage on NAT approaches that on ice *Ih* as the relative humidity increases: The number of adsorption sites on “ $\text{H}_2\text{O}$ -rich” NAT which are able to form a  $\text{Cl}\cdots\text{H}$  hydrogen bond (with HCl and the dangling OH group of an  $\text{H}_2\text{O}$  molecule either adsorbed on or incorporated into the surface) will be greater.

An increased surface coverage of HCl on “ $\text{H}_2\text{O}$ -rich” NAT may explain at least partially the rate enhancement of chlorine activation on “ $\text{H}_2\text{O}$ -rich” NAT and water ice. Chlorine activation on “ $\text{HNO}_3$ -rich” NAT is still appreciable compared to the prohibitively slow gas-phase reaction between closed-shell molecules. Our results in section 5.3.3 suggest that molecular HCl adsorbed at the NAT surface is predominant. By contrast, two dangling OH groups at the ice *Ih*

(0001) face interacting strongly with adsorbed HCl induce partial dissociation that is both kinetically rapid and thermodynamically favorable.<sup>16</sup> While dissociation of adsorbed HCl is not expected at the “HNO<sub>3</sub>-rich” NAT surface, other pathways for lowering the activation energy of Rx. (5.3) are possible: HCl incorporation into the NAT bulk and subsequent ionization following the proposed mechanism on ice *I<sub>h</sub>* by Hynes and co-workers<sup>10-12</sup> (involving a concerted proton transfer) may be one mechanism. Other possibilities are that adsorbed HCl is partially dissociated via the interaction of adsorbed HCl with nearby dangling OH groups in NAT surface defect regions. On “H<sub>2</sub>O-rich” NAT, HCl probably interacts with co-adsorbed H<sub>2</sub>O molecules. Additional theoretical studies are needed in order to verify these possibilities.

## 5.5. CONCLUSIONS

The NAT bulk and low index faces were modeled and characterized theoretically, and the adsorption and dynamics of HCl on (001) and (100) faces fully representative of the variety of adsorption sites on NAT were investigated. Only one site per simulation cell on the thermodynamically likely (001) face exhibits a high affinity for HCl, resulting in the formation of a NO<sub>3</sub><sup>-</sup>••HCl••H<sub>2</sub>O surface binding complex, with an uncorrected binding energy of 27 kJ/mol and a binding energy and enthalpy at 190 K corrected for zero-point energies of 23 and 25 kJ/mol, respectively. The HCl surface coverage on the (001) face of “HNO<sub>3</sub>-rich” NAT is estimated to be lower than that on “H<sub>2</sub>O-rich” NAT and ice *I<sub>h</sub>*, qualitatively consistent with experimental studies of HCl uptake on these surfaces and rates of chlorine activation, i.e., Rx. (5.3). A different site on the (100) face with two nearby dangling OH groups also exhibits a high affinity for HCl, resulting in a NO<sub>3</sub><sup>-</sup>••HCl••2H<sub>2</sub>O complex. However, during Car-Parrinello MD simulations at either high affinity site, dissociation of HCl is not observed, suggesting that a molecular form of adsorbed HCl is preferred kinetically. Additionally, dissociated HCl re-forms molecular HCl, suggesting that the molecular form is also preferred thermodynamically. Chlorine activation on NAT may occur solely as a result of HCl dissociation in the bulk, at surface defects, or in the presence of co-adsorbed H<sub>2</sub>O molecules (not considered in this study), in contrast to ice *I<sub>h</sub>*, for which HCl dissociation on/atop the (0001) face is also predicted.

## 5.6. ACKNOWLEDGMENTS

This work was partially supported by the NASA Upper Atmospheric Research Program (Grant No. NAG5-8887). Y.A.M. acknowledges partial support from the MIT Center for Global Change Sciences. This work was partially supported by the National Computational Science Alliance under a Boston University MARINER/Alliance startup allocation (Project No. 60390) and under Proposal No. CTS990016Nr01 and CHE010020N and utilized the Boston University SGI/CRAY Origin2000 and the NCSA SGI/CRAY Origin2000, respectively.

## REFERENCES FOR CHAPTER 5

- (1) Seinfeld, J. H.; Pandis, S. N. *Atmospheric Chemistry and Physics: From Air Pollution to Climate Change*; Wiley: New York, 1998.
- (2) Solomon, S. *Rev. Geophys.* **1999**, *37*, 275.
- (3) Sander, S. P.; Friedl, R. R.; DeMore, W. B.; Golden, D. M.; Kurylo, M. J.; Hampson, R. F.; Huie, R. E.; Moortgat, G. K.; Ravishankara, A. R.; Kolb, C. E.; Molina, M. J. *Chemical Kinetics and Photochemical Data for Use in Stratospheric Modeling, Supplement to Evaluation 12: Update of Key Reactions*; Jet Propulsion Laboratory: Pasadena, CA, 2000.
- (4) DeMore, W. B.; Sander, S. P.; Golden, D. M.; Hampson, R. F.; Kurylo, M. J.; Howard, C. J.; Ravishankara, A. R.; Kolb, C. E.; Molina, M. J. *Chemical Kinetics and Photochemical Data for Use in Stratospheric Modeling*; Jet Propulsion Laboratory: Pasadena, CA, 1997.
- (5) Petrenko, V. F.; Whitworth, R. W. *Physics of Ice*; Oxford University Press: New York, 1999.
- (6) Schaff, J. E.; Roberts, J. T. *J. Phys. Chem.* **1994**, *98*, 6900.
- (7) Geiger, F. M.; Pibel, C. D.; Hicks, J. M. *J. Phys. Chem. B* **2001**, *105*, 4940.
- (8) Bianco, R.; Hynes, J. T. *J. Phys. Chem. A* **1998**, *102*, 309.
- (9) McNamara, J. P.; Hillier, I. H. *J. Phys. Chem. A* **1999**, *103*, 7310.
- (10) Gertner, B. J.; Hynes, J. T. *Science* **1996**, *271*, 1563.
- (11) Gertner, B. J.; Hynes, J. T. *Faraday Discuss.* **1998**, *110*, 301.
- (12) Bianco, R.; Hynes, J. T. *J. Phys. Chem. A* **1999**, *103*, 3797.
- (13) Bianco, R.; Thompson, W. H.; Morita, A.; Hynes, J. T. *J. Phys. Chem. A* **2001**, *105*, 3132.
- (14) McNamara, J. P.; Tresadern, G.; Hillier, I. H. *J. Phys. Chem. A* **2000**, *104*, 4030.
- (15) Molina, M. J. The probable role of stratospheric 'ice' clouds: Heterogeneous chemistry of the 'ozone hole'. In *The Chemistry of the Atmosphere: Its Impact on Global Change*; Calvert, J. G., Ed.; Blackwell Scientific Publications: Oxford, 1994; p. 27.
- (16) Mantz, Y. A.; Geiger, F. M.; Molina, L. T.; Molina, M. J.; Trout, B. L. *Chem. Phys. Lett.* **2001**, *348*, 285.
- (17) Mantz, Y. A.; Geiger, F. M.; Molina, L. T.; Molina, M. J.; Trout, B. L. *J. Phys. Chem. A* **2001**, *105*, 7037.

- (18) Mantz, Y. A.; Geiger, F. M.; Molina, L. T.; Molina, M. J.; Trout, B. L. *J. Chem. Phys.* **2000**, *113*, 10733.
- (19) Bolton, K.; Pettersson, J. B. C. *J. Am. Chem. Soc.* **2001**, *123*, 7360.
- (20) Svanberg, M.; Pettersson, J. B. C.; Bolton, K. *J. Phys. Chem. A* **2000**, *104*, 5787.
- (21) Mebel, A. M.; Morokuma, K. *J. Phys. Chem.* **1996**, *100*, 2985.
- (22) Haas, B.-M.; Crellin, K. C.; Kuwata, K. T.; Okumura, M. *J. Phys. Chem.* **1994**, *98*, 6740.
- (23) Van Doren, J. M.; Viggiano, A. A.; Morris, R. A. *J. Am. Chem. Soc.* **1994**, *116*, 6957.
- (24) Hanson, D. R. *J. Phys. Chem.* **1995**, *99*, 13059.
- (25) Sodeau, J. R.; Horn, A. B.; Banham, S. F.; Koch, T. G. *J. Phys. Chem.* **1995**, *99*, 6258.
- (26) Horn, A. B.; Sodeau, J. R.; Roddis, T. B.; Williams, N. A. *J. Chem. Soc., Faraday Trans.* **1998**, *94*, 1721.
- (27) Oppliger, R.; Allanic, A.; Rossi, M. J. *J. Phys. Chem. A* **1997**, *101*, 1903.
- (28) Hanson, D.; Mauersberger, K. *Geophys. Res. Lett.* **1988**, *15*, 855.
- (29) Worsnop, D. R.; Fox, L. E.; Zahniser, M. S.; Wofsy, S. C. *Science* **1993**, *259*, 71.
- (30) Tolbert, M. A.; Toon, O. B. *Science* **2001**, *292*, 61.
- (31) Abbatt, J. P. D.; Molina, M. J. *J. Phys. Chem.* **1992**, *96*, 7674.
- (32) Barone, S. B.; Zondlo, M. A.; Tolbert, M. A. *J. Phys. Chem. A* **1997**, *101*, 8643.
- (33) Henson, B. F.; Wilson, K. R.; Robinson, J. M. *Geophys. Res. Lett.* **1996**, *23*, 1021.
- (34) Hanson, D. R.; Ravishankara, A. R. *J. Geophys. Res.* **1993**, *98D*, 22931.
- (35) Carslaw, K. S.; Peter, T. *Geophys. Res. Lett.* **1997**, *24*, 1743.
- (36) Peter, T. *Annu. Rev. Phys. Chem.* **1997**, *48*, 785.
- (37) Chu, L. T.; Leu, M. T.; Keyser, L. F. *J. Phys. Chem.* **1993**, *97*, 7779.
- (38) Lee, S.-H.; Leard, D. C.; Zhang, R.; Molina, L. T.; Molina, M. J. *Chem. Phys. Lett.* **1999**, *315*, 7.
- (39) Leu, M.-T.; Keyser, L. F.; Timonen, R. S. *J. Phys. Chem. B* **1997**, *101*, 6259.
- (40) Foster, K. L.; Tolbert, M. A.; George, S. M. *J. Phys. Chem. A* **1997**, *101*, 4979.
- (41) Poshusta, R. D.; Tseng, D. C.; Hess, A. C.; McCarthy, M. I. *J. Phys. Chem.* **1993**, *97*, 7295.
- (42) Tóth, G. *J. Phys. Chem. A* **1997**, *101*, 8871.
- (43) Sullivan, D. M.; Bagchi, K.; Tuckerman, M. E.; Klein, M. L. *J. Phys. Chem. A* **1999**, *103*, 8678.
- (44) Hutter, J.; Alavi, A.; Deutsch, T.; Bernasconi, M.; Goedecker, St.; Marx, D.; Tuckerman, M.; Parrinello, M. *CPMD*; Max-Planck Institut für Festkörperforschung and IBM Zurich Research Laboratory, 1995-99.
- (45) Becke, A. D. *Phys. Rev. A* **1988**, *38*, 3098.
- (46) Lee, C.; Yang, W.; Parr, R. G. *Phys. Rev. B* **1988**, *37*, 785.
- (47) Goedecker, S.; Teter, M. P.; Hutter, J. *Phys. Rev. B* **1996**, *54*, 1703.
- (48) Troullier, N.; Martins, J. L. *Phys. Rev. B* **1991**, *43*, 1993.
- (49) Kirkpatrick, S.; Gelatt, C. D., Jr.; Vecchi, M. P. *Science* **1983**, *220*, 671.
- (50) Frisch, M. J.; Trucks, G. W.; Schlegel, H. B.; Gill, P. M. W.; Johnson, B. G.; Robb, M. A.; Cheeseman, J. R.; Keith, T. A.; Petersson, G. A.; Montgomery, J. A.; Raghavachari, K.; Al-Laham, M. A.; Zakrzewski, V. G.; Ortiz, J. V.; Foresman, J. B.; Cioslowski, J.; Stefanov, B. B.; Nanayakkara, A.; Challacombe, M.; Peng, C. Y.; Ayala, P. Y.;

Chen, W.; Wong, M. W.; Andres, J. L.; Replogle, E. S.; Gomperts, R.; Martin, R. L.; Fox, D. J.; Binkley, J. S.; Defrees, D. J.; Baker, J.; Stewart, J. P.; Head-Gordon, M.; Gonzalez, C.; Pople, J. A. *Gaussian 94 (Revision E.3)*; Gaussian, Inc.: Pittsburgh, PA, 1995.

(51) Wong, M. W. *Chem. Phys. Lett.* **1996**, 256, 391.

(52) Huber, K. P.; Herzberg, G. *Molecular Spectra and Molecular Structure IV. Constants of Diatomic Molecules*; Van Nostrand: New York, 1979.

(53) McGraw, G. E.; Bernitt, D. L.; Hisatsune, I. C. *J. Chem. Phys.* **1965**, 42, 237.

(54) Car, R.; Parrinello, M. *Phys. Rev. Lett.* **1985**, 55, 2471.

(55) Marx, D.; Hutter, J. Ab initio molecular dynamics: Theory and implementation. In *Modern Methods and Algorithms of Quantum Chemistry*; Grotendorst, J., Ed.; John von Neumann Institute for Computing: Jülich, 2000; Vol. NIC Series, Vol. 1; p. 301.

(56) Sugino, O.; Car, R. *Phys. Rev. Lett.* **1995**, 74, 1823.

(57) Sprik, M.; Hutter, J.; Parrinello, M. *J. Chem. Phys.* **1996**, 105, 1142.

(58) Tao, F.-M.; Higgins, K.; Klemperer, W.; Nelson, D. D. *Geophys. Res. Lett.* **1996**, 23, 1797.

(59) Donaldson, D. J.; Orlando, J. J.; Amann, S.; Tyndall, G. S.; Proos, R. J.; Henry, B. R.; Vaida, V. *J. Phys. Chem. A* **1998**, 102, 5171.

(60) Staikova, M.; Donaldson, D. J. *Phys. Chem. Chem. Phys.* **2001**, 3, 1999.

(61) Canagaratna, M.; Phillips, J. A.; Ott, M. E.; Leopold, K. R. *J. Phys. Chem. A* **1998**, 102, 1489.

(62) Cox, A. P.; Ellis, M. C.; Attfield, C. J.; Ferris, A. C. *J. Mol. Struct.* **1994**, 320, 91.

(63) Benedict, W. S.; Gailer, N.; Plyler, E. K. *J. Chem. Phys.* **1956**, 24, 1139.

(64) Taesler, I.; Delaplane, R. G.; Olovsson, I. *Acta Crystallogr.* **1975**, B31, 1489.

(65) Goto, A.; Hondah, T.; Mae, S. *J. Chem. Phys.* **1990**, 93, 1412.

(66) Colbeck, S. C. *J. Cryst. Growth* **1985**, 72, 726.

(67) Hobbs, P. V. *Ice Physics*; Clarendon Press: Oxford, 1974.

(68) Becke, A. D.; Edgecombe, K. E. *J. Chem. Phys.* **1990**, 92, 5397.

(69) Trout, B. L.; Parrinello, M. *J. Phys. Chem. B* **1999**, 103, 7340.

(70) Kroes, G.-J.; Clary, D. C. *J. Phys. Chem.* **1992**, 96, 7079.

(71) Dimitrova, Y. *J. Mol. Struct. (Theochem)* **2000**, 532, 41.

(72) Dunning, T. H., Jr. *J. Phys. Chem.* **1984**, 88, 2469.

(73) Tabazadeh, A.; Turco, R. P. *J. Geophys. Res.* **1993**, 98D, 12727.

**TABLE 5.1. Optimized geometry and binding energy of HNO<sub>3</sub>•H<sub>2</sub>O, and geometries of isolated HNO<sub>3</sub> and H<sub>2</sub>O (Bond Lengths in Å, Bond Angles in Degrees, Binding Energy in kJ/mol, and Uncertainty in Parenthesis)**

parameter (Fig. 5.1)	BLYP/PW <sup>a</sup>		BLYP/PW <sup>b</sup>		MP2/6-311++G(2d,p) <sup>c</sup>		experiment		
	fixed planar	fully relaxed	HNO <sub>3</sub> or H <sub>2</sub> O	fully relaxed	HNO <sub>3</sub> or H <sub>2</sub> O	fully relaxed	HNO <sub>3</sub> or H <sub>2</sub> O	HNO <sub>3</sub> •H <sub>2</sub> O <sup>d</sup>	HNO <sub>3</sub> <sup>e</sup> or H <sub>2</sub> O <sup>f</sup>
r(NO <sub>cis</sub> )	1.24	1.24	1.23	1.28	1.27	1.23	1.22		1.213(2)
r(NO <sub>trans</sub> )	1.22	1.22	1.22	1.26	1.26	1.21	1.21		1.198(2)
r(N-O'H)	1.43	1.43	1.49	1.45	1.49	1.38	1.41		1.410(2)
r(O'H)	1.01	1.01	0.98	1.03	1.00	1.00	0.98		0.941(3)
<O <sub>cis</sub> NO <sub>trans</sub>	128.8	128.7	131.5			128.5	130.5		130.2(2)
<O <sub>cis</sub> NO'	116.7	116.7	115.3			116.9	115.7		115.7(2)
<O'NO <sub>trans</sub>	114.5	114.5	113.2			104.2	102.2		114.1(2)
<NO'H	104.4	104.1	101.8	104.1	102.3				102.6(3)
r <sub>w</sub> (OH)	0.97	0.97	0.97	0.99	0.99	0.96	0.96		0.9572(3)
<HOH	106.2	106.4	104.4	105.4	103.8	106.1	104.6		104.52(5)
R	1.69	1.70				1.71		1.779(33)	
α	178.5	176.0		173.8		176.4		174.50(41)	
β	102.7	103.2				101.3		92(8)	
φ	45.9					49.9		30(10)	
R <sub>sec</sub>	2.61	2.57				2.4		2.30	
θ	106.1	105.7				~105		119.3	
BE <sup>g</sup>	- ? E <sub>e</sub> <sup>B</sup> = 35			- ? E <sub>e</sub> <sup>B</sup> = 32		- ? E <sub>o</sub> <sup>B</sup> = 41			

<sup>a</sup> This work. <sup>b</sup> Reference 42. <sup>c</sup> Reference 58. <sup>d</sup> Reference 61. <sup>e</sup> Reference 62. <sup>f</sup> Reference 63. <sup>g</sup> Computed either with (- ? E<sub>o</sub><sup>B</sup>) or without (- ? E<sub>e</sub><sup>B</sup>) zero-point energies taken into account and with the counterpoise correction for basis set superposition error (which is equal to zero in plane-wave calculations).

**TABLE 5.2. NAT experimental and calculated bulk and (001) face geometries (d's in Å, a's in Degrees)**

parameter (Fig. 5.3)	experiment <sup>a</sup>	bulk	(001) face
d1 (d <sub>NO</sub> )	1.256(2)	1.28	1.28
d2	1.247(2)	1.27	1.27
d3	1.265(2)	1.29	1.29
d4 (d <sub>OO</sub> )	2.798(2)	2.84	2.84
d5	2.755(2)	2.76	2.77
d6	2.800(2)	2.81	2.83
d7	2.576(2)	2.60	2.59
d8	2.626(2)	2.62	2.63
d9	2.482(2)	2.50	2.52
d10	2.809(2)	2.80	2.80
a1 (<ONO)	120.3(1)	120.3	120.3
a2	121.2(1)	121.4	121.4
a3	118.5(1)	118.4	118.3
a4 (<NOO)	109.9(1)	114.9	114.6
a5	106.6(1)	110.9	110.9
a6	110.0(1)	112.3	112.2
a7	116.9(1)	109.2	109.2
a8 (<OOO)	133.0(1)	138.0	138.1
a9	115.5(1)	113.6	113.1
a10	127.2(1)	126.3	126.6
a11	102.1(1)	97.5	97.6
a12	102.1(1)	105.9	105.9
a13	118.2(1)	120.2	120.3
a14	91.6(1)	91.3	91.3
a15	103.1(1)	104.3	104.0
a16	112.8(1)	113.9	113.8
a17	116.8(1)	119.7	119.5
a18	122.7(1)	121.4	120.1
a19	99.6(1)	105.7	105.6
a20	124.4(1)	121.3	121.4

<sup>a</sup> Reference 64.

**TABLE 5.3. Calculated destabilization energies per unit area of optimized faces relative to bulk NAT**

face	func-tional	cell dimensions			area ( $\text{\AA}^2$ )	DE
		x ( $\text{\AA}$ )	y ( $\text{\AA}$ )	z ( $\text{\AA}$ )		$\left(\frac{\text{kJ/mol}}{\text{\AA}^2}\right)$
(100)	BLYP	17.72	15.05	7.04	106	4.49
	LDA	17.25	14.32	6.70	96	6.54
$\bar{1}00$	BLYP	17.72	15.05	7.04	106	4.49
	LDA	17.25	14.32	6.70	96	6.54
(010)	BLYP	9.72	23.05	7.04	68	3.14
	LDA	9.25	22.32	6.70	62	5.38
$0\bar{1}0$	BLYP	9.72	23.05	7.04	68	3.11
	LDA	9.25	22.32	6.70	62	5.38
(001)	BLYP	9.72	15.05	15.04	146	0.43
	LDA	9.25	14.32	14.70	132	2.40
$00\bar{1}$	BLYP	9.72	15.05	15.04	146	0.43
	LDA	9.25	14.32	14.70	132	2.40



## LIST OF FIGURES FOR CHAPTER 5

Figure 5.1. Labels and definitions of geometric parameters for  $\text{HNO}_3 \cdot \text{H}_2\text{O}$

Figure 5.2. Six-cell periodic representations of our optimized bulk crystalline NAT simulation cell shown from orthogonal perspectives. Plotted are the energies in kJ/mol relative to the most stable simulation cell obtained with either the BLYP or LDA functional as a function of relative lattice constants.

Figure 5.3. Labels and definitions of geometric parameters for our crystalline NAT simulation cell

Figure 5.4. Simulation-cell depictions of four optimized NAT faces. Proton transfers from the surface  $\text{H}_3\text{O}^+$  to an underlying  $\text{H}_2\text{O}$  molecule yield  $\text{NO}_3^- \cdot \text{H}_3\text{O}^+ \cdot \text{H}_2\text{O}$  complexes (dash-enclosed).

Figure 5.5. Two-simulation-cell periodic representation of the optimized NAT (001) face, and ELF isosurfaces for this face and bulk

Figure 5.6. Density of states calculated for the NAT (001) face and bulk. A bin size of 0.3 eV was used.

Figure 5.7. Optimized configurations of one HCl placed in 18 different configurations and two HCl's in four configurations on the NAT (001) face. Only chemical moieties involved in binding to HCl are shown; the rest of the face is omitted. Specified are  $d_{\text{HCl}} = 1.31 - 1.42 \text{ \AA}$ ,  $d_{\text{H}\cdots\text{O}} = 1.47 - 2.30 \text{ \AA}$ ,  $\angle\text{ClHO} = 132.0 - 175.2^\circ$ , and  $d_{\text{Cl}\cdots\text{H}} = 2.09 - 3.09 \text{ \AA}$ ; italicized values were obtained with the LDA (as opposed to BLYP) functional. Binding energies at 0 K are specified with respect to HCl and the isolated slab, i.e.,  $\text{HCl} + \text{NAT} ? \text{HCl} \cdot \text{NAT}$  or  $2\text{HCl} + \text{NAT} ? 2\text{HCl} \cdot \text{NAT}$ , and are not corrected for zero-point energies, estimated to be  $-4$  to  $-5$  kJ/mol.

Figure 5.8. Optimized configurations of one HCl placed in two different configurations on the NAT (100) face. See the caption of Figure 7 for additional details. Specified are  $d_{\text{HCl}} = 1.33 \text{ \AA}$ ,  $d_{\text{H}\cdots\text{O}} = 1.96 \text{ or } 2.09 \text{ \AA}$ ,  $\angle\text{ClHO} = 148.4 \text{ or } 153.4^\circ$ , and  $d_{\text{Cl}\cdots\text{H}} = 2.40 - 3.00 \text{ \AA}$ .

Figure 5.9. Optimized, isolated  $\text{HNO}_3\cdot\text{HCl}$  complexes studied in order to estimate zero-point energy and thermal corrections to the binding energies in Figures 5.7 and 5.8

Figure 5.10. Evolution of atomic distances during three CPMD simulations at 155 K for (a) 0.99, (b) 0.44, or (c) 0.49 ps with HCl initially adsorbed at the (a) 27-kJ/mol (BLYP) or (b) 79-kJ/mol (LDA) binding site on the NAT (001) face (Figure 5.7), or at the (c) 23-kJ/mol (BLYP) binding site on the (100) face (Figure 5.8).

Figure 5.1

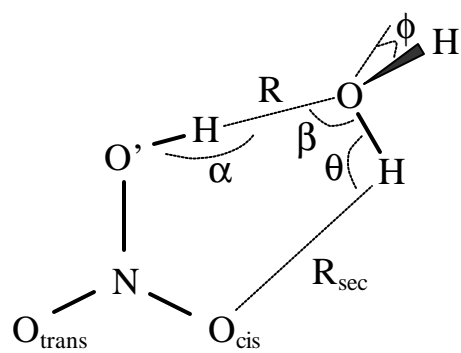


Figure 5.2

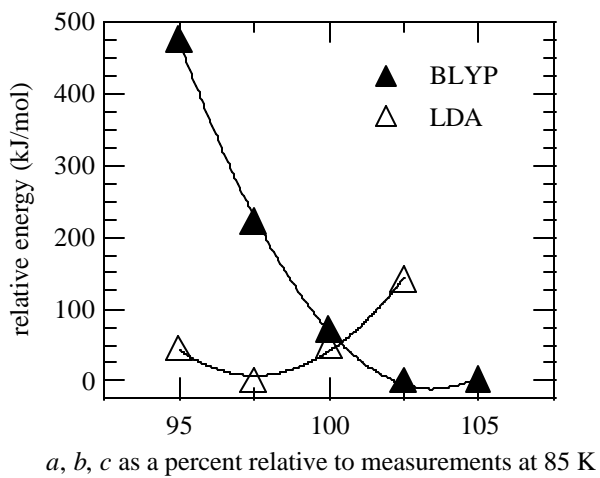
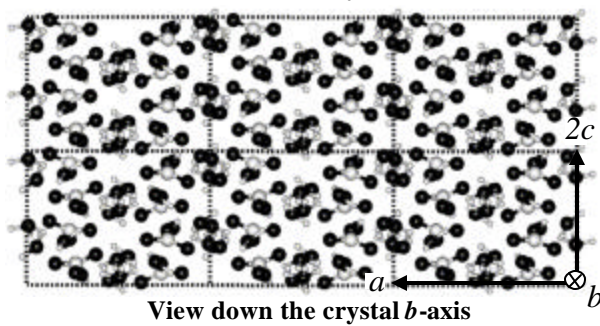
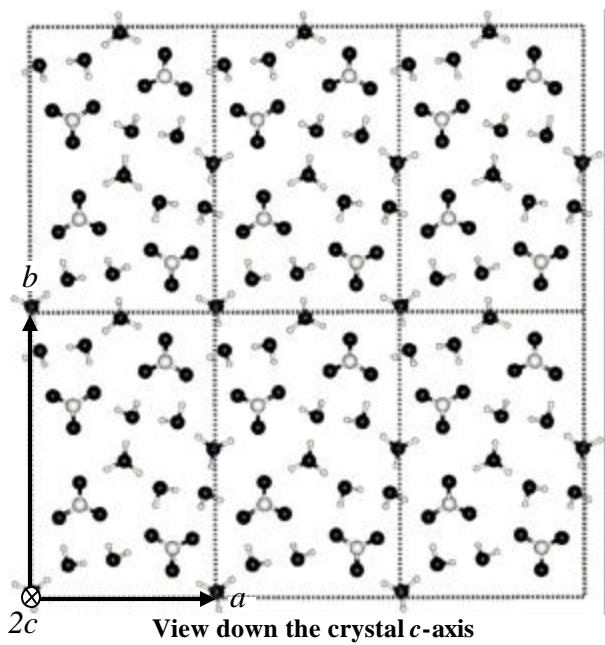


Figure 5.3

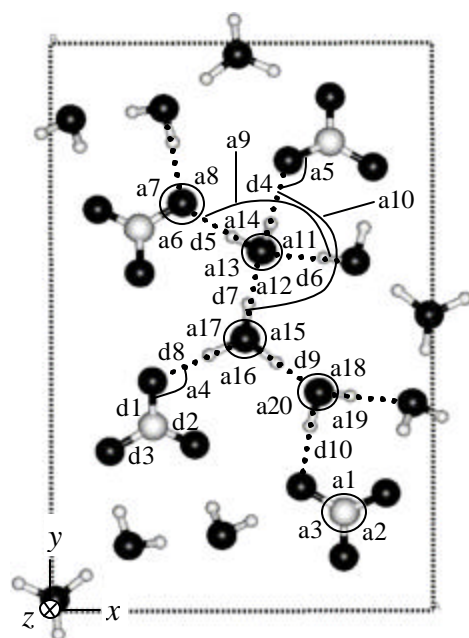
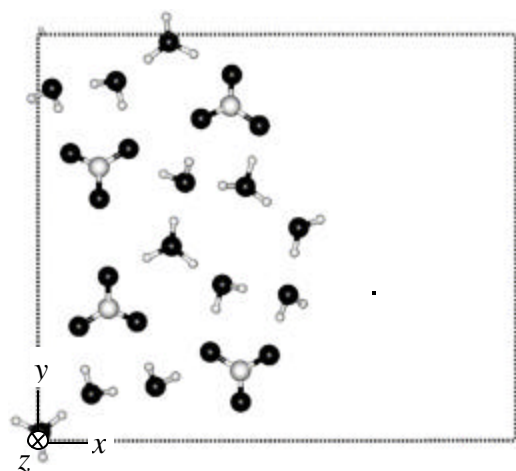
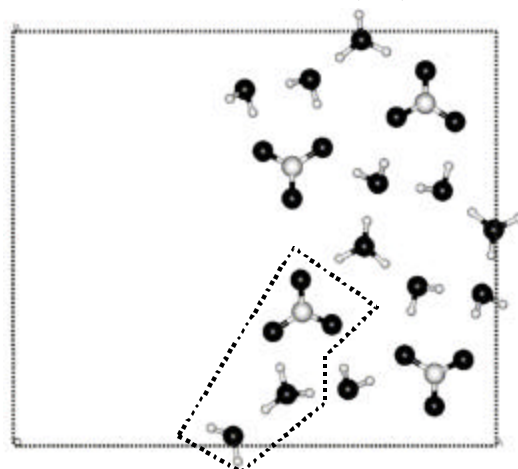


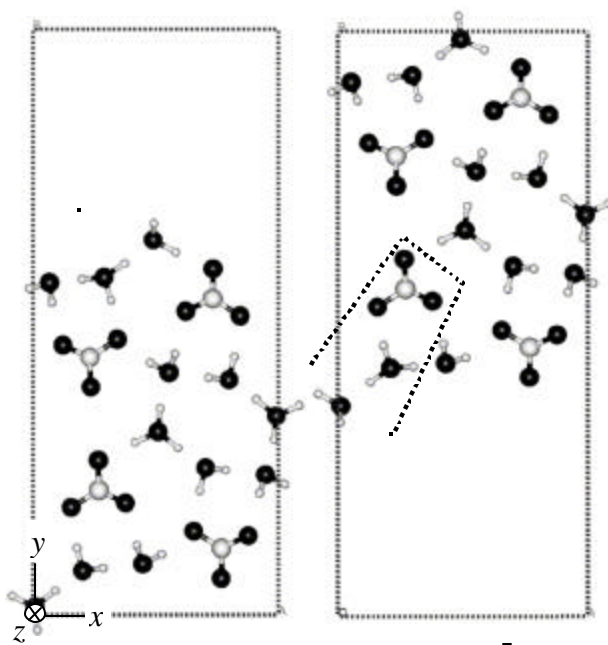
Figure 5.4



Side view of the optimized (100) face



Side view of the optimized  $\bar{1}00$  face



Side views of optimized (010) (left) and  $\bar{0}\bar{1}0$  faces

Figure 5.5

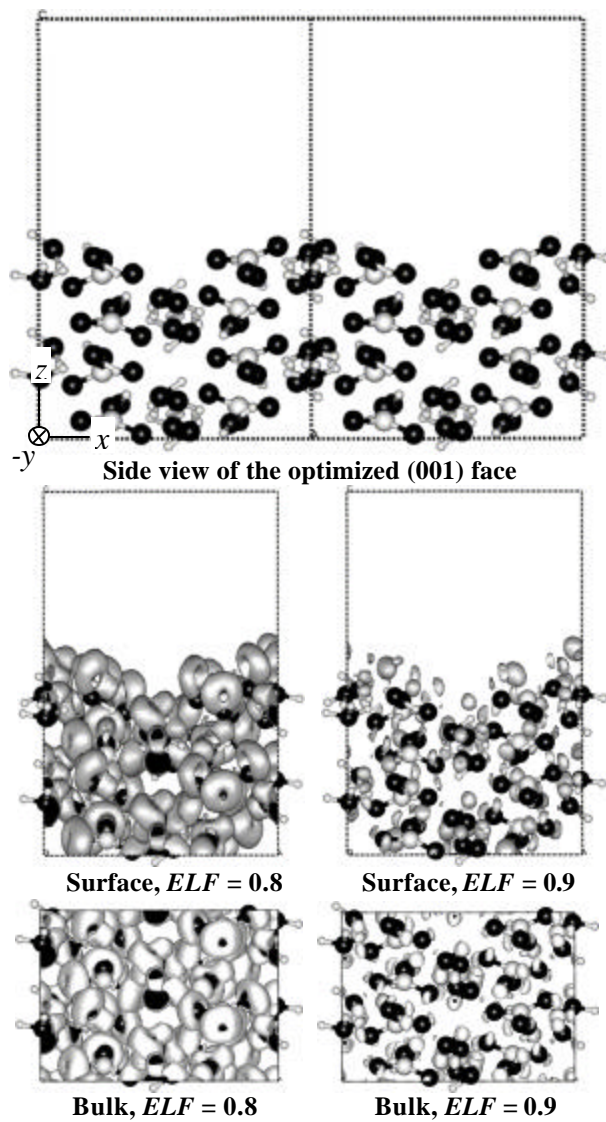


Figure 5.6

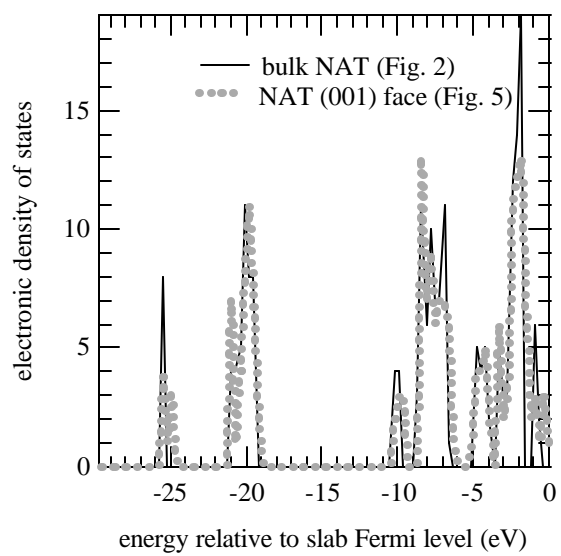
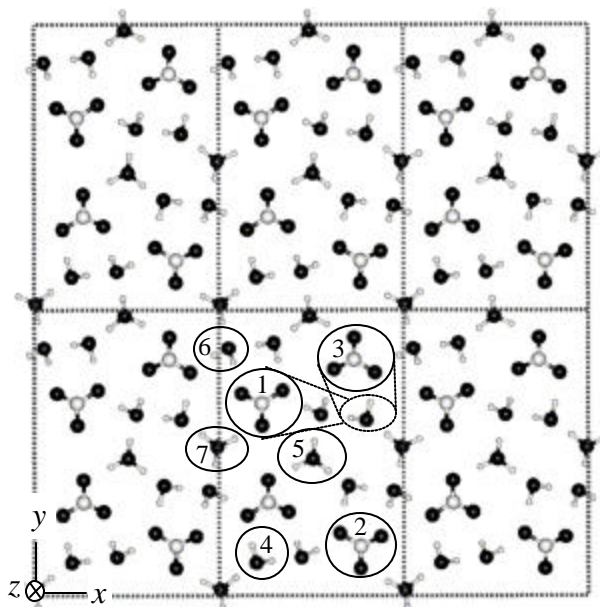
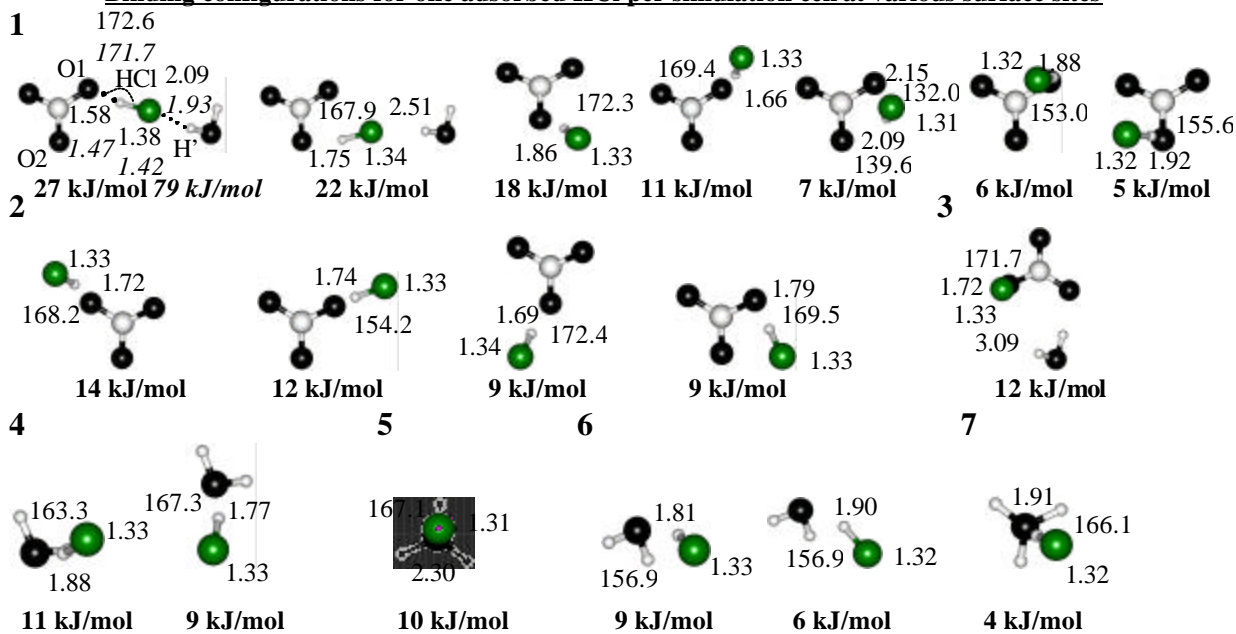




Figure 5.7



**Binding configurations for one adsorbed HCl per simulation cell at various surface sites**



**Binding configurations for two adsorbed HCl's per simulation cell at various surface sites**

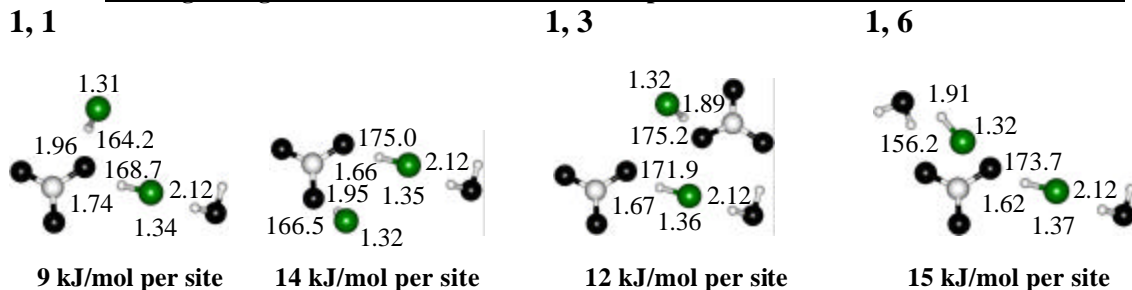
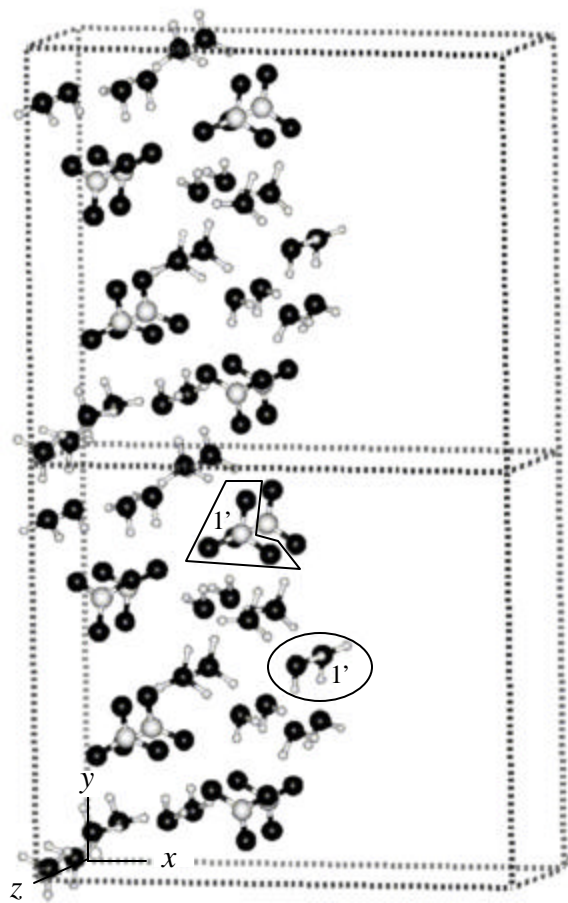


Figure 5.8



**Binding configurations for one adsorbed HCl per simulation cell at surface site 1'**

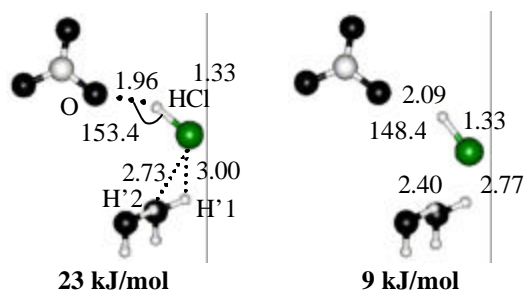
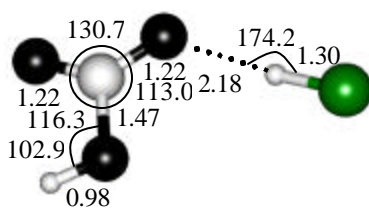
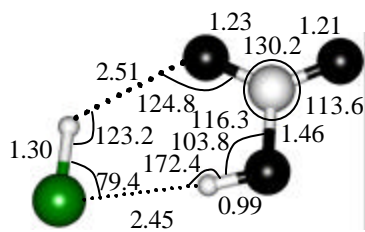


Figure 5.9

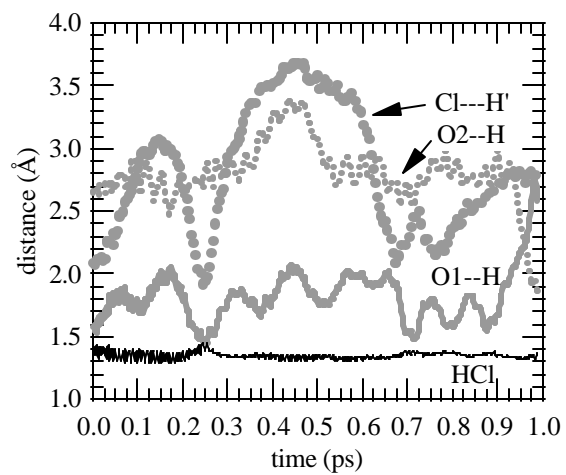


**Isomer without a Cl...H hydrogen bond**

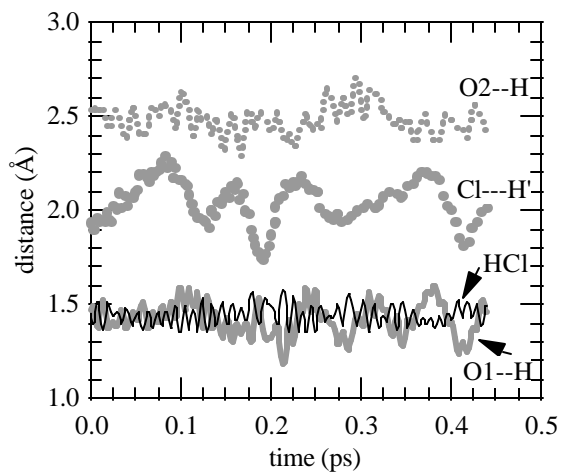


**Isomer with a Cl...H hydrogen bond**

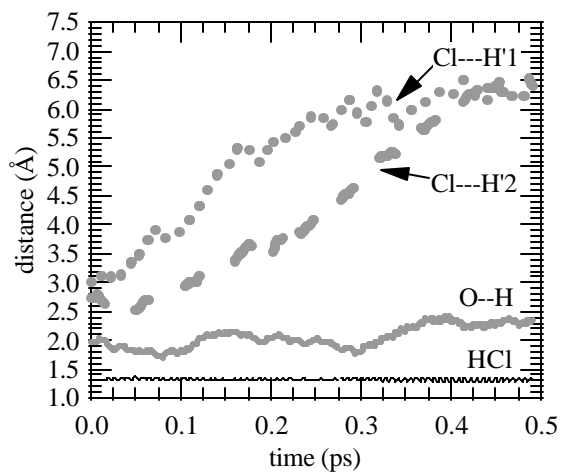
Figure 5.10



(a)



(b)



(c)

## Chapter 6: The Reaction Probability of ClONO<sub>2</sub> + HCl on SRM Emissions

### ABSTRACT

The observed pseudo-first order rate constant of the heterogeneous chlorine activation reaction  $\text{HCl} + \text{ClONO}_2 \rightarrow \text{Cl}_2 + \text{HNO}_3$  on small particulate samples of solid rocket motor (SRM) emissions was determined experimentally using an apparatus consisting of a capillary tube interfaced to a quadrupole mass spectrometer with a chemical ionization detection scheme. Micron-sized laboratory  $\alpha$ -alumina was taken as a proxy and was compared to real SRM emissions. The substrates were deposited on the walls of the flowtube using inert halocarbon wax as a support. The experiments were performed under reactant partial pressure and temperature conditions similar to those encountered in the mid-latitude lower stratosphere. Our results indicate that, within experimental error, the chlorine activation reaction studied proceeds with the same rate constant on  $\alpha$ -alumina and SRM emissions. Assuming that the rate constants are identical, because the reaction probability of  $\text{HCl} + \text{ClONO}_2 \rightarrow \text{Cl}_2 + \text{HNO}_3$  on  $\alpha$ -alumina was previously measured to be 0.02 [Molina, M. J.; Molina, L. T.; Zhang, R. Y.; Meads, R. F.; Spencer, D. D. *Geophys. Res. Lett.* 1997, 24, 1619], we conclude that the reaction probability is 0.02 on SRM emissions as well. In the Appendix, we describe how ClONO<sub>2</sub> is synthesized, discuss in detail two of the common data-correction methods employed by flowtube kineticists, and derive expressions for the reaction probability.

### 6.1. INTRODUCTION

Ariane 5, Atlas II, Delta II and Titan IV rockets, the Space Shuttle, and (ultimately) the X-33 VentureStar all use solid rocket motors (SRMs) that run with fuel containing aluminum (Al) and ammonium perchlorate (NH<sub>4</sub>ClO<sub>4</sub>). A specific emission profile of, e.g., the Space Shuttle suggests that one third of the emissions, mostly aluminum oxide (alumina, Al<sub>2</sub>O<sub>3</sub>), hydrogen chloride and water are deposited in the stratosphere (~112 t alumina / launch).<sup>1</sup>

Interest in the impact of SRM emissions on stratospheric ozone was initially confined to the effect of the injection of chlorine.<sup>2,3</sup> Model studies suggest that ozone depletion is localized near the exhaust plume.<sup>4</sup> The extent of ozone loss depends on the amount of chlorine emitted

into the stratosphere.<sup>5-7</sup> Crucial to the gas-phase destruction of ozone is the amount of exhausted HCl converted into active chlorine (mainly  $\text{Cl}_2$ , but also Cl), via reaction with free radicals (OH, H, O),<sup>8</sup> a process known as afterburning. One model study suggests that 20 – 50 % of emitted chlorine is transformed into reactive chlorine (up to an altitude of 25 km).<sup>9</sup> This result was corroborated by in-situ measurements in the SRM exhaust plume.<sup>10</sup> The influence of chlorine injected by SRMs into the stratosphere is, however, short term and makes relatively little impact on global ozone loss computations.<sup>2,6,10-12</sup>

Also of interest is the significance of alumina deposited in the stratosphere as a potentially efficient heterogeneous catalyst. The ozone loss in the exhaust plumes of two Delta II rockets was measured 12 and 39 minutes after lift-off in a recent study.<sup>13</sup> These rockets were powered by a combination of liquid (liquid oxygen = LOX / kerosene) and solid ( $\text{NH}_4\text{ClO}_4$  / Al) fuel. The measured ozone loss, comparable to that observed in the exhaust plume of much larger Titan IV rockets (which exclusively use solid propellant), exceeded the estimate by a factor of approximately two. The estimate included only the impact of the gas-phase chlorine emissions.

The concentration of aluminum-containing particles in the atmosphere was observed to increase significantly during the 70s and early 80s.<sup>14,15</sup> Emitted alumina particles have been collected and characterized (Figure 6.1).<sup>16</sup> They appear to be spherical, exist in cubic- $\gamma$  and hexagonal- $\alpha$  phases, have trace amounts of K, Na, Ti, Fe and Si and surface contaminations of chlorides and oxychlorides.

<Figure 6.1 here>

The environmental impact of alumina depends in part on its size distribution, which is correlated to stratospheric lifetime and reactivity. Brady and Martin suggest that roughly 80 % of the alumina emitted is in the so-called “large mode” with an average particle size of 0.56  $\mu\text{m}$ ,<sup>17</sup> whereas others measure a size distribution from 30  $\mu\text{m}$  down to several  $\mu\text{m}$  independent of altitude in the range 2.4 to 7.2 km.<sup>16,18</sup> Coagulation of “large” alumina particles with background sulfuric acid aerosols is unlikely,<sup>19</sup> which means a long “active” lifetime of alumina. Hence, alumina is proposed to function as a catalyst for slow gas phase reactions<sup>20</sup> such as Rx. (6.1)



especially at mid-latitudes where polar stratospheric clouds (PSCs) do not form. At these latitudes, stratospheric sulfate aerosols do not promote Rx. (6.1), because they are too concentrated (> 70% by weight liquid H<sub>2</sub>SO<sub>4</sub>), and HCl is insoluble at the prevailing temperatures.<sup>4</sup>

The reaction probability  $\gamma$ , defined as<sup>21</sup>

$$\gamma = \frac{\text{number of collisions with a clean surface leading to reaction}}{\text{total number of collisions with a clean surface}}, 0 \leq \gamma \leq 1, \quad (6.2)$$

of Rx. (6.1) on glass and on  $\alpha$ -alumina, a proxy for the particulate emissions, was recently measured by our laboratory<sup>19</sup> under mid-latitude stratosphere conditions ( $1-10 \times 10^{-6}$  Torr HCl). On a thin, non-porous  $\alpha$ -alumina tube,  $\gamma$  was measured to be 0.02 using two detection schemes, chemical ionization mass spectrometry (CIMS) (208 – 223 K) and electron impact mass spectrometry (EIMS) (195 – 230 K). When the  $\alpha$ -alumina tube is first baked in an oven,  $\gamma \ll 0.02$ , but is restored to 0.02 by humidifying the He carrier gas. The  $\gamma$  was also measured on spherical  $\alpha$ -alumina particles using Eq. (6.3), and the same value of 0.02 was reported.

$$\gamma(\alpha\text{-Al}_2\text{O}_3) = \frac{\text{growth of Cl}_2^+ \text{ signal on } \alpha\text{-Al}_2\text{O}_3 \text{ particles}}{\text{growth of signal on glass beads}} \times \gamma(\text{glass flow tube}) \quad (6.3)$$

Rx. (6.1) on laboratory  $\alpha$ -alumina, with  $\gamma = 0.02$ , was subsequently added to the Goddard Space Flight Center two-dimensional photochemistry and transport atmospheric model<sup>22</sup> in order to estimate the impact of the particulate emissions.<sup>23</sup> Using a historic launch scenario from 1970 – 1997 and the trimodal size distribution determined by Brady and Martin,<sup>17</sup> an annually averaged global total ozone (AAGTO) loss of 0.025 % for 1997 in an alumina and HCl perturbed stratosphere was calculated. Alumina, it was estimated, is responsible for about one third of this loss, whereas the hydrogen chloride emissions contribute two thirds. The decrease of AAGTO is based on the assumption that 10 % of the alumina mass resides in the smallest mode.

The first in-situ measurement of the alumina size distribution in the stratosphere was recently carried out.<sup>13</sup> It was reported that the distribution in the low to sub- $\mu\text{m}$  range is trimodal

with modes of approximately 0.005, 0.09 and 2.03  $\mu\text{m}$ . In contrast to previous studies concluding that the smallest mode contributes up to 12 % of the alumina mass,<sup>17</sup> less than 0.05 % of the mass was determined to reside in the smallest mode and therefore it was concluded that alumina plays an insignificant role in AAGTO loss.<sup>13</sup> A Mobile Lidar Trailer (MLT) was applied to identify particle species and size of launch vehicle plumes of two Space Shuttle missions by wavelength dependence of Mie scattering.<sup>24</sup> The backscattering signal up to 30 minutes after the launches and from an altitude of less than 25 km was dominated by particles with an upper size limit of 0.05  $\mu\text{m}$ .<sup>24</sup> The backscattering signal early after the launch might stem from alumina or other particles like, e.g., water ice, HCl droplets, or alumina coated with ice.<sup>24</sup> The extent to which ozone loss in a Space Shuttle wake affects ozone on a global scale was also recently investigated<sup>25</sup> using the Atmospheric and Environmental Research, Inc. two-dimensional model. Assuming a worst-case scenario (i.e., all SRM chlorine is emitted as molecular chlorine, the alumina size distribution is identical to that reported by Brady and Martin,<sup>17</sup> and the Shuttle path follows a vertical straight line), an upper bound for global ozone loss was estimated to be 1 – 10 ppmv. This is at least one order of magnitude less compared to globally dispersed SRM chlorine emissions. In a later investigation,<sup>26</sup> the accumulation of alumina particles in the atmosphere was studied by using a three-dimensional chemistry-transport model, and ozone perturbations caused by chlorine activation on alumina were estimated with a two-dimensional model. Assuming a size distribution reported by Beiting,<sup>27</sup> and taking into account washout, gravitational sedimentation, and coagulation with background sulfuric acid aerosols, a maximum steady state density of 0.09  $\text{ng}/\text{m}^3$  was determined, less than that of background sulfuric acid aerosols by a factor of  $\sim 1000$ . The AAGTO was calculated to be 0.0028 % due to alumina, about four times less compared to chlorine emissions but sensitive to the size distribution of the alumina particles. The ozone depletion potential (ODP) of alumina was calculated to be 0.35 with a size distribution as found by Brady and Martin.<sup>17</sup> Such a high value, in conjunction with the uncertainties regarding alumina size distribution at different altitudes, suggests the need for further in-situ measurements.<sup>26</sup>

The purpose of this study was to investigate whether  $\gamma$ 's of Rx. (6.1) on clean laboratory  $\alpha$ -alumina and alumina emitted from SRMs are similar. The fact that chlorides and oxychlorides are present as contaminants on SRM emissions indicates that the surfaces of laboratory  $\alpha$ -alumina and SRM emissions are different.<sup>19</sup> Hence, the adsorbed water layers, as well as the



reaction probability, might be dissimilar. Also, real SRM emissions consist of a mixture of  $\alpha$ - and  $\gamma$ -alumina,<sup>22</sup> heretofore neglected in laboratory studies. Because only small SRM sample amounts were obtained, a traditional apparatus consisting of a wide-bore flowtube with the substrate deposited on the walls or else entrained in the carrier gas was not used. Instead, a small-bore capillary tube (from 1" to 1/4" o.d.) was interfaced to a CIMS. We report measurements of  $k_{\text{obs}}$  on glass, micron-sized  $\alpha$ -alumina, SRM dust and slack under temperature and reactant partial pressure conditions similar to those in the lower stratosphere at mid-latitudes. While a significantly lower (i.e., a factor of  $\sim 100$ ) partial pressure of water vapor was used than is typically encountered, we argue that this does not adversely affect the results.

## 6.2. EXPERIMENTAL SETUP

### 6.2.1. Miniaturized Flowtube CIMS

The experimental apparatus is shown in Figures 6.2 and 6.3. It consists of a Pyrex glass flowtube ( $\sim 4$  mm I.D. and 15 cm long) interfaced to a chemical ionization quadrupole mass spectrometer (ABB Extrel). The limiting reagent ClONO<sub>2</sub> was injected through a movable injector (stainless steel tubing, 1/16" O.D.) while a diluted mixture of HCl (0.09 % in N<sub>2</sub>, Matheson) in He was mixed upstream with additional He (UHP 5.0, BOC) carrier gas. The injector was centrally aligned to prevent removal of the particles deposited on the flowtube walls while sliding the injector back and forth. The ClONO<sub>2</sub> was synthesized over a few weeks<sup>28-32</sup> (Section 6.6) and prepared in a bulb at a mixing ratio of  $10^{-3}$ . The decay of ClONO<sub>2</sub> in the bulb was monitored by UV spectroscopy. The ClONO<sub>2</sub>/He from the bulb was diluted with additional He (dilution typically was 1:100) and split injected into the He carrier gas stream. We note that as long as the pressure in the mixing tube was  $> 1$  atm and the excess flow was substantial ( $> 10$  sccm), back diffusion of ambient air into the system was expected to be negligible.

<Figures 6.2 and 6.3 here>

The flowtube was inserted in a cooling stage machined from an aluminum block with boreholes for three heating cartridges (100 watt) and for two copper-constantan thermocouples.

The temperature was controlled by a liquid nitrogen reservoir counterbalanced by resistive heaters coupled to a temperature controller.

Using this CIMS approach, detection sensitivity for ClONO<sub>2</sub> and C<sub>2</sub>H<sub>2</sub> was achieved with a linear detector response between 10<sup>9</sup> and 5 × 10<sup>10</sup> molecule/cm<sup>3</sup> (3.0 × 10<sup>-8</sup> – 1.5 × 10<sup>-6</sup> Torr). The negative reagent ion, SF<sub>6</sub><sup>-</sup>, was generated by passing neutral SF<sub>6</sub> (4.0, Matheson) in a flow of nitrogen through a radioactive polonium ion source (<sup>210</sup>Po, Model P2031, NRD Inc.). The lowest practical N<sub>2</sub> flow in this system was 375 sccm. At this flow, sufficient SF<sub>6</sub><sup>-</sup> was supplied in order to maintain adequate sensitivity, while keeping the total pressure in the flowtube sufficiently low (~25 Torr), thus avoiding a diffusion-limited regime. The species ClONO<sub>2</sub>, HCl and C<sub>2</sub>H<sub>2</sub> were detected as F<sup>-</sup>ClONO<sub>2</sub><sup>-</sup> (116 amu), SF<sub>5</sub><sup>-</sup>Cl (162 amu) and C<sub>2</sub>H<sub>2</sub><sup>-</sup> (70 amu), respectively.<sup>33</sup> From the calculated leakrate of the apparatus, and having an estimate of the humidity in the He tank, the water vapor concentration was estimated to be at least 2 × 10<sup>-6</sup> Torr, which was confirmed by a humidity monitor. This is roughly 100 times less than that encountered in the mid-latitude stratosphere. However, poisoning of the reactive surface by the reaction product HNO<sub>3</sub> was not observed, likely due to the short exposure time of experiments.

During a typical kinetics measurement, HCl concentration was at least in fivefold and typically in tenfold excess over ClONO<sub>2</sub> to ensure pseudo-first-order reaction conditions. Typical reagent concentrations were in the range from 3 to 5 × 10<sup>10</sup> molecule/cm<sup>3</sup> (1.0 – 1.6 × 10<sup>-6</sup> Torr) for ClONO<sub>2</sub> and 3 × 10<sup>11</sup> molecule/cm<sup>3</sup> (10<sup>-5</sup> Torr) for HCl, respectively. Other parameters are summarized in Table 6.1. The k<sub>obs</sub>'s were obtained from decay of the F<sup>-</sup>ClONO<sub>2</sub><sup>-</sup> signal, monitored while pulling back the injector in 2-cm increments over a total length of 8 – 10 cm (Figure 6.4). Despite the 1:1 reaction stoichiometry, the signal corresponding to production of C<sub>2</sub>H<sub>2</sub>, though observed, was too small to determine a rate constant from accurately, a consequence of the fact that reaction of C<sub>2</sub>H<sub>2</sub> with SF<sub>6</sub><sup>-</sup> is one order of magnitude slower than the corresponding reaction of ClONO<sub>2</sub>.<sup>33</sup> We also note that signal decays obtained over the first 2 – 4 cm were discarded because of slow mixing and because the film was not uniform at the edges.

<Table 6.1 and Figure 6.4 here>

### **6.2.2. Sampling of Particulate SRM Emissions**

The SRM dust, provided by Dr. R. R. Bennett, was collected from static test firings of rocket motors containing SRM propellant. The sample was obtained by igniting each time roughly 150 g of propellant in a small rocket motor and expanding the plume out of a graphite nozzle into an 8-inch diameter sheet metal tube. The tube was five feet long and opened into a 30-gallon barrel. The center of the lid of the barrel had previously been removed, and another 8-inch diameter and 6-feet long metal tube had been inserted. The end of the tube extended about two feet into the barrel. This set-up was chosen in order to cause sufficient turbulence to be able to sample the SRM dust from the walls of the barrel and the tubes. The exhaust flow was so high and the particles were so small that the amount sampled was only about 100 mg. Besides this method of collection, a solid block of coagulated SRM emissions provided by Dr. V. Lang was ground to yield particles with a diameter of 1 – 2  $\mu\text{m}$ , hereafter referred to as SRM slack. This block was sampled from the ground of a launch site and consisted of alumina particles baked together with smaller amounts of contaminants, i.e., graphite and aluminum.

### **6.2.3. Characterization of the Alumina Particles**

The two types of sample (SRM dust and SRM slack) and different size samples of reference laboratory  $\alpha$ -alumina (0.88, 2.86 and 10 – 45  $\mu\text{m}$  average particle size) were examined with an optical microscope (Zeiss Axioskop). The SRM samples were grayish in color, most likely due to solid aluminum dust impurities and / or graphite ablation from the engine nozzles. The size of the particles was estimated to be 1 – 2  $\mu\text{m}$  in diameter, at the limit of resolution of the light microscope (Figure 6.5). Therefore, the laboratory  $\alpha$ -alumina with a Fisher size of 0.88  $\mu\text{m}$  (Cerac Inc.) was taken as a proxy for the preparation of the flowtubes.

<Figure 6.5 here>

### **6.2.4. Substrate Tube Preparation**

Two approaches were taken to coat the tubes with particles: firstly, physically adsorb the particles in a so-called wall coated open tubular (WCOT) style and secondly, apply a sticky, non-

reactive support (e.g., wax or grease) in a support coated open tubular (SCOT) fashion. Although micron-size alumina particles tend to stick to plain glass, a complete, uniform layer is not easily achieved. The SCOT version, on the other hand, was easy to prepare. The utilization of halocarbon wax (Series 600, Halocarbon Prod. Inc., River Edge, NJ) was preferred, because a uniform and thin layer was achieved more easily than with the grease (Apiezon®). Moreover, the particles stick readily when shaken in the glass tube upon deposition of wax on the glass. A thin wax film ( $\ll 1$  mm) was obtained by means of melting the wax in the tube and flowing  $N_2$  ( $\sim 1$  slpm) through the tube. The wax, once at ambient temperature, formed a uniform, translucent layer. Afterwards, the particles (either  $\alpha$ -alumina or SRM sample) were placed in excess in the tube, the ends of the tube were capped off, and the tube was shaken vigorously for several minutes. Excess particles and loosely sticking particles were removed by physically emptying the tube, and then by blowing air through it. Finally, a 1/8" glass rod was lightly rolled in the tube, and particles that were non-cohesive were blown off by a very high flow of  $N_2$  (tube head pressure,  $\sim 2$  atm). Complete surface coverage by the particles was inferred, because the tubes appeared opaque. Moreover, a high HCl background was produced by the SRM samples at the beginning of the experiments, corresponding to approximately  $10^5$  Torr HCl, confirming that the particles were in contact with the carrier gas and were not covered by wax. We were able to coat only one tube with the small amount of SRM dust sample, justifying our effort to downsize the flowtube. Three tubes of the slack sample were prepared as well as three tubes of the laboratory  $\alpha$ -alumina.

Semi-quantitative HCl breakthrough experiments were conducted on tubes of uncoated Pyrex glass, halocarbon wax-coated glass, SRM alumina, and reference laboratory  $\alpha$ -alumina in order to estimate and compare the reactive surface area of the particles deposited. The experiments<sup>34</sup> were performed as follows: After establishing a signal, the HCl flow was diverted to pass over the substrate of interest. The signal dips sharply before gradually recovering to its original level after an elapsed breakthrough time. From the standard flow of HCl, the temperature and pressure in the tube, the breakthrough time, the ratio of the area under the breakthrough curve compared to the total area, and the tube radius, the number of adsorbed HCl molecules per unit area was calculated; also, 1 monolayer (ML) =  $10^{15}$  molecule/cm<sup>2</sup>. Breakthrough experiments were carried out at least three times at 223 K. Based on the results, it was concluded that all samples have comparable surface areas to within a factor of five, a

reasonable result given that the method of tube preparation was consistent and sample particle sizes were comparable. The number of particles deposited on the tube walls was ~1 ML, based on experiments in which glass slides were coated with halocarbon wax, laboratory  $\alpha$ -alumina was deposited, and the thickness of the alumina layer with a light microscope was estimated.

### 6.3. RESULTS AND DISCUSSION

#### 6.3.1. Spectroscopic Determination of Decay of ClONO<sub>2</sub>

In order to determine the actual partial pressure of ClONO<sub>2</sub> employed during experiments, the decay of ClONO<sub>2</sub> in a quartz cell of length L at partial pressure  $p_{\text{ClONO}_2}$  transferred from a glass bulb of mixing ratio  $y_{\text{ClONO}_2}$  was determined from the measured absorbance A using Beer's law, where  $\sigma$  is the cross section of ClONO<sub>2</sub>.<sup>35</sup>

$$A_{215 \text{ nm}} = L\sigma_{215 \text{ nm}}[\text{ClONO}_2] = L\sigma_{215 \text{ nm}} \frac{p_{\text{ClONO}_2} N_A}{RT} = L \frac{\sigma_{215 \text{ nm}}^{\text{lit}}}{2.303} \frac{p_{\text{ClONO}_2} N_A}{RT} \quad (6.4)$$

<Figure 6.6 here>

where the ideal gas law is used to rewrite  $[\text{ClONO}_2]$ , and  $\sigma$  (reported in base e in the literature) is converted to base 10 by dividing by 2.303 (which is how A is obtained). Rearrangement of Eq. (6.4) and substitution of  $T = 296 \text{ K}$ ,  $L = 10 \text{ cm}$ , and  $\sigma_{215 \text{ nm}}^{\text{lit}} = 3.6 \times 10^{-18} \text{ cm}^2$  yields

$$p_{\text{ClONO}_2} = \frac{7.11}{3.6} A_{215 \text{ nm}} \quad (6.5)$$

From the expected ClONO<sub>2</sub> partial pressure,  $y_{\text{ClONO}_2} P$ , where P is the total pressure of the gaseous mixture, the % decay is given simply by

$$\% \text{ decay} = \left(1 - \frac{7.11 A_{215 \text{ nm}}}{3.6 y_{\text{ClONO}_2} P}\right) \times 100 \% \quad (6.6)$$

The decay of ClONO<sub>2</sub> in the bulb was determined every ~12 hours (Figure 6.7). It was observed to level off after ~50 hours at 27 ± 3%. The partial pressure of ClONO<sub>2</sub> in kinetics measurements was consequently corrected by multiplying by 0.73.

<Figure 6.7 here>

### 6.3.2. Kinetics Measurements

In order to test our new apparatus, Rx. (6.1) was first investigated on Pyrex glass, in order to verify that  $\gamma = 0.02$  as obtained previously.<sup>19</sup> This verification was carried out using a “capped” injector specifically designed to inject ClONO<sub>2</sub> against the flow of He carrier gas in order to ensure perfect mixing and to enable the use of standard flowtube equations with diffusion corrections for calculation of  $\gamma$  (as detailed below).<sup>36</sup> It was impossible to use a capped injector for measurements on substrates, because substrate would have been scraped off the walls while sliding the capped injector back and forth. Subsequent measurements were therefore carried out using a straight injector without a cap on its tip. First, measurements were performed on halocarbon wax to determine the pseudo-first order rate constant  $k_{\text{obs}}$  on this support surface. Measurements were then performed on glass and lastly on  $\alpha$ -alumina, on SRM dust, and on SRM slack. These sets of experiments provided only relative  $k_{\text{obs}}$  values due to imperfect mixing, and because the substrate surface areas were not exactly equal to the geometric surface area of the glass tube, and are therefore not used to calculate  $\gamma$ 's; however, it is valid to compare  $k_{\text{obs}}$ 's obtained under identical experimental conditions.

Pseudo-first-order rate constants  $k_{\text{obs}}$ 's were calculated as follows: For Rx. (6.1), the reaction rate is

$$\text{reaction rate} = -\frac{d[\text{ClONO}_2]}{dt} = k'[\text{ClONO}_2][\text{HCl}] \sim k_{\text{obs}}[\text{ClONO}_2] \quad (6.7)$$

where  $[\text{HCl}] \gg [\text{ClONO}_2]$ , and  $k_{\text{obs}} = k'[\text{HCl}]$ . Solving the first-order linear differential Eq. (6.7) by separation of variables,

$$\ln \left( \frac{[\text{ClONO}_2]}{[\text{ClONO}_2]_0} \right) = \ln \left( \frac{S^{116}}{S_0^{116}} \right) = -k_{\text{obs}}t = -k_{\text{obs}} \frac{v}{l} \quad (6.8)$$

where  $S^{116}$  is the mass signal of  $\text{ClONO}_2$  at time  $t$ ,  $v$  is the flow velocity given by Eq. (6.9) from standard flows  $f$  and the flow tube radius  $r$ , and  $l$  is the injector position (or reaction “length”).

$$v = \frac{f}{\pi r^2} = \frac{(f_{\text{HCl}} + f_{\text{ClONO}_2} + f_{\text{He}}) \frac{760 \text{ torr}}{P} \frac{T}{273 \text{ K}}}{\pi r^2} \quad (6.9)$$

From Eq. (6.8), a plot of  $\ln \left( \frac{S^{116}}{S_0^{116}} \right)$  vs.  $t$  yields  $k_{\text{obs}}$  (Figure 6.8). In order to calculate average

$k_{\text{obs}} \pm 2\sigma$  for a particular surface (Table 6.2), individually measured  $k_{\text{obs}}$  and standard deviations (Table 6.3) are averaged. The mathematical deviation from the mean  $\pm 2\sigma$  in Table 6.2 provides an estimate of the random error and takes into account fluctuations in the pressure ( $\pm 1 - 2$  Torr), and temperature ( $\pm 3 - 5$  °C) that occurred during and between experiment, as well as irreproducibility in film preparation.

<Figure 6.8 and Tables 6.2 and 6.3 here>

From the pseudo-first-order reaction rate constant  $k_{\text{obs}}$  determined for the control experiment on glass with the capped injector, the (wall) loss rate constant  $k_w$  was computed assuming additivity of kinetic resistances<sup>36</sup> or, alternatively, the Brown method<sup>37</sup> (Section 6.6).

$$\frac{1}{k_{\text{obs}}} = \frac{1}{k_d} + \frac{1}{k_w} = \frac{3.66D_c}{r^2} + \frac{1}{k_w} \quad (6.10)$$

The diffusion coefficient  $D_c$  for  $\text{ClONO}_2$  in He at 200 K is  $176 \text{ Torr cm}^2 \text{ s}^{-1}$ ,<sup>38</sup> estimated assuming a dependence of  $T^{1.76}$ . Lastly,  $\gamma$  is obtained from  $k_w$  using Eq. (6.11), derived from the

expression for the gas-kinetic flux of molecules on a flat extended surface<sup>39</sup> modified due to reaction on a lossy surface (Section 6.6),<sup>38,40-42</sup> where  $\omega = \sqrt{\frac{8RT}{\pi M}}$  is the mean thermal velocity.

$$\gamma = \frac{2rk_w}{\omega + rk_w} \quad (6.11)$$

An absolute  $\gamma = 0.0155 \pm 0.015$  ( $2\sigma$ ) for Rx. (6.1) on glass with a capped injector (i.e., the control experiment) with perfect mixing and a smooth surface was determined. This result is comparable to the value of 0.02 determined earlier,<sup>19</sup> validating the system.

For every surface except wax, about ten reactant decays were determined at each temperature, summing up to approximately 100 experiments. The averaged relative pseudo-first-order rate constants  $k_{\text{obs}} \pm 2\sigma$  for experiments on samples without the capped injector are shown in Table 6.2. The  $k_{\text{obs}}$ 's reported in Table 6.2 represent only relative values, in part due to the use of a straight open injector: Mixing of the reactant plume at the operating pressure of ~25 Torr is relatively slow under these conditions. With few exceptions, the regression coefficients of the  $k_{\text{obs}}$  fits were at least 0.97. Non-linear behavior was never observed.

As seen in Table 6.2, the blank test on a tube covered only with halocarbon wax exhibits a comparatively small pseudo-first-order rate constant  $k_{\text{obs}}$  for the chlorine activation reaction. Its absolute value is higher than expected, however, which may mean that the halocarbon wax (as deposited) cracks at cold temperatures, yielding additional surface area and possibly exposing the glass underneath. However, our HCl uptake measurements indicate that all deposited films have roughly the same surface area, and consequently we proceed under the assumption that wax is a suitable support.

In contrast to earlier experiments, which indicate that the reaction probability is the same on glass and on  $\alpha$ -alumina, a significantly higher value for  $k_{\text{obs}}$  compared to glass is observed (Table 6.2). The most likely reason for this discrepancy is that the surface of the flowtube containing the particulate samples is rough/porous, with a reactive surface area larger than the geometric surface area, whereas in our calculations we assume a smooth cylindrical flowtube surface. Formally, correction for porosity is possible,<sup>43</sup> as described in the Appendix (Section 6.6). However, it is difficult to estimate accurately the magnitude of the various correction



factors. It is assumed that the discrepancy between the values on glass and on particles is due to surface porosity. Comparison with the result obtained on smooth glass with a capped injector indicates that in this particular case the effects of porosity and imperfect mixing are offsetting.

The  $k_{\text{obs}}$ 's have essentially the same value on all the alumina samples – SRM dust, SRM slack, and laboratory  $\alpha$ -alumina – , and the  $k_{\text{obs}}$ 's are temperature-independent from 223-238 K. Because the different alumina samples all have similar  $k_{\text{obs}}$ 's (as well as similar surface areas), it follows that the errors associated with approximating actual SRM emissions (which consist of  $\alpha$ - and  $\gamma$ -alumina with surface impurities) using laboratory  $\alpha$ -alumina in kinetics measurements are likely offsetting and, given that the concentration of surface impurities is low, probably quite small. To probe the reaction mechanism, it would be useful to study the impact of dehumidifying the SRM samples (i.e., by baking) or coating the alumina samples with sulfuric acid (and other surface impurities) in order to determine the effect on Rx. (6.1).

Our results suggest that atmospheric modelers may, with added confidence, use the value for  $\gamma$  that was measured earlier for Rx. (6.1) on  $\alpha$ -alumina.<sup>19</sup> Our results do not contradict in any way modelers' conclusions<sup>23</sup> regarding the negligible effect of alumina on mid-latitude ozone depletion. It would be useful to confirm with additional field measurements the size distribution of particulate found by Ross et al.<sup>44</sup> Another priority is to project reliable forecasts of launch rates in the upcoming 20 to 30 years; these might dramatically rise due, e.g., to space tourism gradually becoming economically realistic. Factoring these factors into existing models will help to finally pin down the true impact of SRM-driven shuttles.

## 6.4. CONCLUSIONS

In this paper, a new technique based on a capillary tube interfaced to a CIMS was developed in order to study reaction kinetics on small particulate sample amounts. Flowtube preparation and attachment to the system requires less than one hour. The pseudo-first order rate constants  $k_{\text{obs}}$ 's for the reaction of  $\text{ClONO}_2 + \text{HCl}$  on laboratory  $\alpha$ -alumina, on SRM dust and slack were measured under temperature and reactant partial pressure conditions similar to those encountered at mid-latitudes in the lower stratosphere. On all these surfaces, the  $k_{\text{obs}}$ 's are identical (Table 6.1), within the sensitivity and associated errors (i.e., potentially cracked wax support at cold temperatures and similar but not identical substrate surface areas and imperfect

mixing) of the measurements. Our preliminary results support the conclusion that on a global scale the ozone depletion effect of the particles emitted by SRMs can be considered comparable to the effect of the chlorine emissions from the SRMs and under the current launch rate scenario are negligible. More work needs to be done to determine the future impact of SRM emissions, specifically a comprehensive set of field measurements to determine the particulate size distribution as well as a study to predict launch rates during the upcoming 20 to 30 years.

## 6.5. ACKNOWLEDGEMENTS

Financial support from the Air Force Office of Scientific Research (Grant No. F49620-96-1-0034) is acknowledged. Yves A. Mantz thanks the M.I.T. Center for Global Change for partial financial support. This work was performed in close collaboration with Dr. Markus M. Haider, who thanks the Alexander-von-Humboldt - foundation / Germany for a Feodor Lynen Postdoctoral Fellowship. We thank Dr. R. R. Bennett of Thiokol Propulsion, Inc for providing the SRM dust and Dr. V. Lang of the Aerospace Corporation for providing the SRM slack.

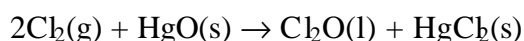
## 6.6. APPENDIX

In Section 6.6.1, we describe in detail the synthesis of  $\text{ClONO}_2$ . In Section 6.6.2, we describe the Brown correction for radial diffusion, and errors associated with it and the sum-of-resistance method. In Section 6.6.3, we describe the Keyser correction for porosity and internal diffusion. In Section 6.6.4, we derive an expression for  $\gamma$ .

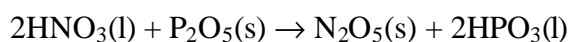
### 6.6.1. Synthesis of Chlorine Nitrate

Because it is thermally and photolytically unstable,  $\text{ClONO}_2(\text{g})$  was synthesized in the laboratory in three steps over the course of several weeks.<sup>28-32</sup> First, fresh  $\text{HgO}(\text{s})$  (Mallinckrodt) was prepared by successively washing  $\text{HgO}(\text{s})$  coated with  $\text{HgCl}_2(\text{s})$  and mixed in with glass beads with a saturated (98.9 %) solution of  $\text{NaOH}$  (Mallinckrodt) in a Buchner funnel, until the pH of the decantate was seven (using indicator paper). The  $\text{Cl}_2\text{O}(\text{l})$  was synthesized by filling the finger of a two-piece ampoule with  $\text{HgO}(\text{s})$  packed with glass wool, and adding  $\text{Cl}_2(\text{g})$  (99.9%, Matheson). Because  $\frac{1}{2}$  bottle  $\sim 125 \text{ g} = \frac{1}{4}$  mole of  $\text{HgO}(\text{s})$  was used, an excess ( $> \frac{1}{2}$

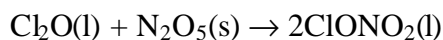
mole) of  $\text{Cl}_2$  was added, corresponding to  $PV = nRT = \frac{1}{2} \text{ mole} \times 0.08314 \text{ L-bar}/(\text{mol K}) \times 298 \text{ K} = 15 \text{ L-bar}$ , or  $> 15 \text{ L-bar}$  additions of  $\text{Cl}_2$  from a 1-L glass bulb. The  $\text{Cl}_2\text{O}(\text{l})$  was trapped as a liquid in a finger immersed in liquid  $\text{N}_2$ . Once additions were complete, the finger was stored for 2 – 3 days in a dry ice/isopropanol bath ( $-78 \text{ }^\circ\text{C}$ ), allowing reaction to transpire. The  $\text{Cl}_2\text{O}(\text{l})$  was distilled by vapor transfer from the ampoule immersed in dry ice/isopropanol into a clean finger in an ethanol/liquid  $\text{N}_2$  bath ( $-120 \text{ }^\circ\text{C}$ ), with everything wrapped in aluminum foil for darkness. The top fraction was richest in dissolved  $\text{Cl}_2(\text{g})$ , while the bottom fraction was rich in  $\text{Cl}_2\text{O}(\text{l})$ .



Secondly, solid  $\text{N}_2\text{O}_5$  was prepared by combining excess (200 g)  $\text{P}_2\text{O}_5$  (99.8%, J.T. Baker) with 100 mL of fuming  $\text{HNO}_3$  ( $> 90\%$ , Mallinckrodt) in a three-neck flask cooled in dry ice/isopropanol under an atmosphere of pure  $\text{O}_2(\text{g})$ . To activate the reaction, the dry ice/isopropanol bath was then replaced with a room-temperature water bath, and collection of  $\text{N}_2\text{O}_5(\text{s})$  proceeded for six hours with stirring until production of noxious  $\text{NO}_2(\text{g})$ , a decomposition product, subsided, at which time  $\text{N}_2\text{O}_5(\text{s})$  was transferred from the collection finger with the entire distillation apparatus wrapped in foil for darkness (similar to  $\text{Cl}_2\text{O}$ ).



Thirdly, the white  $\text{N}_2\text{O}_5(\text{s})$  and dark red  $\text{Cl}_2\text{O}(\text{l})$  were combined by transferring  $\text{Cl}_2\text{O}(\text{l})$  at  $-40 \text{ }^\circ\text{C}$  to a finger containing  $\text{N}_2\text{O}_5(\text{s})$  in liquid  $\text{N}_2$ , then putting the mixture into a dry ice/isopropanol bath in order to form light yellow chlorine nitrate  $\text{ClONO}_2(\text{l})$ , with darker fractions containing dissolved  $\text{Cl}_2(\text{g})$ .



This sample was distilled several times to remove lower vapor pressure  $\text{HNO}_3$ , and higher vapor pressure  $\text{Cl}_2\text{O}$  and  $\text{Cl}_2$  impurities. The entire  $\text{ClONO}_2(\text{l})$  sample was transferred to four fingers (in case one finger was damaged/exposed) and stored in dry ice/isopropanol in the dark.

### 6.6.2. Correction for Radial Diffusion

In determining  $k_{\text{obs}}$  from Eq. (6.8), we assume plug flow conditions and average velocity  $v$  in order to calculate  $t$  in Eq. (6.9). However, the flow in our reactor is laminar, characterized by a parabolic velocity profile of the reactant ClONO<sub>2</sub> (where the speed of molecules near the center is  $2v$  and near the walls approaches zero). Accordingly,  $k_{\text{obs}}$  will need to be adjusted upwards, due to the slower speed of molecules near the walls.<sup>45</sup> The standard method of adjustment or correction in order to obtain  $k_w$  is the so-called Brown method.<sup>37</sup>

Using this method to calculate  $k_w$  from  $k_{\text{obs}}$ , several experimental parameters including standard flows  $f(\text{He})$ ,  $f(\text{HCl})$ , and  $f(\text{ClONO}_2)$ , the total pressure  $P$ , absolute temperature  $T$ , tube radius  $r$ , and molecular weight  $M$  of ClONO<sub>2</sub> are required. With this information, the following quantities are calculated:

$$\text{Thermal speed of ClONO}_2, \omega = \sqrt{\frac{8RT}{\pi M_{\text{ClONO}_2}}} \text{ (cm/s)}$$

$$\text{Total standard gas flow, } f(\text{STD}) = f(\text{He}) + f(\text{HCl}) + f(\text{ClONO}_2) \text{ (sccm)}$$

$$\text{Gas flow in flowtube, } f = f(\text{STD}) \frac{760 \text{ torr}}{P} \frac{T}{273 \text{ K}} \text{ (ccm)}$$

$$\text{Linear velocity of ClONO}_2, v = \frac{f}{\pi r^2} \text{ (cm/s)}$$

$$\text{Plug-flow residence time, } t = \frac{1}{v} \text{ (s)}$$

$$\text{Diffusion coefficient}^{38} \text{ of ClONO}_2 \text{ in He, } D_{\text{ClONO}_2/\text{He}} = \frac{176 \text{ torr}}{P} \left( \frac{T}{200 \text{ K}} \right)^{1.76} \text{ (cm}^2/\text{s)}$$

Next, a dimensionless diffusion coefficient is determined in order to simplify the form of the boundary condition for the continuity equation (which is a partial differential equation in, e.g., [ClONO<sub>2</sub>] with a flow term, radial and axial diffusion terms, and a reaction term).<sup>37</sup>

$$D = \frac{D_c}{2rv}$$

Dimensionless diffusion coefficient, D

Diffusion coefficient of species c in carrier gas, D<sub>c</sub> (cm<sup>2</sup>/s)

Flow tube radius, r (cm)

Carrier gas velocity, v (cm/s)

For identical reasons, a dimensionless rate constant is determined.

$$K = k_{\text{obs}} \frac{r}{v}$$

Dimensionless rate constant, K

Observed pseudo-first-order rate constant, k<sub>obs</sub> (s<sup>-1</sup>)

Flow tube radius, r (cm)

Carrier gas velocity, v (cm/s)

Next, several other dimensionless quantities, including α, B<sub>i</sub>, and K<sub>w</sub>, are also calculated.

$$\alpha = K^2 + \frac{K}{D}$$

$$B_0 = 1 \text{ (arbitrary)}$$

$$B_1 = -\frac{\alpha}{4}$$

$$B_n = \frac{1}{4n^2} \left[ B_{n-2} \frac{K}{D} - \alpha B_{n-1} \right] \quad (n \geq 2)$$

$$K_w = \frac{-2D \sum_{n=0}^{\infty} 2nB_n}{\sum_{n=0}^{\infty} B_n} \approx \frac{-2D(0 + 2B_1 + 4B_2 + 6B_3 + 8B_4 + \dots + 40B_{20})}{(B_0 + B_1 + B_2 + B_3 + B_4 + \dots + B_{20})}$$

Once the corrected unitless rate constant is determined, the deposition velocity  $\kappa_w$  in cm/s and corrected pseudo-first-order rate constant  $k_w$  are easily determined.

$$\kappa_w = vK_w \text{ (cm/s)}$$

$$\kappa_w = k_w \frac{V}{A} = k_w \frac{r}{2}$$

where  $V$  and  $A$  are the geometric volume and surface area, respectively. An alternative method that works equally well in this experiment is the sum-of-resistance method,<sup>36,46</sup> i.e., Eq. (6.10). A major source of uncertainty in both methods is the error in  $D_c$ , likely in error by  $\pm 15\%$  using the expression of Hanson and Ravishankara.<sup>38</sup> If the reaction is diffusion limited, or  $k_d \ll k_w$ , then the rate of reaction is controlled by diffusion to the surface, and distinction between large  $\gamma$  is not possible. (The bigger the ratio  $\frac{k_d}{k_w}$ , the better for measurement of large  $k_w$  or  $\gamma$ ).

### 6.6.3. Correction for Internal Diffusion

The substrate deposited on the walls of a flowtube may be inefficiently as well as irregularly packed, with a rough surface, and porous, resulting in a surface area greater than the geometric surface area of the flowtube. The reaction time increases due to the additional surface area, and consequently  $\gamma$  calculated after considering radial diffusion (but before considering internal diffusion) may be too large. In principle, a method exists for correcting for this

additional internal surface area.<sup>43</sup> Unlike radial diffusion, this error is most serious for small  $\gamma$ ,<sup>47,48</sup> and may result in an error of an order of magnitude or more;<sup>43</sup> for large  $\gamma$  (~0.1), most of the molecules react on the surface of the substrate before diffusing inwards. We now outline the steps necessary in order to make this correction, which we refer to as the Keyser correction after the lead author of the 1991 paper,<sup>43</sup> in a stepwise manner.

In the case of laminar flow & radial diffusion where  $[\text{ClONO}_2] = f(r)$ ,

$$\text{reaction rate} = - \frac{d[\text{ClONO}_2]}{dt} = k_w[\text{ClONO}_2] = \kappa_w \frac{A}{V} [\text{ClONO}_2]$$

Brown-corrected pseudo-first-order rate constant,  $k_w$  ( $\text{s}^{-1}$ )

Brown-corrected deposition velocity,  $\kappa_w$  (cm/s)

$$k_w = \kappa_w \frac{A}{V} = \kappa_w \frac{2}{r}$$

Now considering internal diffusion (or the internal surface area of the substrate),

$$\text{reaction rate} = - \frac{d[\text{ClONO}_2]}{dt} = Ck_s[\text{ClONO}_2] = \kappa_s \frac{(A_e + \eta A_i)}{V} [\text{ClONO}_2]$$

Ratio of effective to geometric area (needed to “increase”  $\kappa_s$  to obtain the same

rate using  $k_w$ ),  $C = \frac{(A_e + \eta A_i)}{A}$  (unitless)

Keyser-corrected pseudo-first-order rate constant (or the true constant  $k$ ),  $k_s$  ( $\text{s}^{-1}$ )

Keyser-corrected deposition velocity,  $\kappa_s$  (cm/s)

$$k_s = \kappa_s \frac{A}{V} = \kappa_s \frac{2}{r}$$

External surface area,  $A_e$  ( $\text{cm}^2$ )

Effectiveness factor (or fraction of internal surface which takes part in reaction),  
 $\eta$  (unitless)

$$\eta = \frac{\text{observed diffusion - limited rate}}{\text{observed rate (very fast diffusion)}} \rightarrow 1 \text{ for small } \gamma, \quad 0 \leq \eta \leq 1$$

Internal surface area,  $A_i$  ( $\text{cm}^2$ )

The effectiveness factor  $\eta$  is introduced because the rate is affected only by that fraction of the inner surface that takes part in reaction or promotes additional  $\text{ClONO}_2$  loss. For large  $\gamma$ ,  $\eta$  is very small, because most of the molecules finding pores react immediately on the outer part of the inner surface; the converse is true for small  $\gamma$ .

Equating the two reaction rate expressions,

$$\kappa_w \frac{A}{V} [\text{ClONO}_2] = \kappa_s \frac{(A_e + \eta A_i)}{V} [\text{ClONO}_2]$$

Canceling terms and dividing each side by  $A$ ,

$$\kappa_w = \kappa_s \frac{(A_e + \eta A_i)}{A}$$

Deriving expressions for  $A$ ,  $A_e$ , and  $A_i$ ,

$$A = 2\pi(r - h)l \cong 2\pi rl$$

Film thickness,  $h$  ( $\mu\text{m}$ )

Film length,  $l$  (cm)

$$A_e = 2\pi(r - h)l(1 - \theta)\sigma \cong 2\pi rl(1 - \theta)\sigma$$



Porosity,  $\theta$  (unitless)

$$\theta = \frac{\text{volume of void in solid}}{\text{total solid volume}}$$

$$\theta = 1 - \frac{\rho_b}{\rho_t}$$

Bulk density,  $\rho_b$  (g/cm<sup>3</sup>)

True density (from x-ray crystallography),  $\rho_t$  (g/cm<sup>3</sup>)

Roughness factor,  $\sigma$  (unitless)

$$\sigma = \frac{\text{external area}}{\text{geometric area}} > 1$$

$$A_i = \pi[r^2 - (r - h)^2]\rho_b S_g \cong 2\pi r h \rho_b S_g$$

Specific surface area,  $S_g$  (cm<sup>2</sup>/g)

Substituting in the different area expressions, an expression similar to eq. (7) in the original paper is obtained.<sup>43</sup>

$$\kappa_w = \kappa_s [ (1-\theta)\sigma + \eta h \rho_b S_g ]$$

In order to determine  $\kappa_s$  from  $\kappa_w$ , experimental determination of  $\rho_b$  and  $S_g$  is needed, and  $\theta$ ,  $\sigma$ ,  $\eta$ , and  $h$  are required. First, calculation of substrate thickness  $h$  and  $\eta$  is discussed.

$$h = \frac{w}{2\pi r \rho_b} \text{ (valid if } h > d = 6/\rho_t S_g \text{ for spherical granules)}$$

Sample weight,  $w$  (mg)

$$\eta = \phi^{-1} \tanh \phi \quad (\text{eq. 9 from Keyser, L.F. et al, 1991})$$

Theta modulus,  $\phi$  (unitless)

$$\phi = h \sqrt{\frac{rk_s \rho_b S_g}{2D_e}} \quad (\text{eq. 10 from Keyser, L.F. et al, 1991})$$

$$\phi = h \sqrt{\frac{\kappa_s \rho_b S_g}{D_e}} > 0$$

Inactive surface:  $k_s$  small,  $\phi$  small,  $\eta \sim 1$

Active surface:  $k_s$  large,  $\phi$  large,  $\eta \sim \phi^{-1}$

Effective diffusion coefficient,  $D_e$  ( $\text{cm}^2/\text{s}$ )

$$D_e = \frac{\theta D_k}{\tau} = \frac{2\theta r_p \omega}{3\tau}$$

Knudsen diffusion coefficient,  $D_k$  ( $\text{cm}^2/\text{s}$ )

$$D_k = \frac{2r_p \omega}{3}$$

Pore radius,  $r_p$  ( $\mu\text{m}$ )

$$r_p = \frac{2V_g}{S_g} = \frac{2\theta}{S_g \rho_b}$$

$V_g$ : pore volume per unit wgt ( $\text{cm}^3/\text{g}$ )

$$V_g = \frac{\theta}{\rho_b}$$

Tortuosity,  $\tau > 1$  (unitless)

Unfortunately, to determine  $\phi$ ,  $\kappa_s$  is needed, but  $\kappa_s$  is desired in the first place. Rewriting the  $\phi$  expression in terms of  $\kappa_s$ ,

$$\kappa_s = \frac{D_e \phi^2}{h^2 \rho_b S_g}$$

and substituting into the  $\kappa_w$  expression above and rearranging, a new equation is obtained.

$$\Omega \equiv \frac{\rho_b S_g h^2 \kappa_w}{D_e} = \phi^2 [ (1-\theta)\sigma + \eta h \rho_b S_g ] \quad (\text{basically eq. 13 in Keyser, L.F. et al, 1991})$$

Before using the above equation, determination of  $\Omega$ , followed by estimation of other unknowns except  $\eta$ , is necessary. Then  $\eta$  is varied until both sides are equal. Equivalently,  $\Omega$  vs.  $\eta$  is plotted, and the  $\eta$  corresponding to the experimental  $\Omega$  is found. The  $\eta$  is used to solve for  $\kappa_s$  in  $\kappa_w = \kappa_s [ (1-\theta)\sigma + \eta h \rho_b S_g ]$ . Finally, to obtain the correct reaction probability, the following equation is used:

$$\gamma_s = \frac{4\kappa_s}{\omega + 2\kappa_s} \quad (\text{exact})$$

As an exercise, and to illustrate how difficult it is to implement this correction in practice, an attempt is now made to correct hypothetical  $\gamma$ 's for internal diffusion in the  $\alpha$ -alumina columns prepared in Section 6.2.3.

First, determination of  $\Omega$  is attempted using the defining equation and estimates of the various quantities.

$$\Omega \equiv \frac{\rho_b S_g h^2 \kappa_w}{D_e} = \phi^2 [ (1-\theta)\sigma + \eta h \rho_b S_g ]$$

$$\rho_t \sim 3.9 \text{ g/cm}^3 \text{ (from } \alpha\text{-alumina MSDS)}$$

$$\rho_b = (\pi/6)\rho_t \text{ (cubic packing of spheres; eq. 26 in Keyser, L.F. et al, 1991)}$$

$$\rho_b \sim 2.04 \text{ g/cm}^3$$

$$d \sim 0.0001 \text{ cm (approximate Fisher size of } \alpha\text{-alumina)}$$

$$S_g = 6/(\rho_t d) \sim 15385 \text{ cm}^2/\text{g} \text{ (eq. 3 in Keyser, L.F. et al, 1993)}$$

$$h = \frac{W}{2\pi r l \rho_b} \sim (0.030 \text{ g}) / (2\pi \times 0.19 \text{ cm} \times 20 \text{ cm} \times 2.0 \text{ g/cm}^3) = 6.28 \times 10^{-4} \text{ cm}$$

$$\kappa_w = (r/2)k_w = 0.19 \text{ cm}/2 \times 442.8 \text{ s}^{-1} = 42.1 \text{ cm/s}$$

$$\theta = 1 - \rho_b/\rho_t = 0.5 \text{ (eq. 19 in Keyser, L.F. et al, 1991)}$$

$$r_p = \frac{2\theta}{S_g \rho_b} \sim 1/(15385 \times 2.04) = 3.2 \times 10^{-5} \text{ cm (eq. 20 in Keyser, L.F. et al, 1991)}$$

$$\tau \sim 2 \text{ (for most materials, usually 1-8; } k \text{ is not very sensitive to } \tau)^{43}$$

$$D_e = \frac{2\theta r_p \omega}{3\tau} \text{ (eq. 18 in Keyser, L.F. et al, 1991)}$$

$$D_e \sim 2.04 \times 0.5 \times 3.2 \times 10^{-5} \text{ cm} \times 21000 \text{ cm s}^{-1} / (3 \times 2) = 0.112 \text{ cm}^2/\text{s}$$

$$\text{So, } \Omega \sim 2.04 \times 15385 \times (3.22 \times 10^{-4})^2 \times 42.1 / 0.112 = 1.23$$

Next, another unknown is estimated before rewriting the above equation:

$$\sigma \sim 2 \text{ (for most surfaces; equal to 4 in the limit of half-spheres touching)}^{43}$$

$$\Omega \equiv \frac{\rho_b S_g h^2 \kappa_w}{D_e} = \varphi^2 [(1-\theta)\sigma + \eta h \rho_b S_g]$$

$$1.23 = \varphi^2 [1 + 19.71\eta]$$

Next, from the relation  $\eta = \varphi^{-1} \tanh \varphi$ ,  $\Omega$  is calculated and compared to 1.23:

$\varphi$	$\eta$	$\underline{\Omega}$
1	0.762	16.01
0.5	0.924	4.80
0.25	0.9797	1.269
0.24	0.9812	1.172

So,  $\eta \sim 0.98$ .

Finally, for  $\kappa_s$  and  $k_s$  and  $\gamma_s$ ,

$$\kappa_w = \kappa_s [ (1-\theta)\sigma + \eta h \rho_b S_g ]$$

$$\kappa_s = \kappa_w / [ (1-\theta)\sigma + \eta h \rho_b S_g ] \sim 42.1 \text{ cm s}^{-1} / [1 + 0.98 \times 19.71] \sim 2.07 \text{ cm/s}$$

$$k_s = (2/r)\kappa_s \sim 2/0.19 \text{ cm} \times 2.07 \text{ cm/s} \sim 21.8 \text{ s}^{-1}$$

$$\gamma_s = \frac{4\kappa_s}{\omega + 2\kappa_s} \sim 4 \times 2.07 \text{ cm s}^{-1} / [21000 \text{ cm/s} + 2 \times 2.07 \text{ cm/s}] = 0.00039$$

Comparing this to  $\gamma = 0.02$  (the result obtained prior to performing the correction), it is clear that the correction is significant and adjusts downward by roughly a factor of 50 under typical experimental conditions using best “guesses” for the unknown parameters.

#### 6.6.4. Derived Expressions for the Reaction Probability

Recalling that  $\gamma$  is defined as

$$\gamma = \frac{\text{number of collisions with a clean surface leading to reaction}}{\text{total number of collisions with a clean surface}}, 0 \leq \gamma \leq 1,$$

an approximate expression is derived by considering the Boltzmann flux  $J$  (in molec  $\text{cm}^{-2} \text{s}^{-1}$ ) of molecules incident on an infinite, nonreactive, planar surface. This expression is given by the concentration  $[\text{ClONO}_2]$  times the Boltzmann expression for the average speed in the direction normal to the surface ( $+z$ ), identical to the expression for the flux through an  $xy$  plane. That is, the number of  $\text{ClONO}_2$  collisions per unit area of unreactive surface per second is<sup>39</sup>

$$J = [\text{ClONO}_2] \int_0^{\infty} f(v_z) v_z dv_z = [\text{ClONO}_2] \sqrt{\frac{RT}{2\pi M}} = [\text{ClONO}_2] \frac{\omega}{4}$$

where  $\omega = \sqrt{\frac{8RT}{\pi M}}$ ,  $R = 8.31 \frac{\text{J mol}}{\text{K}}$ , and  $M = 0.097 \frac{\text{kg}}{\text{mol}}$  for  $\text{ClONO}_2$ . The number of collisions per second  $N$  (molec  $\text{s}^{-1}$ ) on the entire surface of area  $A = 2\pi r l$  (where  $r$  is the flow tube radius) is

$$N = JA = [\text{ClONO}_2] \frac{\omega}{4} A$$

The number of  $\text{ClONO}_2$  reacting per second (on an active surface) is simply  $\gamma N$ ; so the reaction rate  $-\frac{d[\text{ClONO}_2]}{dt}$ , or the number of  $\text{ClONO}_2$  per unit volume reacting per second, is simply

$$-\frac{d[\text{ClONO}_2]}{dt} = \gamma \frac{N}{V} = \frac{\gamma \omega}{4} \frac{A}{V} [\text{ClONO}_2] = k_w [\text{ClONO}_2]$$

Comparing the latter two terms,

$$k_w = \frac{\gamma \omega}{4} \frac{A}{V} = \kappa_w \frac{A}{V}$$

where the wall loss rate coefficient  $\kappa_w = \frac{\gamma \omega}{4}$  is equivalent to a deposition velocity. Substituting expressions into the above for the geometric surface area  $A = 2\pi r l$  and volume  $V = \pi r^2 l$ ,

$$k_w = \frac{\gamma\omega}{2r} = \kappa_w \frac{2}{r}$$

and solving for  $\gamma$

$$\gamma = \frac{2rk_w}{\omega}$$

$$\gamma = \frac{4\kappa_w}{\omega}$$

which is a good approximation for small  $\gamma$ . However, the above expression needs to be modified due to reaction on a lossy, or reactive, surface.<sup>38</sup> Intuitively, the actual flux  $J$  perpendicular to the surface is increased relative to the Boltzmann flux due to (reactive) uptake; molecules with  $+z$  velocity components are taken up, leading to a shifting of the Boltzmann velocity profile and an increase in the flux. Taking this effect into account, the  $\gamma$  given above is too large.<sup>40</sup> It is thus desirable to recalculate the net flux at the (substrate) boundary and determine  $\gamma$ . (Originally, this was desirable in the context of atom recombination on walls).<sup>42</sup> The boundary condition that the flux  $J^+$  in the direction of the concentration gradient is equal to the net flux  $J$  at the  $\text{Al}_2\text{O}_3$  boundary, or that  $\gamma J^+(\text{@ boundary}) = J$ , is written<sup>41</sup>

$$\gamma \frac{[\text{ClONO}_2]\omega}{4} - \gamma \frac{1}{6} \lambda \frac{\delta[\text{ClONO}_2]}{\delta z} \omega = -\frac{1}{3} \lambda \frac{\delta[\text{ClONO}_2]}{\delta z} \omega$$

where  $\lambda$  is the mean free path.<sup>49</sup> The second and third terms are the result of considering molecular motion and collision. Molecules moving so as to make an angle  $\theta$  with respect to  $+z$  are supposed to come from a point of which the  $z$  coordinate is  $z = z_0 - \lambda \cos\theta$ , and at this point,  $[\text{ClONO}_2] = [\text{ClONO}_2](z_0) - \lambda \cos\theta \frac{\delta[\text{ClONO}_2]}{\delta z}$ . Using this expression for  $[\text{ClONO}_2]$ , the more complicated Boltzmann expression is integrated. (In this special case, the initial velocity of the molecules in the  $+z$  direction is zero due to the carrier gas flow being perpendicular to  $+z$ ). As a check, the above equation correctly implies that if reaction is negligible (or  $\gamma = 0$  making the left-

hand side zero), the net flux is zero (since the only non-zero term is  $\frac{\delta[\text{ClONO}_2]}{\delta z}$ ). Solving for

$$\frac{\delta[\text{ClONO}_2]}{\delta z} \text{ in the above equality and substituting into the expression } J = -\frac{1}{3}\lambda \frac{\delta[\text{ClONO}_2]}{\delta z} \omega$$

and simplifying, the net flux J is correctly determined.

$$J = [\text{ClONO}_2] \frac{\omega}{4} \frac{\gamma}{1 - \frac{\gamma}{2}}$$

This expression for the flux is twice as great as the simpler expression given completely efficient reaction ( $\gamma = 1$ ). As above, this expression for J is used to determine N and  $k_w$ :

$$N = JA$$

$$k_w = \frac{\omega}{4} \frac{\gamma}{1 - \frac{\gamma}{2}} \frac{A}{V} = \frac{\omega}{2r} \frac{\gamma}{1 - \frac{\gamma}{2}}$$

Solving for  $\gamma$ , we obtain

$$\gamma = \frac{2rk_w}{\omega + rk_w} \quad (\text{exact})$$

$$\gamma = \frac{4\kappa_w}{\omega + 2\kappa_w} \quad (\text{exact})$$

## REFERENCES FOR CHAPTER 6

- (1) Brady, B.; Fournier, E.; Martin, L.; Cohen, R. "Stratospheric Ozone Reactive Chemicals Generated by Space Shuttle Launches Worldwide," Aerospace Corporation, 1994.
- (2) Prather, M. J.; García, M. M.; Douglass, A. R.; Jackman, C. H.; Ko, M. K. W.; Sze, N. D. *J. Geophys. Res.* **1990**, *95D*, 18583.
- (3) Granier, C.; Brasseur, G. *J. Geophys. Res.* **1992**, *97D*, 18015.



- (4) Albritton, D. L.; Watson, R. T.; Aucamp, P. J.; Mégie, G. "WMO/UNEP Scientific Assessment of Ozone Depletion: 1998," World Meteorological Organization Global Ozone Research and Monitoring Project, 1998.
- (5) Danilin, M. *Ann. Geophys.* **1993**, *11*, 828.
- (6) Denison, M.; Lamb, J.; Bjordahl, W.; Wong, E.; Lohn, P. *J. Spacecraft Rockets* **1994**, *31*, 435.
- (7) Krüger, B. *Ann. Geophys.* **1994**, *12*, 409.
- (8) Burke, M.; Zittel, P. *Combust. Flame* **1998**, *112*, 210.
- (9) Ross, M. *J. Spacecraft Rockets* **1996**, *33*, 144.
- (10) Ross, M.; Ballenthin, J.; Gosselin, R.; Meads, R.; Zittel, P.; Benbrook, J.; Sheldon, W. *Geophys. Res. Lett.* **1997**, *24*, 1755.
- (11) Jones, A.; Bekki, S.; Pyle, J. *J. Geophys. Res.* **1995**, *100D*, 16651.
- (12) Ross, M.; Benbrook, J.; Sheldon, W.; Zittel, P.; McKenzie, D. *Nature* **1997**, *390*, 62.
- (13) Ross, M.; Toohey, D.; Rawlins, W.; Richard, E.; Kelly, K.; Tuck, A.; Proffitt, M.; Hagen, D.; Hopkins, A.; Whitefield, P.; Benbrook, J.; Sheldon, W. *Geophys. Res. Lett.* **2000**, *27*, 2209.
- (14) Brownlee, D. E.; Ferry, G. V.; Tomandl, D. *Science* **1976**, *191*, 1270.
- (15) Zolensky, M. E.; McKay, D. S.; Kaczor, L. A. *J. Geophys. Res.* **1989**, *94D*, 1047.
- (16) Cofer, W. R., III; Winstead, E. L.; Key, L. E. *J. Propul. Power* **1989**, *5*, 674.
- (17) Brady, B.; Martin, L. "Modeling Solid Rocket Booster Exhaust Plumes in the Stratosphere," Aerospace Corporation, 1995.
- (18) Cofer, W. R., III; Purgold, G. C.; Winstead, E. L.; Edahl, R. A. *J. Geophys. Res.* **1991**, *96D*, 17371.
- (19) Molina, M. J.; Molina, L. T.; Zhang, R. Y.; Meads, R. F.; Spencer, D. D. *Geophys. Res. Lett.* **1997**, *24*, 1619.
- (20) Molina, L. T.; Molina, M. J.; Stachnik, R. A.; Tom, R. D. *J. Phys. Chem.* **1985**, *89*, 3779.
- (21) Kolb, C. E.; Worsnop, D. R.; Zahniser, M. S.; Davidovits, P.; Keyser, L. F.; Leu, M.-T.; Molina, M. J.; Hanson, D. R.; Ravishankara, A. R. Laboratory studies of atmospheric heterogeneous chemistry. In *Advances in Physical Chemistry Series (Progress and Problems in Atmospheric Chemistry)*; Barker, J. R., Ed.; World Scientific: London, 1995.
- (22) Jackman, C. H.; Considine, D. B.; Fleming, E. L. *J. Geophys. Res.* **1996**, *101D*, 12523.
- (23) Jackman, C. H.; Considine, D. B.; Fleming, E. L. *Geophys. Res. Lett.* **1998**, *25*, 907.
- (24) Dentamaro, A. V.; Dao, P. D.; Farley, R.; Ross, M. *Geophys. Res. Lett.* **1999**, *26*, 2395.
- (25) Danilin, M.; Ko, M.; Weisenstein, D. *J. Geophys. Res.* **2001**, *106D*, 3591.
- (26) Danilin, M.; Shia, R.; Ko, M.; Weisenstein, D.; Sze, N.; Lamb, J.; Smith, T.; Lohn, P.; Prather, M. *J. Geophys. Res.* **2001**, *106D*, 12727.
- (27) Beiting, E. *J. Spacecraft Rockets* **1997**, *34*, 303.
- (28) Molina, L. T.; Spencer, J. E.; Molina, M. J. *Chem. Phys. Lett.* **1977**, *45*, 158.
- (29) Schack, C. J. *Inorg. Chem.* **1967**, *6*, 1938.
- (30) Schack, C. J.; Lindahl, C. B. *Inorg. Nucl. Chem. Lett.* **1967**, *3*, 387.
- (31) Cady, G. H. *Inorg. Syn.* **1957**, *5*, 156.

78. (32) Gruenhut, N. S.; Goldfank, M.; Cushing, M. L.; Caesar, G. V. *Inorg. Syn.* **1950**, 3, 772.
- (33) Huey, L. G.; Hanson, D. R.; Howard, C. J. *J. Phys. Chem.* **1995**, 99, 5001.
- (34) Abbatt, J. P. D.; Beyer, K. D.; Fucaloro, A. F.; McMahon, J. R.; Wooldridge, P. J.; Zhang, R.; Molina, M. J. *J. Geophys. Res.* **1992**, 97D, 15819.
- (35) Molina, L. T.; Molina, M. J. *J. Photochem.* **1979**, 11, 139.
- (36) Zasyplin, A.; Grigor'eva, V.; Korchak, V.; Gershenson, Y. *Kinet. Catal.* **1997**, 38, 772.
- (37) Brown, R. L. *J. Res. Nat. Bur. Stand.* **1978**, 83, 1.
- (38) Hanson, D.; Ravishankara, A. R. *J. Geophys. Res.* **1991**, 97D, 18015.
- (39) Alberty, R. A.; Silbey, R. J. *Physical Chemistry*; John Wiley & Sons: New York, 1992.
- (40) Worsnop, D. R.; Zahniser, M. S.; Kolb, C. E.; Gardner, J. A.; Watson, L. R.; Van Doren, J. M.; Jayne, J. T.; Davidovits, P. J. *J. Phys. Chem.* **1989**, 93, 1159.
- (41) Motz, H.; Wise, H. *J. Chem. Phys.* **1960**, 32, 1893.
- (42) Wise, H.; Ablow, C. M. *J. Chem. Phys.* **1958**, 29, 634.
- (43) Keyser, L. F.; Moore, S. B.; Leu, M.-T. *J. Phys. Chem.* **1991**, 95, 5496.
- (44) Ross, M. N.; Whitefield, P. D.; Hagen, D. E.; Hopkins, A. R. *Geophys. Res. Lett.* **1999**, 26, 819.
- (45) Howard, C. J. *J. Phys. Chem.* **1979**, 83, 3.
- (46) Poschl, U.; Canagaratna, M.; Jayne, J. T.; Molina, L. T.; Worsnop, D. R.; Kolb, C. E.; Molina, M. J. *J. Phys. Chem. A* **1998**, 102, 10082.
- (47) Keyser, L. F.; Moore, S. B.; Leu, M.-T. *J. Phys. Chem.* **1993**, 97, 2800.
- (48) Hanson, D.; Ravishankara, A. R. *J. Phys. Chem.* **1993**, 97, 2802.
- (49) Jeans, J. *The Dynamical Theory of Gases*, 4th ed.; Dover: New York, 1954.

**Table 6.1. Typical system parameters and experimental conditions used during experiments. Calculation of the Reynolds Number  $Re = vdr/h$ , assuming  $v \sim 2000$  cm/s,  $d = 0.37$  cm, the ideal density  $r$  of He (at 223 K and 22.7 Torr) is  $6.5 \times 10^{-4}$  g/cm<sup>3</sup>, and the viscosity  $h$  of He at 223 K is  $1.6 \times 10^{-4}$  g/(cm-s). Mean free path of ClONO<sub>2</sub>  $l \sim 1/(p d(He)^2 N^*)$  with molecular diameter of He  $d(He) = 2.2 \times 10^{-8}$  cm and a He number density  $N^*$  of 30 Torr =  $9.6 \times 10^{15}$  molecule/cm<sup>3</sup>.**

N <sub>2</sub> make-up gas flow	500 – 750 sccm
SF <sub>6</sub> flow and mixing ratio	1 sccm (10 % in N <sub>2</sub> )
NO <sub>2</sub> flow and mixing ratio	0.5 sccm (0.1 % in N <sub>2</sub> )
He (4.7) carrier gas flow	750 sccm
Re / $\lambda$	$\sim 30$ (laminar) / 7 $\mu$ m
ClONO <sub>2</sub> / HCl mixing ratio in bulbs	$10^{-3} / 10^{-4}$
Humidity in flowtube	$> 6 \times 10^{10}$ molecule/cm <sup>3</sup> ( $> 2 \times 10^{-6}$ Torr)
Pressure P in flowtube	22 – 30 Torr
Reaction temperature T	223 , $\sim 230$ , 238 K
Maximum reaction distance l	10 cm
Pressure in ionization region	1 – 10 Torr
Ionization reaction time	1 – 3 ms
Orifice diameter / voltage	0.5 mm / -85 V
ClONO <sub>2</sub> concentration	$3 - 5 \times 10^{10}$ molecule/cm <sup>3</sup> ( $1.0 - 1.6 \times 10^{-6}$ Torr)
HCl concentration	$3 \times 10^{11}$ molecule/cm <sup>3</sup> ( $10^{-5}$ Torr)
LOD - ClONO <sub>2</sub>	$3 \times 10^9$ molecule/cm <sup>3</sup> ( $10^{-7}$ Torr)
LOD – HCl	$7 \times 10^9$ molecule/cm <sup>3</sup> ( $2 \times 10^{-7}$ Torr)
LOD - Cl <sub>2</sub> (without NO <sub>2</sub> )	$1 \times 10^{10}$ molecule/cm <sup>3</sup> ( $3 \times 10^{-7}$ Torr)
LOD - Cl <sub>2</sub> (with NO <sub>2</sub> )	$7 \cdot 10^9$ molecule/cm <sup>3</sup> ( $2 \cdot 10^{-7}$ Torr)

**Table 6.2.** Average pseudo-first-order rate constant  $k_{\text{obs}}$  on various surfaces, calculated from the results in Table 6.3. The investigation of the chlorine activation reaction on glass in conjunction with a capped injector served as a control experiment. The absolute values for  $k_{\text{obs}}$  and reaction probability  $g$  on glass with a capped injector compare reasonably well with earlier measurements.

Surface	Temperature [K]	HCl molecules per unit area ( $10^{15}/\text{cm}^2$ )	$k_{\text{obs}} \pm 2\sigma$ ( $\text{s}^{-1}$ )
Glass (capped injector)	230	0.5	$440.4 \pm 43.5$ $\gamma = 0.0155 \pm 0.0015$
Halocarbon wax	223	0.3	$106.0 \pm 34$
Halocarbon wax	238	0.3	$145.5 \pm 13$
Glass (open injector)	223	0.5	$167.1 \pm 18.2$
Glass (open injector)	238	0.5	$191.7 \pm 23.8$
$\alpha$ -alumina (0.88 $\mu\text{m}$ )	223	0.2	$442.8 \pm 82.3$
$\alpha$ -alumina (0.88 $\mu\text{m}$ )	238	0.2	$516.6 \pm 79.1$
SRM dust ( $\sim 1 \mu\text{m}$ )	223	0.9	$470.6 \pm 48.2$
SRM dust ( $\sim 1 \mu\text{m}$ )	238	0.9	$442.5 \pm 86.0$
SRM slack ( $\sim 1 \mu\text{m}$ )	223	0.4	$339.0 \pm 28.0$
SRM slack ( $\sim 1 \mu\text{m}$ )	238	0.4	$413.0 \pm 34.9$

**Table 6.3. Measured experimental pseudo-first-order rate constants  $k_{\text{obs}} \pm s(k)$  and where applicable reaction probabilities  $g \pm 2s(g)$  for different surfaces at different temperatures. The average of the results for a particular surface at a given temperature is given in Table 6.2. Not shown are correlation coefficients  $R^2$  that are  $> 0.97$  except for a few cases.**

Surface (T) K ( $s^{-1}$ )	$\sigma(k)$ ( $s^{-1}$ )	Surface (T) k ( $s^{-1}$ )	$\sigma(k)$ ( $s^{-1}$ )	$\gamma$	$2\sigma(\gamma)$	Surface (T) k ( $s^{-1}$ )	$\sigma(k)$ ( $s^{-1}$ )	Surface (T) k ( $s^{-1}$ )	$\sigma(k)$ ( $s^{-1}$ )
<b>Glass</b> (223 K)		<b>Glass w/ capped injector</b> (~ 230 K)				<b>Wax</b> (223 K)		<b>Shuttle Slack</b> (223 K)	
242	9	414.27	30.17	0.0134	0.0020	116	30	212	8
224	17	427.28	30.44	0.0145	0.0021	96	4	251	5
321	10	419.83	14.4	0.014	0.0010	(238 K)		213	13
95	5	450.24	10.6	0.01632	0.0008	141	5	224	9
88	5	442.18	25.62	0.01539	0.0018	150	8	221	11
135	5	488.77	19.23	0.01913	0.0015	<b>Lab a-alumina</b> (223 K)		253	17
119	10	<b>Shuttle Dust</b>				512	39	282	6
113	12	(223 K)				292	15	271	17
149	11	508	22			441	58	458	28
160	9	589	13			330	25	448	18
166	3	465	27			431	76	485	22
193	13	586	80			528	77	456	8
(238 K)		388	1			395	1	439	6
256	13	473	26			417	87	411	15
198	19	368	23			447	58	461	27
201	12	388	1			451	46	(238 K)	
189	8	(238 K)				462	10	244	15
148	9	621	72			533	13	291	25
189	9	530	66			518	30	254	13
221	11	386	34			(238 K)		287	5
168	14	405	30			588	98	274	15
172	10	357	72			396	19	247	12
168	10	438	45			458	55	550	20
199	16	391	24			460	42	528	17
		412	1			488	36	532	16
						471	5	497	18
						469	91	400	12
						555	37	389	21
						663	32	480	19
						573	14	514	18
						562	6	515	28
								450	12
								502	24
								480	24

## LIST OF FIGURES FOR CHAPTER 6

Figure 6.1. Previously published electron micrographs of alumina collected from the stratosphere (Reference 14). The spheres are colorless and pure alumina. Departures from sphericity are small.

Figure 6.2. Schematic representation of the mini-flowtube CIMS developed in this work. All tubing consists of 1/8" stainless steel up to point labeled 5; beyond, it consists of 1/4" glass tubing. 1: Dew point measurement; 2: Pressure measurement to determine the humidity in the reaction zone; 3: HCl injection into He carrier gas; 4: Injection of ClONO<sub>2</sub> through movable 1/16" stainless steel injector; 5: Pre-flowtube pressure measurement; 6: Cooler; 7: Post-flowtube pressure measurement; 8: Ionization of reactants and products; 9: Ion extraction through a 0.5 mm orifice biased at -105 V; 10: quadrupole mass spectrometer.

Figure 6.3. Photo of the mini-flowtube CIMS developed. The system is compact and easy-to-use. In the center of the apparatus, the black, insulated cooler is displayed, containing the flowtube, while the ClONO<sub>2</sub> reagent bulb is visible at the top. The mass spectrometer is in the rear beside the electronic tuning rack, and the computer for data processing is in the forefront.

Figure 6.4. Representative F<sup>35</sup>ClONO<sub>2</sub><sup>-</sup> signal at m/e = 115.1 on Shuttle Dust as a function of injector distance obtained on December 3, 1998.

Figure 6.5. Optical microscope images of commercial  $\alpha$ -Al<sub>2</sub>O<sub>3</sub> (top; average particle diameter 0.88  $\mu$ m, measuring bar = 25  $\mu$ m), Shuttle Dust (middle; average diameter  $\sim$ 1  $\mu$ m, measuring bar = 25  $\mu$ m), and Slack (bottom; average diameter  $\sim$ 1  $\mu$ m, measuring bar = 40  $\mu$ m) employed.

Figure 6.6. Typical background-subtracted absorbance spectrum of a  $0.9 \times 10^{-3}$  mole fraction ClONO<sub>2</sub> in He mixture at P = 1076 Torr.

Figure 6.7. Decay of  $10^{-3}$  mole fraction ClONO<sub>2</sub> in He mixture in a quartz cell measured over several days. Black circles correspond to ClONO<sub>2</sub> in 5.0 Grade He passed through a  $\gamma$ -alumina molecular sieve water trap. Gray squares correspond to ClONO<sub>2</sub> in 4.7 Grade He not dried.

Figure 6.8. Representative plot used for the determination of  $k_{\text{obs}}$  of Rx. (1) on glass at 228 K and 26.5 Torr using a capped injector (perfect mixing). At each specified time, the background (74 counts/s) was first subtracted from the signal  $S$  (ranging from 151 – 421 counts/s) before calculating  $S/S_0$ . The reaction length was transformed into reaction time using a linear gas velocity of 2759 cm/s, and  $R^2$  stands for the square regression coefficient.

Figure 6.1

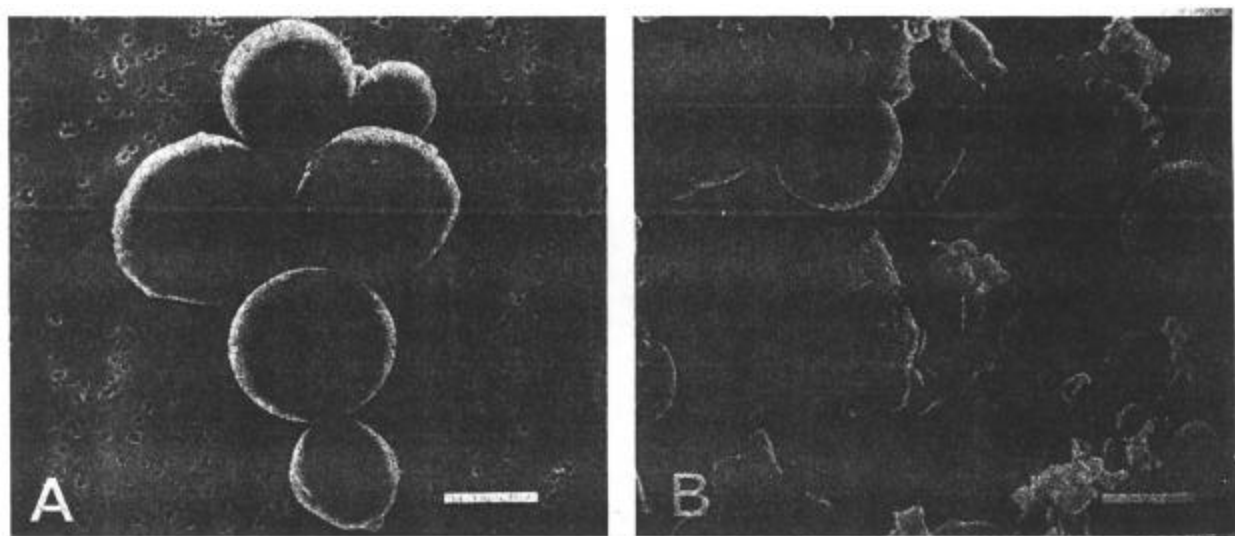




Figure 6.2

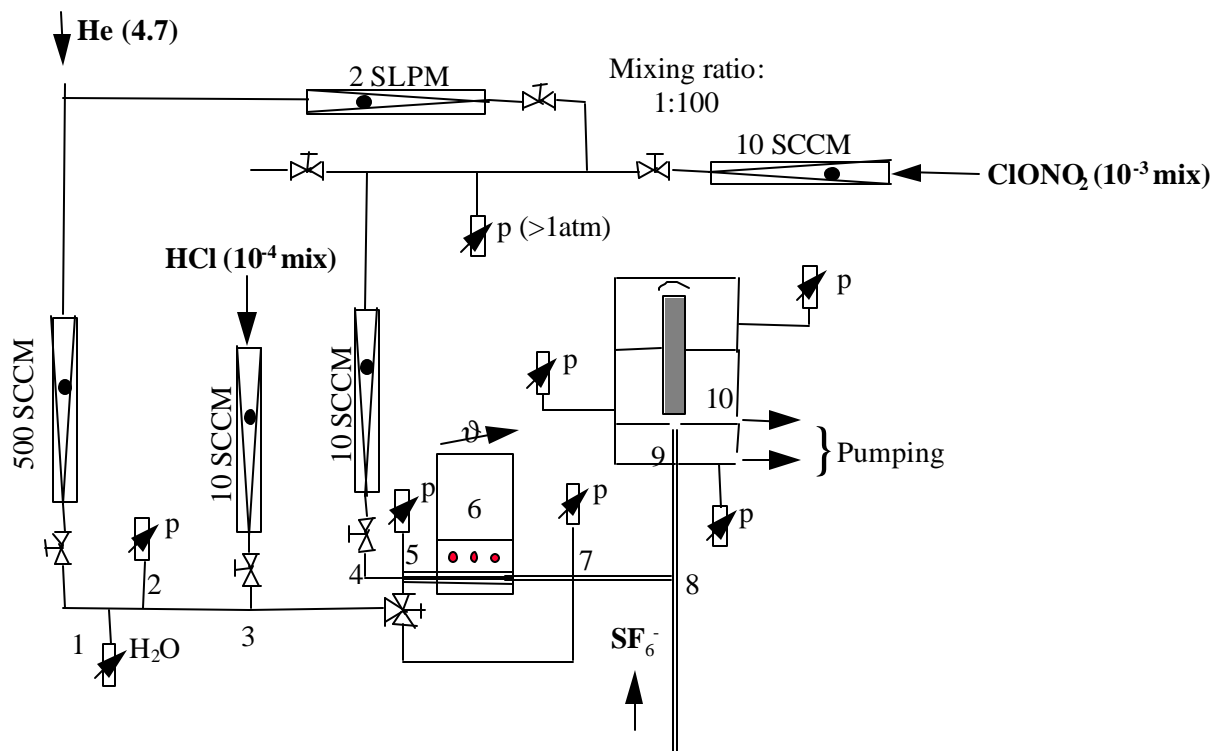


Figure 6.3

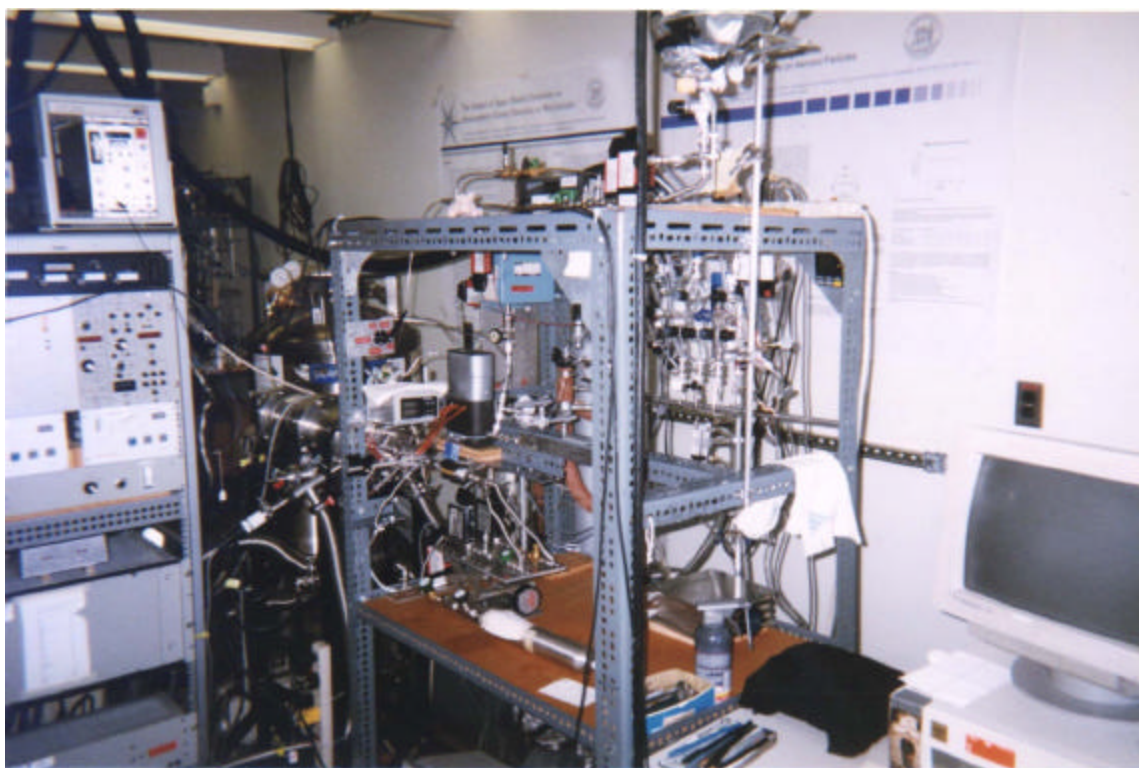


Figure 6.4

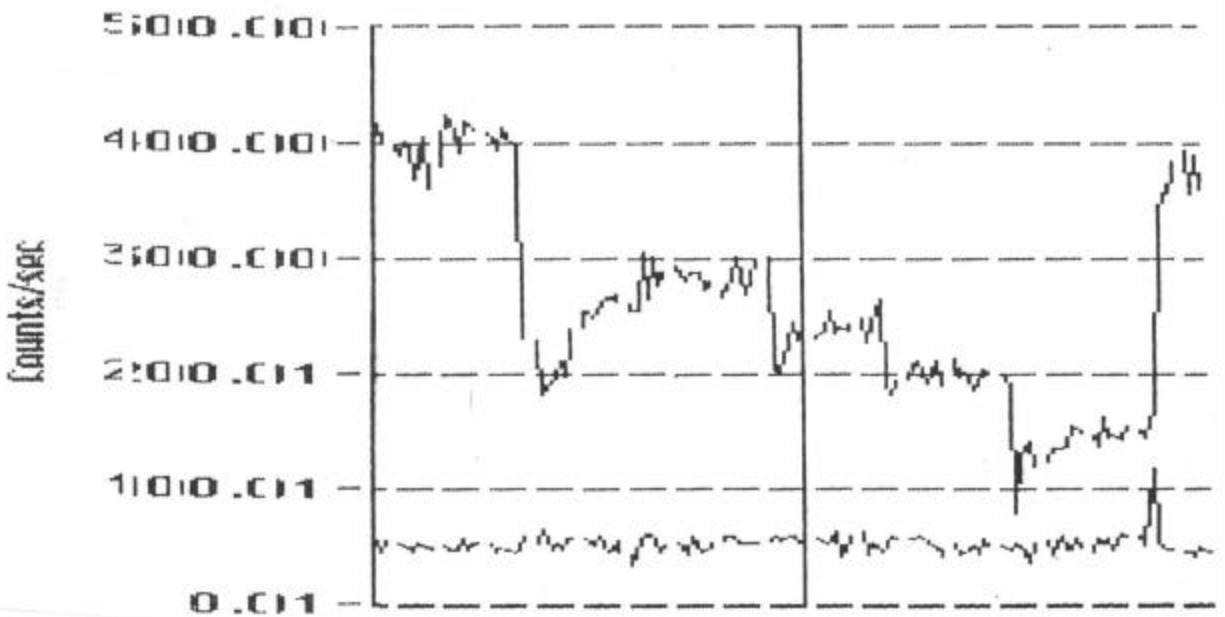


Figure 6.5

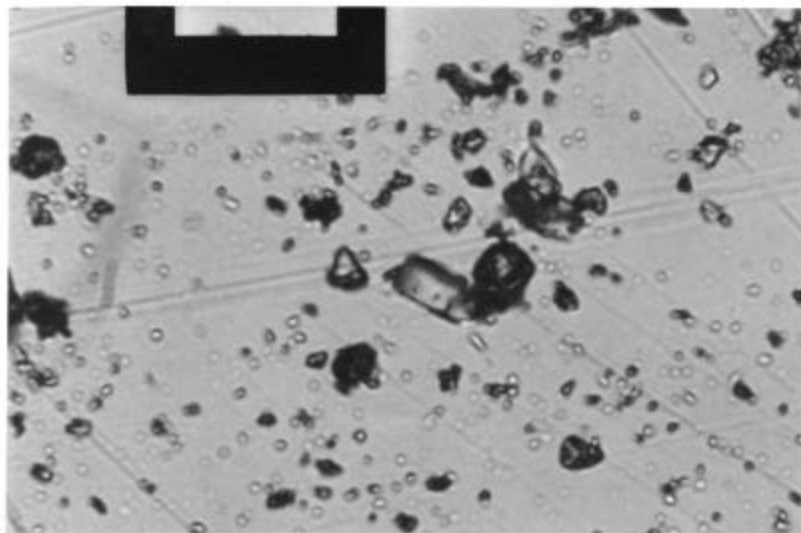
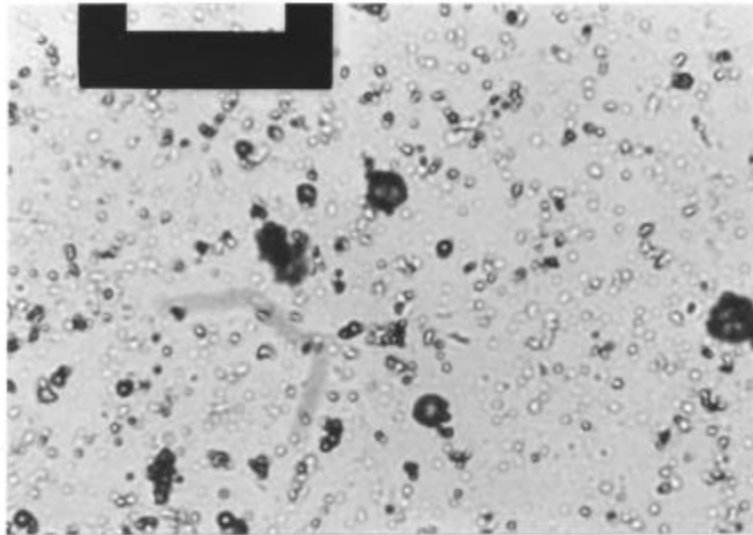
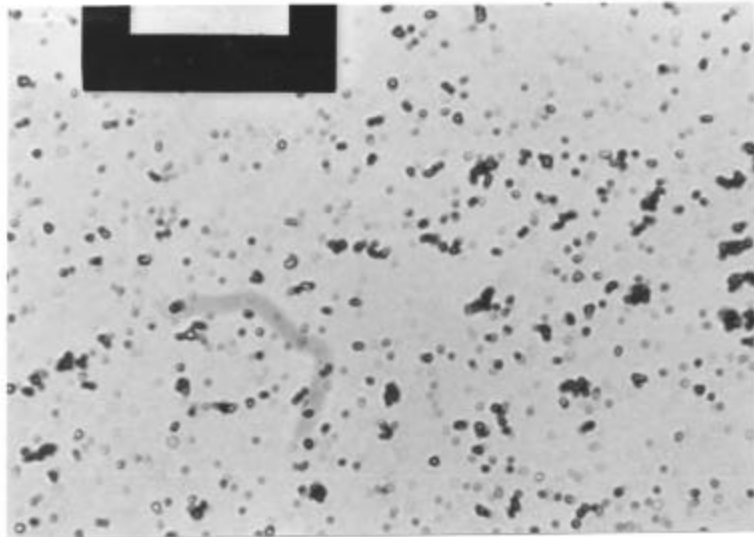


Figure 6.6

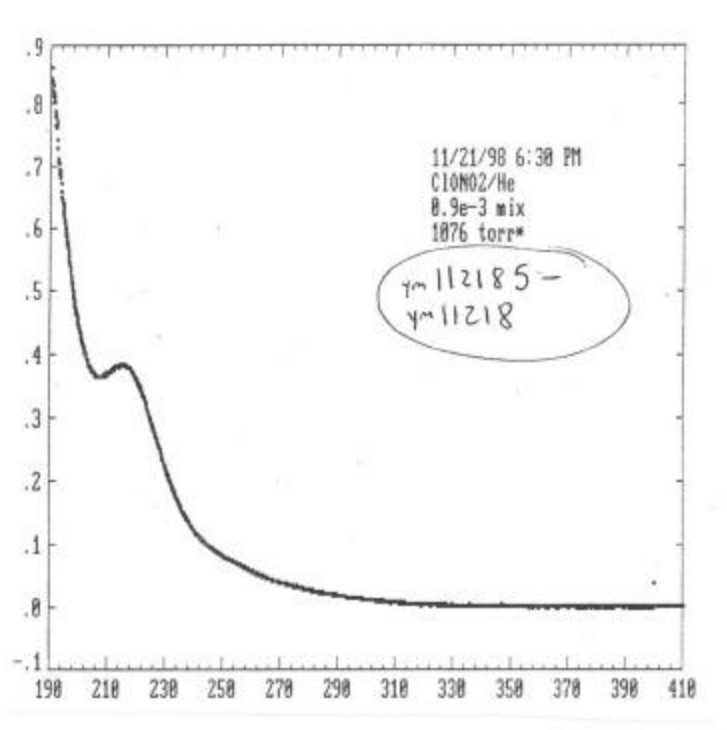


Figure 6.7

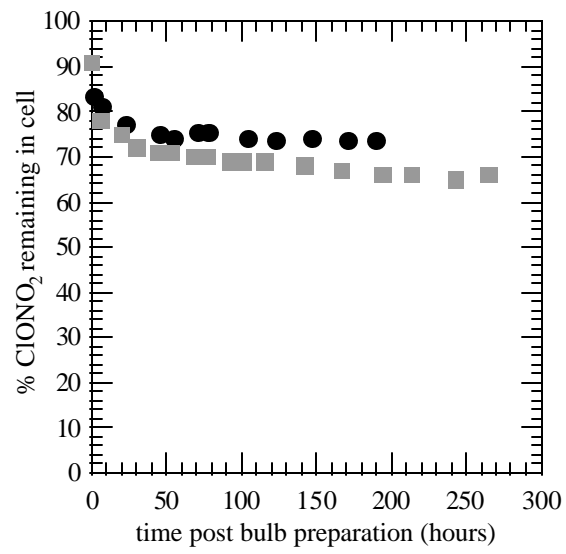
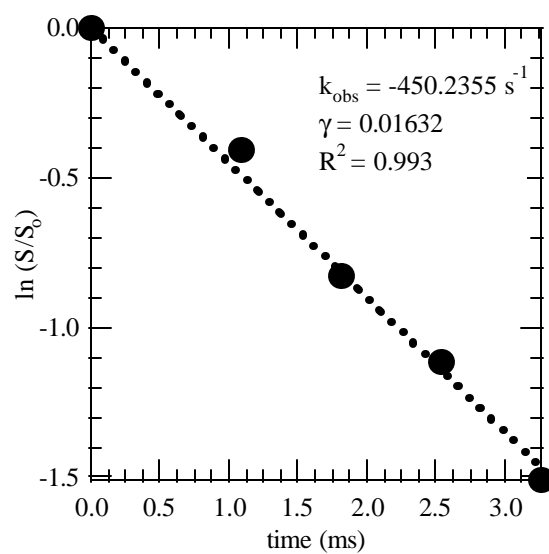


Figure 6.8



## Chapter 7: Conclusions and Future Directions

In this work, we approach the problem of understanding better polar stratospheric ozone depletion from a molecular-level perspective in a systematic manner. Using sophisticated computational methods, we determine the atmospheric fate of HCl adsorbed on ice and NAT, a key step prior to chlorine activation in the polar stratosphere, paying particular attention to the role that is played by surface dangling OH groups and the effect of HCl on ice surface disordering. The key findings described in Chapter 2 – 5 are:

- (1) There is (at least) one site on the ice *h* surface at which the dissociation of HCl is both kinetically rapid and thermodynamically favorable, i.e., when HCl (adsorbed at a surface H<sub>2</sub>O molecule) is strongly interacting with two nearby dangling OH groups. The concentration of these sites on PSC cloud particles is, however, unknown. In addition, because the surface coverage of HCl is high ( $\frac{1}{4}$  ML), significant disordering of the ice surface is observed. At other sites where HCl is interacting less strongly or is interacting with only one dangling OH group, dissociation is not likely, and disordering of the ice surface is not observed, despite the fact that the surface coverage of HCl remains high.
- (2) Although there are (at least) two sites on crystalline NAT that exhibit a high affinity for HCl, dissociation of HCl at either of these sites is not likely, due to the fact that nearby dangling OH groups do not interact effectively with adsorbed HCl.

These findings lead to (1) progress towards the resolution of the state of HCl on ice, i.e., either molecularly or ionically adsorbed, which is unclear from experimental studies, (2) a prediction of the state of HCl on NAT, i.e., molecularly adsorbed, and (3) the prediction of an alternative mechanism of chlorine activation on ice.<sup>1</sup> This alternative mechanism involves the partial dissociation of HCl atop the surface prior to reaction with HOCl or ClONO<sub>2</sub> (as also proposed by others),<sup>2,3</sup> effectively lowering the barrier to reaction with either closed-shell molecular species. It is expected that this new mechanism will compete favorably with other proposed mechanisms of chlorine activation, including (1) HCl dissociation involving concerted



proton transfer within the dynamic ice lattice in conjunction with  $S_N2$  attack by  $Cl^-$ ,<sup>4-6</sup> and (2) HCl dissolution in a proposed “quasi-liquid,” or disordered, surface.<sup>7,8</sup> Thus, it is referred to as a complementary mechanism.<sup>2,3</sup> In order to address the relative efficiency of these different proposed mechanisms, the following future directions are suggested, ideally in conjunction with carefully planned and executed experimental studies:

- (1) The theoretical study of the reaction of partially dissociated HCl with  $ClONO_2$  and HOCl, employing the same computational approaches and extended surface models in order to characterize the molecular-level dynamics and thermodynamics.
- (2) A transition-state search and a reaction-path, and thus barrier-height, determination, using one or a combination of high-level theoretical methods, including transition search in Gaussian,<sup>9</sup> nudged elastic band<sup>10</sup> and transition path sampling;<sup>11,12</sup>
- (3) If necessary, the study of the mechanisms proposed by others on the same extended ice model with the same theoretical method in order to have a direct comparison of alternative mechanisms. For example, removing a surface water molecule and replacing it with HCl and performing a CPMD simulation would be one possible simulation in the study of the “quasi-liquid layer” hypothesis, while the simulations performed by Hynes and co-workers would be easily adapted to our method/model. Size effects (i.e., increasing lateral dimensions systematically) and/or varying the reactant surface coverage and adding defect sites are important variables to consider.

Other possible future directions of interest include:

- (1) The study of the hydrolysis of  $ClONO_2$  with our method/model, which might shed additional light on whether or not an  $H_2OCl^+$  intermediate is involved.<sup>13</sup>
- (2) The theoretical study of the autocatalytic reaction of  $ClONO_2$  with HOCl, recently demonstrated experimentally,<sup>14</sup> but the proposed microscopic mechanism of which would be useful to verify or refute using a theoretical approach.
- (3) A parallel study of the analogous reaction and processes involving bromine compounds, which are suspected on a per-atom basis to be more significant than those involving chlorine compounds.

Chlorine activation on ice is a complex problem that requires a highly interdisciplinary approach in order to solve. The CPMD methodology is undoubtedly successful and applicable to the resolution of this problem, as the results presented herein suggest. However, no single approach, either experimental or theoretical, will be successful by itself in elucidating the mechanism. Consequently, we emphasize the importance of a concerted attack of this problem.

\*\*\*\*\*

We also present in this work our best and most recent attempt to measure the pseudo-first-order rate constant of the heterogeneous reaction of  $\text{ClONO}_2 + \text{HCl}$  on laboratory  $\alpha$ -alumina, a proxy for SRM emissions from spacecraft,<sup>15</sup> and small samples of the actual emissions themselves, in order to determine the effect of the SRM emissions on stratospheric ozone at mid-latitudes. Based on the measurements described in Chapter 6, our tentative conclusion is that laboratory  $\alpha$ -alumina and SRM emissions promote equally efficiently the activation of chlorine, a reasonable conclusion given that the differences between laboratory  $\alpha$ -alumina and SRM emissions are comparatively small, i.e., SRM emissions consist of a mixture of hexagonal- $\alpha$  and cubic- $\gamma$  forms and have trace surface impurities.<sup>15</sup> Consequently, the prediction by atmospheric modelers<sup>16,17</sup> that SRM emissions have relatively little impact on annually averaged total global ozone loss does not need to be revisited.

In principle, it would be possible to repeat the measurements using a reconfigured mass spec-flowtube apparatus with orders-of-magnitude greater sensitivity in order to measure definitively the pseudo-first-order rate constants, and/or design a careful experiment in order to determine the reaction probability independent of the reaction probability on laboratory  $\alpha$ -alumina. The measurements might be performed at room temperature in order to circumvent the problem of cracked and porous wax at cold temperatures introducing a systematic error and contributing to the observed reaction probability. Larger amounts of SRM sample might be required, necessitating collection of grams, as opposed to milligrams, of sample, from an actual shuttle launch site. However, it is unlikely that the measured reaction probability on SRM emissions will deviate significantly from 0.02, which recent modeling studies indicate is not large enough to impact ozone on a global, or even a regional, scale.<sup>16,17</sup> Consequently,

performing an additional, careful set of measurements at this time is not a priority and is not recommended.

## REFERENCE FOR CHAPTER 7

- (1) Mantz, Y. A.; Geiger, F. M.; Molina, L. T.; Molina, M. J.; Trout, B. L. *Chem. Phys. Lett.* **2001**, *348*, 285.
- (2) Bolton, K.; Pettersson, J. B. C. *J. Am. Chem. Soc.* **2001**, *123*, 7360.
- (3) Svanberg, M.; Pettersson, J. B. C.; Bolton, K. *J. Phys. Chem. A* **2000**, *104*, 5787.
- (4) Bianco, R.; Hynes, J. T. *J. Phys. Chem. A* **1999**, *103*, 3797.
- (5) Gertner, B. J.; Hynes, J. T. *Faraday Discuss.* **1998**, *110*, 301.
- (6) Gertner, B. J.; Hynes, J. T. *Science* **1996**, *271*, 1563.
- (7) Molina, M. J. The probable role of stratospheric 'ice' clouds: Heterogeneous chemistry of the 'ozone hole'. In *The Chemistry of the Atmosphere: Its Impact on Global Change*; Calvert, J. G., Ed.; Blackwell Scientific Publications: Oxford, 1994; p. 27.
- (8) Abbatt, J. P. D.; Beyer, K. D.; Fucaloro, A. F.; McMahon, J. R.; Wooldridge, P. J.; Zhang, R.; Molina, M. J. *J. Geophys. Res.* **1992**, *97D*, 15819.
- (9) Frisch, M. J.; Trucks, G. W.; Schlegel, H. B.; Gill, P. M. W.; Johnson, B. G.; Robb, M. A.; Cheeseman, J. R.; Keith, T. A.; Petersson, G. A.; Montgomery, J. A.; Raghavachari, K.; Al-Laham, M. A.; Zakrzewski, V. G.; Ortiz, J. V.; Foresman, J. B.; Cioslowski, J.; Stefanov, B. B.; Nanayakkara, A.; Challacombe, M.; Peng, C. Y.; Ayala, P. Y.; Chen, W.; Wong, M. W.; Andres, J. L.; Replogle, E. S.; Gomperts, R.; Martin, R. L.; Fox, D. J.; Binkley, J. S.; Defrees, D. J.; Baker, J.; Stewart, J. P.; Head-Gordon, M.; Gonzalez, C.; Pople, J. A. *Gaussian 94 (Revision E.3)*; Gaussian, Inc.: Pittsburgh, PA, 1995.
- (10) Jónsson, H.; Mills, G.; Jacobson, K. W. Nudged elastic band method for finding minimum energy paths of transition. In *Classical and Quantum Dynamics in Condensed Phase Simulations*; Berne, B. J., Ciccotti, G., Coker, D. F., Eds.; World Scientific Publishing Co.: Singapore, 1998; p. 385.
- (11) Geissler, P. L.; Dellago, C.; Chandler, D.; Hutter, J.; Parrinello, M. *Science* **2001**, *291*, 2121.
- (12) Dellago, C.; Bolhuis, P. G.; Csajka, F. S.; Chandler, D. *J. Chem. Phys.* **1998**, *108*, 1964.
- (13) Bianco, R.; Thompson, W. H.; Morita, A.; Hynes, J. T. *J. Phys. Chem. A* **2001**, *105*, 3132.
- (14) Geiger, F. M.; Pibel, C. D.; Hicks, J. M. *J. Phys. Chem. B* **2001**, *105*, 4940.
- (15) Molina, M. J.; Molina, L. T.; Zhang, R. Y.; Meads, R. F.; Spencer, D. D. *Geophys. Res. Lett.* **1997**, *24*, 1619.
- (16) Danilin, M.; Shia, R.; Ko, M.; Weisenstein, D.; Sze, N.; Lamb, J.; Smith, T.; Lohn, P.; Prather, M. *J. Geophys. Res.* **2001**, *106D*, 12727.
- (17) Jackman, C. H.; Considine, D. B.; Fleming, E. L. *Geophys. Res. Lett.* **1998**, *25*, 907.

## YVES A. MANTZ

### EDUCATION

- Massachusetts Institute of Technology**, Cambridge, MA  
Ph.D. in Chemistry 02/2002  
Thesis title: *Theoretical and Experimental Studies of Heterogeneous Chemical Processes leading to Stratospheric Ozone Depletion*  
Co-advisors: Professors Mario J. Molina (Chemistry) and Bernhardt L. Trout (Chemical Engineering)
- Franklin & Marshall College**, Lancaster, PA  
B.A. Chemistry, Physics minor *Summa Cum Laude* and Chemistry Honors thesis 05/1996  
Honors thesis title: *Polarized Specular Reflectance Spectroscopy of a Manganese Methyl TACN Dimer and Calculations of Perturbations in Metal Tetracyanonickelates, Models of One-Dimensional Conductors*

### RESEARCH EXPERIENCE

- IBM T. J. Watson Research Center** 2002–  
As a postdoctoral associate employed by Indiana University, studying the structural and dynamic properties of biochemical and catalytic materials using state-of-the-art theoretical techniques
- MIT Department of Chemistry** 1996–02  
Discovered a (potentially) significant new mechanism for ozone depletion in the polar stratosphere  
• Developed computer models of the atmospherically relevant substrates ice *I<sub>h</sub>* and nitric acid trihydrate  
• Characterized physisorption and surface dynamics of small molecules (i.e., HCl)  
• Quantified effect of adsorbates on surface disordering  
• Employed state-of-the-art theoretical techniques on SGI Origin workstations & supercomputers  
• First-authored scientific publications in peer-reviewed journals and contributed talks and posters  
• Participated in preparing a three-year NSF research grant proposal  
*Other graduate research experience:*  
• Made preliminary measurements of the efficiency of HCl + ClONO<sub>2</sub> on Space Shuttle dust using a specially modified chemical ionization mass spectrometer and on vapor-deposited ice
- Franklin & Marshall College Department of Chemistry** 1995–96  
• Used CAChe (Computer Aided Chemistry), polarized reflectance spectroscopy, x-ray diffraction
- Franklin & Marshall College Department of Physics** 1991,94  
• Monitored CO concentration near a major roadway using a state-of-the-art tunable diode laser system  
• Analyzed infrared spectra of PbEuTe alloys to optimize laser performance

### COMPUTER SKILLS AND LANGUAGE PROFICIENCY

- *Operating Systems:* SGI Irix, Windows NT, Redhat Linux, Apple Macintosh
- *Programming Languages:* FORTRAN 77, BASIC, C, HTML, Pascal
- *Chemistry/Mathematical Software:* CPMD 3.3, Gaussian 94/Gaussview, Cerius<sup>2</sup>, Mathematica, CAChe
- French (seven years of classroom study)

### AWARDS AND SOCIETY MEMBERSHIPS

- Center for Global Change Science Fellowship (MIT research fellowship) 1997–01
- MIT Martin Society for Environmental Sustainability Fellow 1998
- Honorable Mention NSF Graduate Fellowship 1996
- John Marshall Scholarship (academic scholarship awarded by Franklin & Marshall College) 1992–96
- John Kershner Scholar in Physics and Astronomy (high undergraduate physics GPA) 1996
- The Theodore Alexander Saulnier Chemistry Prize (high undergraduate chemistry GPA) 1996
- The W.E. Weisgerber Chemistry Award (departmental leadership) 1996
- American Institute of Chemists Student Award (undergraduate research) 1996
- Phi Beta Kappa and Sigma Pi Sigma National Physics Honor Society 1996
- Hackman Summer Research Scholar (physics, chemistry) 1994,95

## **TEACHING EXPERIENCE AND TUTORING**

### **MIT Department of Chemistry**

- *Kinetics of Chemical Reactions (5.68), Teaching Assistant* 2000  
Graded problem sets and exams and assisted students individually with homework problems and course concepts (one section, five graduate students)
- *Thermodynamics and Kinetics (5.60), Teaching Assistant* 1997  
Prepared and presented a weekly recitation lecture, graded problem sets and exams, and assisted students individually (two sections, fifteen students each)
- *Advanced Chemical Experimentation (5.33), Laboratory Assistant* 1996  
Taught and supervised the experiment Molecular Spectroscopy of Acetylene, graded students' oral presentations, and assisted students individually (15 weekly sections, three students each)

### **MIT Office of Minority Education**

- *Chemistry Tutor* 1997  
Assisted a group of five students weekly with understanding General Chemistry concepts  
Related experience: Tutored privately three students at different times over a four-year period (1991–94) in Organic Chemistry, Physics, Precalculus, and French

### **Johns Hopkins University – Center for Talented Youth**

- *Selected Topics in Advanced Chemistry, Laboratory Assistant* 1993,94  
Set up lab and delivered a prelab lecture daily, supervised and assisted students, and graded lab reports and quizzes

## **PRESENTATIONS CONTRIBUTED AT CONFERENCES, ORAL AND POSTER**

- (1) “Car-Parrinello simulations of the disordering of ice and dissociation of HCl, relevant to stratospheric chemistry” 08/2001  
YA Mantz, FM Geiger, LT Molina, MJ Molina, BL Trout  
The 222<sup>nd</sup> National Meeting & Exposition Program of the American Chemical Society, Chicago, IL
- (2) “Car-Parrinello molecular dynamics study of the interaction of HCl with the (0001) face of hexagonal ice: Mechanistic implications for ozone hole formation” 06/2001  
YA Mantz, FM Geiger, LT Molina, MJ Molina, BL Trout  
The 2001 Meeting of the Division of Computational Physics, American Physical Society, MIT
- (3) “A New GC-MS Apparatus to Investigate Atmospheric Chemical Reactions on Aerosol Particles” 05/1998  
MM Haider, YA Mantz, LT Molina, MJ Molina  
1998 Spring Meeting of the American Geophysical Union, Boston, MA  
  
(A similar poster was presented at the 1998 MIT EAPS Fall Retreat, Waterville Valley, NH).
- (4) “Spectroscopy of a Manganese Methyl TACN Dimer and Calculations of Perturbations in Metal Tetracyanonickelates” 04/1996  
YA Mantz and RL Musselman  
Intercollegiate Student Chemists Convention at Ursinus College
- (5) “Determination of Carbon Monoxide (CO) Concentration in the Atmosphere using a Trace Gas Monitoring System” Fall 94  
YA Mantz, AW Mantz, and other student co-authors  
30<sup>th</sup> Annual Meeting of the Student Section of the APS Southeastern Section at Penn State University  
  
Other posters presented at the 1994 and 1995 Hackman Research Fairs at Franklin and Marshall College based on summer research completed.

## **PUBLICATIONS**

- (1) "A Theoretical Study of the Interaction of HCl with Crystalline NAT"  
YA Mantz, FM Geiger, LT Molina, MJ Molina, BL Trout, submitted to *J. Phys. Chem. A*, **2001**
- (2) "The interaction of HCl with the (0001) face of hexagonal ice studied theoretically via Car-Parrinello molecular dynamics"  
YA Mantz, FM Geiger, LT Molina, MJ Molina, BL Trout, *Chem. Phys. Lett.* 348, 285-292, **2001**
- (3) "First-Principles Theoretical Study of Molecular HCl Adsorption on a Hexagonal Ice (0001) Surface"  
YA Mantz, FM Geiger, LT Molina, MJ Molina, BL Trout, *J. Phys. Chem. A* 105, 7037-7046, **2001**
- (4) "First-principles molecular-dynamics study of surface disordering of the (0001) face of hexagonal ice"  
YA Mantz, FM Geiger, LT Molina, MJ Molina, BL Trout, *J. Chem. Phys.* 113, 10733-10743, **2000**
- (5) "Measurements of the refractive index of PbEuTe in the 3-10  $\mu\text{m}$  region of the infrared"  
Z Feit, R Woods, D Kostyk, R Papez, YA Mantz, MA Cummings, AW Mantz, *Appl. Optics* 32, 966-970, **1993** and *errata, ibid.*, 6187

## **REFERENCES**

Professor Glenn J. Martyna  
IBM T. J. Watson Research Center  
P.O. Box 218  
Yorktown Heights, NY 10598  
(914) 945-1578  
martyna@us.ibm.com  
gmartyna@indiana.edu

Professor Mario J. Molina  
Department of Earth, Atmospheric, and Planetary Sciences and of Chemistry  
Massachusetts Institute of Technology Rm 54-1814  
Cambridge, MA 02139  
(617) 253-5081  
mmolina@mit.edu

Professor Bernhardt L. Trout  
Department of Chemical Engineering  
Massachusetts Institute of Technology Rm 66-556  
Cambridge, MA 02139  
(617) 258-5021  
trout@mit.edu

Professor Jeffrey I. Steinfeld  
Department of Chemistry  
Massachusetts Institute of Technology Rm 2-221  
Cambridge, MA 02139  
(617) 253-4525  
jisteinf@mit.edu